INL/EXT-14-33319

Advanced Test Reactor Core Modeling Update Project

David W. Nigg and Kevin A Steuhm

September 2014

The INL is a U.S. Department of Energy National Laboratory
operated by Battelle Energy Alliance

INL/EXT-14-33319

Advanced Test Reactor Core Modeling Update Project

David W. Nigg and Kevin A Steuhm

September 2014

Idaho National Laboratory

Idaho Falls, Idaho 83415

http://www.inl.gov

Prepared for the
U.S. Department of Energy
Office of Nuclear Energy
Under DOE Idaho Operations Office
Contract DE-AC07-05ID14517

INL/EXT-14-33319

Advanced Test Reactor Core Modeling Update Project

Annual Report for Fiscal Year 2014

Edited by: David W. Nigg, Principal Investigator

and

Kevin A. Steuhm, Project Manager

September 2014

Advanced Test Reactor Core Modeling Update Project

Annual Report for Fiscal Year 2014

Edited by: David W. Nigg, Principal Investigator and

Kevin A. Steuhm, Project Manager

Idaho National Laboratory
Nuclear Science and Technology Directorate
for the
ATR Life Extension Program
Idaho Falls, Idaho 83415

Prepared for the
U.S. Department of Energy
Office of Nuclear Energy
Under DOE Idaho Operations Office
Contract DE-AC07-05ID14517

Nuclear Science and Technology Directorate

Advanced Test Reactor Core Modeling Update Project
Annual Report for Fiscal Year 2014

INL/EXT-14-33319
September 2014

EXECUTIVE SUMMARY

Legacy computational reactor physics software tools and protocols currently used for support of Advanced Test Reactor (ATR) core fuel management and safety assurance, and to some extent, experiment management, are inconsistent with the state of modern nuclear engineering practice, and are difficult, if not impossible, to verify and validate (V&V) according to modern standards. Furthermore, the legacy staff knowledge required for effective application of these tools and protocols from the 1960s and 1970s is rapidly being lost due to staff turnover and retirements. In late 2009, the Idaho National Laboratory (INL) initiated a focused effort, the ATR Core Modeling Update Project, to address this situation through the introduction of modern high-fidelity transport theory based computational software and models to replace the legacy methods, with appropriate verification and validation (V&V) protocols according to applicable national standards. The project has now completed its fifth, and last, full year of development activity, and has entered an accelerated deployment phase that is expected to run through 2015.

New computational tools include:

- The 2-dimensional HELIOS deterministic transport code for integrated ATR core fuel and experiment management and Core Safety Analysis Package (CSAP) physics data generation
- The MCNP5 3-dimensional stochastic simulation (Monte Carlo) code for verification and validation applications and for specialized ATR core analysis along with its longstanding traditional role in experiment support
- The 2-dimensional deterministic NEWT transport code and the 3-dimensional KENO6 stochastic simulation code, with their SCALE-based support infrastructure for use in V&V applications and as supporting modules for sensitivity-uncertainty analysis via the TSUNAMI system
- The ATTILA 3-dimensional discrete-ordinates transport code for specialized experiment support and possibly other applications

The advanced 3-dimensional stochastic simulation codes MC21 and SERPENT are also under study for possible formal inclusion in the updated ATR physics methods portfolio at an appropriate time in the future. Furthermore, several new benchmark-quality code validation measurements based on neutron activation spectrometry have been conducted at the ATRC and protocols for validation of computed neutron flux distributions and spectra as well as for validation of computed fission power distributions, based on well-recognized least-squares statistical analysis techniques, have been established and demonstrated**.**

Although the comprehensive demonstration of a few detailed procedure-specific technical capabilities for ATR Core Safety Analysis (CSAP) support remains to be completed during the 2015 implementation campaign, the new computational reactor physics methodologies are now generally operational, they have been applied retrospectively to all cycles since 145A (August 2009), and are now being used for informal preparation of prospective CSAP physics data in parallel with the established PDQ7-based CSAP physics support process. Furthermore, extensive neutron flux and fission power distribution validation protocols based on current national standards have been established and demonstrated for all of the key new reactor physics codes of primary interest.

The new methodology for ATR computational reactor physics applications will provide significantly higher fidelity with fewer mathematical approximations via a transport theory based approach, in contrast to the diffusion theory based legacy methodology. The new approach permits direct, detailed, explicit modeling of the ATR core as well as explicit modeling of hardware loaded in the flux traps and other experiment positions, with or without fissile content. It is not necessary to pre-compute effective diffusion theory parameters for experiments and highly-absorbing regions of the core such as control shim blades based on various equivalence theory approximations, as is done in the legacy methodology. These new capabilities will greatly facilitate the management of multiple, potentially interacting experiments in each cycle. Furthermore, the new verification and validation protocols offer significantly improved rigor for quantification of uncertainties associated with

computed fission power distributions throughout the core fuel elements as well as for neutron spectra within the ATR core fuel elements and within the various experiment positions.

While it should be noted that code validation in reactor physics is a continuous process of data assimilation and model improvement throughout the software life cycle, this Annual Report and its predecessors provide a number of specific validation protocol example applications from which one can deduce the following basic parameters related to the estimated statistical bias and uncertainty of the new methodology as applied to the ATR and ATRC:

- Calculated absolute volume-integrated fission powers in unirradiated fuel elements have been demonstrated to have *a priori* uncertainties in the range of 3%-6% (1σ) relative to corresponding measurements in the case of the ATR and the ATRC with standard 7F type fuel elements, depending on which specific modeling code is used. This is comparable to the documented uncertainty of the validation measurements themselves. The computed *a priori* fuel element power uncertainties increase slightly, to the range of 3%-8% (1σ) for ATRC with its standard Mark IV, Mark V and Mark VI type fuel elements, most likely due to uncertainties in the boron content of these older types of elements. In almost all cases, the three-dimensional models tend to exhibit *a priori* uncertainties nearer the lower ends of the ranges quoted, and the two dimensional models tend to have uncertainties nearer the higher ends.

- Calculated (HELIOS) absolute pointwise fission powers within unirradiated ATR 7F core fuel elements in the ATRC have *a priori* uncertainties in the range of 8%-10% (1σ), with negligible systematic bias except for points very near the outer azimuthal side plates of each fuel element. In these regions there appears to be a mean downward bias of about 13% in the calculations relative to measurements at the core axial midplane. A similar bias and uncertainty pattern was also observed with the legacy PDQ7 model of the ATR core. This appears to be a three-dimensional effect associated with the presence of side plate flow vents in the under-moderated fuel elements at various axial heights.

- Calculated lobe powers for typical ATR core fuel loading patterns that include both fresh as well as irradiated fuel elements have *a priori* uncertainties of approximately 5% (1σ) relative to corresponding ^{16}N system measurements, averaged over all ATR cycles run since August 2009 (Cycle 145A onward). This is comparable to the estimated uncertainties of the online lobe power measurements themselves. A slight downward trend in the lobe power uncertainties was observed over time since 2009, possibly due to continuous improvement of the fuel element nuclide inventory data base as more and more cycles are modeled with HELIOS. This offers an indirect validation of the HELIOS methodology for power calculations in irradiated fuel elements, but only on a lobe-integrated basis. Validation on an element basis will require development of additional experimental data, via post-cycle non-invasive measurements of the burnup of each element, online element power measurements, or some combination of the two.

- Detailed neutron spectra in the flux traps and core fuel elements of the ATRC (and by extension, the ATR) can be quantified to an absolute *a priori* accuracy of 10% -15% (1σ) in the thermal, epithermal, and fission neutron emission energy ranges relative to corresponding activation measurements.

- Approximately 90% of the retrospective HELIOS initial critical shim cylinder rotation predictions for all ATR cycles run since August 2009 (Cycle 145A forward) fell within the procedural acceptance criteria, without reliance on the standard "empirical" adjustment used to help estimate critical shim rotations in concert with the legacy PDQ7 methodology. Furthermore, 100% of the retrospective HELIOS initial critical shim rotation estimates since Cycle 150A fell within the procedural acceptance criteria, again possibly due to improvement in the fuel nuclide inventory data base over time. Finally, the observed mean systematic bias of the *a priori* initial critical shim rotation predictions since August 2009 was approximately half of that associated with the corresponding PDQ initial critical shim rotation predictions.

In summary, experience to date, including the new developments summarized in this Annual Report, indicates that the computational reactor physics methodology based on the HELIOS code and supporting auxiliary software can replace the capabilities of the legacy PDQ7-based methodology via a focused formal deployment campaign within the next 6-12 months, with the relatively minor caution that significant additional validation will be needed

prior to full deployment of a planned MCNP5-based method for correction of two-dimensional HELIOS results for axial effects as a routine replacement for the legacy ROSUB data post-processing formulations. In the meantime, the established ROSUB methodology will continue to be used, augmented as needed on a case by case basis by the MCNP5-based approach as it matures.

It is also important to recognize that the ATR Core Modeling Update Project represents not only an investment in new technology. It also represents a key investment in the new generation of INL scientific and engineering staff who will, by demographic necessity, assume leadership roles in the overall ATR enterprise over the next several years. Accordingly, several students and early-career INL Scientific and Engineering staff members have been proactively integrated into the effort, one student earned his doctoral degree in 2012, and two additional students (1 MS and 1 PhD) completed their advanced degrees early in Fiscal Year 2014 as a result of their involvement in the project.

Finally, we note that although formal implementation of the new computational models and protocols is anticipated to extend through 2015, interim informal applications of the new capabilities in the much nearer term have already proven useful. For example, these demonstrations included an analysis that was useful for understanding the cause of some ATR operational issues in February 2013 that were triggered by a larger than acceptable discrepancy between the estimated and measured critical shim position for Cycle 153A. Additionally, some initial computational support for a planned ATR irradiation experiment being conducted for a foreign customer was initiated in 2013 using the new methods. Furthermore, the new code system is also being used extensively for core design calculations associated with the possible conversion of the ATR to a low-enriched uranium (LEU) type fuel. As the Core Modeling Update Project proceeds, we anticipate further such interim, informal applications in parallel with formal qualification of the system under applicable INL and external Quality Assurance procedures and standards.

CONTENTS

ACRONYMS

AGR	Advanced Gas Reactor
ANS	American Nuclear Society
ATR	Advanced Test Reactor
ATRC	Advanced Test Reactor Critical Facility
CIC	Core Internals Changeout
CSAP	Core Safety Assurance Package
ENDF	Evaluated Nuclear Data File
EPP	Effective Plate Power
EPtP	Effective Point Power
NGNP	Next Generation Nuclear Plant
NST	Nuclear Science and Technology
NSUF	National Scientific User Facility
RERTR	Reduced Enrichment for Research and Test Reactors
V&V	Verification and Validation
DHA	Detector Housing Assembly
HPGe	High Purity Germanium
HPXe	High Pressure Xenon
INL	Idaho National Laboratory
$LaBr_3$	Lanthanum Bromide
OSCC	Outer Shim Control Cylinder
ESAP	Experiment Safety Analysis Package
IRPhE	OECD International Reactor Physics Experiment Evaluation (Program)
OECD	Organization for Economic Cooperation and Development
QA	Quality Assurance
LEP	(ATR) Life Extension Program
ICSBE	OECD International Criticality Safety Benchmark Experiment Evaluation (Program)
DOE	(US) Department of Energy
NR	Naval Reactors
UFSAR	ATR Updated Final Safety Analysis Report
USQD	Unreviewed Safety Question Determination
USQ	Unreviewed Safety Question
VTT	National Research Centre (Finland)

ACKNOWLEDGEMENTS

The authors and editors of this Annual Report gratefully acknowledge the many absolutely essential technical contributions of INL scientific staff members Anthony LaPorta, James Parry, Mark DeHart, William Skerjanc, Ben Chase, Troy Unruh, Doug Crawford, and Scott Lucas to the ATR Core Modeling Update Project. We also thank Charles Wemple, Studsvik Scandpower, for his valuable assistance in the setup of the various HELIOS models, for the training of key INL staff members in the use of HELIOS, and for his overall review of the HELIOS ATR model effort as it has proceeded. Additionally, we thank Christine White (INL) for her assistance with many of the graphic illustrations in the various reports that have been published during the project, Neil Boyce (INL) for the fabrication of new experimental hardware for use in the ATRC and ATR flux traps, and INL Radiation Measurements Laboratory (RML) staff members Chris Jensen, Larry Smith, Gene Taylor and Ron Murray for their assistance in development of the physics measurement data associated with the validation experiments conducted in the ATRC, the operation of which was led by Kirk Steuve and Craig Jackson. We also acknowledge the management and administrative staff of the ATR Life Extension Program for their steadfast support of the ATR Core Modeling Update Project over the past 5 years, with a special thanks to Paul Henslee for his overall program leadership during the entire time. Additionally, we wish to thank Dr. John Williams, University of Arizona, for his valuable counsel with regard to the least-square adjustment based validation protocols that have been adapted for use with the ATR. Finally, we gratefully acknowledge the key support of Art Clark, INL Deputy Laboratory Director, for his forward vision that was essential for originally initiating the ATR Core Modeling Update project.

1.0 INTRODUCTION AND BACKGROUND

David W. Nigg

Longstanding diffusion theory based computational reactor physics software tools and modeling protocols for support of Advanced Test Reactor (ATR) core fuel management and safety assurance and, to some extent, experiment management, are no longer consistent with the state of modern nuclear engineering practice. They are also difficult to verify and validate (V&V) according to modern standards. Furthermore, the legacy staff knowledge required for application of these tools and protocols from the 1960s and 1970s is declining due to staff turnover and retirements. In response, the Idaho National Laboratory (INL) has initiated a focused effort, the ATR Core Modeling Update Project, to address this situation through the introduction of modern high-fidelity computational software, along with corresponding validation protocols that are consistent with current standards.

The ATR Core Modeling Update Project began in late 2009 and has now completed the fifth, and last, full year of the currently-planned developmental workscope. Key accomplishments to date have encompassed both computational as well as experimental work. A new suite of modern stochastic and deterministic transport theory based reactor physics codes and their supporting nuclear data libraries has been installed at the INL under various licensing arrangements. Corresponding models of the ATR and its companion critical facility (ATRC) are now operational, demonstrating the basic feasibility of the new code packages for their intended purpose, as described in Chapter 3 of this Annual Report. Furthermore, a set of as-run core depletion HELIOS calculations for all ATR cycles since August 2009 through April 2014 (Cycle 145A through Cycle 155B), has been completed, providing key validation data. This major effort supported a decision in Fiscal 2014 to proceed with the phased incorporation of the HELIOS methodology into the ATR Core Safety Analysis Package (CSAP) preparation process during Fiscal 2015, initially running informally in parallel with the legacy PDQ7-based methodology (Pfeiffer, 1971).

On the experimental side of the project, the first five of six new, application-specific, ATRC physics code validation measurements based on neutron activation spectrometry have been completed in accordance with applicable national and international standards. These experiments complement the validation data obtainable from the online instrumentation systems in the ATR itself. Some results of the fifth experiment, along with a major extension of the analysis of a previously-reported (Nigg and Steuhm, 2013) ATRC physics experiment designed to support a "depressurized" low-power run (Cycle 152A) of the ATR that was conducted late in 2012 are presented in this Annual Report The ATRC validation measurements and analysis will continue through the first half of Fiscal 2015 and will include the introduction of additional new experimental hardware to broaden the scope of the protocols.

1.1 Description of the Advanced Test Reactor and the ATR Critical Facility

The ATR is one of only a few high-power research reactors of its type in the world, with a variety of missions involving accelerated testing of nuclear fuel and other materials in a very high neutron flux environment, medical and industrial isotope production, and other applications. Along with its companion critical facility, the ATRC, the ATR is one of the key nuclear engineering research and testing facilities within the US Department of Energy (DOE) National Laboratory Complex. The ATR and ATRC also serve as the centerpieces of the recently-formed ATR National Scientific User Facility (NSUF), whose purpose is to facilitate the current trend toward broadening the applications of the ATR beyond its traditional base.

The ATR (Figures 1.1 and 1.2) is a geometrically-complex heterogeneous light-water and beryllium moderated, beryllium reflected, light-water cooled system with highly-enriched (93% ^{235}U) plate-type fuel elements arranged in a serpentine pattern. Gross reactivity and power distribution control during operation is achieved through the use of eight pairs of rotating control drums with hafnium neutron absorber plates on one side as can be seen in Figure 1.1. There are several design features incorporated into the ATR and ATRC to optimize experimental capabilities. These features include: a) the use of flux traps to provide high thermal neutron fluxes for irradiation of experiments in nine regions, b) incorporation of special control shim design features to help retain axial flux

symmetry to the extent possible throughout an ATR fuel cycle; and c) regional power control to provide capability for power shifting between core lobes to optimize the transverse neutron flux distribution for a wide range of simultaneous experiments. The ATR can be operated at powers as high as 250 MW although most routine applications do not require the maximum power. Typical thermal neutron fluxes in the flux traps can be as high as 5.0×10^{14} n/cm^2-s. Typical operating cycle lengths are in the range of 45–60 days. The core fuel configuration and the experiment loadings are usually rearranged between cycles and each fuel element is typically burned for two or three cycles during its useful lifetime.

The ATRC (Figures 1.3 and 1.4) is an open-pool nuclear mock-up of the ATR that typically operates at approximately 600 W and produces thermal neutron flux levels in the traps in the range of 1.0×10^9 n/cm^2-s. As is the case for the ATR, the core consists of a 4-ft-high (122 cm), uniform-width, vertical 40-element fuel annulus shaped in a serpentine fashion between and around the nine primary flux-trap regions located in a three-by-three square array. The cruciform fixture inside the serpentine is called the neck shim housing. As with the ATR, the reactivity of the ATRC core is controlled by: (a) five vertically withdrawn safety rods that use cadmium as the poison material; (b) 24 vertically withdrawn hafnium neck shim rods; and (c) eight pairs of rotating outer shim control cylinders (OSCCs) that use hafnium poison plates.

ATRC criticality can normally be stably attained at a power as low as 0.25 mW and the maximum rated power is 5 kW. The ATRC facility is typically used with prototype experiments to characterize in advance, with precision and accuracy, the expected changes in core reactivity and fission power distribution for the same experiments in the ATR. Useful physics data can also be obtained for evaluating the worth and calibration of control elements as well as thermal and fast neutron distributions.

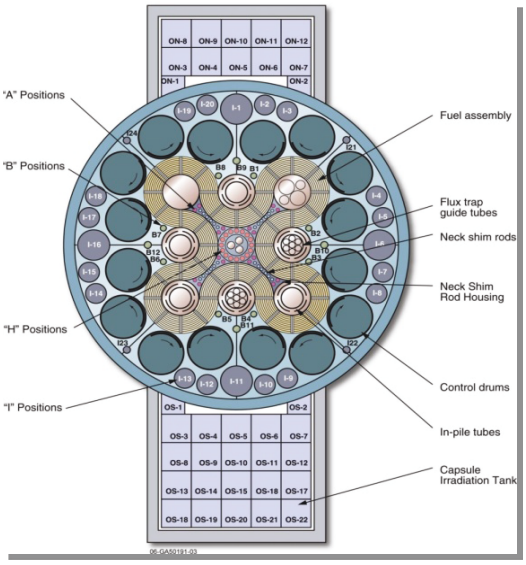

Figure 1.1. Core and reflector geometry of the Advanced Test Reactor.

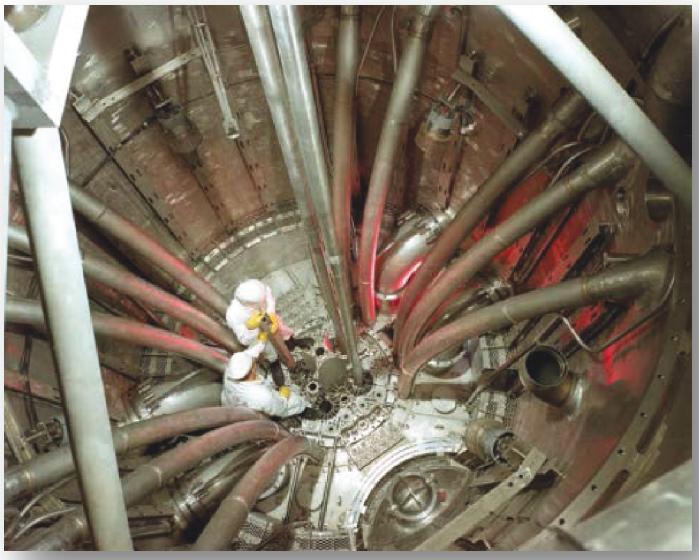

Figure 1.2. View into the ATR pressure vessel (File Photo, ca 1967).

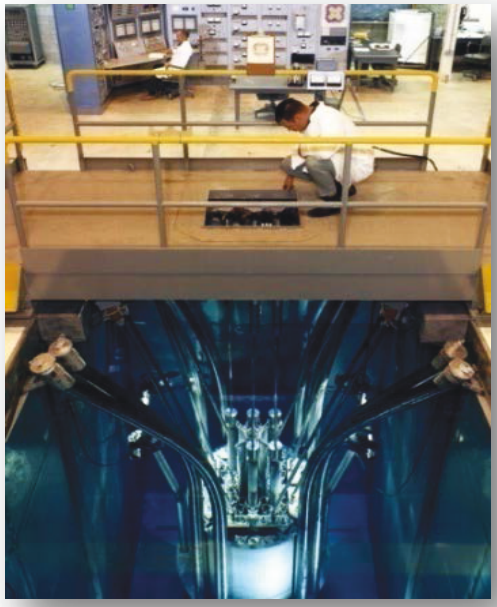

Figure 1.3. The Advanced Test Reactor Critical Facility (File Photo, ca 1967).

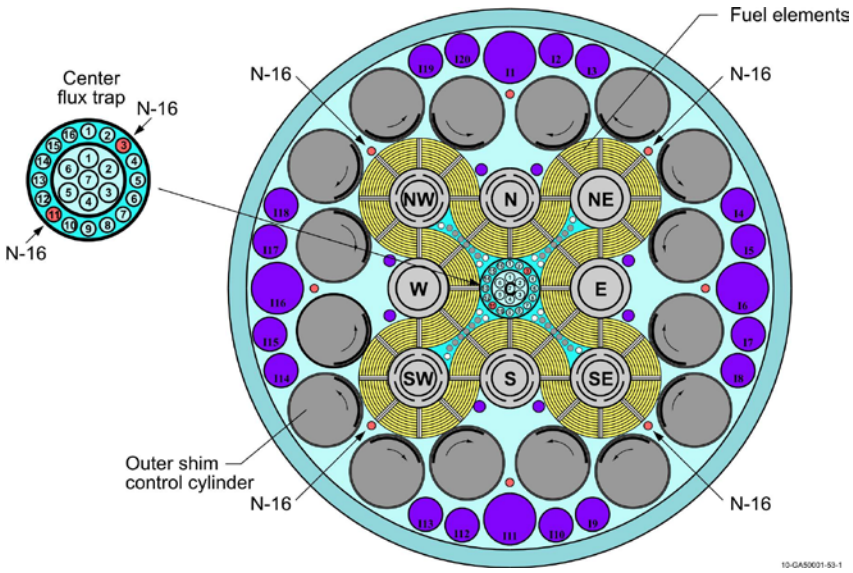

Figure 1.4. Example ATRC Configuration (File Illustration, ca 1967).

1.2 Rationale and Objectives for Update of ATR Core Physics Modeling Methods

Computational reactor physics modeling is used extensively to support current ATR operations and HEU fuel cycle management, core and experiment safety analysis, experiment hardware design, and many other applications. Experiment hardware design and analysis for the ATR generally involves very detailed and sophisticated three-dimensional Monte Carlo analysis, typically using the internationally-recognized continuous-energy MCNP5 code (Goorley et al., 2004) or an equivalent methodology, coupled to extensive fuel isotope buildup and depletion analysis where appropriate. On the other hand, the computational reactor physics software tools and protocols currently used for ATR core fuel cycle analysis and operational support are largely based on four-group diffusion theory in Cartesian geometry as implemented in the PDQ7 code (Pfeifer et al., 1971) with heavy reliance on "tuned" nuclear parameter input data. The latter methods have been superseded in the general reactor physics community by high-fidelity multidimensional stochastic and deterministic transport-theory-based methods. As a result, the historical approach to ATR reactor physics operational support is no longer consistent with the state of modern nuclear engineering practice as defined, for example, in ANSI/ANS-19.3 (ANS, 2005). Furthermore, in some situations the legacy models can be nearly impossible to validate against experiment data according to typical modern protocols as defined in ASTM Standards E-261, E262, E944 (ASTM, 2010, 2008, 2008) and in related documentation.

In response to this situation, the INL is engaged in a multiyear effort to modernize the computational reactor physics tools and validation protocols needed for support of ongoing ATR operations. The ATR Core Modeling Update Project has now completed its final full year (Fiscal 2014) under the auspices of the ATR Life Extension Program (LEP) funded by the DOE Office of Nuclear Energy. The ATR Core Modeling Update Project is an aggressive computational and experimental campaign that will have a broad strategic impact on the operation of the ATR, both in terms of improvement of current HEU operations as well as in terms of providing a modern computational capability to support the currently-ongoing conceptual design effort associated with the possible conversion of the ATR to Low-Enriched Uranium (LEU), without reliance on the legacy physics methods at any stage.

1.2.1. Reactor Physics Computational Methods Upgrades. Figure 1.5 shows the suite of new reactor physics computational tools that are being brought into operation under the ATR Core Modeling Update Project, how they generally relate to one another, and how they will support ATR operations. Extensive details of the code capabilities, the selection process and various V&V strategies have been published separately (Nigg and Steuhm, 2011, 2012, 2013; Nielsen et al., 2013; Nigg et al., 2012a, 2012b). The illustration in Figure 1.5 is not a computational flow chart or procedure *per se*. Specific computational protocols using the tools shown in Figure 1.5 for routine ATR support applications will be defined in approved procedures and other operational documentation. These documents will prescribe the geometric modeling input files, nuclear data files, and other aspects of each specific computational protocol. For example there will be an updated procedure for computation of Core Safety Analysis Package (CSAP) physics support data for a particular ATR operational cycle using the new tools.

The following general requirements associated with the improved core analysis methodology were identified and refined during the project:

- The models used must be based on state-of-the-art analytical methods that can be run on modern desktop computer systems and high-performance clusters in a machine-independent manner. Application of existing standards, current computational methodologies, validation strategies, and proven software accepted in the international commercial nuclear industry is highly preferred wherever possible. Although development of even higher-fidelity reactor physics computational tools is always ongoing, the emphasis in the current phase of this project has been on verified, US commercial or National Laboratory reactor physics software.

- The models used in the development must be verified and validated against existing data and reference calculations, and against new measured validation data as warranted. Wherever practical, computational biases and uncertainties should be quantified using modern sensitivity/uncertainty analysis and least-squares statistical adjustment techniques.

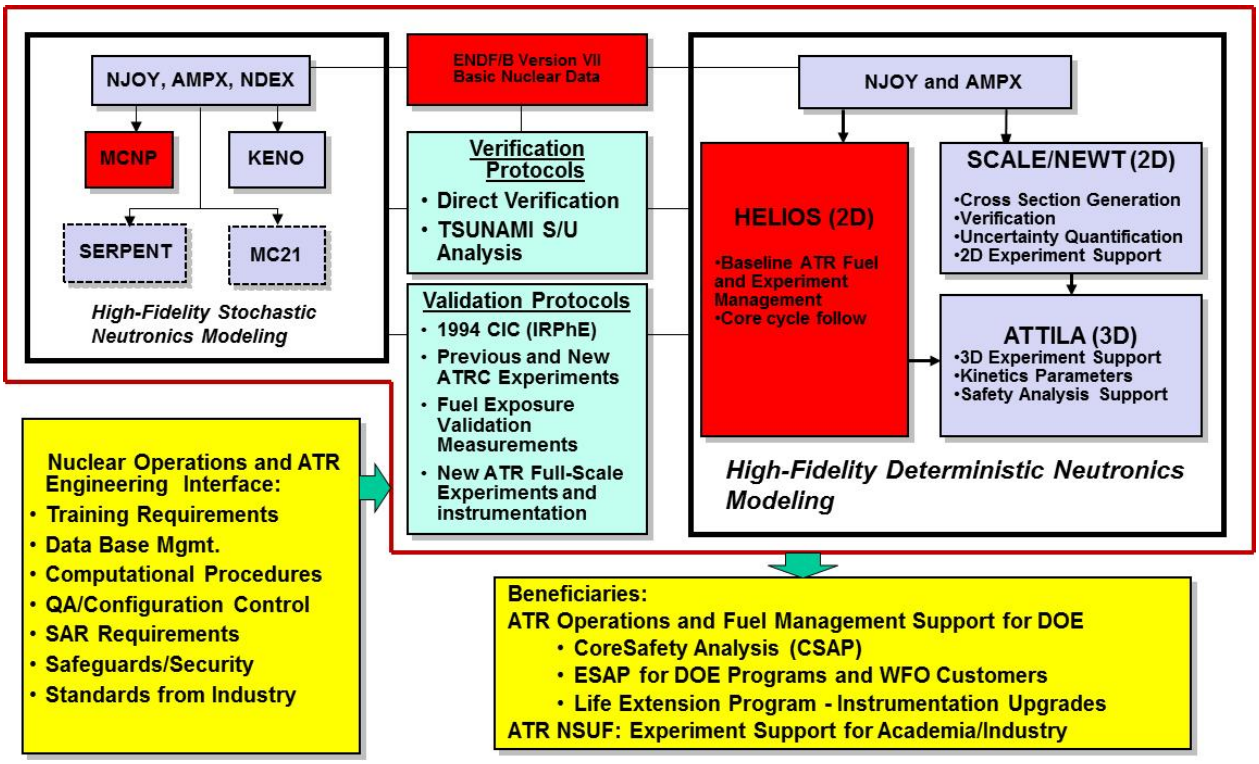

Fgure 1.5. Advanced computational tool suite for support of HEU operations of the ATR and ATRC, with supporting verification, validation, and administrative infrastructure.

Referring again to Figure 1.5 in somewhat more detail, the most recent release of the Evaluated Nuclear Data Files (ENDF/B Version 7) is used to provide the basic cross section data and other nuclear parameters required for all of the modeling codes. The ENDF physical nuclear data files are processed into computationally-useful formats using the standard publically-available NJOY or AMPX (Radiation Safety Information Computational Center, 2010) codes or, in the case of MC21, the NDEX code (Trumbull and Caro, 2009) as shown at the top of Figure 1.5. Some of the modeling codes can use the output data files from the processing codes directly, while others require further manipulation of the data into a suitable format before use.

As noted earlier, the MCNP5 three-dimensional stochastic neutron and photon transport simulation code is already used extensively for ATR experiment design and analysis and, to some limited extent, core analysis. MCNP5 has a very broad base of users worldwide, and it is often considered to be the "Gold Standard" for cross-verification of other neutronic modeling codes per ANS 19.3 guidelines because of its very high-fidelity modeling capabilities, including the use of pointwise representations of the basic nuclear data as a function of neutron energy and the ability to represent very complicated geometric configurations essentially exactly. Furthermore there is already a broad base of validation data for MCNP5 applications to the ATR and the ATRC with HEU fuel at the INL. Thus MCNP5 will be a key component of the overall suite of new modeling tools for core analysis and fuel management as well.

Under the ATR Core Modeling Update Project, we are also introducing the KENO stochastic simulation code (Hollenbach et al., 1996). The KENO code is useful both as a stand-alone analysis and verification tool as well as in conjunction with the TSUNAMI (Broadhead et al., 2004, Williams and Rearden, 2008) sensitivity-uncertainty analysis system available with the SCALE nuclear system analysis package (Bowman et al., 2009). It is this latter application of KENO (Aryaienejad et al., 2010) that is of the most utility for ATR applications, both for HEU as well as possibly for LEU in the future.

Furthermore, we are also incorporating the well-developed MC21 (Sutton et al., 2007) and the relatively new Serpent (Leppänen, 2012) stochastic simulation and depletion codes into the new suite on a provisional basis, as potential additional tools for V&V in the near term via intercode comparisons per ANS 19.3 and possibly as advanced platforms for full three-dimensional Monte Carlo based ATR fuel cycle analysis and fuel management in the longer term. Both of these codes feature integrated capabilities for fuel depletion analysis, facilitating their potential long-term utility for the latter application. Acquisition of Serpent and MC21 was initiated during 2012 and both are now operational at the INL.

The right-hand side of Figure 1.5 shows the new high-fidelity deterministic transport computational tools that are being integrated into the system. HELIOS™ (Studsvik Scandpower, 2008) is a very-mature and well-recognized commercial two-dimensional neutron transport code with general geometry and integrated fuel management and depletion capabilities. Like MCNP5, HELIOS has a very broad international base of users, and it has been validated by Studsvik against a wide variety of Light Water Reactor (LWR) experimental data. It features a self-contained fine-group cross section library, processed from the basic ENDF/B Version 7 files, with an integrated online resonance self-shielding capability that is well-suited for LWR applications. HELIOS is in place at the INL under a permanent sitewide license and, coupled with MCNP5 for treatment of non-separable neutronic effects in the axial dimension when required, as will be discussed later, it will serve for the foreseeable future as the primary reload core design and fuel management tool for ATR, replacing the PDQ7-based four-group diffusion theory methodology.

NEWT (DeHart, 2006) together with its SCALE-based cross section processing support infrastructure (Bowman, 2009) is a well-established and verified software tool developed within the DOE National Laboratory system. It is a two-dimensional transport code based on the "step-characteristic" method for spatial discretization on an arbitrary mesh structure. In the case of INL ATR and ATRC applications, NEWT has served primarily as a lattice code for cross-section generation and as an independent cross-verification tool for HELIOS. NEWT collapses cross section libraries into specified group structures for each nuclide in each material mixture in the model. Cross sections are flux weighted by using the average flux in the mixture (material) for each energy group in the library. As part of the SCALE code package, NEWT is also capable of performing fuel burnup calculations using the ORIGEN-S module of SCALE.

ATTILA (McGhee et al., 2006) is a commercial grade software product in place at the INL under sitewide licenses. It is a three dimensional discrete-ordinates (Sn) neutron transport code that uses the Linear Discontinuous Galerkin (LDG) solution technique. ATTILA requires a preprocessed, resonance-shielded cross section library as an input file, typically generated using SCALE/NEWT or a similar lattice code sequence as mentioned earlier. ATTILA may be useful on occasion for support of ATR and ATRC operations as a cross-verification tool, and it is also available as an experiment analysis tool in situations where full three-dimensional transport calculations are required, but where the stochastic nature of MCNP5 puts it at a disadvantage, for example when attempting to quantify the neutronic effects of small perturbations in the geometry or material composition of one or more components of the overall reactor system being modeled.

All of the code packages described above have various strengths and weaknesses, but taken together they provide the necessary high-fidelity stochastic and deterministic neutron and gamma transport capability that is required for various aspects of ATR and ATRC core physics modeling, both for current HEU operations as well as for support of the anticipated LEU conversion and follow-on operation.

1.2.2 Validation Protocols. Theory and experiment must be consistent in any scientific or engineering enterprise, and any biases and uncertainties must be quantified. This is the function of the validation process for the new code suite. Validation protocols for the various computational ATR physics models are primarily based on neutron activation spectrometry. The protocols for this are designed in accordance with applicable national standards for high-fidelity neutron spectrum measurements (e.g. ASTM-944) and on local INL extensions of those protocols to accommodate applications to fission power distributions (Nigg and Steuhm, 2013, Nielsen et al., 2013). The same protocols will be directly transferrable to LEU core design model validation in the ATRC at such time as one or more prototype LEU fuel plate subassemblies or full fuel elements are available for testing in ATRC and ATR.

Additional validation capabilities using post-irradiation burnup measurements for selected fuel elements are anticipated in the longer term as well (Nigg and Steuhm, 2011, 2012). The latter capabilities may be of particular importance with possible future LEU-fueled cores for the ATR, with their increased plutonium production relative to the current HEU fuel.

Finally we note that verification, i.e., the formal demonstration that a given computer software package is correctly performing its intended mathematical function, is also crucial. However this is largely addressed separately (e.g. in the code reference documents and the Software Quality Assurance Plan associated with the ATR Core Modeling Update Project, and in pertinent refereed literature) in the case of the tools illustrated in Figure 1.5. Nonetheless, Chapter 4 describes a few ATR-specific code verification exercises that have been specifically conducted as part of the project.

1.3 Current Status

The current phase of the ATR Core Modeling Update Project has required approximately 60 months to complete, and the various components of the new methodology are targeted for phased implementation during Fiscal Year 2015 and beyond as noted earlier. Some key accomplishments in the first 60 months of the effort are briefly summarized below, along with a description of ongoing activities and planned next steps in several areas as the project proceeds through the implementation stage in late 2014 and 2015.

- HELIOS, NEWT, ATTILA, and MCNP5 models of ATR and ATRC, with initial direct validation against experimental data, are operational.
- Acquisition of the MC21 and Serpent 3D stochastic simulation codes from DOE-NR and VTT-Finland respectively was completed in FY-2013 and both are now operational at the INL. These codes offer significant additional V&V capability now, as well as a potential longer-term route to full 3D Monte Carlo ATR fuel management and CSAP physics analysis support at an appropriate time in the future. Initial Serpent models of the ATR and the ATRC have been demonstrated, and development of validated MC21 models of ATR and ATRC is underway.
- A production-level HELIOS model of the ATR with fuel depletion and replacement is operational and "as run" retrospective fuel cycle analyses beginning with ATR Cycle 145A and proceeding through Cycle

155B have been completed, with all flux trap experiments and other key core details explicitly represented in the model database. This will provide the basis for additional model upgrades as well as more formal acceptance testing and qualification of the core fuel cycle computational models and protocols in 2015, with the goal of having sufficient technical capability in place to enable a decision to begin using the new computational methods and fuel cycle models as the primary analysis tools by the end of 2015, or any time thereafter as deemed appropriate.

- Capability for rigorous sensitivity-uncertainty analysis using KENO/TSUNAMI is available and has been demonstrated for the ATR (Aryaeinejad, 2010)
- Validation protocol development and demonstration are underway, with a focus on consistency with ASTM-944, which establishes standard protocols for high-fidelity analysis of activation spectrometry data. Complete, peer-reviewed results of statistical validation analyses for the first four (of 6) ATRC irradiations specific to the ATR Core Modeling Update Project were recently published (Nigg et al., 2012a, 2012b).
- The fifth project-specific validation experiment was run in the ATRC late in 2013 as described in this Annual Report, with detailed data analysis completed in 2014. Analysis of additional direct fuel element power validation data referenced to ATR Cycle 152A (the 2012 "Depressurized Run") and the corresponding ATRC supporting configurations was initiated in 2012 (Nigg and Steuhm, 2012) and significantly extended as described in this Annual Report.
- A new algorithm for fuel element power-fitting and uncertainty quantification based on least-squares adjustment techniques is now operational and is currently being applied for support of the depressurized operations of the ATR as well as for future measurements in the ATRC. This original algorithm makes use of a novel method for estimating the fuel element-to-element power covariance matrix required for the adjustment process (Nielsen et al., 2013).
- Feasibility measurements for a permanent non-invasive fuel burnup measurement system were completed using actual irradiated ATR fuel in the ATR canal (Nigg and Steuhm, 2011, 2012) and a proposal for construction of the new system has been submitted to DOE-NE. Some additional improvements to the data analysis algorithms to be used with the proposed system were completed in 2013.

2.0 GENERAL REQUIREMENTS FOR ATR CSAP ANALYSIS

Emily T. Swain

Several different types of physics analyses are performed to satisfy the ATR Updated Final Safety Analysis Report (UFSAR) requirements for each operational cycle. The analyses pertaining to the ATR core as a whole and specifically to the driver fuel are reported in the Core Safety Assurance Package (CSAP). Analyses pertaining to experiments are reported in corresponding documentation created for each experiment, Experiment Safety Assurance Package (ESAP). Taken together, this documentation is intended to demonstrate that the UFSAR requirements are being met for each cycle.

ATR UFSAR requirements documented in the CSAP can be categorized into three general classes of information, as illustrated in Figure 2.1. These classes consist of required neutronic modeling that has traditionally been performed utilizing 2D PDQ diffusion theory core models and strict axial profile assumptions, reactivity estimates intended to conservatively account for three-dimensional effects, and requirements outside of the various neutronic calculations. The focus of the ATR Core Modeling Update Project has been to fully replace the required neutronic modeling with transport-theory-based methodologies and expand the axial profile assumptions so that an increased range of experiments can be accommodated. Requirements outside of the various neutronic calculations are generally detached from or completely independent from neutronic calculations and thus are not expected to be replaced by ATR Core Modeling Update Project codes.

The required neutronic modeling and associated physics data is currently produced by the existing suite of codes associated with the diffusion code PDQ as noted above. The modernization effort underway is designed to replace the current PDQ-based physics analysis methodology with an improved methodology capable of calculating and analyzing data that is ultimately reported in the CSAP documentation per current protocols. Thus, the calculational process used to determine ATR UFSAR requirements has evolved, while the UFSAR requirements themselves have not.

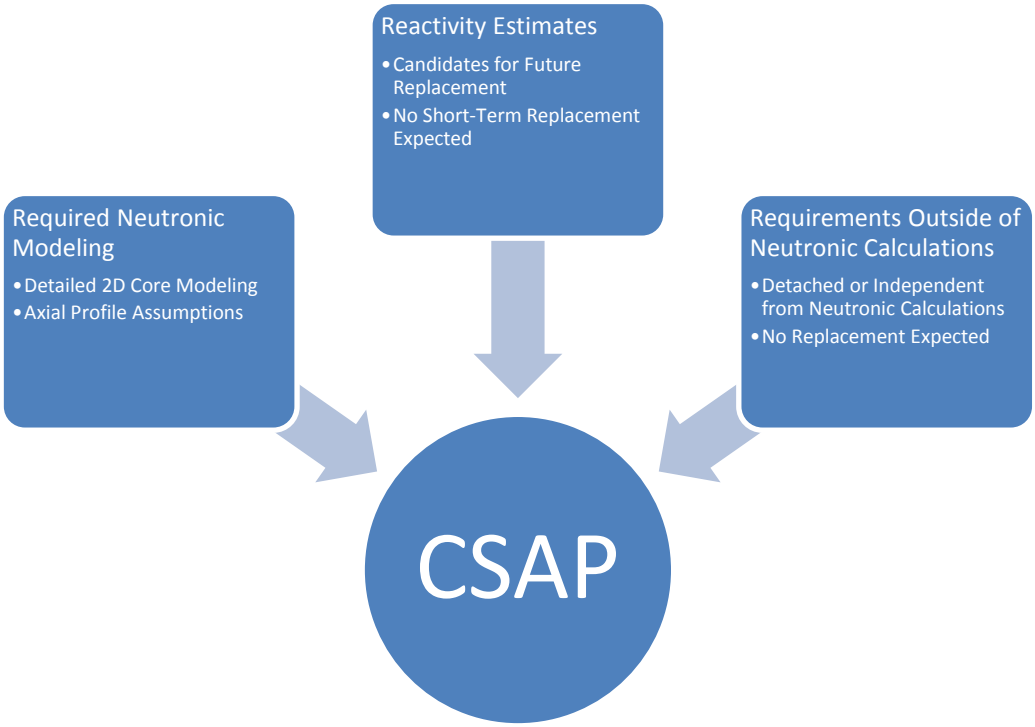

Figure 2.1. Information Classes Relevant to CSAP Production

Figure 2.2 provides an overview of the ATR Core Modeling Update Project status relative to the neutronic modeling requirements specified in the ATR UFSAR, particularly with regard to initial HELIOS deployment. As shown, all modeling requirements have at least a working proof-of-concept available. It is also worth noting that a significant portion of the requirements have capabilities that are currently undergoing comprehensive demonstration prior to being declared ready for deployment. A more detailed assessment pertinent to the current stage of the Modeling Update Project is also available in Table 2.1 at the end of this section.

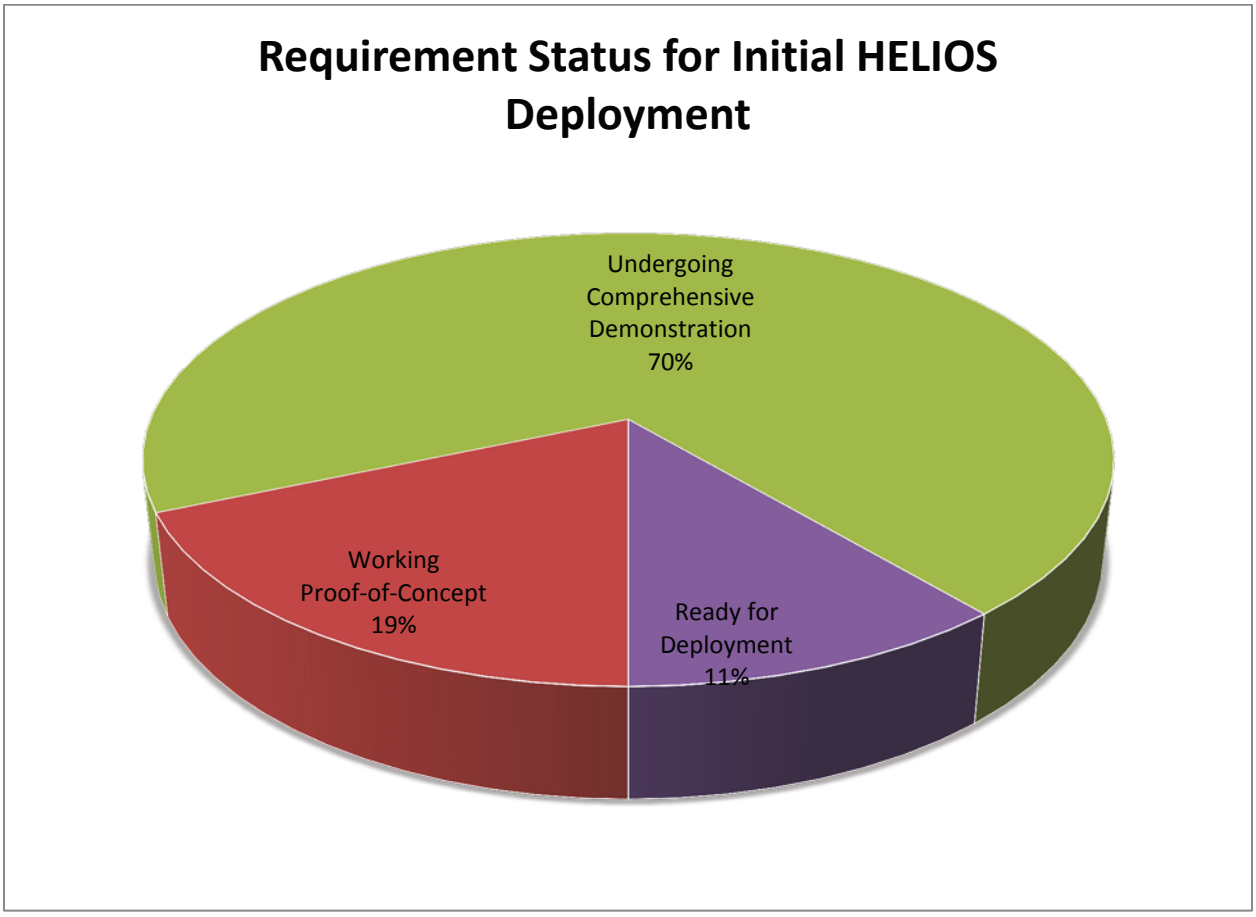

Figure 2.2. Requirement status summary for initial HELIOS deployment.

To successfully replace the historical methods, both the calculational process and the requirements represented in Table 2.1 must be fulfilled. Fulfillment of Table 2.1 requirements does not guarantee a successful replacement if an appropriate process is not developed; likewise process demonstration does not guarantee a successful replacement if requirements cannot be satisfied. Successful methodology replacement implementation must include a rigorous and comprehensive demonstration of the capabilities associated with the calculational process as well as demonstration of the functionalities directly associated with the requirements (as illustrated, for instance, by the cycle modeling exercise documented in Chapter 5.6.3 that includes lobe power functionality).

Final verification and validation of both aspects (calculational process and UFSAR requirements) must be completed and documented with an appropriate level of separation from the methodology developers in order to meet NQA-1 standards. Validation efforts will include both direct validation via available measurement data and code-to-code validation for components that do not have direct measurement data available. Verification efforts will include comparisons to the current codes of record as well as other codes of similar fidelity to the HELIOS code. Detailed acceptance bands must also be developed in collaboration with the ATR Engineering and

Operations organizations for use during acceptance testing of functionalities associated with UFSAR requirements. Reconciling all of these complementary objectives will be a key objective as the ATR Core Modeling Update Project evolves into an accelerated implementation readiness stage during Fiscal Year 2015.

It is also worth noting that the current schedule for initial implementation of the HELIOS-based methodology may require that some requirements not be fully addressed and thus that mitigations be put in place. It is also assumed that assumptions associated with ROSUB multipliers will require replacement to meet specific experiment needs. Deferred improvements associated with the HELIOS-based methodology may include the following: 1) Automation of the Outer Shim Control Cylinder (OSCC) and Neck Shim (NS) position selection process is planned such that selection can be made in a timely manner. In the interim, PDQ may be used to provide the initial estimation of the position selection process, although this may require more manpower than creation of the automation scripts themselves and thus is not preferred. 2) Additional EPP and EPtP constraints and/or sorting methods are needed to significantly decrease the human performance risk associated with meeting the related safety requirements. Multiple detailed reviews may be needed in the interim to mitigate this risk, although attempting to merely mitigate this risk may not be prudent. 3) Modeling of safety rod positioning will be needed whenever physics testing of these components are warranted. It is expected that physics testing of safety rods in the ATR will not be needed within the first few years of implementation. It would also be expected that advanced notice of safety rod physics testing would be available such that deferring deployment of this capability would not adversely affect implementation or general ATR scheduling.

Since the UFSAR requirements have not changed, it is appropriate to evaluate the transition from the PDQ-based methodology to the HELIOS-based methodology purposed by the ATR Core Modeling Update Project in terms of the Unreviewed Safety Question (USQ) process. In order to determine that no Unreviewed Safety Question exists (i.e. that an Unreviewed Safety Question Determination (USQD) would be found to be negative), then all of the UFSAR requirements and underlying computational processes will need to addressed. Addressing these requirements and processes will necessitate that the associated capabilities of the HELIOS-based methodology are ready for deployment or appropriate mitigations are in place at the time of implementation. Additional advancements are needed before a USQD can be initiated.

The scope of this Annual Reporteport is generally confined to the capabilities that are to be used to describe the physics present in the ATR reactor. Thus, the calculational process discussed above has been largely addressed, while the UFSAR requirements will need further discussion and advancements to support the USQ process. This discussion is currently planned to occur in a separate document that may also serve to comprehensively demonstrate requirements that cannot directly be validated via physical measurements, such as Effective Plate Power (a non-physical construct of the ATR UFSAR) and fission density (unvalidated due to the lack of depletion measurements). This separate document will likely draw on several sources of information, including this Annual Report, to clearly show that no additional uncertainty (due to calculational or process changes) will be incurred by the transition to the HELIOS-based methodology.

As noted earlier, Table 2.1 below contains a complete list of the 49 physics requirements applicable to ATR core safety analyses. Also included in this table is the current status of the ATR Core Modeling Update Project as it relates to each requirement and the underlying computational processes. In summary,

- 0 requirements are associated with functionalities that are in development without a working proof-of-concept at this point,
- 5 requirements are associated with a working proof-of-concept,
- 19 requirements are associated with functionalities that are undergoing comprehensive demonstration,
- 3 requirements are associated with functionalities that are expected to be ready for deployment,
- 14 requirements are associated with functionalities that have no short-term plan for replacement but that may optionally be replaced in the future using the capabilities of one or more of the codes in the ATR Core Modeling Update Project suite, and
- 8 requirements are associated with functionalities that have no immediate need or long-term plan for replacement.

Table 2.1 SAR Physics Requirement Identification, Reference Information, and Current Status.

Property or Parameter	**Stated Limits and Surveillances**	**SAR, TSR, or USQ Section(s)**	**Current Reporting Mechanism(s)**	**Status / Supporting Sections**	**Known Deficiencies**
Core parameters	Document parameters	15.0.2.4	Physics Report & CSAP	Undergoing Comprehensive Demonstration	Demonstration will be provided by Cycle 157B and 158A HELIOS analysis.
Operating Envelope	Determine operating envelope	15.0.2.4	Physics Report & CSAP	Undergoing Comprehensive Demonstration	Demonstration will be provided by Cycle 157B and 158A HELIOS analysis.
Reactor power	< 250 MW <= 0.5 MW during depressurized operations	4.3.1.3.1, 4.3.2.2, 15.0.4.3, 16.2.2.2, TSR LCO 3.3.1.1a, TSR LCO 3.3.2.1a	Physics Report & CSAP	Ready for Deployment / See Sections 4.1.3, 5.1, & 5.6.3	None Identified.
Power variation	Investigate anomalies.	4.3.1.6.2, 4.3.2.4.3, 4.3.2.7	Surveillance Report	No Long-Term Plan for Replacement	None Identified.
Lobe and source powers	<= 60 MW SIPT <= 34 MW LIPT <= 50 MW AHTL	4.4.2.3, TSR LCO 3.6.1a Table 3.6.1-1	Physics Report & CSAP	Undergoing Comprehensive Demonstration / See Sections 3.2.5, 4.1.3, 5.1, & 5.6.3	Demonstration will be provided by preliminary Cycle 158B HELIOS analysis of KJRR.
Frequency of high power operations	< 20% over 34 MW lobe power < 6% over 47 MW lobe power Assumes <=75% ATR operation availability	15.0.14, 15.6.1, 15.6.2, 15.6.5, 15.6.6	CSAP	No Long-Term Plan for Replacement	None Identified.
Fuel element powers	Maximum calculated value used to calculate minimum cooling time before core is off-loaded	16.2.2.12, TSR LCO 3.5.1 Table 3.5.1-1, TSR SR 4.5.1.1	Physics Report & CSAP	Ready for Deployment / See Sections 3.2.5, 3.3.3, 4.1.1, 4.1.2, 5.2.2, & 5.3.2	None Identified.

Property or Parameter	Stated Limits and Surveillances	SAR, TSR, or USQ Section(s)	Current Reporting Mechanism(s)	Status / Supporting Sections	Known Deficiencies
Fuel element status	Confirm procurement specifications and restrictions Operations confirm core properly loaded	4.2.1, 4.2.3.4.6, 4.3.2.4, 16.2.2.12, 17.4.5, 17.11.2, TSR LCO 3.5.4, TSR SR 4.6.3.1	Physics Report & CSAP	Undergoing Comprehensive Demonstration / See Section 3.3.3 & SQA Testing Results	Demonstration will be provided by SQA testing of THECPT.
Fuel element oxide thickness	< 1.0 mil Confirm prefilming Confirm via analysis and measurements	4.2.1.1.2, 4.2.1.8.1, 4.2.3.1.1, 15.10.7.1, Table 15.0-2, TSR LCO 3.6.3, TSR SR 4.6.3.1	Element Quality Assurance Records, Inspection Letters, Fuel Loading Letter, & CSAP	Undergoing Comprehensive Demonstration / See SQA Testing Results	Demonstration will be provided by SQA testing of THECPT.
Fuel element inspection	No scratches or unclearable debris No cladding breach Post-cycle surveillances required Restrictions tracked	4.2.1, 4.2.1.1.2, 4.2.1.8, 4.2.1.8.1, 4.2.3.1.1, 15.10.1.2, 17.4.5, 17.11.2	Element Quality Assurance Records, Inspection Letters, Fuel Loading Letter, Spent Fuel Database, & CSAP	Undergoing Comprehensive Demonstration / See SQA Testing Results	Demonstration will be provided by SQA testing of THECPT.

Property or Parameter	Stated Limits and Surveillances	SAR, TSR, or USQ Section(s)	Current Reporting Mechanism(s)	Status / Supporting Sections	Known Deficiencies
Experiment Safety Analysis	Compliance to Plant Protection Criteria	10.1, 10.1.6, 10.1.7, 10.1.7.5, 10.2.1.3.1, 15.0.2.4, ADD-7 5.2.3, TSR LCO 3.9.1, TSR SR 4.9.1.1	ESAP	No Long-Term Plan for Replacement	None Identified.
Loop experiment power	Total < 1 MW	ADD-8 5.2.1	CSAP	No Short-Term Plan for Replacement	None Identified.
Loop void worth	< 1.00$ LIPT < 0.80$ SIPT < 4.00$ total Include test failures Include step reactivity for minimum SR calculation	4.3.2.3, 10.2.6.2.2, 10.2.6.4.1, 10.2.6.4.3, 15.0.2.4, 15.4.1.1, 15.4.6.2.1, TSR SR 4.7.1.1, TSR SR 4.7.1.4, USQ-2013-094 SR 1	CSAP	No Short-Term Plan for Replacement	None Identified.
Loop minimum temperature	Determined from void worth limits	4.3.2.3, 10.2.6.2.2, 10.2.6.4.1, 10.2.6.4.3, 15.4.1.1, 15.4.6.2.1, TSR SR 4.7.1.4, SD-11.2.8	CSAP	No Short-Term Plan for Replacement	None Identified.

Property or Parameter	Stated Limits and Surveillances	SAR, TSR, or USQ Section(s)	Current Reporting Mechanism(s)	Status / Supporting Sections	Known Deficiencies
Regulating rod worth	<= 0.57$ < Delayed neutron fraction <1.05$/sec, controlled by PPS at <0.24$/sec	3.1.2.4.2, 4.3.1.4.1, 4.3.2.4.2, 4.3.2.4.5, 15.4.7.1, 16.2.2.1, Table 4.3-17	CSAP, Facility Change Process	No Short-Term Plan for Replacement	None Identified.
Movement of Driven Experiments	Reactivity compensated by RR	4.3.2.4.2, 10.2.5.1.3, 10.2.6.4.2, 10.2.6.4.3, 15.4.7.7.1, 15.4.7.7.2, 15.4.7.7.3, Add-3	CSAP	No Short-Term Plan for Replacement	None Identified.
Outer Shim Control Cylinder and Neck Shim reactivity	Subcritical with SRs withdrawn and with OSCCs and NSs fully inserted	4.3.1.5.1, 4.3.1.5.2, 4.3.2.4, 4.3.2.4.1, 4.3.2.4.4	Physics Report & CSAP	Undergoing Comprehensive Demonstration / See Section 3.3.1	Issues between measurement data and calculations should be resolved/quantified.
Control element reactivity measurements	Periodic measurements of OSCCs, NSs, RRs, and SRs	4.3.2.4	CSAP	No Long-Term Plan for Replacement	None Identified.
OSCC positioning during measurements	Analyze measurement procedures	4.3.2.4, 4.3.2.5.2, 15.11.13.1.2	Physics Report & CSAP	Ready for Deployment / See Section 3.2.4	None Identified.
Safety rod positioning during measurements	Analyze measurement procedures	4.3.2.4, 4.3.2.5.1, TSR LCO 3.7.1c, TSR SR 4.7.1.1, USQ-2013-094	Physics Report & CSAP	Undergoing Comprehensive Demonstration	Demonstration will be provided by MCNP analysis of KJRR in ATRC.

Property or Parameter	Stated Limits and Surveillances	SAR, TSR, or USQ Section(s)	Current Reporting Mechanism(s)	Status / Supporting Sections	Known Deficiencies
Minimum operable safety rods	>= 4 SRs Interim: >=5 SRs if total loop step worth <= 4$; = 6 SRs if total loop step worth > 4$	3.1.3.8.2, Table 4.3-16, TSR LCO 3.7.1a Table 3.7.1-1, TSR LCO 3.7.1b Table 3.7.1-2, TSR SR 4.7.1.1, USQ-2013-094	CSAP	No Short-Term Plan for Replacement	None Identified.
Shutdown worth of the N-1 least-reactive safety rods	>= 5.8$ (3 PCPs) >= 6.4$ (2 PCPs) Provide Safe Shutdown Earthquake (SSE) assurance: 4 minimum SRs >= 9.6$, 5 minimum SRs >=12.0$	3.1.3.8.2, 4.3.1.5.2, 4.3.2.4, 4.3.2.4.3, TSR LCO 3.7.1a Table 3.7.1-1, TSR LCO 3.7.1b Table 3.7.1-2, TSR SR 4.7.1.1	CSAP	No Short-Term Plan for Replacement	None Identified.
Minimum safety rod worth	Must be used in specified calculations	TBD.	CSAP	No Short-Term Plan for Replacement	None Identified.
Holddown reactivity margin	>= 6.7$ Calculation includes OSCC, NS, and RR depletion Calculation includes conservatively low SR reactivity values	4.3.1.5.2, 4.3.2.4.1, 4.3.2.4.2, 4.3.2.4.3, 4.3.2.4.4, 16.2.2.12, TSR LCO 3.5.7, TSR LCO 3.5.7 Action A.2, TSR SR 4.5.7.1	CSAP	No Short-Term Plan for Replacement	None Identified.
Xenon walk-away/ recriticality event reactivity	>= 2.0$	15.4	CSAP	No Short-Term Plan for Replacement	None Identified.

Property or Parameter	Stated Limits and Surveillances	SAR, TSR, or USQ Section(s)	Current Reporting Mechanism(s)	Status / Supporting Sections	Known Deficiencies
Excess Reactivity	Critical on outer shims at BOC $2 excess at EOC Calculation includes OSCC, NS, and RR depletion	3.1.3.8.2, 4.3.1.5.2, 4.3.2.1, 4.3.2.4, 4.3.2.4.1, 4.3.2.4.2, 4.3.2.4.4, 4.3.2.5.1, 7.7.1.5	Physics Report & CSAP	Undergoing Comprehensive Demonstration / See Sections 3.2.4, 3.3.1, 3.5.1, 3.10, & 5.6.2	ROSUB multiplier replacements are undergoing demonstration. Quadrant excess reactivity may be a priority, despite the lack of a specific safety requirement.
Critical shim positions at initial startup	Calculation includes reflector poison effects Calculation includes OSCC, NS, and RR depletion Detect fully inserted safety rod Projected using count rate monitoring	4.3.2.2.7, 4.3.2.4, 4.3.2.4.1, 4.3.2.4.2, 4.3.2.4.4, 4.3.2.4.7, 15.11.11.2.2, TSR AC 5.5.1e(i)	Shim Prediction Letter & CSAP	Undergoing Comprehensive Demonstration / See Sections 3.2.4, 3.3.1, 3.3.2, 3.5.1, & 3.10	ROSUB multiplier replacements are undergoing demonstration. Additional V&V of reflector poison effects and control surface depletion is needed to quantify bias and uncertainty.

Property or Parameter	Stated Limits and Surveillances	SAR, TSR, or USQ Section(s)	Current Reporting Mechanism(s)	Status / Supporting Sections	Known Deficiencies
Critical shim positions during reactor restart	Critical on outer shims at restart Calculation includes reflector poison effects Detect fully inserted safety rod	4.3.1.5.2, 4.3.2.2.7, 4.3.2.4, 4.3.2.4.7, 15.11.11.2.2, TSR AC 5.5.1e(i)	Xenon Restart Estimated Critical Shim Position Letter	No Short-Term Plan for Replacement	None Identified.
Reflector poison effects	Must be used in specified calculations	TBD.	Included in Physics Report results	Undergoing Comprehensive Demonstration	Demonstration will be provided by Cycle 157B and 158A HELIOS analysis.
Startup Power Division	Establishes Log-N chamber positions	7.2.1.1.3.8, SD-11.2.8	Startup Power Division Letter, Requested Lobe Powers For Startup Letter & Xenon Restart Estimated Critical Shim Position Letter	Undergoing Comprehensive Demonstration / See Sections 3.2.4, 4.1.3, & 5.6.3	Demonstration (including center power predictions) will be provided by 157B and 158A HELIOS analysis.
Log-N calibration	Established via startup power division Calibration settings derived during depressurized operations	4.3.2.2.8.1, 7.2.1.1.3.8, 7.6.4, TSR SR 4.3.2.1.2, SD-11.2.8	CSAP	No Long-Term Plan for Replacement	None Identified.
Radial, azimuthal, and axial power distribution	Available for power split calculations Confirm experiment effects are neglibible	4.3.2.2, 4.3.2.5.2, 15.11.13.1.2	Physics Report & CSAP	Undergoing Comprehensive Demonstration / See Sections 3.5.2, 5.3.2, 5.4, 5.5.4	Axial power distribution calculations have working proof-of concepts available. Other calculations are undergoing comprehensive demonstration.

Property or Parameter	Stated Limits and Surveillances	SAR, TSR, or USQ Section(s)	Current Reporting Mechanism(s)	Status / Supporting Sections	Known Deficiencies
Effective Plate Power (EPP)	See TSR LCO 3.6.1a Table 3.6.1-1	4.4.4.3, 4.4.4.5.3, 15.0.4.3, 15.0.15, TSR LCO 3.6.1a Table 3.6.1-1, TSR SR 4.6.1.1, OMM 7.1.13.1.3.7	Physics Report & CSAP	Working Proof-of-Concept / See Section 3.2.5, 3.5.2, 3.6.1, & 3.7	Known errors in the calculation need to be corrected. Additional EPP constraints and/or sorting methods needed. Comparisons to prior calculated quantities are needed to provide appropriate V&V information.
Maximum unbalanced lobe powers	Used to calculate Quadrant ΔT setpoints	TSR LCS 3.1.1 Table 3.1.1-1	Physics Report & CSAP	Undergoing Comprehensive Demonstration	Demonstration will be provided by 157B and 158A HELIOS analysis.
Reference Lobe Power for Quadrant Delta T Setpoints	Used to calculate Quadrant Delta T setpoints	TSR LCS 3.1.1 Table 3.1.1-1	Physics Report (preliminary) & CSAP (final)	Undergoing Comprehensive Demonstration	Demonstration will be provided by 157B and 158A HELIOS analysis.
Quadrant N-16 to thermal power ratios	<= 1.042 or value derived from EPP results Always <=1.08	TSR 4.6.1.5, TSR LCO 3.6.1b, TSR LCO 3.6.1 Action D.2, TSR SR 4.6.1.1	CSAP & Xenon Restart Estimated Critical Shim Position Letter	No Long-Term Plan for Replacement	None Identified.
Effective Point Power (EPtP)	See TSR LCO 3.6.1a Table 3.6.1-1 <= 1.65 MW between 10 and 90% from plate edge during depressurized operations	4.2.1, 4.4.1.2.1, 15.0.4.3, Table 4.4-5, TSR LCO 3.6.2b, TSR SR 4.6.2.1	Physics Report & CSAP	Working Proof-of-Concept / See Section 3.2.5, 3.5.2, 3.6.1, & 3.7	Corrections to calculations specific to EPtP needed. Additional EPtP constraints and/or sorting methods needed. ROSUB multiplier replacements are undergoing demonstration.

Property or Parameter	Stated Limits and Surveillances	SAR, TSR, or USQ Section(s)	Current Reporting Mechanism(s)	Status / Supporting Sections	Known Deficiencies
Fuel thermal stress	< unirradiated yield strength, Enforced via EPtP	4.2.1.5.1, 4.2.3.4.1, 4.3.1.3.1, 15.0.14	CSAP, SINDA results	Working Proof-of-Concept / See Section 3.2.5, 3.5.2, 3.6.1, & 3.7	EPtP calculations have working proof-of-concepts available.
Fuel temperature	< 700 F with 95% confidence < 500 F if > 1.5e21 fissions/cc, Enforced via EPtP	4.2.1, 4.3.1.3.1, 4.4.1.2.1, Table 4.4-5	CSAP, SINDA results	Working Proof-of-Concept / See Section 3.2.5, 3.2.6, 3.5.2, 3.6.1, 3.7, & 3.8	Fission density and EPtP calculations have working proof-of-concepts available.
Point-to-average power density ratio	Highest power density selected for fuel inspection <= 3.3 between 10 and 90% from plate edge during depressurized operations	4.2.1.8.1, 15.0.4.3, TSR LCO 3.6.2a, TSR SR 4.6.2.1	Physics Report	Undergoing Comprehensive Demonstration / See Sections 3.2.5, 3.5.2, 4.1.2, 5.3.1, & 5.5.4	Confirmation of appropriate calculation when utilizing YA elements needed. Develop appropriate multipliers for YA elements due to fuel distribution assumptions.
Fission Density	< 2.3e21 fissions/cc (equivalent to over 350000 MWd/MTU), Affects EPtP limits	4.2.1.2.3, 4.2.1.8.1, 4.2.3.3.4, 4.3.1.1.2	Physics Report & CSAP	Working Proof-of-Concept / See Section 3.2.6, 3.3.3, 3.5.2, 3.8, & SQA Testing Results	Tracking methods with regard to axial effect needed. V&V of fuel depletion needed. Develop appropriate multipliers for YA elements due to fuel distribution assumptions. ROSUB multiplier replacements are undergoing demonstration.
Total and lobe exposures for reflector and elements	Used to calculate reflector lifetime Used to determine ROSUB multipliers for fuel element fission density, EPP, and EPtP calculations	4.2.1.2.3, 4.2.1.7.2, 4.2.1.8.3, 4.2.3.6.1, 15.15, 16.2.2.12	Physics Report & CSAP	Undergoing Comprehensive Demonstration / See Section 3.2.5, 3.3.3, 3.4.1, 5.3.2, & 5.6.3	Confirmation of proper calculation of lobe powers when including experiment powers is needed.

Property or Parameter	Stated Limits and Surveillances	SAR, TSR, or USQ Section(s)	Current Reporting Mechanism(s)	Status / Supporting Sections	Known Deficiencies
Projected reflector lifetime	Increase inspections, use YA elements when < 2 sigma from cracking, Effects EPP limits	4.2.1.8.3, 4.2.3.6.1, 15.15, 16.2.2.12, TSR LCO 3.6.1a Table 3.6.1, TSR SR 4.6.1.1	CSAP	No Short-Term Plan for Replacement	Fast fluence effects in the reflector can be used to predict reflector lifetime. These effects can likely be calculated by HELIOS and/or MCNP. Need FLX output interface?
Fast fluence of reactor vessel base metal and welds	Base Metal: < 1.2e19 n/cm2 Welds: < 3.1e18 n/cm2	4.3.2.8, 5.3.1.4	CSAP	No Long-Term Plan for Replacement	None Identified.
Thermal fluence of reactor vessel base metal and welds	Base Metal: < 7.62e20 n/cm^2 Welds: < 2.27e20 n/cm^2	4.3.2.8, 5.3.1.4	CSAP	No Long-Term Plan for Replacement	None Identified.
Safety rod average vertical fast flux	Used to calculate component fluence	4.2.1.6.2, 4.2.1.8.2	Letter to appropriate ATR engineer based upon Physics Analysis data	Undergoing Comprehensive Demonstration / See Sections 3.2.7 & 3.9	V&V of surveillance results is needed.
Hafnium component fast fluence	< 5e22 n/cm^2	4.2.1.6.2, 4.2.1.8.2, 13.1.2.2.2	CSAP	No Short-Term Plan for Replacement	None Identified.
Pressure tube average vertical fast flux	Used to calculate pressure tube and detector fluence	TSR AC 5.7.6	Letter to appropriate ATR engineer based upon Physics Analysis data	Undergoing Comprehensive Demonstration / See Sections 3.2.7 & 3.9	V&V of surveillance results is needed.
Element heat generation rate	<= 300 Watts decay heat	PLN-936 7.1 SAC #6	ATR Spent Fuel Element Transfer Cask Shipping List	No Short-Term Plan for Replacement	None Identified.

Definition of terms in Table 2.1:

In Development: No proof-of-concept is available to demonstrate functionality. Work is between 0% and 50% complete.

Working Proof-of-Concept: A proof-of-concept is available to demonstrate basic scientific functionality. Full functionality that meets requirements is under development. Verification and Validation Process is defined. Work is between 50% and 80% complete.

Undergoing Comprehensive Demonstration: Full engineering functionality and accuracy is being demonstrated over multiple cycles. Demonstration is utilizing appropriate acceptance testing, verification, code-to-code validation (where appropriate) and/or direct validation with available data. Work is between 80% and 95% complete.

Ready for Deployment: Anticipate that engineering deployment requirement has been fulfilled and method verified and validated. Customer feedback is needed to ensure product meets expectations. Work is between 95% and 100% complete.

No Short-Term Plan for Replacement: Current methodology for completing this requirement is expected to remain in place at the time of initial HELIOS deployment.

No Long-Term Plan for Replacement: Methodology replacement has not been explored at this time.

3.0 OVERVIEW AND STATUS OF ATR COMPUTATIONAL METHODOLOGIES

Samuel E. Bays, Emily T. Swain

When the ATR and ATRC were brought into operation in the late 1960s computer technology was such that two-dimensional diffusion theory reactor physics analysis was the most advanced practical multidimensional method available for routine reactor core analysis and fuel management support. While several well-developed production-level one-dimensional transport codes were commonly used, and some pioneering work had been done in the area of deterministic multidimensional transport code development, the latter codes would have been impractical for routine ATR fuel management applications due to the limited computer speed and memory capacities available to the INL at the time. Early three-dimensional Monte-Carlo transport codes such as MCNP were available as well, but these would also have been impractical for routine ATR applications, again because of limited computer speed and memory available at the time. The PDQ7 two-dimensional (2D) diffusion code, originally developed at Bettis Atomic Power Laboratory (Pfeiffer, 1971) and viewed as one of the most sophisticated computational tools of its type (then and even now) was thus established as the preferred methodology for ATR operations and fuel management support. The following two sections summarize the PDQ7-based methodology, followed by a more detailed description of the replacement physics methodology based on the HELIOS system as noted earlier.

3.1 Legacy PDQ7-Based ATR Reactor Physics Computational Protocols

The current ATR physics analysis that supports the core safety assurance package (CSAP) documentation is performed by utilizing a suite of computer codes that were specifically created to interact with a PDQ7 model of the ATR and provide data in support of ATR operation in a manner illustrated in Figure 3.1. The method incorporates the use of several different PDQ7 input files, some pre-processing codes that are used to collate information for use in a specific cycle, and post-processing codes that produce the necessary information to satisfy safety analysis report (SAR) commitments. This discussion will focus on the key software associated with post-processing PDQ7 data and the associated analyses.

There are basically three categories of post-processing calculations performed to meet the explicit SAR commitments. The first category encompasses general cycle-specific data such as excess reactivity and element powers. The second category of calculations is based upon the peak power density modeled by PDQ7. The final set of calculations lead to the assurance that a fission density limit is not expected to be exceeded by the fuel elements used in the cycle. In addition to the explicit SAR commitment calculations, cycle-specific calculations are performed for the worst-case situation and the as-run end of cycle results. For the worst-case calculations, power data regarding all fueled regions in a lobe are obtained from PDQ7 edit sets and then used to ensure that reactor set points are properly set. For the end of cycle calculations, nuclide concentration data pertinent to each fuel element is obtained for use in future analysis.

One key post-processing code used in the PDQ7-based methodology, shown in Figure 3.1, is the PQMAP code. PQMAP converts the data obtained from PDQ7 in to a variety of tables and plots that can be used in the Core Safety Assurance Package that is produced for each cycle. The PQMAP program also performs some calculations on the input data. These calculations primarily perform power adjustments, such as conversions from the nominal lobe powers modeled in PDQ7 to the maximum lobe powers allowed during the cycle.

The GRAMS code calculates the B10, U235, U236, U238, Pu239, Pu240, Pu241, and total uranium and total plutonium content of fuel from nuclide concentration data for each fuel element. The GRAMS data is used to maintain a database of fuel inventory data.

The ROSUB code performs a variety of cycle-specific calculations and provides the results to many of the other post-processing codes in the physics analysis network. One of the calculations performed by ROSUB is the excess reactivity available in the core at each time step. The CRITOS program is then used to convert the excess reactivity determined by ROSUB into a critical startup position for the Outer Shim Control Cylinders (OSCC).

PQXSPL provides figures illustrating estimated total core and quadrant excess reactivity for a projected cycle. These plots can then be used to predict the cycle length of the operating cycle.

The ROSUB program also calculates several normalization factors that are ultimately used by other post-processing programs. The Power Density Normalization Factor is used to convert the power density calculated by the homogeneous PDQ7 model into the power density within a heterogeneous element. The Power Density Normalization Factor also contains the axial peak-to-average power density multiplier for converting x-y power density into a value representative of the true x-y-z behavior. Another normalization factor calculated by ROSUB and used by other post-processing programs is the Cumulative Fissioned Atom Density (CFAD) normalization factor. This factor is used to convert the fission density calculated by the homogeneous PDQ7 model into the fission density within a heterogeneous element. The CFAD normalization factor also contains the peak-to-average fission density multiplier.

The GOPP post-processing program is used to determine the point-to-average power and fission desnity ratios azimuthally along each selected plate of an element. The program performs linear interpolation to convert homogenized data over a x-y PDQ7 region into plate-specific information. GOPP solves for 20 point-to-average data points for plates 1, 2, 3, 5, 8, 15, 16, 17, 18, 19 of each fuel element position. Many of the normalization factors determined by ROSUB are then applied to the plate-specific output from the GOPP program before this output is supplied to the LMFIS and POWCOR programs.

The POWCOR post-processing code uses linear interpolation of the GOPP azimuthal point-to-average power density data to find the values at 5%, 10%, 90%, 95% of the distance along each plate. The maximum of these interpolated values is found for each core position. This information is then passed to RPCR2 for conversion into Effective Point Power (EPtP) and Effective Plate Power (EPP). The interpolation of power data at 5%, 10%, 90% and 95% is a significant detail for explaining the current legacy methodologies approach for mapping heat input from PDQ7 into the thermal-hydraulic sub-channel code ATR-SINDA used for ATR safety analysis.

The LMFIS post-processing code is used to calculate a variety of parameters based upon the peak fission densities of elements. For instance, the LMFIS code uses the lobe exposures and peak fission densities from various time steps to determine a fission build-up rate for each tracked plate position. This rate is used by LMFIS to determine the minimum lobe exposures needed to surpass the SAR limitations on fission density at each position. The LMFIS code also uses the fission build-up rate to project an EOL fission density for each element based upon the nominal exposure expected in each lobe during the cycle. Finally, the build-up rate is used to predict the maximum fission density allowed in a recycled element at the beginning of a cycle for each position in the core.

The RPCR2 program performs the calculations needed to determine the limiting EPPs and EPtPs. While most of the RPCR2 program calculations involve power density data, it also outputs results relating to the fission density calculation results. The RPCR2 program uses the peak fission density values to obtain the element positions with fission densities over 1.5E21 fissions/cc. This fission density limit is used to implement 7F element EPtP limits on any element exceeding the stated fission density.

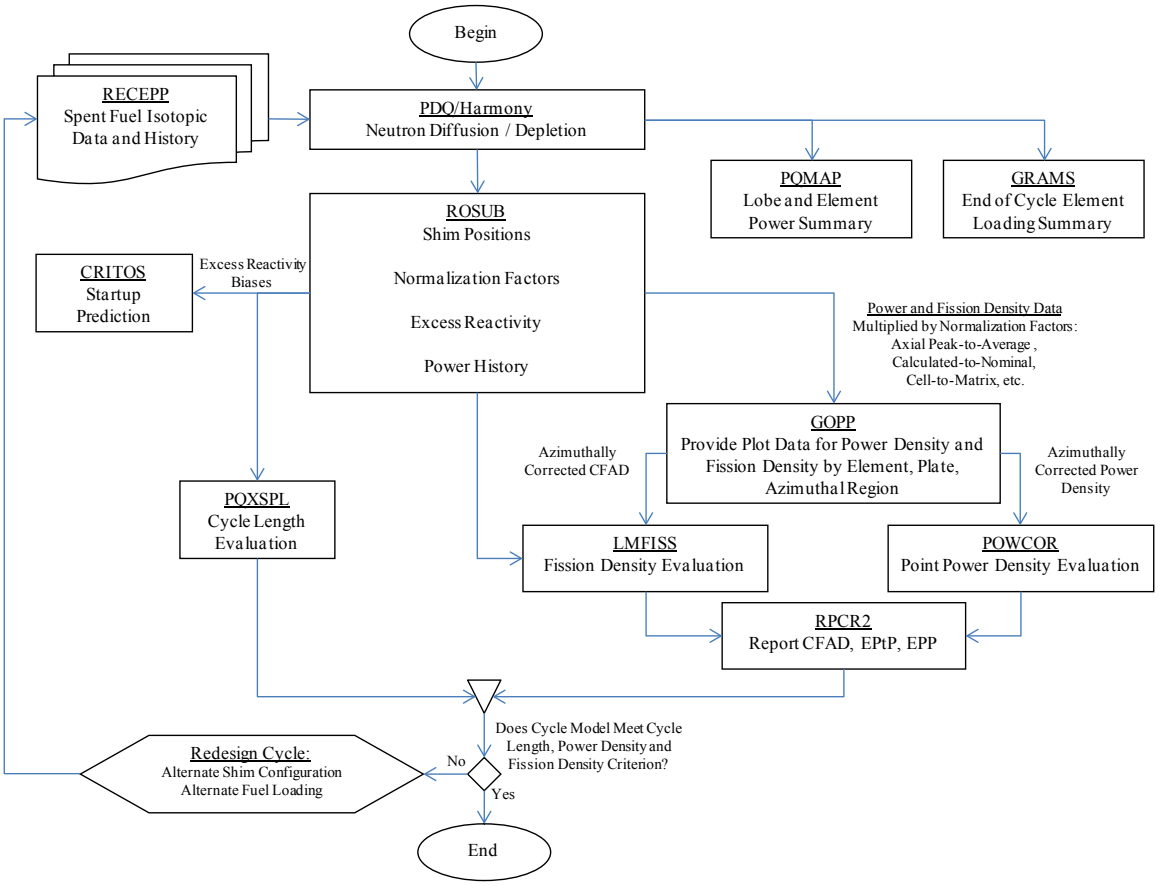

Figure 3.1 Current ATR Physics Analysis Data Flow Diagram

After cycle completion, RECEPP collects data relevant to spent fuel isotopics and history, such as cumulative fission densities, element position, etc. and stores this information in a database so that the information can be retrieved for future cycle analyses.

3.2 Overview of the New HELIOS/MCNP5 Based Methods

Once the new physics methodology is fully implemented, ATR fuel cycle physics analysis and corresponding CSAP support will be conducted using a protocol based on the HELIOS and MCNP5 codes. Other codes included in the new suite shown previously in Figure 1.5 will support verification and validation and other ancillary tasks such as computation of specialized effective cross sections etc.

3.2.1 HELIOS Code Description

HELIOS is a 2-D lattice physics code developed by Studsvik Scandpower that has been applied to a number of different reactor types, with an emphasis on light-water moderated systems having essentially any geometry. The solution method uses current coupling collision probabilities (CCCP) or the Method of Characteristics (MOC) to solve the neutron transport equation with minimal geometric approximation. Commercial and research reactors have been modeled. There is a large collection of verified and validated benchmark cases for HELIOS. HELIOS is used to generate cross sections, flux, power generation, fuel exposure and other reactor physics calculations pertinent to core design as well as operational support and safety analysis.

Complex two-dimensional descriptions of the problem geometry are created by HELIOS from a library of basic geometric figures (circles, polyhedrons, etc). The code supports property overlays, such as composition, temperature and density, mapped to this arbitrary 2D geometry. Very large and complex geometries are

supported by subdividing the geometry into smaller subsystems. These subsystems are solved explicitly via the collision probability transport solution method and then current-coupled with adjacent subsystems (Studsvik Scandpower, 2009; Stamm'ler and Abbate, 1983). The code also offers a method-of-characteristics option for the transport solution (Studsvik Scadpower, 2009; Vladimirov, 1959; Marchuck, 1961).

An infinite homogeneous flux calculation with resonance absorbers is calculated as part of the base calculation in HELIOS. Geometry-corrected resonance integrals are then calculated on-the-fly for every spatial region of the heterogeneous geometry description using the subgroup resonance treatment (Studsvik Scandpower, 2009). The critical flux values are then calculated including the up scattering terms. The fluxes are used to define full power, isotopic depletion and buildup and safety parameters.

HELIOS depletes all fissile materials as applicable in any given single spatial region (i.e., meshes are depleted separately). New property overlays can be added during the course of the depletion (e.g., change in control poison configuration, coolant density change, fuel temperature change, etc.). The code also supports tracking of gamma rays and gamma ray heating of core internals, though this feature has not been explored for the ATR at this time.

The original ATR HELIOS model was based solely on a description of the low power physics tests following the core internals change-out prior to cycle 103A-2 in 1994. This critical experiment was eventually included as an internationally peer reviewed criticality benchmark in the 2005 publications of the International Handbook of Evaluated Reactor Physics Benchmark Experiments (IRPhE) and International Handbook of Evaluated Criticality Safety Benchmark Experiments (Kim et al., 2005). The ATR HELIOS model and a companion MCNP model have since been brought current with Rev 4 of this published benchmark (Figure 3.2). Additional corrections (Bays et al., 2011) to the model (pertaining to the geometry description of the two regulating rods in the 1994 CIC) have also been performed.

The ATR HELIOS model has since been evolved considerably to fulfill the functional requirements of the Physics Analysis, replacement of PDQ7 related roles in the CSAP, and the UFSAR.

- The reflector mesh description has been refined such that the current coupling does not divide any capsule facility lying on any North-South, East-West, Northwest-Southeast, Northeast-Southwest axis.

- The reflector was refined with depletable zones for communicating with an external beryllium depletion algorithm.

- The fuel element mesh was refined to produce a heat structure that is compatible with the ATR-specific thermal-hydraulic code, SINDA.

- Mesh refinement studies were conducted on the OSCCs to determine the azimuthal and radial mesh appropriate for timely, yet detailed flux and critical eigenvalue calculations.

- The safety rod and In-Pile Tubes (IPTs) geometry definition has been redefined for allowing fast fluence tracking in these hardware components.

- A methodology was implemented for transitioning hafnium burnup "fraction-of-original-worth" values, normally computed by the PDQ7/HFBURN code into actual hafnium nuclide densities that are used to microscopic deplete the hafnium neck shims in HELIOS.

- An ATRC version of the ATR internals model has been created for the purpose of validation with ATRC measurements.

- A HELIOS component model for all flux trap experiment, drop-in capsule, isotope capsule, backup, filler, flow-restrictor, etc. have been created for Cycles 145A to 154A have been developed for the purpose of following the ATR from late 2009 to current. The core-follow calculations have supported retrospective

As-Run validation, prospective startup prediction, and prospective Physics Analysis comparison between PDQ7 and HELIOS.

- The ATR HELIOS model input description has been distributed into a file directory hierarchy system. This hierarchical system allows the super-majority of all ATR/ATRC modeling inputs to be "SET", version controlled and validated separately from the actual cycle-design models produced for each ATR cycle. This directory system is referred to as the Base Model. Each new experiment or capsule is represented by an experiment component file that can be used in either an ATRC HELIOS model for validation purposes or in an ATR HELIOS model for production purposes. An actual cycle-model is controlled by four basic control files: CYCLE.INP, EXPR.SET, FUEL.SET, INTR.SET, representing neutron poison configuration and depletion control, experiment loading configuration, fuel loading configuration, internals definition control, respectively.

- A system of UNIX shell scripts has been created to facilitate integrating the Base Model, Experiment Component Files, single-fuel-element-HERMES "nuclide composition files", and the four control files.

- HELIOS post-processing options have been developed for meeting the needs of Verification and Validation; and also for converting the standard output data-types of HELIOS into the derived data-types defined by the ATR UFSAR. These output options also enable management of detailed fuel, neck shim, and reflector nuclide databases. These output options also enable management of detailed fluence databases for safety rod followers and IPTs.

- A databases management software called Total Heuristic Evaluator – Critical Process Transformer (THECPT) has been developed for assisting the user maintain fuel and nuclide databases. This new software tool also automatically creates various HELIOS inputs and UNIX shell scripts as a time-saving measure for the user. THECPT also performs its own beryllium depletion calculation for the ATR reflector using the 4th Order Runge-Kutta algorithm.

Additional information on the structure, functional organization, or logistics of the Base Model, UNIX scripts, THECPT, database strategy, post-processing features, etc. can be found in the ATR HELIOS model user's manual, GDE-667.

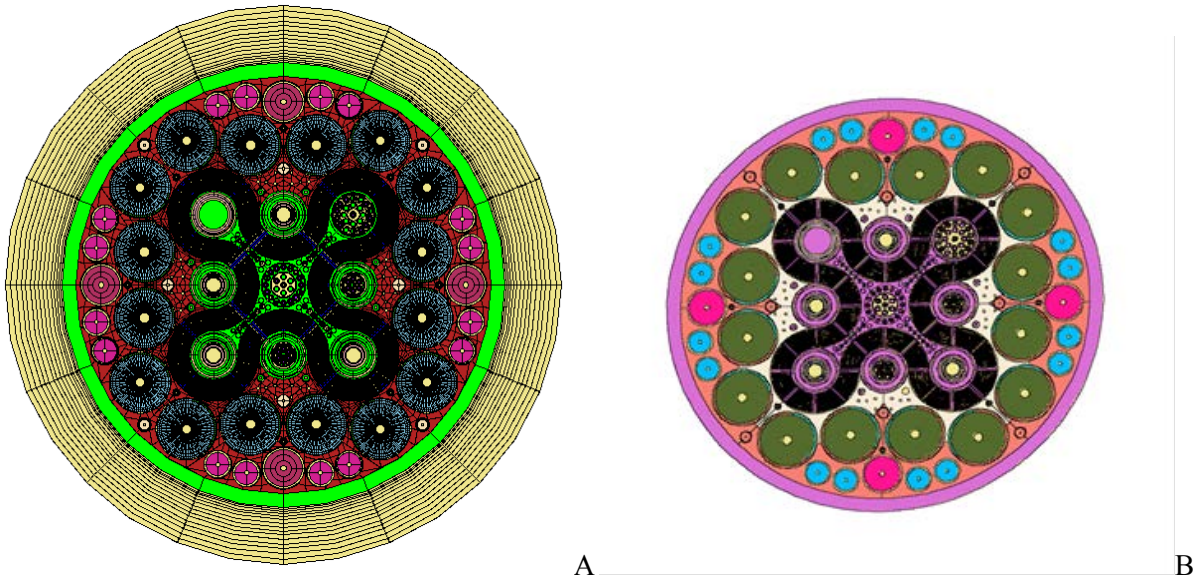

Figure 3.2. Transverse geometry of the 1994 CIC IRPHE Benchmark with: (A) HELIOS, (B) MCNP

3.2.2 MCNP Code Description

Monte Carlo Nth Particle (MCNP) uses the Monte Carlo method for solving particle (e.g, neutron and photon) transport in a continuous energy, angle and three-dimensional space representation of the reactor core. The Monte Carlo solution method represents particle interaction as probabilistic collisions between traveling particles and atomic nuclei. Therefore, the MCNP solution can be considered to be a near exact representation of reality to within the accuracy of the input nuclear interaction probability (cross section) data. However, this level of solution fidelity comes at greater computational expense compared to a 2D deterministic code such as HELIOS. Therefore, until advancements in computer technology enable speeds amenable to full core Monte Carlo solutions, there will be a need for 2D deterministic codes such as HELIOS. The primary limitation of HELIOS is that it is constrained to the x-y domain of the ATR. However, it is theoretically possible to apply MCNP to solve for the axial behavior (e.g., excess reactivity bias, peak-to-average power density multipliers, etc.) that cannot be computed by HELIOS.

The 3D ATR MCNP model can be coupled to ORIGEN2 such that it can provide the exposure-dependent axial peak-to-average power density factors for each element. The factors will be applied to the localized peak power region in the 2D HELIOS Model to determine the three-dimensional heat generation effects. Like the PDQ7 methodology, the HELIOS 3D-to-2D methodology assumes separability of power and spectrum effects in the x-y plane from those in the z-plane.

Previously, the MCNP experiment modules were developed for each civilian ATR experiment in preparations for the ESAP of that experiment. These models have not been leveraged to inform the ATR CSAP. For ESAP preparation, generally these modules have not been combined in such a way prior to reactor startup as to reflect the true configuration of the core. Due to the relatively decoupled nature of each of the five ATR lobes, a generic model is used for all lobes except for the one containing or nearest to the experiment of interest. In these experiment-centric ATR MCNP models, the analyst adjusts the OSCC positions such as to deliver the correct lobe-power split in the full-core model. Under these prototypic conditions, the localized fission and gamma ray heating in the experiment of interest is well predicted.

3.2.3 Interactions between HELIOS and MCNP

The PDQ7-based methodology uses previously tabulated peak-to-average (i.e., core-average) power density multipliers which are stored as polynomial functions of lobe exposure within the ROSUB code. These polynomials were computed early on in the PDQ7 methodology development with little change since the mid-1980's. In the context of axial factors for HELIOS, MCNP will be run to support every cycle. The peak-to-average axial power multiplier will then be handed off to the HELIOS post-processing model (written using the HELIOS/ZENITH post-processing language) for use in ATR cycle-design.

With the new methodology, finalization of all ESAP's will continue to be a pre-requisite for finalization of the CSAP. Once the ESAP's are finalized, an ATR MCNP model for the current cycle can be configured. This model can be created during the early phases of CSAP preparation so that axial reactivity biases and axial power multipliers for each element can be fed into the analysis for prediction of OSCC startup position and peak localized power density, respectively. Alternatively, the applicable reactivity biases and power multipliers currently in place in ROSUB have been encoded into the ZENITH post-processing protocol in the event that all ESAP's are not completed in the early phases of CSAP preparation. Figure 3.3 gives a high level hierarchical relationship between HELIOS and MCNP applications. Notice that in general, the work flows for both codes are separate and independent until the very end of cycle-design.

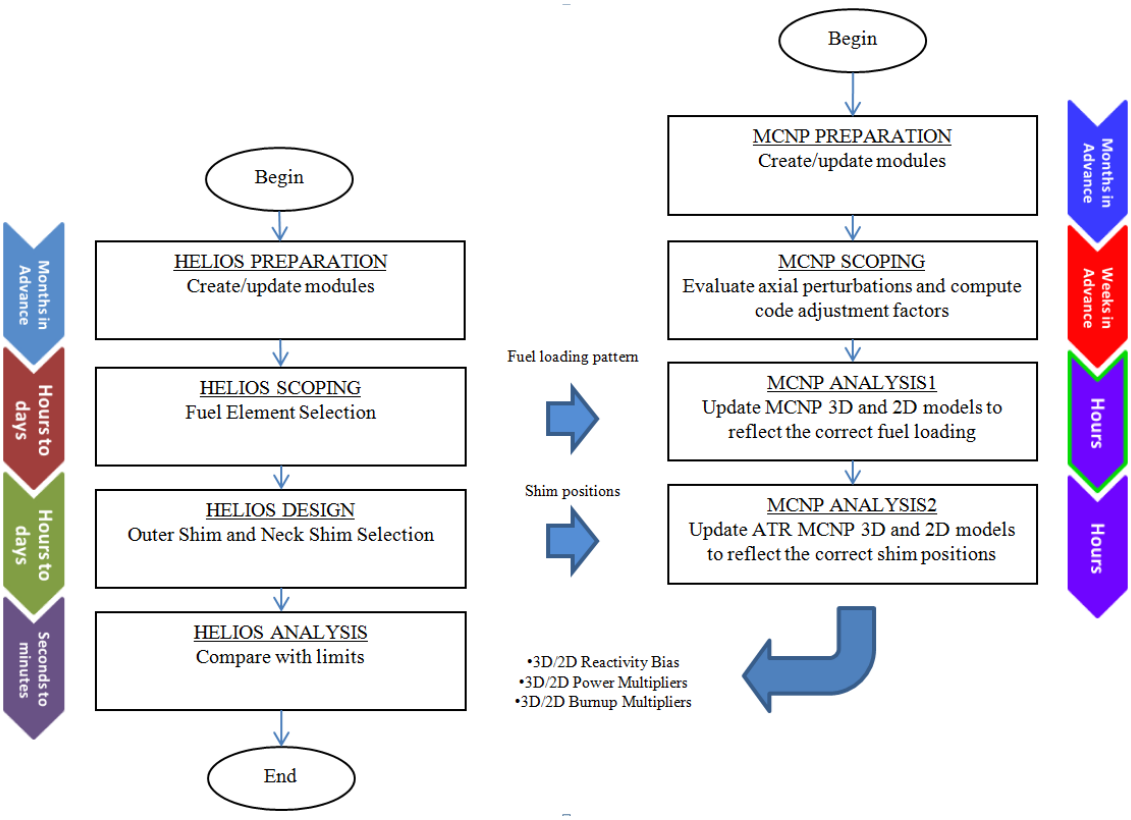

Figure 3.3. Phases of HELIOS and MCNP model development and cycle design data dependencies. Also provided is a rough time-frame for each phase for both codes.

In Figure 3.3, MCNP serves two purposes. The first purpose is to evaluate the "adjusted" axial shape bias and uncertainties in conjunction with an ATRC flux run. This requires a 3D ATRC model of the ATRC flux run and the least-squares adjustment technique discussed in Section 3.5. The covariance weighted least squares method solves for the adjusted axial profile based on the a-priori calculated and measured values. The least squares method uses both calculation and measurement uncertainties to guide the adjustment.

The second purpose of MCNP is to predict the 3D/2D reactivity, power and burnup adjustment for use in lieu of the ROSUB polynomials. Computation of 3D/2D reactivity bias, power and burnup multipliers requires both a 3D and 2D model of the target ATR cycle under design. The 3D/2D reactivity bias and power multipliers can be found by modeling the startup configuration, based on a preliminary HELIOS startup prediction assuming the ROSUB polynomials. The 2D MCNP model is a 2D facsimile to the 3D model but also is a twin to the HELIOS model at BOC. Generally, the 2D MCNP and HELIOS model assume axial homogenization of nuclide compositions, or the composition and geometry at the mid-plane can be assumed "as-is" thus assuming axial extrusion.

The 3D/2D burnup multipliers can be found by modeling the entire HELIOS cycle-design in MCNP (coupled to the ORIGEN2.2 code) For the MCNP depletion calculation, the OSCC and neck shim configuration should come from the preliminary cycle design found with HELIOS assuming the ROSUB polynomials. Figure 3.4 provides a conceptual graphic for demonstrating collapsing the x-y-z frame in MCNP to the x-y frame in HELIOS.

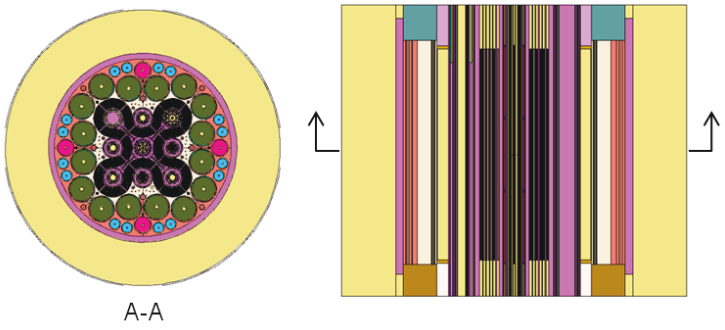

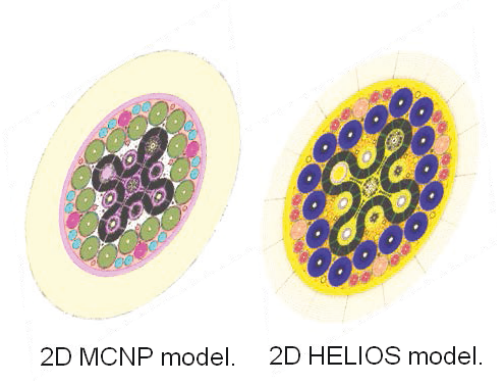

Figure 3.4. Conceptual representation of data translation between the 3D MCNP model to the 2D HELIOS model.

Simplistically for chopped cosine shaped power distributions, the peak-to-average axial power factor is defined as the average power density at the mid-plane divided by the volumetric average of the core power density Equation 3.1.

$$A(t) = \frac{P_m(t)/V_m}{\sum P_z(t)/\sum V_z} = \frac{P'''_m(t)}{P_a(t)} \qquad (3.1)$$

Where: P_m and V_m are the regional power and volume at the midplane. P_z and V_z are the regional power and volume for each z-slice of the problem geometry. P'''_m is the power density at core mid-plane. P_a is the volumetric average power density of all slices in the z dimension.

In PDQ7, the numerator of Equation 3.1 is the average power density at the core mid-plane of a right circular cylinder representing an ATR lobe. The denominator is a summation over all regions in a standard lobe. However, with the 3D/2D MCNP calculations, a value of A can be computed for every fuel plate or even sub-plate fuel region. If the MCNP fuel element model represents all 19 plates, then a table of 19×40=760 values for A can be fed to ZENITH. Also, the 3D/2D MCNP methodology is not restricted to the core mid-plane. With advanced experiment designs, the peak may not occur at the mid-plane. Thus, the maximum axial power for each radial region (e.g., a plate) can be chosen to compute A_r. Also, the denominator is no longer defined as the volumetric average lobe power density. Instead, it is defined as the volumetric average fuel element power density, Equation 3.2.

$$\underset{\frac{3D}{2D}}{Averge} A_r(t) = \max_z \left({}^{3D}P'''_{z,r} \Big/ \left(\sum_r^R {}^{3D}P_r \Big/ \sum_r^R V_r \right) \right) \qquad (3.2)$$

Where: $P'''_{z,r}$ is the power density at position r in the x-y plane and height z in the axial dimension in the 3D MCNP model. P_r and V_r are the region power and volume, respectively, at position r in the x-y plane of the 2D MCNP model. R is the total number of regions in the fuel element of the 2D MCNP model. $\sigma_{z,r}$ is the reduced uncertainty associated with each adjusted power density in r and z. Note that the denominator of Equation 3.2 gives volumetric power density of the fuel element.

For partial length experiments that perturb the axial power shape, a peak-over-average factor may not be appropriate. For these cases, a 2D model of the experiment at core-mid-plane will have the implied physical assumption that the experiment is extruded over the full axial height of the core. In this case a slightly alternate formulation of Equation 3.2 is appropriate, a peak-over-extruded factor. The denominator of the peak-over-extruded factor is the power density of the x-y region in the 2D MCNP model, e.g., the 2D plate power density, Equation 3.3.

$$\underset{\frac{3D}{2D}}{Extrude} A_r(t) = \max_z \left({}^{3D}P'''_{z,r} \Big/ {}^{2D}P'''_r \right) \tag{3.3}$$

Where: $P'''_{z,r}$ is the power density at position r in the x-y plane and height z in the axial dimension in the 3D MCNP model. P'''_r is the power density at position r in the x-y plane of the 2D MCNP model.

3.2.4 Reactivity (Startup) Methodology

The current axial reactivity bias correction is defined as the difference between a 2D r-z and a corresponding axially-homogenized (" r-polar") PDQ7 critical eigenvalue calculation for each burn step along a given depletion path (Brown, 1990). The r-z PDQ7 model approximates a typical lobe containing eight fuel elements. The r-polar PDQ7 model is an equivalent representation with the same average linear power. The reactivity bias curve is corrected for the 2D-to-1D geometry bias prior to depletion as shown in Equation 3.4. In current CSAP analysis, this axial reactivity bias is functionalized with lobe exposure, see Equation 3.5. This polynomial, found in the PDQ7/ROSUB code, corrects each PDQ7 cycle calculation for depletion effects relative to a clean core. However, for HELIOS, the previous cycle critical eigenvalue is chosen as the reference-to-critical. The utility in this strategy is that since the reactor loading configuration of the previous cycle is generally similar (with the exception of PALM cycles) between contiguous cycles, the number of unknown biases needed between the known critical and the target critical is minimized. The most significant bias between two contiguous cycles, which cannot be accounted for in the x-y HELIOS model, is the axial burnup shape. Thus, the axial depletion reactivity bias of the known critical is subtracted from the reactivity bias of the target critical, Equation 3.6.

$$\rho_{1D2D} = \frac{k_{2D}(x) - k_{1D}(x)}{k_{2D}(x) k_{1D,0}(x)} - \frac{k_{2D,0} - k_{1D,0}}{k_{2D,0} k_{1D,0}} \tag{3.4}$$

$$\rho_{1D2D} = C_0 + C_1 x + C_2 x^2 + C_3 x^3 + C_4 x^4 + C_5 x^5 + C_6 x^6 \tag{3.5}$$

$$\rho = \frac{k_T - k_C}{k_T k_C} + \frac{1}{8}\sum_i^{40} \rho_{T,i} - \frac{1}{8}\sum_i^{40} \rho_{C,i} \tag{3.6}$$

Where: ρ is the reactivity of the target system. k denotes the 2D k-effective from the HELIOS calculation. T denotes target system, i.e., the cycle being analyzed. C denotes the known critical system, e.g., corresponding to a previous cycle's zero power startup. $\rho_{T,i}$ is the ρ_{1D2D} axial reactivity biases for fuel element i having a lobe-exposure x prior to irradiation in the target system, T. $\rho_{T,c}$ is same as $\rho_{T,i}$ but having a lobe-exposure corresponding to the BOC of the known cycle. 2D and 1D denote the PDQ7 r-z and polar models, respectively,

of a generalized ATR lobe. x is the lobe-exposure, i.e, the summation over all previous cycles the power of the lobe for which the element resided integrated over cycle length.

There are some obvious drawbacks to the above derivation. First, it requires strict adherence to axial symmetric depletion in the fuel for validity. Second, there is no accountancy for the fact that even with balanced OSCC maneuvers during startup; the reactor will have a power tilt between lobes. This is because each cycle will have a unique distribution of fresh and burned fuel as well as different experiment configuration loading. Thus, the above methodology does not account for differences in localized neutron importance in each lobe's overall contribution to core reactivity. It is expected that these restrictions can be overcome using a 3D-to-2D reactivity bias determination using a modern 3D transport code. This has already been demonstrated using the MCNP code to model the 1994 CIC benchmark found in the IRPhE handbook (Kim, 2008, Bays, 2011), see section 3.4.5. Because the fuel loading is different for the known cycle and the target cycle, the reactivity worth of the difference in disparate axial burnup shapes and 3D experiment effects must be taken into account, Equation 3.7 and Equation 3.8.

$$\rho = \frac{k_T - k_c}{k_T k_c} + \rho_{3D/2D}\big|_T - \rho_{3D/2D}\big|_c \tag{3.7}$$

$$\rho = = \frac{k_T - k_c}{k_T k_c}\Big|^{HELIOS} + \frac{k_{3D} - k_{2D}}{k_{3D} k_{2D}}\Big|_T^{MCNP} - \frac{k_{3D} - k_{2D}}{k_{3D} k_{2D}}\Big|_C^{MCNP} \tag{3.8}$$

The ROSUB polynomial (i.e., Equation 3.5) is currently used to correct the HELIOS derived core reactivity in lieu of the actual 3D/2D reactivity bias from MCNP. The ROSUB code itself is not used, but rather the polynomial is used in both MS-EXCEL spreadsheet as well as the ZENITH post-processing routines.

3.2.5 Power Adjustment Methodology

Because of the axial symmetric power shape assumptions used in the ROSUB polynomials (see section 3.4.1) the PDQ7 methodology generally requires experiment design to have minimum perturbation on the axial power shape. Thus, strong neutron absorbers or sharp changes axially in moderator to metal ratio must be used judiciously. For the more exotic experiments, the axial fission shape is actually measured using a duplicate of the ATR core, the ATR Critical facility, ATRC. The ATRC is a near identical replica of the original ATR core, reflector, internals, etc. that reside in a pool facility adjacent to the actual ATR. ATRC was used to verify physics parameters prior to the startup of the ATR. One of the primary functions of the ATRC is to ensure that the experiment does not violate the chopped cosine power distribution in fresh fuel. The reason for this criterion, formally defined by Tomberlin and Abrashoff is to ensure that the axial uniformity assumptions made to compute the axial reactivity and power shape corrections are valid (Tomberline, 2000).

More recent work by Davis and Roth have explored the effects of various axial power distributions on the thermal safety margins, defined by the maximum Effective Plate Power (EPP) and Effective Point Power (EPtP), of the limiting Condition 4 reactivity insertion accident (RIA) (Davis, 2014). This kind of scenario is the most limiting for failure of an ATR fuel element. Of all the UFSAR transient scenarios, the voiding of the IPT and resulting reactivity insertion leads the greatest decrement of margin to aluminum cladding and fuel melt. The original analysis by Polkinghorne and Ambrosek in the mid-1990's, which is referenced as the bounding thermal safety envelope by the UFSAR, assumed an axially symmetric chopped cosine power distribution for their work with the RELAP, SINDA and SINDA-SAMPLE codes (Polkinghorne, 1994). The work by Davis and Roth repeats the Polkinghorne Condition 4 RIA analysis with the actual axial power perturbation, measured in the ATRC, and checks to ensure that the resulting time-dependent temperature rise of the aluminum cladding and aluminide fuel temperature do not exceed the worst-case temperature rise (during the postulated transient) from the Polkinghorne analysis. This information is then used to inform the PDQ7 analyst to adjust the Polkinghorne limit for peak EPP and EPtP in the fuel plate by a certain amount to conform to the Polkinghorne analysis. It should be noted, however, that even though the peak EPP and EPtP limit is refined with the experiment's axial effect in the ATRC, the computation of the peak power in the ATR is not. This is because with the current PDQ7 methodology, the axial peak power factor calculation is computed by the axial symmetric cosine shape assumption inherent to the

ROSUB polynomial. Given that axial perturbations to date have been relatively small, lack of high axial fidelity in the PDQ7/ROSUB modeling is probably sufficient with the rework of the peak EPP and EPtP limits. However, for significant deviations from axial symmetric cosine shape, it will be prudent to use the same 3D/2D power factor in the ATR HELIOS calculation as was used in the RELAP, SINDA and SINDA-SAMPLE analysis.

In addition to incorporating 3D/2D factors for the current cycle under design, it is also possible to re-evaluate the Kim and McClure bounding physics analysis with the same 3D/2D factors. The Kim and McClure physics analysis used PDQ7 to establish the bounding Point-to-average power Density (P.D.) (Kim, 1992). These worst case point-to-average powers were assumed as the heat structure input to the Polkinghorne work (Kim, 1993a), (Kim, 1993b), (Polkinghorne, 1994). The bounding physics analysis evaluated three different scenarios. The 50/50 scenario assumed balanced OSCC positions together with a core configuration that could give exactly 50 MW in each of the five lobes. The 60/40 scenario attained 60MW in the southwest lobe with 40MW in both northwest and northeast lobes, if total core power were to be normalized to 250MW. The enveloping 70MW case attained 70MW in the southeast lobe. These bounding physics analyses (using ROSUB polynomials for axial effects) are reworked with HELIOS and reported in section 4.1.2. More importantly, the 3D/2D power factors from ATRC measurements can be directly used in the post-processing of these cases, as if the bounding analyses were tailor made for the present-day experiment exhibiting the axial power perturbation. Also, instead of using the verbatim ATRC measurement, the adjusted 3D/2D power factors from folding ATRC MCNP calculated and ATRC measured flux wire data can be used as the adjustment factors of the Kim and McClure bounding physics analyses.

The ATR HELIOS methodology uses a "best estimate plus uncertainty" approach to adjust code output such that the ATR results are statistically consistent with ATRC measurements. The HELIOS protocol uses measurement to evaluate the code bias and uncertainty of the model used to represent an ATRC measurement, e.g., axial power shape.

- This is done by simulating the activation response of dosimeters (e.g., fission wire) placed in the ATRC. This calculated response is used with the actual measured response in a covariance weighted least squares adjustment between both datasets, discussed in Chapter 5.

- The resulting adjusted axial power shape, azimuthal power shape, neutron spectrum, etc. is the best estimate that can be statistically derived from both model and simulation. This adjusted power shape (or neutron spectrum) is weighted by the random and correlated uncertainties of both the measurement and the simulation model. The least squares adjustment also produces the reduced uncertainty associated with each data point in the adjusted power distribution or neutron spectrum. The code bias (axial bias in MCNP, azimuthal bias in HELIOS) is considered to be the difference between the a priori simulated response and the adjusted response.

- The ATRC bias and uncertainty are then added to the ATR calculation, making the ATR calculation adjusted for code bias and bounded by the one sided confidence interval of the reduced uncertainty.

If the ATR calculation plus ATRC evaluated bias and reduced uncertainty fall below the peak power metrics of the bounding physics analysis and/or thermal-hydraulic analysis, discussed above, the current modeling assumptions are considered both valid and bounded. Following this process, the 3D/2D Axial Power Factor used in the HELIOS/ZENITH post-processing system is defined by Equation 3.9.

$$ {}^{Adjusted}_{\frac{3D}{2D}}A_r(t) = \max_z \left(\frac{{}^{3D}P'''_{z,r}}{{}^{2D}P'''_r}\bigg|_{ATR}^{MCNP} + \frac{{}^{Adjusted}P'''_{z,r} - {}^{A\,Priori}P'''_{z,r}}{{}^{fe}P_a}\bigg|_{ATRC}^{MCNP} + \sigma_{z,r} \right) \tag{3.9a} $$

$$ {}^{Adjusted}_{\frac{3D}{2D}}A_r(t) = \max_z \left({}^{ax}A + {}^{ax}\beta + \sigma_{z,r} \right) \tag{3.9b} $$

Where: $P'''_{z,r}$ is the power density at position r in the x-y plane and height z in the axial dimension in the 3D MCNP model. P'''_{r} is the power density at position r in the x-y plane of the 2D MCNP model. ${}^{fe}P_a$ is the volumetric average power density of the fuel element. $\sigma_{z,r}$ is the reduced uncertainty associated with each adjusted power density in r and z. ${}^{ax}A$ and ${}^{ax}\beta$ are the calculated axial multiplier and bias adjustment, respectively.

The HELIOS code also makes use of an azimuthal bias factor plus uncertainty, created using the ATRC 12-5 flux run during 2012, see section 5.4. Two adjusted datasets were created, one for inner fission wires, and another for all wires nearest the side-plates. The reason for this azimuthal bias is chiefly associated with the fact that the ATR HELIOS model assumes a solid aluminum side plate. In reality, there are relatively large "side plate vents" in the side plates near the axial mid-plane where the ATRC fission wires are placed for measuring the axial fission profile. It is reasonable to assume that the added moderation in the real system would cause the measured power density near the side plates to be more peaked than in the simulated system. Thus, there is an inherent bias between the 2D simulation model and the 3D physical system. Following the least squares process, the azimuthal adjustment to the ATR calculated power with ATRC bias and uncertainty is defined by Equation 3.10.

$$^{Adjusted}A_{\varphi}(t) = 1 + \frac{1}{N}\sum_{w}^{N} \frac{^{Adjusted}P'''_{w} - ^{A\,Priori}P'''_{w}}{^{\text{core}}P_a}\Bigg|_{ATRC12-5}^{HELIOS} + \sigma_{\varphi} \quad (3.10a)$$

$$^{Adjusted}A_{\varphi}(t) = 1 + {}^{az}\beta + \sigma_{\varphi} \quad (3.10b)$$

Where: P'''_{w} is the power density in wire w. N is the total number of fission wires for either: (a) nearest the side plates, or (b) interior wires. ${}^{core}P_a$ is the volumetric core average power density. σ_{φ} is the reduced uncertainty associated with either the outer wires, or inner wires. ${}^{az}\beta$ is the azimuthal bias adjustment.

The HELIOS regional power is adjusted for both axial and azimuthal biases during ZENITH post-processing. The biases of Equation 3.9 and Equation 3.10 are treated as separate multipliers that are applied prior to computation of UFSAR power metrics, e.g., P.D., EPP, EPPt. However, the reduced axial and azimuthal uncertainties are not multiplicative or additive, they are propagated. The bias multipliers plus propagated uncertainty equation effectively forms the basis for a modified axial factor, Equation 3.11.

$$^{Adjusted}A = ({}^{ax}A + {}^{ax}\beta)(1 + {}^{az}\beta) + \sigma_u \quad (3.11)$$

Where: ${}^{ax}A$ is the calculated axial factor from either the ROSUB polynomial or the calculated 3D/2D power factor using MCNP. ${}^{ax}\beta$ and ${}^{az}\beta$ are the axial and azimuthal bias adjustment, respectively. Σ_u is the propagated uncertainty of both $\sigma_{z,r}$ and σ_{φ}.

Derivation of the propagated uncertainty follows the standard error propagation formula, Equation 3.12:

$$\sigma_u^2 = \left(\frac{\partial u}{\partial x}\right)^2 \sigma_x^2 + \left(\frac{\partial u}{\partial y}\right)^2 \sigma_y^2 \quad (3.12a)$$

$$\sigma_u^2 = \left(\frac{\partial u}{\partial {}^{ax}\tilde{A}}\right)^2 \sigma_{r,z}^2 + \left(\frac{\partial u}{\partial {}^{az}\tilde{A}}\right)^2 \sigma_{\varphi}^2 \quad (3.12b)$$

Where: U is defined by the adjustment multipliers, Equation 3.13.

$$U = ({}^{ax}A + {}^{ax}\beta)(1 + {}^{az}\beta) \quad (3.13a)$$

$$U = \left({}^{ax}\tilde{A}\right)\left({}^{az}\tilde{A}\right) \quad (3.13b)$$

The partial derivatives of U are simply:

$$\frac{\partial u}{\partial {}^{ax}A} = {}^{az}\tilde{A} \quad \text{and} \frac{\partial u}{\partial {}^{az}A} = {}^{ax}\tilde{A} \tag{3.13c}$$

Thus, Equation 3.12 can be replaced by Equation 3.14.

$$\sigma_u^2 = \left({}^{az}\tilde{A}\right)^2 \sigma_{r,z}^2 + \left({}^{ax}\tilde{A}\right)^2 \sigma_\varphi^2 \tag{3.14a}$$

$$\left(\frac{\sigma_u}{U}\right)^2 = \left(\frac{\sigma_{r,z}}{{}^{ax}\tilde{A}}\right)^2 + \left(\frac{\sigma_\varphi}{{}^{az}\tilde{A}}\right)^2 \tag{3.14b}$$

This equation is encoded into the ZENITH post processing suite. If the ROSUB polynomials are used, there is no uncertainty assigned for the axial multiplier. Thus, if using the ROSUB polynomials, the uncertainty propagation equation reduces further.

$$\left(\frac{\sigma_u}{{}^{ax}A \times {}^{az}\tilde{A}}\right)^2 = \left(\frac{\sigma_\varphi}{{}^{az}\tilde{A}}\right)^2 \tag{3.14c}$$

The reduced uncertainties $\sigma_{r,z}$ and σ_φ represent the uncertainty of the calculation plus bias. To test this assumption, we again apply Equation 3.12 to each term of Equation 3.13.

$${}^{ax}\tilde{A} = {}^{ax}A + {}^{ax}\beta \tag{3.15a}$$

The partial derivatives of ${}^{ax}\tilde{A}$ are simply:

$$\frac{\partial u}{\partial {}^{ax}A} = 1 \quad \text{and} \frac{\partial u}{\partial {}^{ax}\beta} = 1 \tag{3.15b}$$

Thus, the uncertainty propagation formula yields Equation 3.16.

$$\sigma_{{}^{ax}\tilde{A}}^2 = (1)^2 \sigma_{{}^{ax}A}^2 + (1)^2 \sigma_{{}^{ax}\beta}^2 \tag{3.16a}$$

Note that the uncertainty on the calculation is assumed to be zero, but the uncertainty on the bias is the reduced uncertainty from the ATRC measurements. Thus Equation 3.16a reduces to Equation 3.16b.

$$\sigma_{{}^{ax}\tilde{A}}^2 = \sigma_{{}^{ax}\beta}^2 \triangleq \sigma_{r,z}^2 \tag{3.16b}$$

This exact procedure can be repeated to prove that the uncertainty on the azimuthal multiplier ${}^{az}\tilde{A}$ is equivalent to the reduced azimuthal uncertainty, Equation 3.16c.

$$\sigma_{{}^{az}\tilde{A}}^2 \triangleq \sigma_\varphi^2 \tag{3.16c}$$

3.2.6 Fission Density Adjustment Methodology

Simplistically for chopped cosine shaped power distributions, the peak-to-average axial burnup factor is defined as the indefinite integral function of the 3D/2D power factor A(t) with respect to irradiation time, Equation 3.17.

$$B(t) = \frac{\int_0^t P_m'''(t\prime)dt\prime}{\int_0^t P_a(t\prime)dt\prime} \cong \int_0^t A(t')dt' \tag{3.17}$$

Where: P'''_m is the power density at core mid-plane. P_a is the volumetric average power density of all slices in the z dimension. t is the time that the fuel has been irradiated.

In PDQ7, the B value is found by Equation 3.17 and functionalized (i.e., set to a polynomial) where time is in units of lobe exposure. However, with the 3D/2D MCNP calculations, a value of B can be computed directly by performing a 3D depletion with the MCNP code (for computing depletion rates) coupled to the ORIGEN2 code for performing the depletion calculation for every depletable region in the MCNP model. This coupling is performed with the coupling script, MO.PY, see section 3.4. In lieu of an explicit 3D depletion calculation, the power adjustment methodology expressed in Equation 3.11 can be leveraged for adjusting the depletion shape. Thus, a similar axial and azimuthal bias correction is applied to fission density, Equation 3.18.

$$^{Adjusted}B = (^{ax}\mathrm{B}+^{ax}\beta)(1 + {}^{az}\beta) \quad (3.18)$$

Where: ^{ax}B is the calculated axial factor from either the ROSUB polynomial or the calculated 3D/2D burnup factor using MCNP. $^{ax}\beta$ and $^{az}\beta$ are the axial and azimuthal bias adjustment, respectively. Note that the propagated uncertainty term is left off. This is because uncertainties associated for burnup are not well represented by the axial and azimuthal power shape measurements. It should be noted that neither the PDQ7 assessment, made with Equation 3.17, nor the HELIOS assessment, made with Equation 3.18, is truly validated. They both use reasonable assumptions of predicted burnup behavior, but neither has been compared with any actual "depletion" measurement, e.g., gamma-spectroscopy, chemical assay).

3.3 Nuclide Tracking

A significant challenge for transitioning from the PDQ7 to a HELIOS-based methodology is the carryover of nuclide data generated by PDQ7 in a past cycle that is needed by HELIOS in the current and future cycles. There are three different types of carryover nuclide data: fuel, beryllium and hafnium.

3.3.1 Hafnium Neck Shim Depletion

PDQ7 does not explicitly track the hafnium nuclide concentrations of the neck-shims or OSCCs. It should be expected that the OSCCs do experience a reactivity loss due to depletion. However, OSCC depletion is fairly minor compared to that of the neck-shims, thus it is not currently treated in either the PDQ7 or HELIOS methodologies. The neck shim reactivity decrement per cycle is treated via a direct multiplier against the neck-shim hafnium macroscopic cross section (Gregory, 1978). This multiplier, computed by the HFBURN code, is an empirical function of lobe-exposure (in Megawatt-Day) of the nearest ATR lobe. The physical meaning of the multiplier is the "fraction-of-original-worth". Thus, it is computed by taking the rod-worth after a given lobe-exposure and dividing it by the fresh rod-worth. Currently, the fraction-of-original-worth multipliers are functionalized with respect to the fresh rod in that neck-shim location in the 1994 CIC requalification tests.

To generate hafnium nuclide densities for the 24 neck-shims in the HELIOS model, without performing core-follow going back to the last all-fresh rod configuration (the 2004 CIC), several approximations had to be made. First, the hafnium absorption reaction rate is considered fairly invariable between the 2004 CIC, Cycle 134A, and the first cycle analyzed by the Core ATR Core Modeling Upgrade Project, Cycle 145A. This is reasonable given the slow rate of hafnium depletion and the fact that the average core power and lobe-power splits are very consistent from cycle to cycle. The cycle-time weighted mean and standard deviation for total core power during this time frame is 109.2 MW and 7.4 MW, respectively. Finally, it is assumed that rod-to-rod self-shielding, or shadowing, is reasonably represented by the sub-group resonance treatment assuming all the rods are fully inserted and depleted together. This is a crude approximation for the actual rod withdrawal schedule for each cycle. With these assumptions, the hafnium cross section and flux conditions were computed with the 1994 CIC configuration at 110 MW. The flux in each lobe was scaled to the mean lobe-power from 134A through 144B. This data was then input into an MS-EXCEL spreadsheet calculation containing a recursive solution to the Bateman Equations for sequential decay daughters, Equation 3.19. A parallel FORTRAN routine was developed to verify the spreadsheet calculation. All hafnium depletion daughters are sequential with no feedback loops, i.e., daughter transitioning back to a parent. Thus, the recursive analytic solution of the Bateman equations is ideal for

hafnium depletion (Shultis, 2002). Equation 3.19a considers only the transition of parent k to production of daughter j, assuming that the initial condition concerning isotopes downstream of k is zero. Equation 3.19b represents the constant coefficients for Equation 3.19a. Equation 3.19c uses the fact that N_j is in fact the sum of all upstream daughters.

$$n_j(t) = \frac{1}{\lambda_j} N_k(t_o) \sum_{m=1}^{j} C_m e^{-\lambda_m t} \quad (3.19a)$$

$$C_m = \frac{\prod_{i=1}^{j} \lambda_i}{\prod_{i=1, i\neq m}^{j} (\lambda_i - \lambda_m)} \quad (3.19b)$$

$$N_j(t) = \sum_{j}^{k} n_j(t) \quad (3.19c)$$

Where: n_j is the contribution from parent N_k to daughter $_{Nj}$. λ represents a transition coefficient equivalent to microscopic cross-section multiplied by flux in each neck-shim: $\lambda=\sigma\times\varphi$. C_m is the coefficient for each daughter m in the linear chain between j and k. t is time.

Figure 3.5 shows the depletion behavior for the NW-1 neck shim in an independent benchmark created for verifying the MS-EXCEL spreadsheet described by Equation 3.19. In this benchmark, the 94CIC configuration is modified to burn at 110 MW for 120 days. Each burn step was 10 days in length. The hafnium nuclide densities, one-group neutron flux, and microscopic absorption cross-sections for each neck shim was collected at the end of each burn step. The nuclide absorption cross-section for each
isotope was multiplied by the one-group neutron flux to form the transition coefficients for each isotope in each neck shim at each burn step. Equation 3.19 was then applied to deplete each neck shim in the MS-EXCEL spreadsheet from the fresh composition through 120 days. The resulting spreadsheet calculated nuclide densities were then compared against those output from HELIOS. As can be seen from the figure, the analytic approach used in the spreadsheet matches exactly to the HELIOS calculation. Note that HELIOS uses a 4th order Runge-Kutta solution algorithm to solve the Bateman equations.

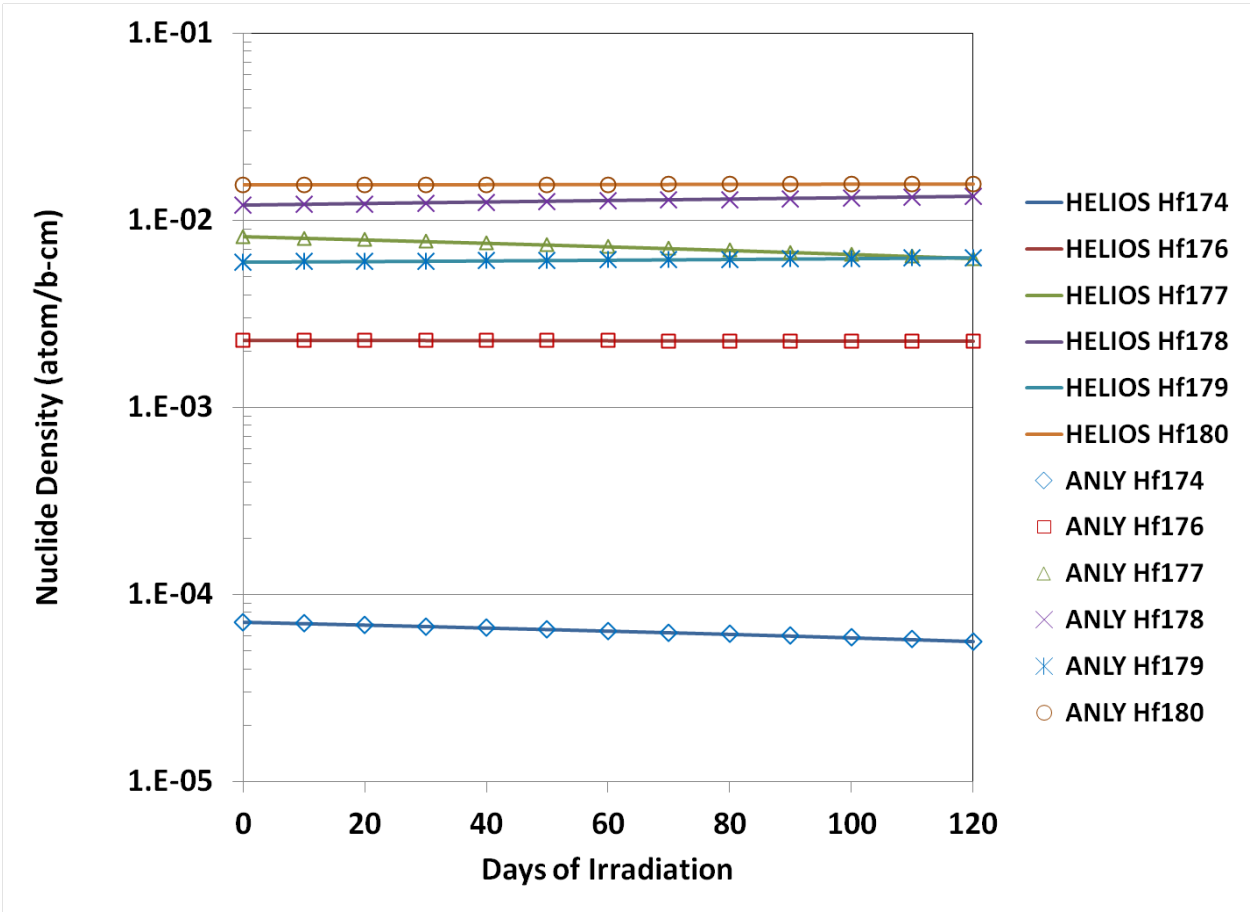

Figure 3.5. Comparison of MS-EXCEL analytic solution with HELIOS using the 94CIC benchmark evaluated at a reactor power of 110 MW burned for 120 days.

Figure 3.6 shows the depletion of hafnium in the southeast-3 neck-shim. Hafnium is selected as a reactivity control material for its slow reactivity loss with burnup. This is due to the fact that Hf-176 through Hf-180 are coupled in a series relationship and that all hafnium nuclides have a reasonably significant absorption cross-section. The total absorption cross-sections for hafnium nuclides calculated by the 1994 CIC case-study for the southeast neck-shim arm are given in Table 3.1.

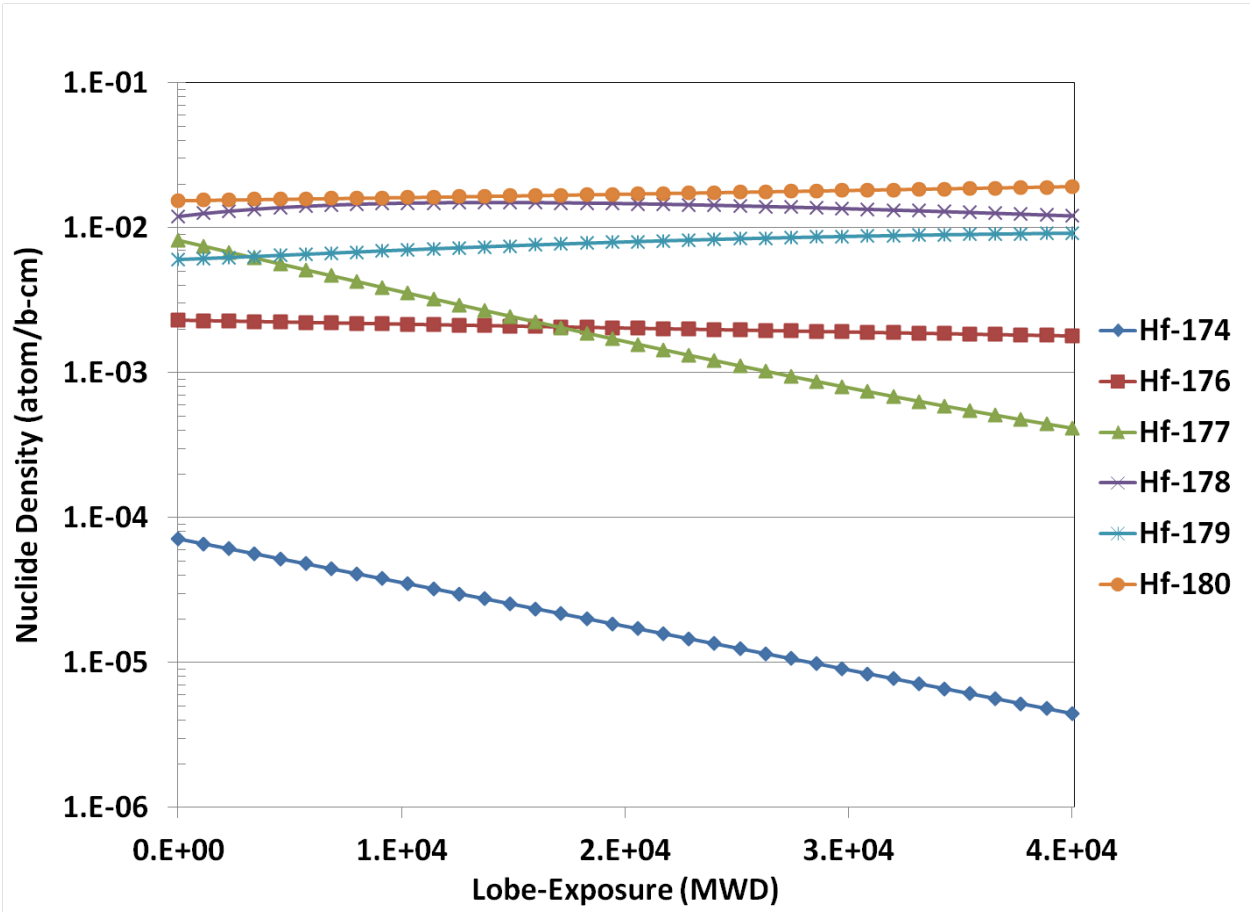

Figure 3.6. Depletion of the southeast-3 neck-shim between the 2004 CIC and the beginning of cycle 145A.

Table 3.1. Hafnium absorption cross-section (barns) computed for the southeast neck-shims.

	SE-1	SE-2	SE-3	SE-4	SE-5	SE-6
Hf-174	38.66	33.98	31.57	30.94	31.54	34.61
Hf-176	3.00	2.85	2.77	2.75	2.77	2.87
Hf-177	44.79	40.48	38.41	37.92	38.44	41.39
Hf-178	7.94	7.11	6.70	6.60	6.69	7.25
Hf-179	7.97	7.51	7.26	7.21	7.26	7.57
Hf-180	1.04	0.93	0.87	0.85	0.87	0.95

Figure 3.7 shows the fraction-of-original-worth computed by HELIOS for the southeast neck-shims, using nuclide densities generated by the spreadsheet, compared with the HFBURN values for the actual cycles 134A-144B. As can be seen from the plot, the derived hafnium nuclide densities give similar reactivity worth values with HELIOS as the empirical function used in HFBURN. Thus, the MS-EXCEL spreadsheet (i.e., analytic solution methodology) was used to estimate hafnium nuclide densities for Cycle 145A BOC.

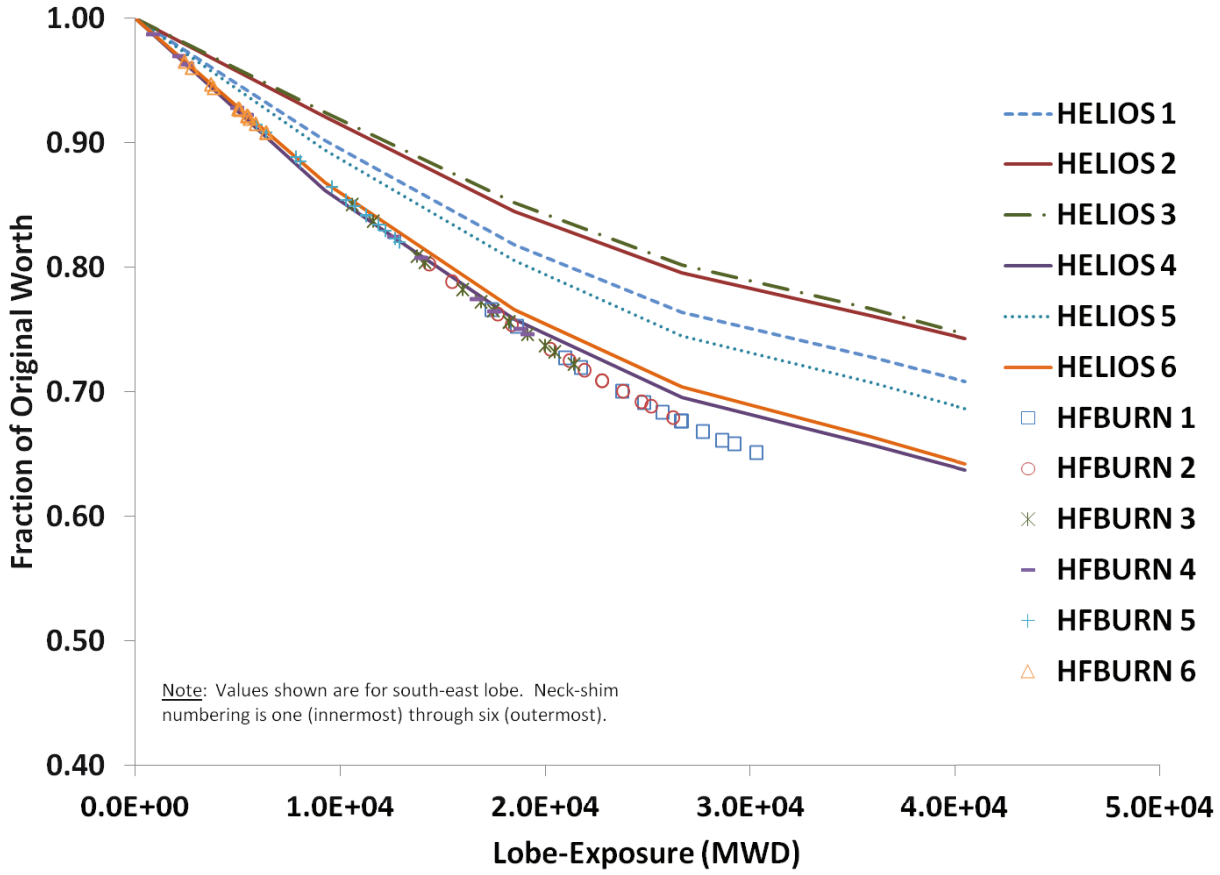

Figure 3.7. Fraction of original worth multipliers computed with HELIOS compared with HFBURN in the southeast lobe.

From Cycle 145A on, HELIOS was used to micro-deplete hafnium in the neck-shims for each time-step in each cycle. Figure 3.8 shows the depletion trend from the 2004 CIC through Cycle 154A. The spreadsheet was used for plot points prior to Cycle 145A. The EOC nuclide densities output from HELIOS, following the As-Run analysis of each of these cycles is printed from cycle 145A-154A. The As-Run anlyses of cycle 145A through 154A is described fully in section 5.6. As can be seen from Figure 3.8 the depletion trends during As-Run are fairly, though not perfectly, consistent with the estimated depletion behavior prior to actually following the ATR.

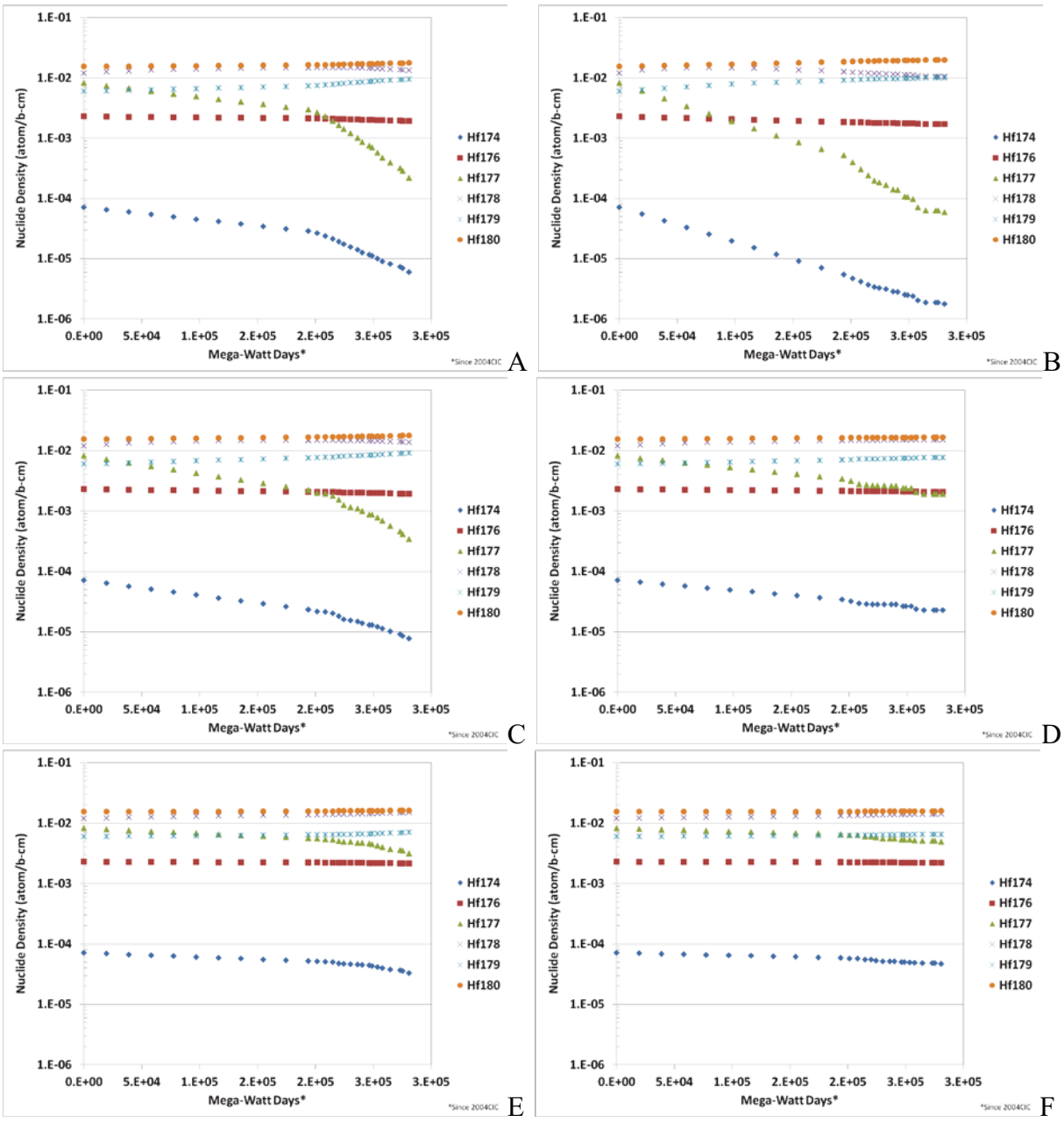

Figure 3.8. Depletion transition from MS-EXCEL analytic depletion model (tied to HFBURN values) to As-Runs with HELIOS for neck shims: (A) northeast-1, (B) northwest-2, (C) southwest-3, (D) northwest-5, (E) northeast-4, (F) southeast-6

3.3.2 Beryllium Reflector Depletion

The beryllium depletion products are transitioned from the PDQ7 reflector composition in Cycle 145A at BOC. From that point on, beryllium nuclides are tracked using the new methodology. PDQ7 tracks Be-9, Li-6, H-3 and He-3 in essentially five regions in the ATR reflector. The HELIOS reflector geometry description has been refined manually to as closely as possible to correlate "visually" with the reflector regions defined in PDQ7, Figure 3.9. Region A is a thin region directly abutting the fuel serpentine. This corresponds to PDQ7 edit set 56, regions 41-45. Region B is a slightly larger region just outside of Region A. This corresponds to PDQ7 edit set 57, regions 46-49, 369-376, 381-384. The inner-reflector exists outside of Region B but generally inside of the OSCC's. This corresponds to PDQ7 edit set 58, regions 50-53, 377-380. The outer-reflector exists outside of the OSCC's. This corresponds to PDQ7 edit set 54, region 10. Finally, the OSCC's constitute the fifth beryllium

depletion region. This corresponds to PDQ7 edit set 53, regions 9, 54-61. The material overlays for the HELIOS model is refined to reasonably approximate the PDQ7 areas, as can be seen in Figure 3.10.

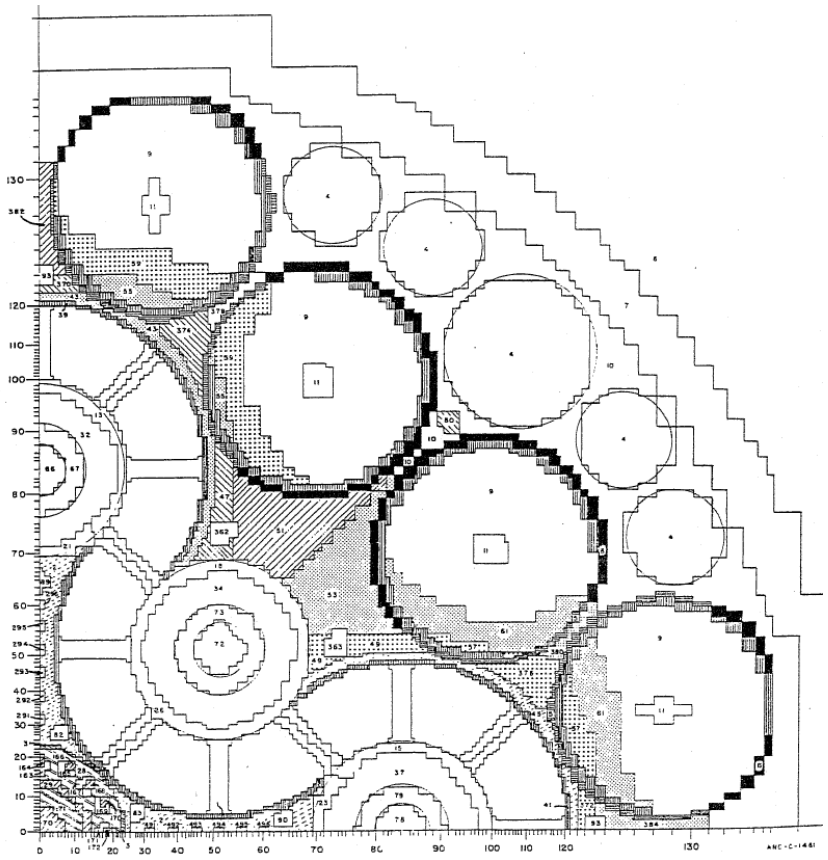

Figure 3.9. PDQWS overlay regions A, B, inner, outer, and OSCC

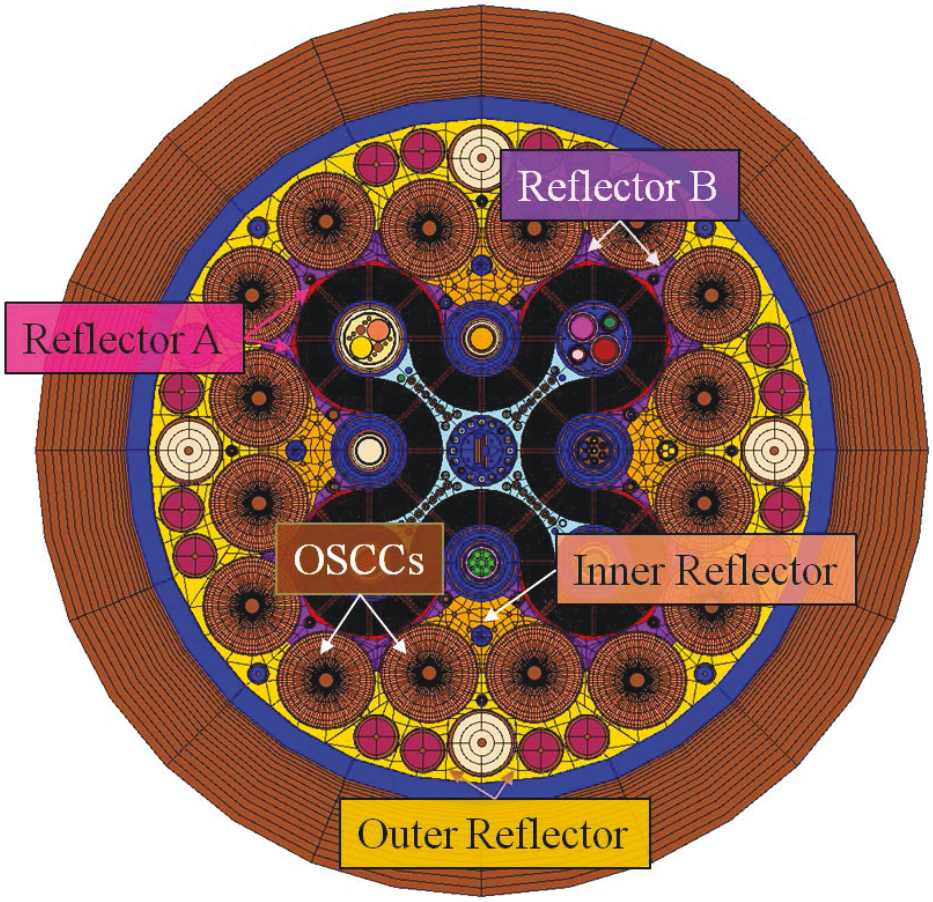

Figure 3.10. HELIOS geometry of Cycle 145A showing the reflector depletion regions A, B, inner, outer, and OSCC

HELIOS is not well adapted for beryllium depletion for two primary reasons. First, the code requires a separate depletion calculation for every single mesh region containing burnable material. In other words there is no averaging of fluxes over macro areas of the core prior to depletion. Secondly, HELIOS does not support all the reaction types necessary to deplete beryllium. HELIOS uses the following neutron reactions to deplete the fuel: (n,γ), (n,f), (n,2n), (n,3n). It does not incorporate (n,p) or (n,α) into its burnup depletion chains.

Given the vast number of HELIOS mesh regions in the beryllium reflector, it is expected that depleting the reflector using HELIOS would greatly increase computer resource requirements. Beryllium depletion contributes a small decrement to core reactivity every cycle (Smith et al, 1990). Thus, updating the reflector composition after every cycle, as opposed to every time-step, is not expected to introduce significant modeling error on the critical eigenvalue or power distribution.

A standalone depletion subroutine was written for the explicit purpose of depleting the ATR beryllium reflector. This subroutine is part of the database management code, THECPT, developed by the Core Modeling Update Project, see section 3.2.1. The depletion chains of all isotopes modeled by THECPT are shown in Figure 3.11. Because of the feedback loop between H-3 decay and the ^{3}He(n,p) reaction, the analytic solution methodology outlined in Equation 3.19 could not be used. Instead, a 4th Order Runge-Kutta (RK4) solution methodology was employed. This is the same form of solution methodology used in HELIOS-2.0 and later versions (Studsvik, 2009). It has also been found to be satisfactorily stable by Aboanber, Bakkari et. al. and Hykes et. al. (Aboanber, 2000), (Bakkari, 2009), (Hykes, 2013)

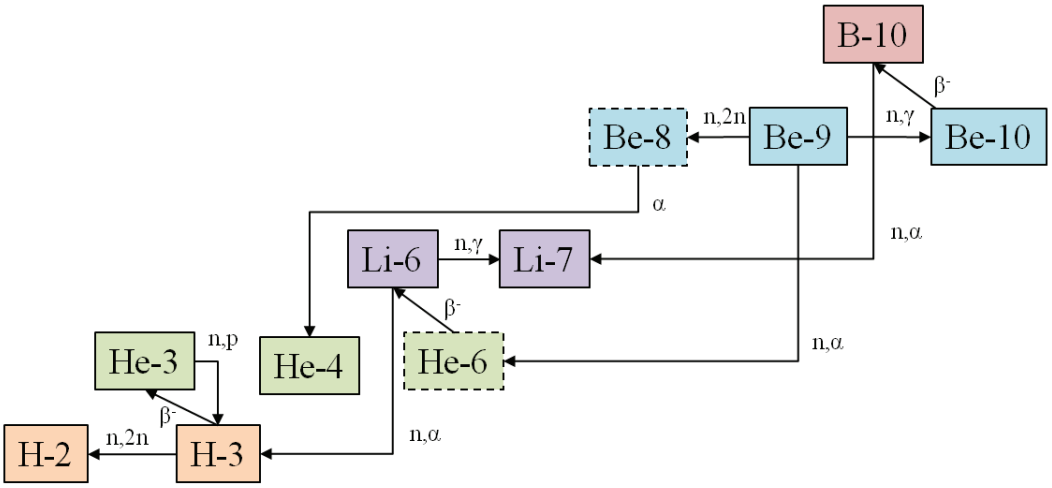

Figure 3.11. Transmutation and decay relationships for Be-9 decay series modeled by THECPT. The dotted boxes represent isotopes half-lives so short that their decay is assumed instantaneous, thus are not explicitly tracked by THECPT. All alpha producing reactions and decay transitions add to He-4 production, though not shown in this graphic.

Runge-Kutta solution techniques are a family of single-step-methods used for evaluating first-order derivative functions such as the Bateman equations, dy/dt=y(t). The derivative function is evaluated as a weighted average of four numerical estimates (A, B, C, D) of the original derivative function, y(t). The basic form of the RK4 procedure implemented in THECPT is as follows.

The Bateman equations for each potential reaction or decay product/daughter i in the Be-9 depletion chains can be expressed as:

$$\frac{\partial N_i}{\partial t} = \sum_{j=1}^{All\ Parents}\left(\sum_g^3 \sigma_{j,g}\varphi_g + \lambda_j\right)N_j(t) - \left(\sum_g^3 \sigma_{i,g}\varphi_g + \lambda_i\right)N_i(t) \quad (3.20a)$$

Note that the transition coefficients for reaction rates assume a three group g flux. In matrix form the system of equations is written as:

$$\frac{\partial \bar{N}}{\partial t} = \bar{\boldsymbol{\Lambda}}\bar{\boldsymbol{N}} \quad (3.20b)$$

Here, N_i is the derivative function to be approximated by:

$$N_{i,t+1} = N_{i,t} + \frac{h}{6}\left(A_{i,t} + 2B_{i,t} + 2C_{i,t} + D_{i,t}\right) \quad (3.21a)$$

Where A, B, C, and D are numeric evaluations of the derivative function $\partial N/\partial t$ at time step t. h is the time step between time t and time t+1

$$A_{i,t} = \left.\frac{\partial N_i}{\partial t}\right|_t \quad (3.21b)$$

$$B_{i,t} = N_{i,t} + \frac{h}{2}A_{i,t} \quad (3.21c)$$

$$C_{i,t} = N_{i,t} + \frac{h}{2}B_{i,t} \quad (3.21d)$$

$$D_{i,t} = N_{i,t} + hC_{i,t} \quad (3.21e)$$

The ATR cycle is divided into a user specified number of time steps. Equation 3.21 is solved for each time step. The previous time step is used to provide the evaluation of the derivative function dN/dt to the next time step. Thus, the derivative function dN/dt for each isotope is evolved from one time step to the next. HELIOS was used to provide the three group fluxes to THECPT. The user selects a representative burn-step within the overall HELIOS depletion, to represent the flux levels over the entire cycle. Said differently, the flux values provided by the HELIOS calculation are not burnup dependent. The (n,γ), (n,2n), (n,p) and (n,α) cross-sections were computed using flux multiplier tallies within the MCNP model of the 94CIC benchmark. One cross-section dataset was created for the inner reflector, i.e., all regions inside of the OSCCs. Another cross-section dataset was created for the outer reflector, including the OSCCs. The cross-section data used for the ATR reflector depletion calculations is provided in Table 3.2.

Table 3.2. Transmutation cross-sections (barns) computed by MCNP 94CIC benchmark for beryllium reflector.

		Inner Reflector			Outer Reflector		
	Lower E	0	0.625eV	0.45MeV	0	0.625eV	0.45MeV
	Upper E	0.625E	0.45MeV	20MeV	0.625E	0.45MeV	20MeV
n,2n	H-3	0	0	1.E-05	0	0	1.E-05
n,p	He-3	4108	125	0.80	4462	146	0.82
n,t (n,α)	Li-6	744	22.40	0.23	809	26.05	0.24
n,γ	Li-6	3.E-02	9.E-04	1.E-05	3.E-02	1.E-03	1.E-05
n,γ	Be-9	7.E-03	3.E-04	1.E-04	7.E-03	3.E-04	1.E-04
n,α	Be-9	0	0	3.E-02	0	0	2.E-02
n,2n	Be-9	0	0	7.E-02	0	0	6.E-02
n,α	B-10	2969	90.63	0.38	3225	106	0.38

One would expect that the RK4 algorithm is not necessary if the depletion cycle (and post-irradiation decay time) can be modeled with sufficiently small time steps using the fully explicit form of the Bateman equations, i.e., Equation 3.20, discretized into infinitesimally small time steps. The fully explicit form, however, could be very unstable if the time steps are not made small enough. Instability occurs when the solution algorithm allows for round off error from one isotope to propagate to the next, ultimately swamping the entire solution. The RK4 subroutine was tested for convergence behavior against the fully explicit method. Figure 3.12 shows the depletion of tritium (normalized to one at the beginning of the depletion) over a 40 year time-period at typical reflector flux levels. The depletion calculation is carried on for this length of time to illustrate convergence error of the solution. Note that the explicit methodology of lower fidelity "courser" time steps converges to the highest fidelity (the 1000 step case) with increasing number of time steps, as is expected. Also note that the RK4 method with as low as 5 steps over 40 years captures the fully explicit 1000 step curve perfectly.

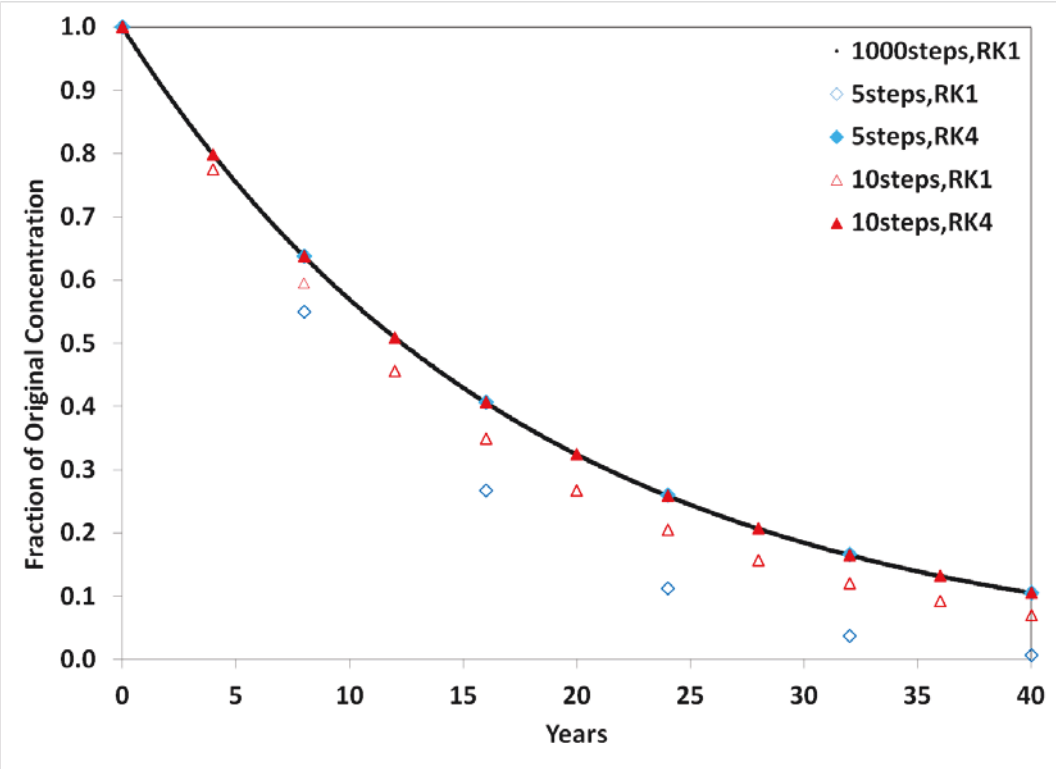

Figure 3.12. Convergence trends for varying time steps with the fully explicit fully resolved solution. Note that RK1 stands for fully explicit.

The Li-6, H-3, and He-3 compositions for beginning of Cycle 145A (i.e, end of the Cycle 144B outage) were used to define the reflector compositions for the Cycle 145A As-Run. These are the only isotopes that PDQ7 tracks for reflector depletion (Smith et. al., 1990). From Cycle 145A on, HELIOS/THECPT was used to micro-deplete beryllium in the ATR reflector regions for each cycle. The Be-9 composition is assumed fresh in each cycle as to isolate the effect of depletion from neutron moderation and reflection. The BOC, EOC, and End-of-Decay (EOD) nuclide densities for Li-6, H-3 and He-3 (as output from THECPT), following the As-Run analysis of each of these cycles is in Figure 3.13, Figure 3.14 and Figure 3.15. The As-Run analyses of cycles 145A through 154A is described fully in section 5.6. As can be seen, the depletion trends for H-3 during the As-Runs are fairly, though not perfectly, consistent with PDQ7. However, the trend is not quite so obvious with He-3. The discrepancy is purely attributed to the difference in the parent of He-3, which is H-3, at the beginning of each outage. The secular equilibrium of concentration of He-3 during irradiation is an order of magnitude less than H-3. When irradiation ends, the destruction of He-3 by (n,p) ends. He-3 is stable. Thus, its buildup behavior during the outage is driven purely by the source rate, $\lambda_{H3}N_{H3}$. Any small difference in the H-3 concentration between PDQ7 and HELIOS at EOC will result in large difference in He-3 at EOD. Differences in H-3 stem from differences in the flux solution of the two codes, different cross-sections used in the reflector depletion calculation and different Bateman solution algorithms.

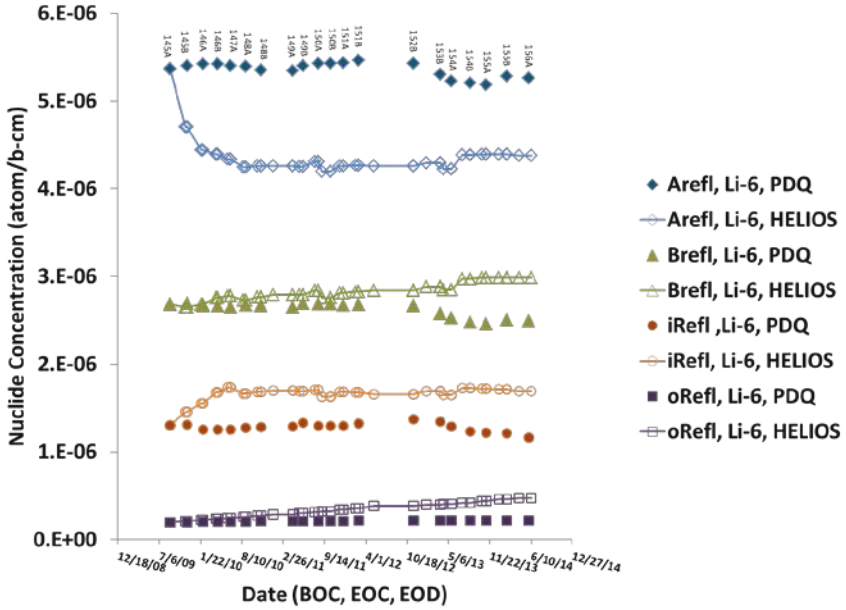

Figure 3.13. As-Run comparison of LI-6 depletion using HELIOS/THECPT RK4 solution versus PDQ7/HARMONY

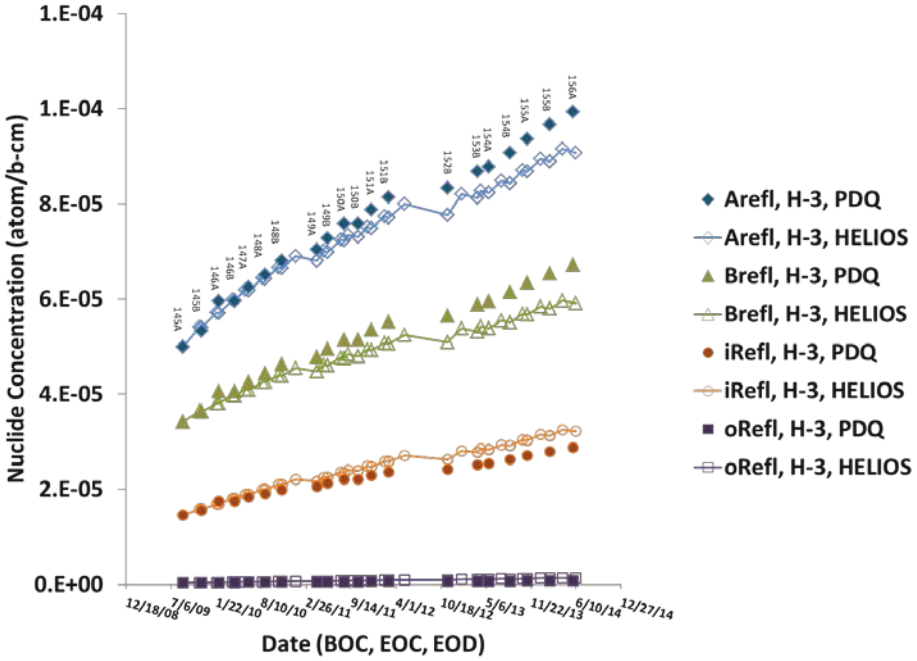

Figure 3.14. As-Run comparison of H-3 depletion using HELIOS/THECPT RK4 solution versus PDQ7/HARMONY

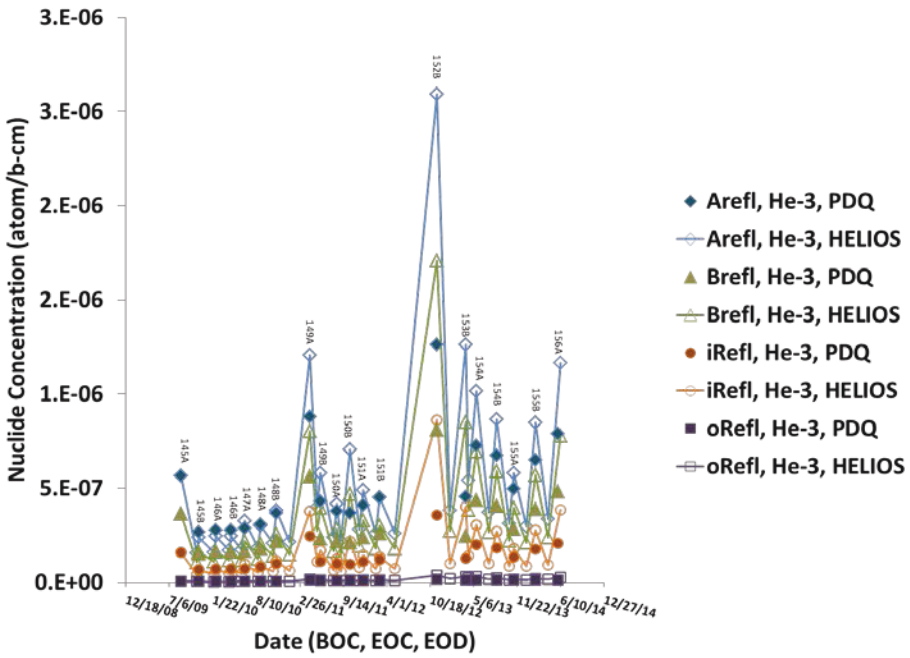

Figure 3.15. As-Run comparison of He-3 depletion using HELIOS/THECPT RK4 solution versus PDQ7/HARMONY

3.3.3 Fuel Depletion

The unique challenge for transferring fuel nuclide data from the PDQ7 methodology to the HELIOS methodology is the fundamental different approximations that are made between the two codes. One of the bigger approximations made by PDQ7 that is not performed by HELIOS is the use of cross-section condensation techniques.

PDQ7 solves the neutron diffusion-depletion problem in 1-D, 2-D and 3-D applications. Only the 2-D implementation (in r-z and x-y) is currently in use. PDQ7 uses seven lethargy groups, whereas HELIOS uses 49 energy groups. Cross-section data may be in microscopic or macroscopic form. A lumped fission product model is used for all but a few fission products and actinides (Holm, 1978). Nuclear cross-section data and shielding factors, provided by the HARMONY code, is interpolated from tables as a function of the concentrations of up to three representative isotopes (Breen et. al., 1965). Current ATR calculations performed with PDQ7 use ENDF/B-V cross-section data libraries. Conversely, HELIOS uses ENDF/B-VII cross-sections in 49 groups. In HELIOS, resonance spatial self-shielding calculations are performed for every region of the core and are solved for every burn-step during depletion. The HELIOS nuclide library contains over 200 depletable fission products, actinides and activation products.

Thus, in order to transfer nuclide data from PDQ7 to HELIOS, the nuclides assignments, homogenized per fuel element in PDQ7, must be redistributed to individual plates and sub-plate fuel mesh regions in the HELIOS model. For recycle fuel elements, this redistribution is founded on the uranium and boron distributions for fresh fuel. Also, there is no clear method for breaking out individual fission product nuclide densities from the fission product lump model. Thus, recycle fuel elements from PDQ7 do not contain fission products when they are first used in the HELIOS model. It is for this reason that the agreement between PDQ7 and HELIOS or ASUDAS and HELIOS tend to improve with increasing number of cycles since Cycle 145A (the first cycle analyzed with HELIOS). This is because once the fuel element enters the HELIOS system the fission products and spatial resolution become tracked and are allowed to evolve depending on the fuel element's life-cycle history. Thus, cycle-by-cycle, a HELIOS pedigree is built up. Also, after sufficient cycles have been modeled with HELIOS,

very few recycle fuel elements with a PDQ7 pedigree are used. Currently, 16 cycles have undergone As-Run with HELIOS accounting for roughly 70% of all fuel elements in the ATR canal.

Figure 3.16 compares the relative difference in the fuel element-averaged U-235 nuclide density between HELIOS and PDQ7 from Cycle 145A through Cycle 154A. All 40 fuel elements in each of the 16 cycles are plotted. The elative difference is defined as: $\varepsilon=(^{235}U_{HEIOS} - {}^{235}U_{PDQ})/{}^{235}U_{PDQ}$. The plot does not contain the fuel element position along the serpentine or the fuel element serial numbers themselves, as this information is irrelevant to showing the variability between HELIOS and PDQ7. Note that the BOC agreement between the codes is nearly perfect for the first few cycles. This is because the first few cycles nearly exclusively borrow data from the PDQ7 database, thus the relative differences is round-off error associated with translating the PDQ7 database to the HELIOS database.

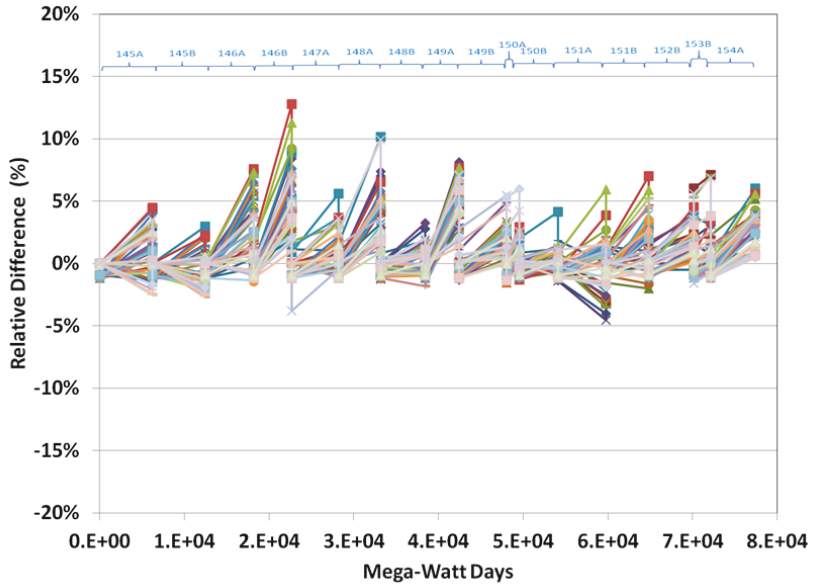

Figure 3.16. Relative difference between HELIOS and PDQ7 fuel element U-235 nuclide density

The mean relative difference over all of the 40×16×2=1280 nuclide comparisons was 0.78%. Fifty-three percent of the relative differences were positive. One can observe from inspection of Figure 3.16 that the magnitude of positive relative errors is generally greater than the negative relative errors. This means that in general, the HELIOS solutions depleted the U-235 at a somewhat lesser rate than PDQ7. In fact, the mean of positive EOC relative differences is 2.6% with a standard deviation of 2.1%, whereas the mean for negative relative differences is -1.0% with a standard deviation of 0.9%.

One of the requirements for the HELIOS code is to report the EOC loading "gram content" of uranium and plutonium isotopes for safeguards accountancy of the ATR fuel elements. One of the features in the ZENITH post processing routines is to compute the total grams B-10, U-235, U-238, Pu-239, Pu-240, Pu-241 at BOC and EOC. Figure 3.17 is a frequency plot that shows the statistical variation of relative differences between PDQ7 and HELIOS of the EOC U-235 mass per fuel element. As can be seen from the plot the prediction of fuel loading has low variability. The mean and standard deviation of the relative differences are 1.40% and 1.5%, respectively. Thus, HELIOS over predicts the gram content of PDQ7 by 1.40% on average.

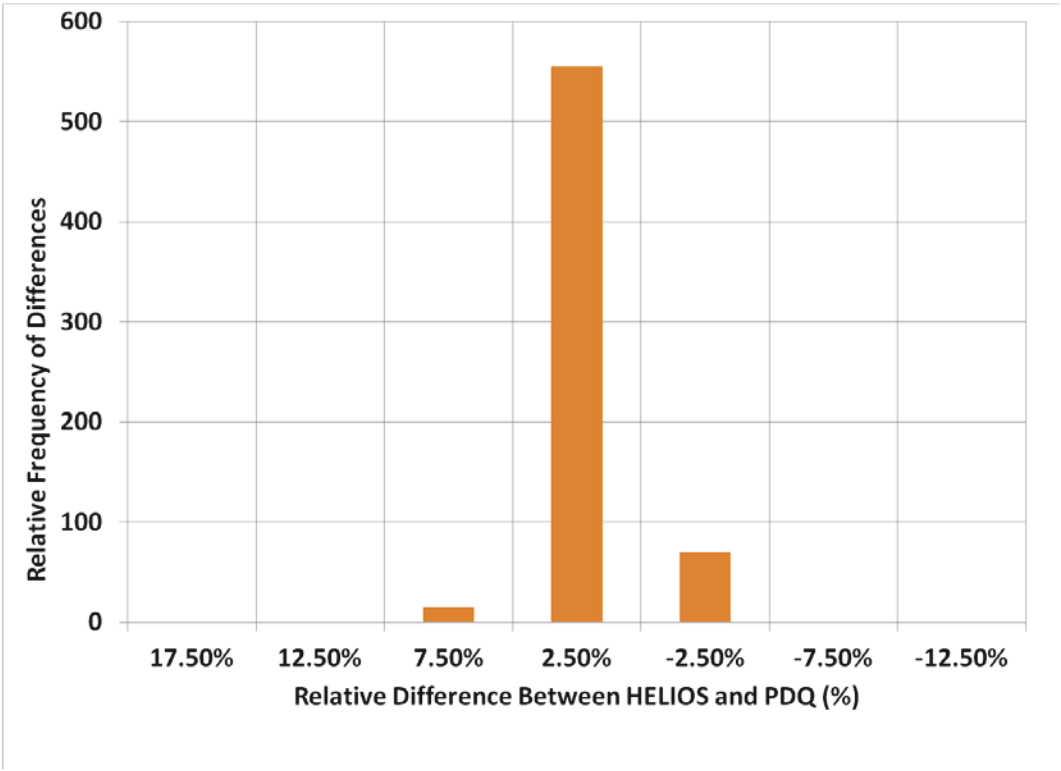

Figure 3.17. Frequency of relative differences in fuel element U235 loading between PDQ7 and HELIOS

Aside from accurately predicting nuclide content, the prediction of lobe exposure is used in both PDQ7, via the ROSUB code, as well as multiple down-stream applications outside of PDQ7. Lobe exposure is also tracked by HELIOS for every fuel element in every cycle and data-based by the THECPT fuel inventory tracking code. Figure 3.18 is a frequency plot that shows the statistical variation of relative differences between PDQ7 and HELIOS of fuel element lobe exposure. As can be seen from the plot the prediction of lobe exposure has low variability. The mean and standard deviation of the relative differences are -1.1% and 3.4%, respectively. Thus, HELIOS under predicts PDQ7 by -1.10% on average.

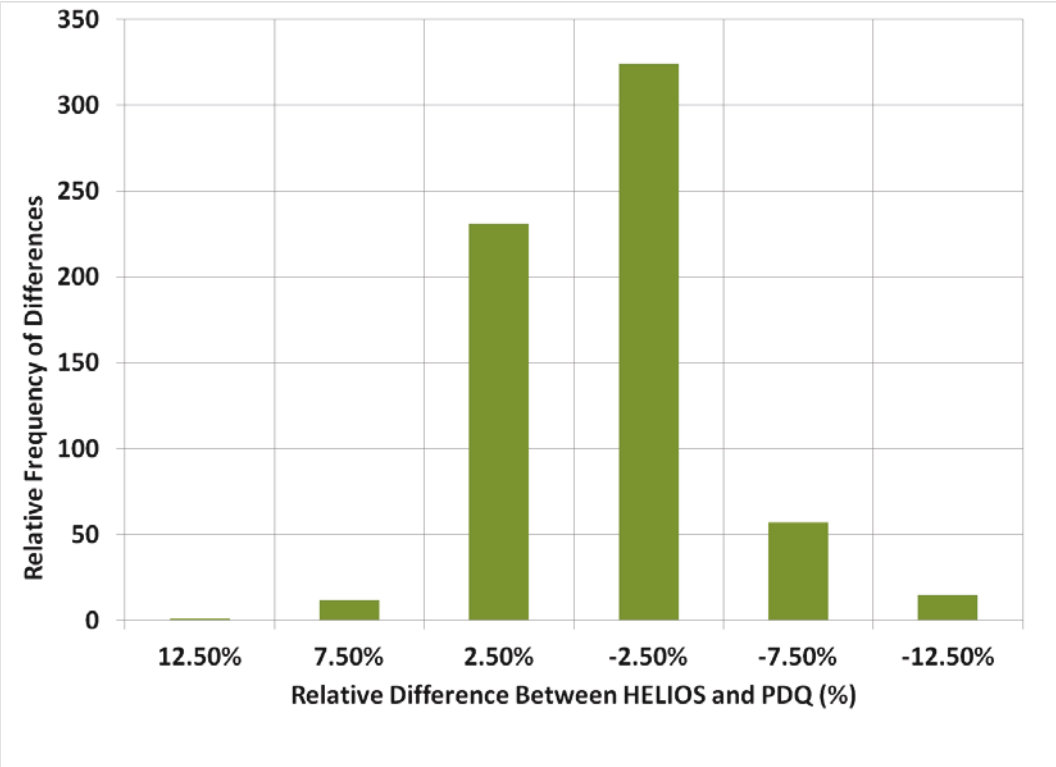

Figure 3.18. Frequency of relative differences in lobe exposure between PDQ7 and HELIOS

3.4 Three-Dimensional Extension of the Two-Dimensional Model

The three-dimensional extension of the HELIOS model will provide needed information about the axial dimension of the ATR. In the long run, it is likely that the state of practice for ATR fuel cycle design will evolve toward exclusive use of full 3D Monte Carlo based techniques as the necessary computer technology advances. Until this capability becomes feasible, it can be expected that a hybrid 2D/3D strategy will provide acceptable high fidelity 3D design and analysis quality information without the expense of solving the 3D geometry of the ATR for every transport solution. Thus, the extension will provide information in the form of biases and multipliers that can be used to enhance the capabilities of the two-dimensional model by accounting for axial effects without explicitly calculating these effects. The three-dimensional extension will ultimately serve as a supplement to the HELIOS model in a similar manner to the current PDQ7-based methodology where ROSUB multipliers are used to enhance PDQ7 results, only with greater flexibility and precision. However, in the intermediate phases of deployment of the new methodology, which will involve "parallel" CSAP computations using both HELIOS and PDQ7, it is most likely that the ROSUB approach will be retained in both methodologies as experience is gained with the planned MCNP5 based approach (see Section 3.5 for additional details).

3.4.1 One-Dimensional to Two-Dimensional Method with PDQ7

As discussed in Section 3.1, a program called ROSUB is used to generate reactivity, power density, fission density, effective plate power, and effective point power multipliers. The sections below discuss how these multipliers were calculated and how these multipliers have traditionally been applied. This discussion also highlights many of the assumptions inherit in these multipliers, such as the assumption regarding a cosine axial burnup shape in the ATR. Note that these assumptions represent restrictions that the hybrid 2D/3D strategy will attempt to remove in their entirety, will allow significant increases in flexibility to accommodate the restrictions, and/or quantify the effects of these restrictions. However, if the assumptions are not overly restrictive, the ROSUB multipliers can continue to be used to provide the needed axial information to the HELIOS model.

3.4.1.1 ROSUB Axial Multipliers

Within the PDQ7-based methodology, a three-dimensional extension to the "x-y" PDQ7 analysis was needed to compute the effect of the axial burnup shape on excess reactivity, point-to-core average power and burnup. PDQ7 can be operated with a 1D "r-dimensional" as well as a 2D r-z coordinate system. These two features were used together to calculate 1D and/or 2D reactivity biases and axial multipliers due to fuel burnup (Brown et. al., 1990). To do this, a single lobe is approximated by a right circular cylinder comprised of a generic in-pile tube (IPT) encircled by eight fresh 7F-type fuel elements (See Figure 3.19, where the inner red ring represents the IPT and the remaining rings represent 7F fuel elements). These 7F fuel elements are represented by seven fueled concentric annuli where no side plates or non-fueled plate ends are included. The annuli describe Plate(s) 1, 2, 3-4, 5-15, 16-17, 18, and 19, respectively. Each fueled annulus is represented by a homogenized cell containing water, aluminum cladding, and UAl_x fuel matrix. The generic IPT was non-depleting and was axially homogeneous, but with a cross-section that was flux weighted in an early r-z model during cross-section condensation. This generic IPT also contained a non-depleting test shroud.

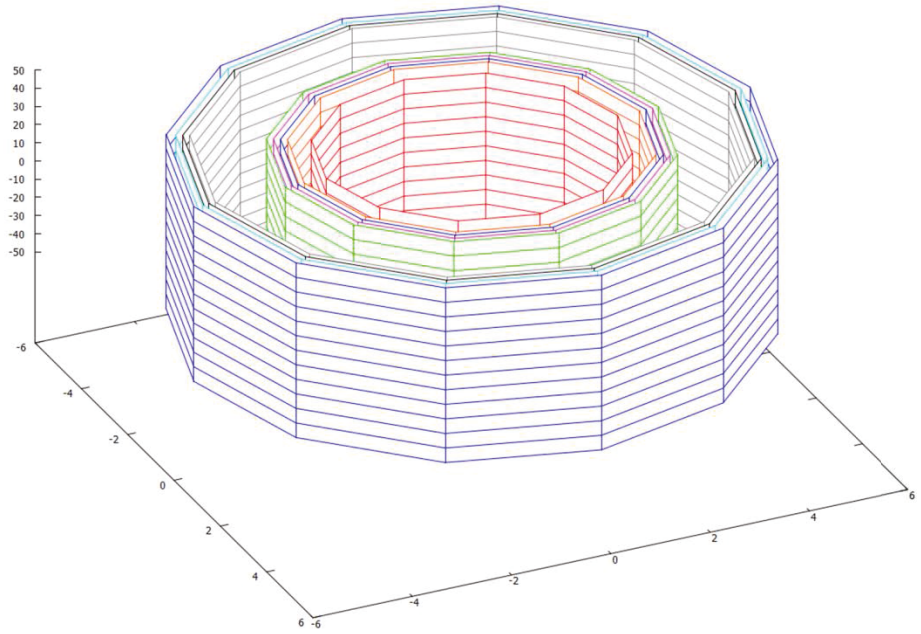

Figure 3.19. Graphical depiction of 2D r-z PDQ7 model. Each annulus represents a different fuel plate.

The concentric lobe model used by ROSUB is founded on a factor called lobe exposure. Lobe exposure is a cumulative quantity defined by the lobe power that the fuel element resides in multiplied by the time at that power. This is equivalent to Equation 3.22 below. Thus, for any given cycle the lobe exposure value obtained during that cycle is identical for all eight fuel elements in a lobe. This methodology puts more emphasis on lobe power than on the fuel element power. This may be due to the fact that with PDQ7 the cumulative power of fuel elements in a lobe is considered the more useful information as it can be directly compared with the ATR N-16 lobe power measurement system. Hence, fuel element powers are not generally used for the purpose of tracking fuel element power history. Using modern transport methods such as HELIOS and MCNP (as well as the other software systems mentioned in Chapter 2), fuel element powers can be trusted as exact. Thus, the fuel element burnup tracked in the HELIOS fuel element database is concerned with fuel element exposure, not lobe exposure. To derive lobe exposure values for the purpose of utilizing the ROSUB ρ, A and B polynomials within HELIOS, one simply needs to multiply the fuel element exposure in MWD by the number eight, as described by Equation 3.23. Adjusting the definition of lobe exposure in this way allows continued use of ROSUB, as appropriate, while

increasing the precision of the ROSUB multipliers based on this quantity. Thus, cumulative lobe exposures calculated using the PDQ7-based methodology can be used by the HELIOS-based methodology to approximate the lobe exposures obtained by each element prior to direct HELIOS modeling.

$$Lobe\ Exposure_{PDQ} = Previous\ Lobe\ Exposure + \sum_8^i (Element\ Power_{PDQ})(Time\ at\ Power) \quad (3.22)$$

$$Lobe\ Exposure_{HELIOS} = Previous\ Lobe\ Exposure + 8(Element\ Power_{HELIOS})(Time\ at\ Power) \quad (3.23)$$

The PDQ7 1D radial model was used only to aid in assessing reactivity bias. The 1D model radial description was identical to the r-z mesh at the mid-plane. The axial reactivity bias of this concentric lobe is solved by the following process.

1. Deplete both the 1D radial and the 2D r-z models to the same average burnup. The lobe power was set to 60 MW and burned to a lobe exposure of 3000 MWd.

2. Correct all eigenvalue points along the 1D radial models depletion by the difference between the 2D and 1D models at the beginning of the depletion. This correction was on the order of 2.0% Δk/k.

3. The total 1D/2D reactivity bias as a function of burnup is then the difference between the 1D radial and the 2D r-z eigenvalue as a function of burnup.

An equation for the reactivity bias procedure was not provided in Brown et al. However, from inspection of the reactivity curves included in the report it is likely that the 1D/2D reactivity correction could be defined as:

$$\rho_{1D2D} = \frac{k_{2D,0} - k_{1D,0}}{k_{2D,0} k_{1D,0}} - \frac{k_{2D}(t) - k_{1D}(t)}{k_{2D}(t) k_{1D}(t)} \quad (3.24)$$

Where: ρ_{1D2D} is the reactivity bias as a function of lobe exposure. k_{2D} is the critical eigenvalue of the 2D r-z PDQ7 model for a given burnup. k_{1D} is the critical eigenvalue of the 1D radial PDQ7 model at the same burnup. The subscript "0" represents the beginning of the cycle (i.e. time equal to zero). Note that the above derivation is for the concentric lobe representation of Figure 3.18. Thus, values of ρ_{1D2D} computed for each non-fresh fuel element must be divided by eight to get the axial reactivity bias associated for that one element.

The 2D rz model was used to compute point-to-average power density, burnup, and excess reactivity axial factors. For the power density axial factors, this was done by simply taking the power density at the mid-plane and dividing by the lobe average power density. The axial peaking factors for the fission density were obtained from the axial fission density peaking factors by the following equation.

$$A(t) = \frac{{}^{P_m(t)}/_{V_m}}{{}^{\sum P_i(t)}/_{\sum V_i}} = \frac{P_r(t)}{P_a(t)} \quad (3.25)$$

$$B(t) = \frac{\int_0^t P_r(t\prime)dt\prime}{\int_0^t P_a(t\prime)dt\prime} \quad (3.26)$$

Where: A is the point-to-average power density axial factor, B is the point-to-average burnup axial factor. P_m and V_m is the local region power and volume at the mid-plane. P_i and V_i are the local region powers of the r-z lobe system. P_r is the power density at the mid-plane, representing the peak power density. P_a is the axial lobe average power density. In this derivation, the average is over the lobe represented in the 2D rz model. In practice, this average represents an average power density over the entire ATR core.

The excess reactivity bias and point-to-average power density factors were calculated for continuous operation and for shutdown intervals of 5, 10 and 25 day following durations of continuous operation. Figures 3.20, 3.21 and 3.22 illustrate the reactivity biases, axial power density factors and burnup factors, respectively, as a function of lobe exposure. The values for continuous operation are plotted on the left y-axis. The factors accounting for burnup shape effects during shutdown intervals are plotted on the right y-axis. These shutdown interval curves account for the effect of xenon decay and samarium buildup on the axial burnup shape and resulting reactivity penalty. These canal-time-sensitive reactivity biases are only applicable for initial criticality because the xenon and samarium nuclide concentrations quickly evolve to their at-power secular equilibrium values, i.e., the continuous operation values. This is also true of the point-to-average axial power density multiplier. For any non-fresh fuel element during the first solution following a shut-down, the point-to-average multiplier for continuous operation (A1 in Figure 3.20) is first subtracted by the xenon and samarium factor (also shown in Figure 3.20) before being applied to downstream codes in the current PDQ7 legacy methodology.

There is yet another axial power multiplier that is used in the legacy methodology. The definition of Effective Plate Power (EPP) is that it is equal to Effective Point Power (EPtP) multiplied by the "Average Axial Factor". The EPP and EPtP will be discussed in greater detail later. The purpose of this secondary normalizing factor is essentially to axially redistribute the EPtP evenly over the active fueled height of the core. Said another way, it essentially divides out the point-to-average axial multiplier. In fact, multiplying the point-to-average axial multiplier (A1) with the average axial factor (A2) gives a value of one for all values of lobe exposure up to about 2500 MWD as can be seen in Figure 3.21. The tapered end of the A1×A2 curve is likely due to inadequacy of the polynomial fits used to represent A1 and A2.

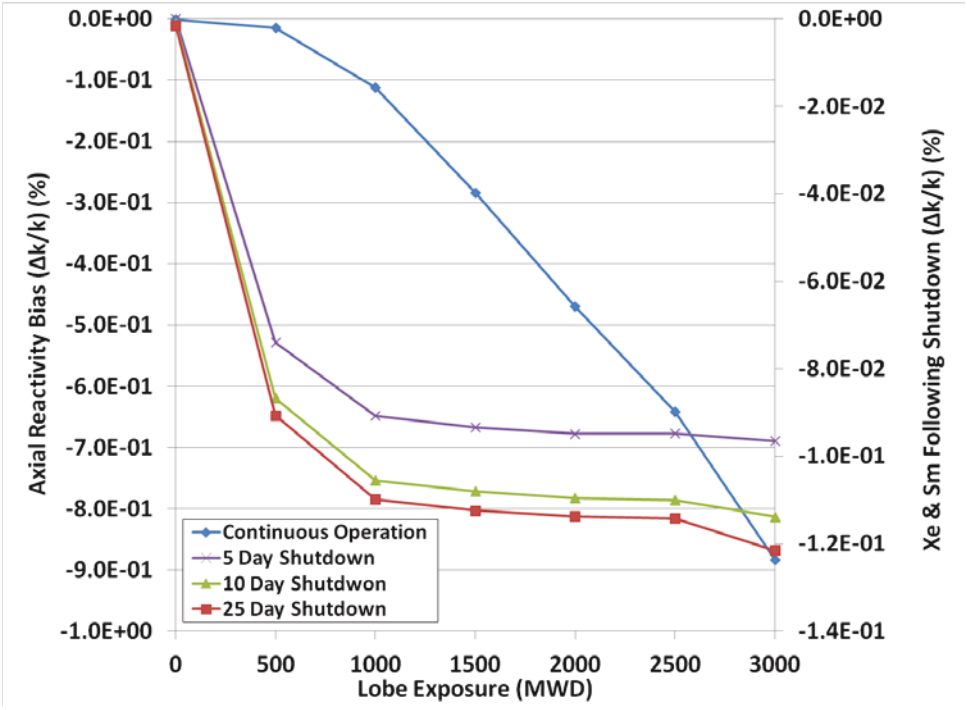

Figure 3.20. Reactivity effects due to axial burnup shape.

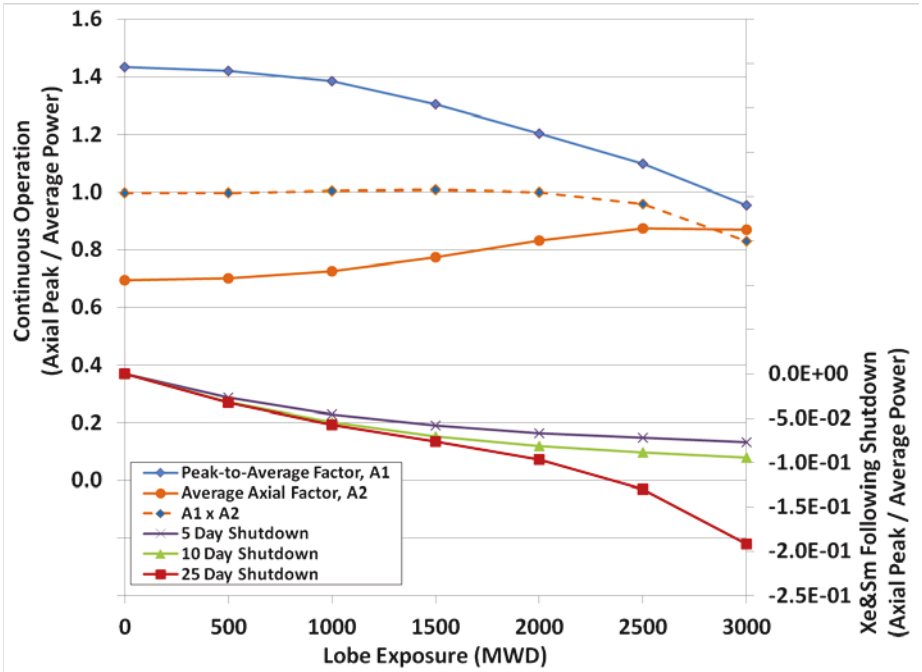

Figure 3.21. Power density multiplier and subtraction factors due to axial burnup shape.

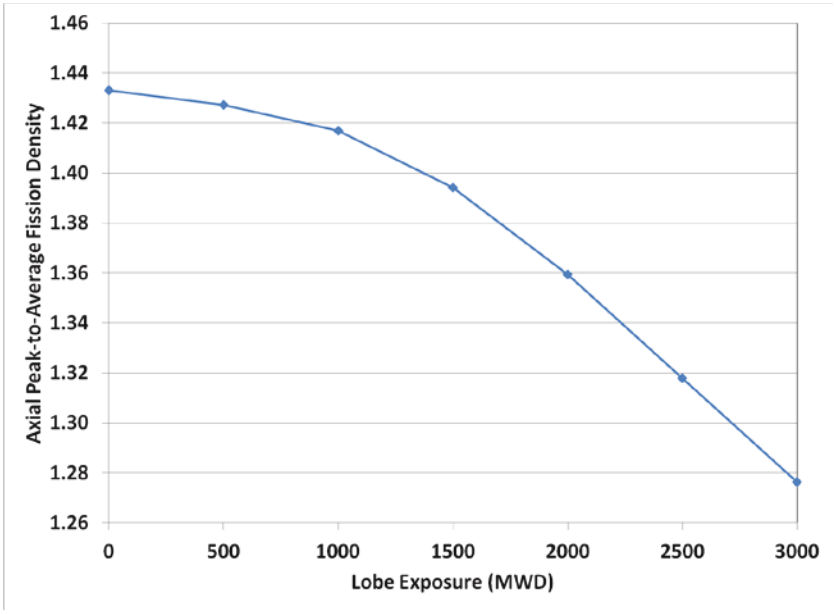

Figure 3.22. Fission density multipliers due to axial burnup shape.

3.4.1.2 Application of Axial Multipliers

In the current PDQ7 methodology, the axial flux and power shape are assumed to be a well behaved cosine shapes or Bessel functions. The methodology depends on this assumption because the axial factors A(t) and B(t) are computed with the concentric lobe model which has no axial geometric or composition variation that could cause axial asymmetry in the PDQ7 neutron diffusion solution. In reality, however, experiments are designed with axial asymmetry to deliver axially varying heat loads, fast neutron fluence, temperatures, etc. to the experiment samples being irradiated. To ensure the validity of the concentric lobe approximation, it is important that the axial or local reactivity effect of the experiment (i.e., neutron importance) does not cause axial power shape perturbations in the fuel (SAR-153, Chapter 10, Section 10.1.7.5). Most experiments are so small or have such small neutron absorption that their presence in the core does very little to perturb the power in the fuel elements. However, as more exotic experiments are proposed, increased perturbation of the neutron axial shape can be expected.

The validity of the concentric lobe model is ensured by regular testing of the axial power profile in the ATRC under prototypic conditions. These prototypic conditions are achieved by installing a mockup of that experiment in the ATRC that best represents the neutronic behavior of the experiment prior to its actual irradiation in the ATR. The ATRC is used to irradiate uranium-aluminum fission wires which can be located axially along the length of a plastic "flux wand". When measuring axial flux variation, twenty-five fission wires are located at two inch intervals along the length of a flux wand. Multiple flux wands can be placed in different coolant channels of the same fuel element. These flux wands are placed within the coolant channels of the fuel element of interest which is generally located nearest the experiment mockup. The irradiation in the ATRC typically takes about 20 minutes at approximately 600 Watts. These irradiations are commonly referred to as "flux runs". The irradiated wires from the wands are sent to the Radiation Measurements Laboratory (RML) where they are counted using a four channel alpha beta counter to determine the saturation fission rate of each wire.

Results of the flux run analysis are used to validate the experiment-specific MCNP models and to evaluate whether any axial perturbations are significant. Evaluations have included EPP adjustments based directly on the ATRC results, such as ECAR-2179 (Davis, 2014) discussed in Section 3.2.5, and adjustments intended to conservatively bound the various other analyses dependent upon the axial profile assumption (e.g. Holtz, 2013). In the PDQ7-based methodology, these adjustments are made by hand after calculations have been performed. In the HELIOS-based methodology, many of these adjustments to the ROSUB multipliers will be able to be made directly in the input to the final safety calculations. Others will be completely replaced by results from MCNP, as described in the next section.

3.4.2 Two-Dimensional to Three-Dimensional Method with MCNP

The hybrid 2D/3D strategy shown in Figure 3.23 involves the use of MCNP to provide supplemental axial power distribution information that can be combined with the basic HELIOS two-dimensional transverse computations. It should be noted that where MCNP is shown in the flow diagram, it would be equally possible to use SERPENT or MC21. Figure 3.23 shows a detailed hierarchical list of the phases of MCNP model development discussed in Section 3.2.3.

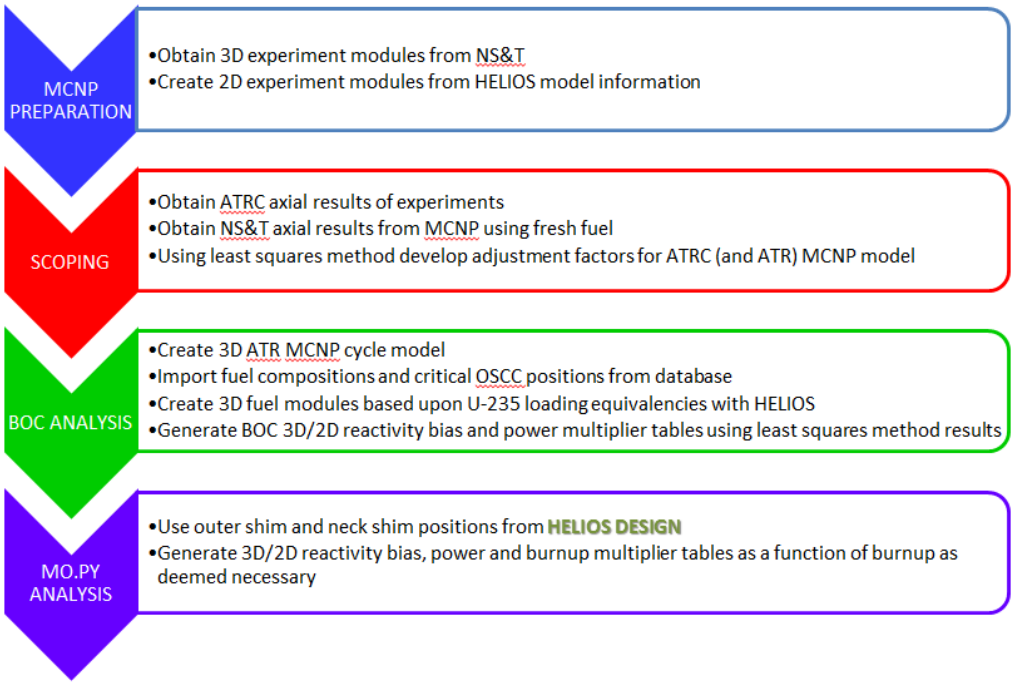

Figure 3.23. Phases of physics model development pertaining to the MCNP code.

3.4.2.1 Cycle Preparation

Below is a table describing the interactions between HELIOS and MCNP during the cycle preparation phase of the HELIOS-based methodology. The interactions at this phase are focused upon obtaining experiment design information and creating 2D and 3D models of those designs, as appropriate. As discussed in Section 3.2.3, modeling decisions regarding experiments such that the 2D representations provide average or extruded results will be made at this stage. Ultimately, the 2D models within HELIOS and MCNP must be created such that they are effectively equivalent to each other. This equivalency allows 3D/2D adjustments in MCNP to be appropriately applied to the HELIOS models directly.

Table 3.3 Sub-tasks during the cycle PREPARATION phase for both HELIOS and MCNP

Phase	**HELIOS Scope Summary**	**MCNP Scope Summary**
1.1	Obtain experiment design information.	Obtain 3D experiment modules from NS&T.
1.2	Create experiment modules for new experiments / modify existing modules.	Create/modify 2D experiment modules based upon HELIOS modules.

3.4.2.2 Cycle Scoping

Below is a table describing the interactions between HELIOS and MCNP during the cycle scoping phase of the HELIOS-based methodology. Note that the MCNP SCOPING phase occurs prior to the HELIOS SCOPING phase with a priority on analyzing perturbations on axial power shape caused by the experiment. At this time fresh fuel must be assumed for the experiment-specific MCNP models during the MCNP SCOPING Phase. The HELIOS SCOPING phase focuses on cycle design scoping, such as fuel selection and OSCC positioning for the first time step.

Table 3.4 Sub-tasks during the cycle SCOPING phase for both HELIOS and MCNP

Phase	HELIOS Scope Summary	MCNP Scope Summary
2.1		Obtain ATRC and MCNP axial results for each experiment.
2.2		Determine least squares adjustment factors for each experiment.
2.3	Decay selected fuel elements to predicted startup date using single-fuel-element calculations.	
2.4	Perform Fuel Element Loading Simulations using intended experiment loading.	
2.5	Perform search for critical OSCC prediction. -Use ROSUB Polynomials until 3D/2D reactivity biases are computed.	

3.4.2.3 Cycle Prediction

Cycle design and analysis are concurrent iterative processes, thus for this section the Cycle Design and Analysis phases of Figure 3.3 in Section 3.2.3 and Figure 3.22 above are combined and defined as “cycle prediction.” Cycle prediction activities involve the combination of experiment-specific information with information associated with the rest of the core. These activities also provide the most significant interactions between HELIOS and MCNP. Nuclide density data and critical OSCC positions are provided by HELIOS to MCNP, while MCNP provides adjustments to HELIOS.

The BOC 3D/2D MCNP calculations occur after the HELIOS fuel selection SCOPING calculation. With the core load pattern found, the MCNP 3D model is loaded with nuclide density distributions generated by the ORIGEN calculations. Next an initial critical OSCC position prediction is made by leveraging the ROSUB polynomials. These estimated OSCC positions are used in the 3D and 2D BOC MCNP models.

The 2D MCNP model fuel nuclide density distribution is loaded with nuclide data from the HELIOS model. In other words, the 2D nuclide densities for every plate in the HELIOS model are output to file and processed into the material cards for the 2D MCNP model. The 2D MCNP and HELIOS models need to be as close as possible in their representation of the cycle as to avoid any biases associated with model inconsistency. Upon completion of the 3D and 2D MCNP calculations, the critical OSCC position prediction can be updated.

To generate detailed axial nuclide density data for MCNP in Phase 3.3, the fuel nuclide densities computed in the x-y plane with HELIOS will be redistributed over the axial dimension. This can be done by starting with the fresh fuel nuclide densities and then performing a point-depletion calculation on this concentration using a "standard" element flux in the fuel tabulated for each axial level. The level of burnup used for each of these point depletion calculations would be constrained in such a way as to ensure that the sum of the ^{235}U inventory in each axial level equals the ^{235}U inventory for the element provided by the HELIOS calculation. Using a point depletion code not only allows the ^{235}U nuclide density to be adjusted, but also the ^{10}B density as well. It also enables building in the entire fission product inventory at each axial level.

Once an acceptable OSCC configuration is found for each step along the depletion PATH, the final design can be used to inform an MCNP depletion calculation, if needed. Suitable point depletion codes are those that provide a solution to the Bateman equations in stand-alone mode, not dependent on a neutron transport solution. Examples of such a code are ORIGEN-S and its predecessor, ORIGEN-2. The most common approach is to couple MCNP to ORIGEN using some form of shell script. The forefront of these coupling scripts is a system called MO.PY. Another possible avenue is the INL code MRTAU. The point depletion protocol can be performed for Beginning-of-Cycle (BOC), End-of-Cycle (EOC) or any intermediate burn-step for which there is a HELIOS solution.

MCNP adjustments are incorporated into the HELIOS process as they become available. Reactivity biases must be incorporated that may result in re-running of HELIOS neutronic calculations if the OSCC and/or neck shim positions initially selected do not provide criticality. Many of the other adjustments can be conveniently and directly applied after the neutronic analysis has been performed, but before results have been finalized without the need for hand calculations.

Table 3.5 Sub-tasks during the cycle prediction activity for both HELIOS and MCNP

Phase	HELIOS Scope Summary	MCNP Scope Summary
3.1	Integrate experiment modules into cycle-specific model	Integrate 2D and 3D experiment modules into cycle-specific models
3.2	Update neck shim and reflector compositions	Update neck shim and reflector compositions, as needed.
3.3	Provide fuel loading selection and OSCC critical position.	Update the ATR MCNP model with the fuel loading from Phase 2.4. Update OSCC to critical position established in Phase 2.5 .

3.4	Model the cycle by determining OSCC rotation and neck shim withdrawal schedule. Confirm schedule maintains criticality and lobe power requirements. -Use ROSUB Polynomials until 3D/2D power factors, burnup factors, and reactivity biases are computed.	Evaluate 3D/2D power factors, burnup factors, and reactivity biases at BOC. Evaluate OSCC positions obtained in Phase 3.1 against those used in Phase 3.2. Determine whether ROSUB multipliers can be used for other time steps.
3.5	Update startup OSCC position using the 3D/2D power factors, burnup factors, and reactivity bias, as necessary. -Update the critical eigenvalue and OSCC and neck shim positions.	If deemed necessary, perform MO.PY simulation, given the OSCC and neck shim withdrawal schedule from HELIOS Phase 3.5, to create 3D/2D power factors, burnup factors, and reactivity biases.
3.6	Evaluate cycle design output and compare with UFSAR limits. Update adjustments as needed. -If CFAD, EPP, EPtP, etc. limits cannot be met, return to Phase 2.3.	
3.7	Analyze branch calculations, such as the "worst case" shim misalignment accident for each lobe. Adjust cycle maximum lobe powers, as needed.	

3.4.4.4 Cycle As-Run

The As-Run phase is necessary to capture the true state-of-affairs of the cycle operation. In other words, it is necessary to adjust predicted behavior to actual core performance. The As-Run phase is also necessary for updating important physics information such as the true burnup of each fuel element. For example, EOC single-fuel-element HERMES files are not DUMPed during the Physics Analysis activity. However, they are created at EOC during the As-Run calculation. Also, hafnium neck shim and beryllium reflector compositions are updated as an output of the As-Run calculation.

Table 3.6 Sub-tasks during the cycle As-Run phase for both HELIOS and MCNP

Phase	HELIOS Scope Summary	MCNP Scope Summary
5.4.1	Collect ASUDAS data and create As-Run HELIOS model.	
5.4.2	Update all fuel, hafnium, and beryllium databases and-single-fuel-element HERMES files.	Generate As-Run 3D/2D power factors, burnup factors, and reactivity biases, as necessary.

3.5 Calculation of 3D/2D Adjustment Factors using the MCNP methodology

The following subsections present some initial example calculations of the various adjustment factors associated with the HELIOS-based methodology when utilizing the factors calculated by the planned MCNP process described by Section 3.4.2 and summarized in the illustration shown in Figure 3.31 further below. Calculations of the various factors can largely be performed utilizing the same set of MCNP models to provide a comparison to the HELIOS 2D model. The model development and adjustment factor calculations derived from these models are discussed below.

3.5.1 Model Development

Adjustment factors are determined through the use of two MCNP models that represent a three-dimensional core and a two-dimensional core, respectively. A simple 3D ATR MCNP model, such as the IRPhE benchmark of the 1994 CIC, can be quickly converted into a 2D representation by bounding the 3D geometry within a thin (1 cm) "slice" having an upper and lower reflective boundary condition about the mid-plane via the use of MCNP's concept of universes. This 3D to 2D conversion of an ATR MCNP model was used to demonstrate a proof-of-concept using a model of Cycle 103A which was used for nuclear requalification following the 1994 Core Internals Change-out. Results of this proof-of-concept are presented in Section 3.5.2.

This concept was expanded such that explicit modeling of driver fuel and experiment design could be captured for any given cycle, thus enabling the process described in Section 3.4 above to be performed on the needed time scale. To accomplish this goal, scripts were created to take advantage of 3D MCNP models already in use by the Experiment Design and Analysis Department of the Nuclear Science and Technology (NS&T) Directorate. This department is responsible for experiment design and analysis of the various DOE-NE and Work For Others experiments that request access to the ATR. As a part of this process, MCNP models are created for each experiment that requests analysis by INL. Although Naval Reactor experiment models are not generally accessible, virtually all other experiments have a MCNP model readily available for use in the adjustment factor process.

The models directly available from the NS&T Directorate generally represent a generic full core with a single experiment of interest inserted such that experiment-specific analyses can be performed. However, the MCNP models needed to perform the axial adjustments must contain all experiments in order to mirror the HELIOS 2D model of a given cycle. Thus, a utility script (i.e. strip_modules.sh) was created that will automatically generate experiment-specific subsections, or modules, from the standardized NS&T MCNP full-core models. Each of these modules has an associated template that can then be used to ensure that the geometric interfaces of each module match those assumed in the MCNP base model. See Figure 3.24 below for an example plot output of these templates. Some of these templates and the base model were available from a previous attempt to modularize the MCNP model, but were modified and/or created to support the automation needed for the HELIOS-based methodology. Modules can be generated not only for the experiment positions but also for the driver fuel positions (as discussed in Section 3.5.4) and the control elements of the ATR. Thus, modules from a variety of different source models could be easily extracted and then combined into a single MCNP model (via a utility script that had been previously developed by NS&T) that is representative of any cycle of choice.

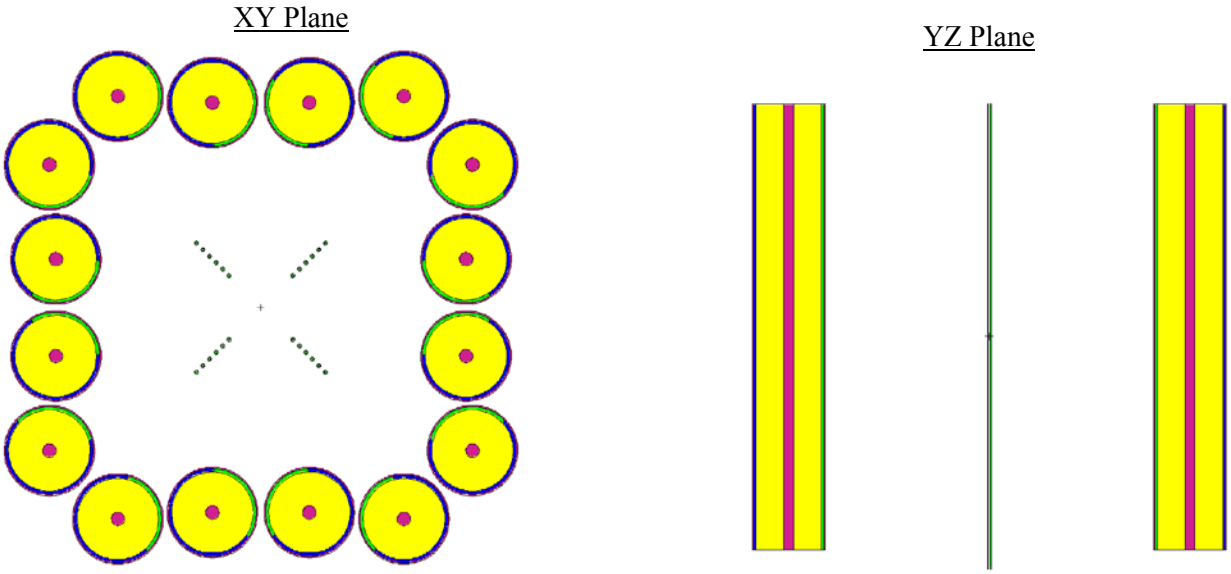

Figure 3.24. Example of plotting ouput for the control element module.

An added concern associated with the combined MCNP model was that it represented a significant increase in model complexity when compared to the typical NS&T MCNP models. This complexity manifested itself in that conflicts in experiment definitions between the various modules were common. The solution to this issue was to exploit the features of the MCNP5 1.60 version of the code, rather than the MCNP5 1.40 version required to be employed by the NS&T organization per its associated software quality assurance program. The specific features of interest were associated with the expansion of available card numbering for the cell, surface, and material definitions in MCNP. These features allowed a numbering scheme to be developed that could be leveraged to remove virtually all expected conflicts between experiment modules while maintaining the ability to utilize scripts and modules already available within the NS&T directorate.

The utility script above was modified to allow the user to request that a given model be updated to reflect the MCNP5 1.60 numbering scheme even if the original model was developed for MCNP5 1.40. While this numbering scheme update is not able to flawlessly update any model, it has been shown to be very robust. For instance, the utility script has been shown to utilize available spacing on each line to dramatically reduce the number of MCNP errors associated with a line exceeding 80 characters. The script has been designed to maximize the number of automatic updates to cell, surface, and material references when defined within a given module, while not performing modifications to other references likely to be defined in the base model. The aim of the numbering scheme scripting has been to enable users with moderate MCNP experience to satisfactorily troubleshoot any encountered errors with the standard MCNP error messages and/or the module templates discussed above while minimizing manual hand corrections. Thus, this tool should enable ATR Reactor Engineering to create a cycle-specific MCNP model for each cycle of interest in the allotted time and with the level of model detail needed to provide confidence in the results.

A demonstration of the module creation and recombination was performed for Cycle 152B. The starting model for this demonstration is discussed in detail in Section 3.5.4. This model contained representative experiment descriptions of Naval Reactor experiment as well as experiments that had been analyzed by the NS&T organization. The model also had all experiment conflicts removed by hand without utilizing the expanded card numbering available in MCNP5 1.60 such that it was able to execute using MCNP5 1.40. The extraction of multiple modules from a single file mirrors the process of obtaining modules from the cycle previous to the cycle of interest, as would be expected during the first step of the typical MCNP preparation stage described in Figure 3.23. The utility script above was then used to successfully extract each of the applicable modules from this single model, both without numbering modification and with the numbering scheme update applicable to MCNP5 1.60.

Minor hand corrections due to the numbering scheme update and modifications to the MCNP base model are discussed below in Table 3.7. It is expected that corrections to modules will be preserved when extracting from a previous cycle model and thus that the number of corrections are not representative of those that would be encountered during typical cycle-specific model creation, while the types of corrections would be characteristic of corrections to new experiment modules. Note that the number of hand corrections needed for each module is highly dependent on the complexity of the experiment being modeled.

Table 3.7. Module Creation Errors Encountered in Original Cycle 152B Model.

Module	Error Description	Resolution
Ten (10) of Eighteen (18) Produced Modules	Number of importance values did not correspond with number of cells in each module. Flagged by standard MCNP error message.	Modified number of importance values in each module.
cft (Center Flux Trap Location)	Module creation failed due to lack of appropriate keywords in model. Flagged by MCNP plotting error and/or identified by visual review of CFT module.	Corrected keywords in original Cycle 152B model. Reran modified file through extraction script.
eft (East Flux Trap Location)	Numbering Update created two (2) duplicate cells within the EFT module. Flagged by standard MCNP error message.	Modified cell numbering of two (2) cells in module.
h_loc (H Position Locations)	Numbering Update created five (5) lines associated with three (3) tallies that extended beyond 80 characters. Flagged by standard MCNP error message.	Deleted unneeded tallies in module.
h_loc (H Position Locations)	Numbering Update did not modify tally surface calls in one (1) tally when surface numbering was altered. Flagged by standard MCNP error message.	Deleted unneeded tally in module.
larg_b (Large B Locations)	Numbering Update created six (6) lines associated with six (6) cells that extended beyond 80 characters. Flagged by standard MCNP error message.	Modified cell definition of six (6) cells in module by creating six (6) additional continuation lines with needed information.
larg_i (Large I Locations)	Module creation failed due to lack of appropriate keywords in model. Flagged by MCNP plotting error and/or identified by visual review of Large I and Small I modules.	Corrected keywords in original Cycle 152B model. Reran modified file through extraction script.
neft (Northeast Flux Trap Location)	Base model boundary for the NEFT was modified from the MCNP 1.40 standardized model to be consistent with other flux traps, creating cell definition errors in the modules. Flagged by MCNP plotting errors when visualizing NEFT module.	Modified original Cycle 152B model by moving one (1) cell definition out of the NEFT module and into the base model. Reran modified file through extraction script.
nft (North Flux Trap Location)	Base model boundary for the NFT was modified from the MCNP 1.40 standardized model to be consistent with other flux traps, creating cell definition errors in the modules. Flagged by MCNP plotting errors when visualizing NFT module.	Modified original Cycle 152B model by moving six (6) cell definitions out of the base model and into the NFT module. Reran modified file

Module	Error Description	Resolution
		through extraction script.
nwft (Northwest Flux Trap Location)	Base model boundary for the NWFT was modified from the MCNP 1.40 standardized model to be consistent with other flux traps, creating cell definition errors in the modules. Flagged by MCNP plotting errors when visualizing NWFT module.	Modified original Cycle 152B model by moving four (4) cell definitions out of the base model and into the NWFT module. Reran modified file through extraction script.
out_a (Outer A Locations)	Numbering Update created one (1) line that extended beyond 80 characters and then were overwritten by comments on the same line when comments were aligned. Flagged by standard MCNP error message and/or identified by visual review of original Cycle 152B model.	Modified one (1) line in original Cycle 152B model by creating one (1) additional continuation line with needed information. Reran modified file through extraction script.
sft (South Flux Trap Location)	Base model boundary for the SFT was modified from the MCNP 1.40 standardized model to be consistent with other flux traps, creating cell definition errors in the modules. Flagged by MCNP plotting errors when visualizing SFT module.	Modified original Cycle 152B model by moving one (1) cell definition out of the base model and into the SFT module. Reran modified file through extraction script.
sft (South Flux Trap Location)	Numbering Update created eighteen (18) lines that extended beyond 80 characters and then were either overwritten by comments on the same line when comments were aligned or could not be resolved by removing extraneous spacing. Flagged by standard MCNP error message and/or identified by visual review of original Cycle 152B model.	Modified eighteen (18) lines in original Cycle 152B model by creating eighteen (18) additional continuation lines with needed information. Reran modified file through extraction script.
sft (South Flux Trap Location)	Numbering Update failed to modify forty-two (42) cell complements on fourteen (14) lines associated with fourteen (14) cells. Flagged by standard MCNP error message.	Modified forty-two (42) cell complement calls within fourteen (14) cells of module to match standardized number scheme.
small_b (Small B Locations)	Numbering Update failed to modify one (1) cell complement associated with one (1) cell. Flagged by standard MCNP error message.	Modified cell complement call within one (1) cell of module to match standardized number scheme.

Module	Error Description	Resolution
small_i (Small I Locations)	Module creation failed due to lack of appropriate keywords in model. Flagged by standard MCNP error message and/or identified by visual review of Large I and Small I modules.	Corrected keywords in original Cycle 152B model. Reran modified file through extraction script.
swft (Southwest Flux Trap Location)	Base model boundary for the SWFT was modified from the MCNP 1.40 standardized model to be consistent with other flux traps, creating cell definition errors in the modules. Flagged by MCNP plotting errors when visualizing SWFT module.	Modified original Cycle 152B model by moving four (4) cell definitions out of the base model and into the SWFT module. Reran modified file through extraction script.
wft (West Flux Trap Location)	Base model boundary for the WFT was modified from the MCNP 1.40 standardized model to be consistent with other flux traps, creating cell definition errors in the modules. Flagged by MCNP plotting errors when visualizing WFT module.	Modified original Cycle 152B model by moving six (6) cell definitions out of the base model and into the WFT module. Reran modified file through extraction script.

Next, it was determined that several experiments were not explicitly modeled in the file discussed in Section 3.5.4 and that these additional experiments could be used to integrate new modules into the final version of the Cycle 152B model. The integration of new experiments into an existing model mirrors the process of inserting new experiments into ATR for an upcoming cycle. Full-core models associated with the EPRI-ZG and MANTRA set of experiments were then obtained from the appropriate members of the Experiment Design and Analysis Department. Modules with updated numbering schemes were successfully generated from these files via the above utility script, although minor hand corrections were needed. The resolution for all of the new modules associated with Cycle 152B was the deletion of unneeded tallies.

Since the current design of modules combines some experiment positions into a single module, such as all Large B positions, additional modifications were needed to create a single module with all needed experiments. Namely, a single module for the Large B locations was needed that would contain MANTRA-1 in B-9, MANTRA-3 in B-11, and AGR-2 in B-12. A single module for the Outer A locations was also needed that would contain three (3) EPRI-ZG experiments in A-14 through A-16 and AFC-3A in A-10. The combining of the various modules was performed successfully by hand, largely due to the extensive comments supplied in the original NS&T models. It is suggested that future modifications to the module design create individual modules for experiment positions that are frequently used. However, the need for this adjustment does not currently appear to be a high priority due to the ease of this step during the Cycle 152B demonstration.

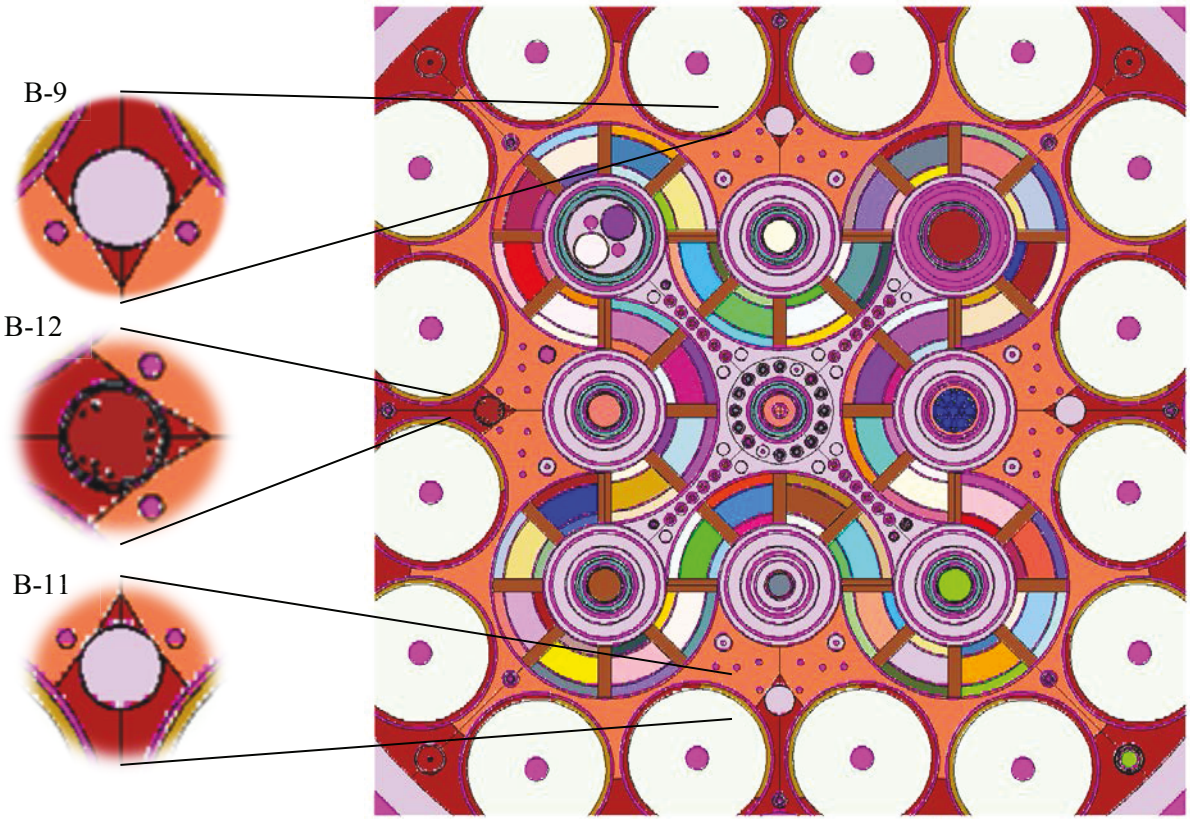

Figure 3.25. XY plane of the final 3D MCNP model of Cycle 152B, viewed at Z=61 cm.

The resulting modules for Cycle 152B were combined to form the final 3D model of Cycle 152B, as shown in Figure 3.29. This recombination is representative of the creation of a cycle-specific 3D model in the BOC Analysis stage described in Figure 3.23. It contains representative 3D driver fuel loading equivalencies and control positions. Experiment-specific tallies were also removed since they are not needed for adjustment factor calculations. The finalized 3D MCNP model produced by this process is to be used to generate the three-dimensional data needed for the various adjustment factors, such as eigenvalue calculations and fission energy deposition tallies associated with the fuel module. However, two-dimensional data from a 2D model is also needed.

A comparison of Figure 3.25 representing a simple 2D slice of the Cycle 152B MCNP model and that of Figure 3.26 below representing the HELIOS 2D model reveals some discrepancies in the geometric representations provided in the two models. Some of these discrepancies are expected and acceptable, such as the level of detail present in the driver fuel geometry. However, the geometry of the experiments in the NEFT, SFT, and Large B positions require some modification before a 2D slice of the MCNP model can be considered representative of the 2D HELIOS model. Thus, the original concept of utilizing universes to slice a 2D model from a 3D model needed to be expanded such that the geometry of the 2D model in MCNP would be able to roughly match the HELIOS 2D model with relatively little effort by the end user. This was performed by simply translating individual experiments in the axial direction until a representative geometry (and ideally, a representative composition) appeared in the axial plane of interest.

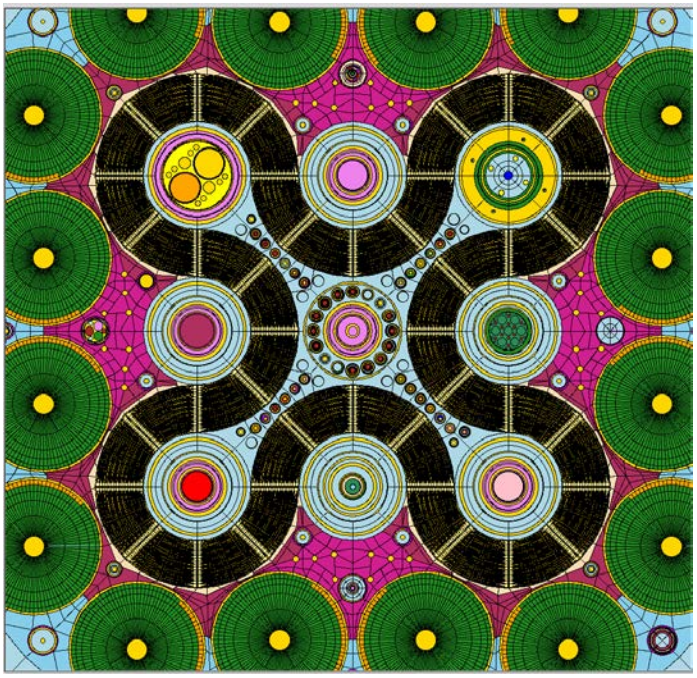

Figure 3.26. 2D HELIOS model of Cycle 152B.

Figure 3.27 below is the output of a series of scripts that modifies the final 3D model discussed above into a 2D model via the use of universes and a 2D MCNP base model. These scripts allow the user to axial translate individual experiments about the Z=61 cm plane by changing a single value associated with that experiment. This translation can be performed within individual modules or after the 2D model is built. The use of universes in the 2D MCNP model allows the full 3D model to be present in the file while not being represented in associated calculations, thus creating maximum flexibility for the end user. The 2D model below has been translated such that NEFT, SFT, and Large B positions each have a geometry similar to that of the 2D HELIOS model.

However, manipulations to the composition of the various components of the core need to be made such that the MCNP 2D model mirrors that of the HELIOS 2D model. As discussed in Section 3.2.3, it cannot be simply assumed that the HELIOS 2D model is an average of the three-dimensional compositions since extrusion of an experiment may be performed in order to best represent an experiment in the HELIOS model. Thus, the most rigorous way to confirm that the MCNP 2D model is representative of the HELIOS 2D model is to extract the material compositions directly from the HELIOS model. If manipulations to the material compositions and translations of experiments were to be performed, then this process would be fully representative of the creation of 2D experiment modules in the MCNP Preparation stage described in Figure 3.23. Manipulations to the material compositions of the driver fuel in both 3D and 2D would be representative of the steps associated with the fuel module in the BOC Analysis stage described in Figure 3.23. An example of this has been performed on the Cycle 152B fuel module, although no other manipulations of the various material compositions have been performed.

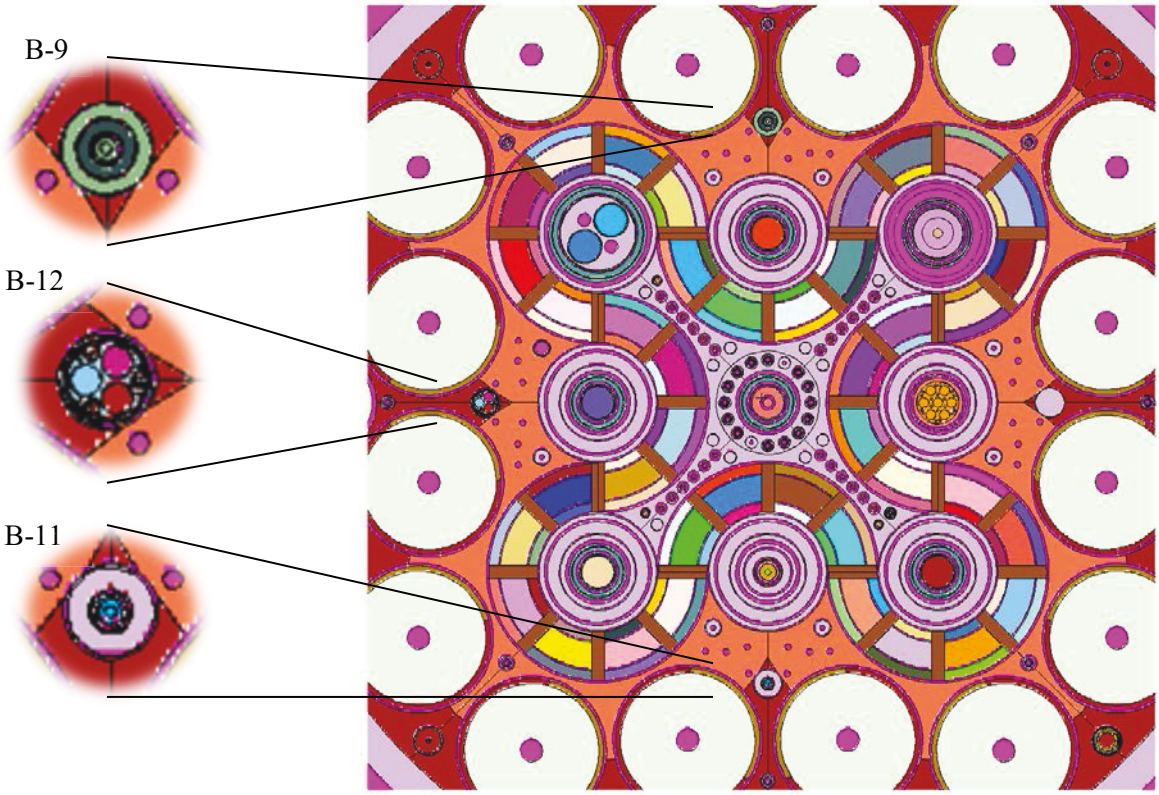

Figure 3.27. Representative 2D MCNP model of Cycle 152B.

Further model development may be warranted if it becomes necessary to perform a MO.PY Analysis as described in Figure 3.23. The results of a MO.PY analysis would be most likely to affect the adjustment factor associated with burnup, although minor corrections to the reactivity bias and power multipliers would be expected. At this time it is suggested that the same adjustment factor that is applied to power also be conservatively applied to burnup if the ROSUB polynomial assumptions regarding axial fission profile are considered insufficient for a given experiment. The corrections to the other adjustment factors are assumed to be inconsequential compared to the accuracy of the method. If additional funding is available for this expansion of capabilities and it has been deemed appropriate to invest in a higher precision calculation of burnup, then the development and use of a MO.PY analysis or other method that couples depletion with a transport solution is encouraged. It is also possible that MO.PY developers will incorporate the needed features in the MCNP model of ATR in support of the NS&T organization. Continued interaction with NS&T and use of the models available from that directorate may advance the capabilities needed to perform a MO.PY analysis and thus periodic review of the available capabilities may also be warranted.

3.5.2 Axial Reactivity Bias

An axial reactivity bias is necessary to quantify the reactivity adjustment needed to correct the 2D assumption of the HELIOS model. The reactivity bias is largely a function of both driver fuel burnup and axial variation in experiment design. The axial reactivity bias adjustment factor is applied to the criticality calculation (i.e. OSCC prediction) performed by HELIOS. The criticality calculation and the application of the reactivity bias adjustment factor are discussed below.

The HELIOS startup criticality method is founded on the concept of the critical eigenvalue, k_c. The k_c is established following each new cycle's startup to represent the calculation model's k-eff for the core configuration that yielded an indicated critical condition at the ATR control console. The critical eigenvalue is the value of k-eff in the neutron balance equation representing the critical condition of the core. This value does

not necessarily equal one in the calculation scheme. Even the most rigorous of three-dimensional transport codes will have a reactivity bias . Since HELIOS is a two dimensional code, the solution of the neutron balance equation does not consider leakage in the axial direction. A value for axial buckling can be provided in the RUN operator, but this value is only used for updating the spectrum used for the depletion calculation.

In the ATR HELIOS methodology, a previous cycle (known cycle) that is representative of the design cycle (target cycle) is used to provide a reference critical eigenvalue. If the target cycle and the known cycle were neutronically identical, then the OSCC position of the target core would be that needed to make k-eff equate to k_c of the known critical, see Figure3.28. However, no two cores are ever perfectly neutronically identical. Even if the experiment configuration between the known and target cycles were identical, the fuel loading would not be identical. Thus, the k_c must be augmented by the reactivity of the fuel loading of the target core.

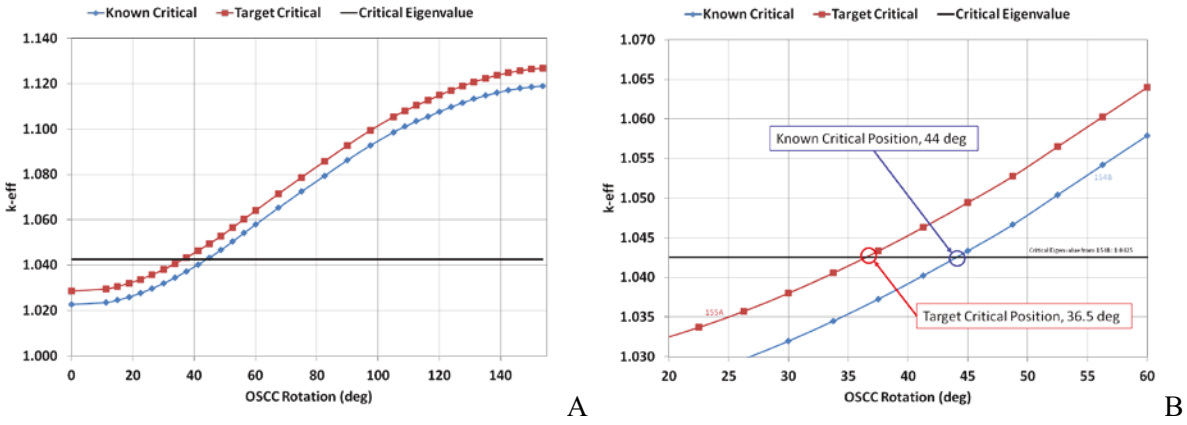

Figure 3.28. Computed k-eff as a function of balanced OSCC rotation for (A) the entire rotational range (Cycle 154B), and (B) showing the critical position for both the known and target cycles

It is simpler to think in terms of reactivity when introducing reactivity biases from outside mechanisms such as the ROSUB polynomials or 3D/2D MCNP calculations. Recasting the critical eigenvalue in terms of computed reactivity is analogous to taking the difference in absolute core reactivity between the known and target systems. Using Equation 3.27, the critical OSCC position is that which yields ρ'=0. This determination is accomplished by running the ATR HELIOS model for the zero power case for multiple balanced OSCC rotations and constructing Figure3.28. Note that Figure3.28 was constructed from only five actual HELIOS calculations. The other data-points were generated via third order spline fits between each HELIOS calculation point. If needed, Figure data allows for generating the OSCC worth curves for the cycle in question, Figure3.29.

$$\rho' = \rho_T - \rho_c = \frac{k_T - 1}{k_T} - \frac{k_c - 1}{k_c} = \frac{k_T - k_c}{k_T k_c} \qquad (3.27)$$

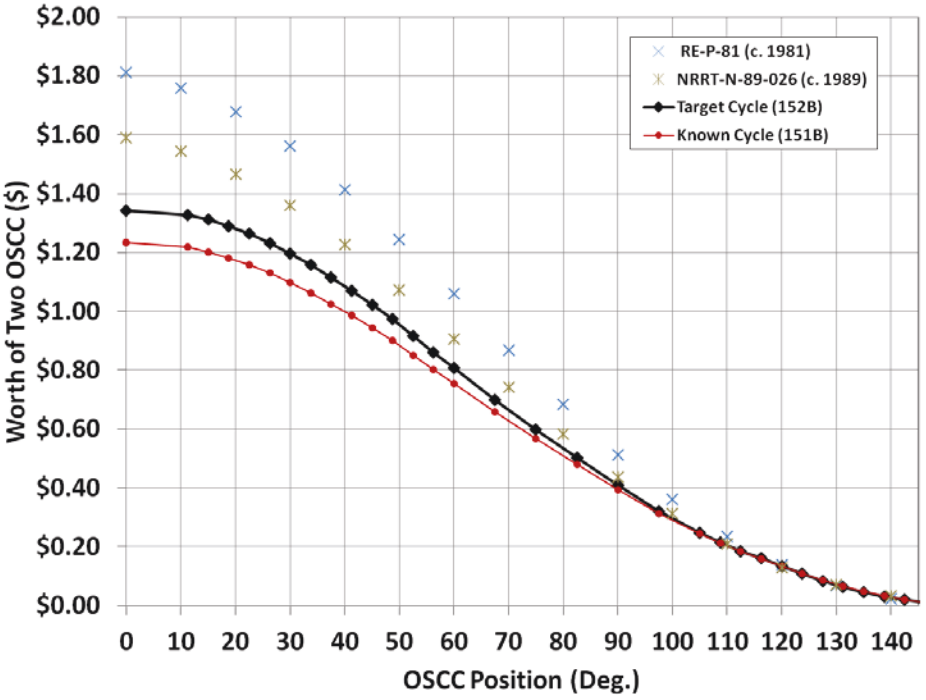

Figure 3.29. Comparison of HELIOS generated OSCC worth curves with published polynomial fits of the outer shim worth curve.

Because the fuel loading is different for the known cycle and the target cycle, the reactivity worth of the difference in disparate axial burnup shapes and 3D experiment effects must be taken into account.

$$\rho' = \frac{k_T - k_c}{k_T k_c} + \rho_{3D/2D}\big|_T - \rho_{3D/2D}\big|_c = \frac{k_T - k_c}{k_T k_c} + \frac{k_{3D} - k_{2D}}{k_{3D} k_{2D}}\Big|_T - \frac{k_{3D} - k_{2D}}{k_{3D} k_{2D}}\Big|_c \quad (3.28)$$

In the absence of a 3D/2D reactivity bias from MCNP, the ROSUB polynomials can be leveraged to approximate the reactivity worth of the fuel loading. Note that ROSUB polynomials assume eight elements in a lobe are providing a reactivity adjustment, so adjustments for each element must be obtained by dividing each ROSUB adjustment by eight. The adjusted reactivity curve provided by the ROSUB polynomials (Equation 3.29) is demonstrated in Figure3.30 for Cycle 152B.

$$\rho' = \frac{k_T - k_c}{k_T k_c} + \frac{1}{8}\sum_i^{40} \rho_{T,i} - \frac{1}{8}\sum_i^{40} \rho_{C,i} \quad (3.29)$$

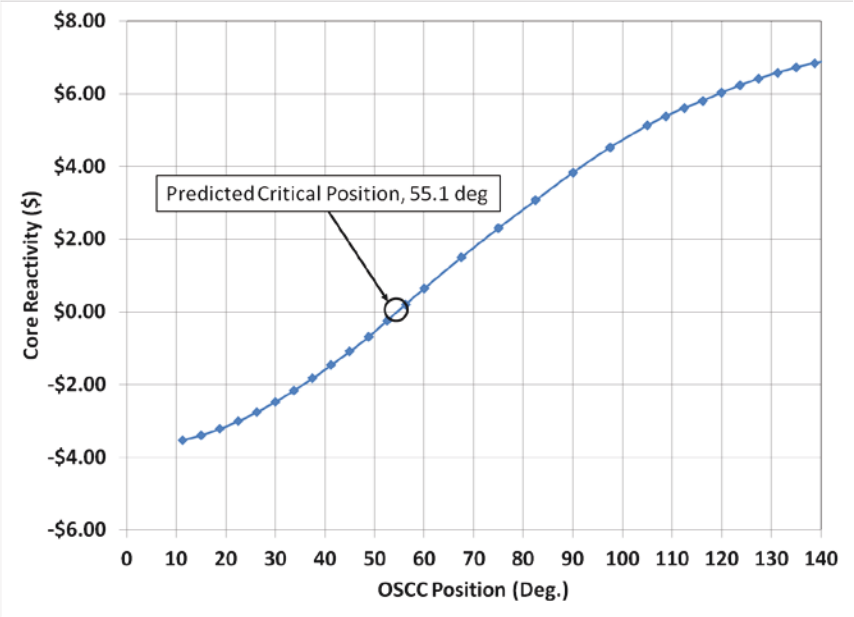

Figure 3.30. Core reactivity prime using ROSUB polynomials as a function of balanced OSCC rotation, Cycle 152B. The critical shim position occurs when core reactivity prime equals zero.

As discussed in Section 3.4, the application of the ROSUB polynomials to adjust for axial effects requires the use of several assumptions that can be removed through the application of adjustment factors derived from MCNP. Table 3.8 shows a breakdown of the 3D/2D modeling bias with MCNP for Cycle 103A, where the known critical OSCC position was used in each model. The use of the known critical position effectively removes many assumptions that must be made when performing predictive calculations. The reactivity worth of the 3D/2D effect in MCNP relative to the 2D MCNP model is -3.51% for the IRPhE benchmark. The 2D model bias between the two codes is -0.19% relative to the 2D HELIOS model. The 2D model bias suggests that the two models are effectively equivalent and thus that the development process for the MCNP 2D model is appropriate. The overall bias determined via the adjustment factor process is -3.70% relative to the 2D HELIOS model while the bias compared to a true eigenvalue of k-eff=1 is 3.78%, resulting in an error of 0.08% relative to the indicated critical position. Thus, the error in calculated bias is considered acceptable, particularly in light of the validation data presented in Section 5.3.

Table 3.8. IRPhE benchmark, MCNP versus HELIOS modeling biases.

Case	k-eff	Stdev	% Bias
MCNP 3D	0.99935	0.00014	--
MCNP 2D	1.03573	0.00014	-3.51%
HELIOS 2D	1.03780	--	-0.19%

Table 3.9 below shows a breakdown of the 3D/2D modeling bias calculated with MCNP for Cycle 152B using applicable elements of the overall ATR fuel cycle simulation logic flow illustrated in Figure 3.31. The known Cycle 152B critical position (54.3 degrees) was not used in the MCNP models, which used 55.7 degrees in this case. The critical eigenvalue would not be available for the current cycle if these calculations were being used to determine an OSCC prediction for an upcoming cycle in any event, so the introduction of this minor difference is representative of the expected process, which would start with an estimated critical shim rotation for the target cycle. The reactivity worth of the 3D/2D effect in MCNP relative to the 2D MCNP model is -3.60% for Cycle 152B (Table 3.9). The HELIOS 2D model for Cycle 152B utilized the best-estimate critical position based on how HELIOS is currently used in the CSAP process to predict critical shim positions *a-priori*, with a slight correction to account for the known critical position (54.3 degrees) in this demonstration. This information would not have been available during an *a-priori* prediction of OSCC position, but provides a useful comparison

between the MCNP and HELIOS 2D models available for this demonstration. The 2D model bias between the two codes is -1.19% as shown in Table 3.9. When compared to the IRPhE benchmark, this represents a significant increase in discrepancy between the two 2D models. This is likely due to the differences in how the OSCC position is represented in HELIOS relative to how it is represented in MCNP due to geometry construction differences and minor differences in how material compositions were coalesced axially in the experiment positions during this demonstration. In addition the 19 fuel plates were each explicitly modeled in HELIOS whereas the plates were transversely homogenized into three fuel regions in the MNCP models for this demonstration. As the 3D-2D reactivity bias estimation methodology initially demonstrated here matures with experience gained during the deployment phase, these recognized inconsistencies will be addressed.

Table 3.9. Cycle 152B, MCNP versus HELIOS modeling biases.

Case	k-eff	Stdev	% Bias
MCNP 3D	1.00417	0.00018	--
MCNP 2D	1.04180	0.00017	-3.60%
HELIOS 2D	1.02905	--	-1.19%

Using the MCNP calculations above, a retrospective calculation can be performed to predict the OSCC position for the Cycle 152B startup as a demonstration, using Cycle 151B as the reference critical. The HELIOS 2D as-run model eigenvalue for Cycle 151B with the outer shims set to the known initial critical rotation for Cycle 151B (38.8 degrees) was 1.03775. This information would be available prior to Cycle 152B startup and the overall calculated bias from Equation 3.28 could be applied to the reference critical eigenvalue. It can be assumed that Cycle 151B had little to no axial fission profile deviation from the standard burnup-corrected cosine axial profile that would have been caused by distortions from axially non-uniform experiments in the various flux traps and other positions. Therefore the IRPhE Cycle 103A 3D/2D reactivity bias value (-3.51%) in Table 3.8 would also be representative of a calculation for Cycle 151B without burnup. The Cycle 151B adjustment factor calculated by the ROSUB polynomial to account for non-uniform axial burnup in the core based on the standard chopped cosine axial power distribution is also known to be -0.94% relative to a fresh core. The overall bias determined via the adjustment factor process is the difference in the MCNP 3D/2D biases produced by Cycle 152B and Cycle 103A (i.e. -0.09%) minus the Cycle 151B ROSUB adjustment applied to the known critical eigenvalue as described by Equation 3.28, resulting in a predicted 2D critical eigenvalue for Cycle 152B of 1.02899 and a prediction of critical at 54.2 degrees based on the HELIOS shim rotation worth curve for this cycle. This agrees quite well with the known critical position of 54.3 degrees. However, significant additional validation (i.e. against all cycles run since 145A) will be needed prior to full deployment of the MCNP-based 3D correction approach described here. In the meantime, the established ROSUB methodology will continue to be used to correct HELIOS results for 3D effects during the initial deployment phase.

3.5.3 Axial Power Multipliers

Upon completion of the 3D/2D MCNP calculations, the maximum point-to-core average power density factor can be tabulated. The point-to-core average power density factor is the ratio representing the axial peaking factor, which is provided to the HELIOS model via ZENITH. Simplistically, for chopped cosine shaped power distributions it is the average power density at the mid-plane divided by the volumetric average of the core power density. The numerator of Equation 3.30 is the power density at each point in the 2D model, whether using PDQ or HELIOS. The denominator is a summation over all regions in the core.

$$A(t) = \frac{P_m(t)/V_m}{\sum P_i(t)/\sum V_i} = \frac{P_r(t)}{P_a(t)} \qquad (3.30)$$

The 3D/2D Burnup Multiplier (B) can also be found upon completion of the 3D/2D MCNP calculations. The ROSUB burnup polynomial assumes that B(t) is essentially the indefinite integral function of A(t) with respect to irradiation time. The explicit method for computing B(t) is to draw A(t) from MO.PY. After completion of the

MO.PY calculation, a table of B values can be solved for every region for every burn step in the ATR HELIOS model. If no MO.PY calculation is performed, (A) can be conservatively substituted for (B).

$$B(t) = \frac{\int_0^t P_r(t\prime)dt\prime}{\int_0^t P_a(t\prime)dt\prime} \cong \int_0^t A(t')dt' \qquad (3.31)$$

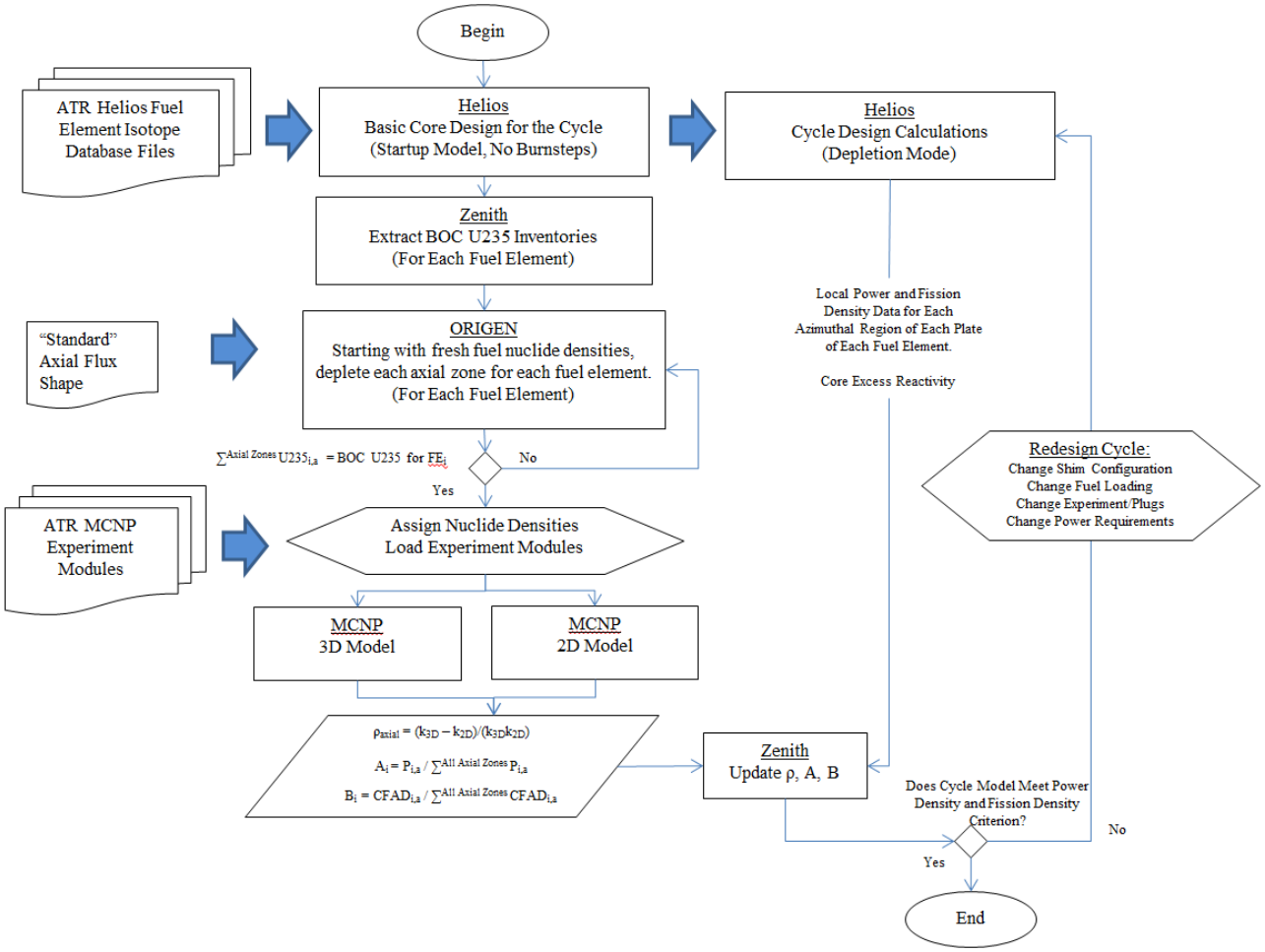

Figure 3.31. Hybrid 3D/2D ATR fuel cycle analysis strategy.

The multipliers associated with EPP would continue to be obtained from analyses such as ECAR-2179 (Davis, 2014) since the thermal/hydraulic aspect of this calculation has not been altered by the HELIOS-based methodology. The input to this analysis would likely be the results of the least squared method, since this has been shown to provide accurate and reproducible results that incorporate ATRC results as well as MCNP modeling results of experiments.

3.5.4 Demonstration of Axial Profile Analysis

This section documents the development and initial demonstration of a set of MCNP5 models and supporting computational protocols (e.g., scripts) that can be used to routinely characterize axial power factors associated with ATR Core Safety Assurance Package (CSAP). These axial power factors, to be used in conjunction with the new HELIOS core safety analysis and fuel management methodology, represent adjustments to 2D calculations that account for axial fission profile effects. The demonstration-level neutronic evaluations presented here were performed using the planned reactor operating conditions and configurations for ATR Cycle 152B (Stanley, 2012). This cycle was selected as an example because extensive physics measurements performed during the previous ATR cycle, 152A (which was a so-called "depressurized run") and the associated supporting

experiments performed in the ATRC provided a great deal of new experimental code validation data pertinent to the current configuration of the ATR.

3.5.4.1 Axial Profile Analysis Background

The current PDQ-based methodology used to characterize axial power factors is performed via the ROSUB code (an internally-developed INL data post-processing tool) utilizing polynomial approximations that assume a chopped cosine axial shape is maintained within ATR. The newly developed protocols can be used to verify this assumption as well as provide the potential to expand the axial shape profiles that can be modeled. In the newly developed protocols, the depletion of driver fuel elements is performed utilizing an axial fission profile representative of a typical ATR core configuration. The initial fuel loading within each region of an element for Cycle 152B is determined by ORIGEN2 according to a) the exposure experienced by the element prior to the start of Cycle 152B and b) the typical axial fission profile determined by MCNP5. Thus, the axial loading of previously-used elements as of the beginning of Cycle 152B is assumed to be preserved.

3.5.4.2 Assumptions

The assumptions used in this analysis are stated below.

1. The MCNP5 models of the ATR core use three radial fuel regions to represent the ATR fuel elements (FEs), as shown by Figure 3.32.

2. The MCNP5 models of ATR utilized in this report contain ATR driver fuel loadings representative of the driver fuel loadings utilized during Cycle 152B.

3. Even axial distribution of the fuel is appropriate when modeling unirradiated fuel elements.

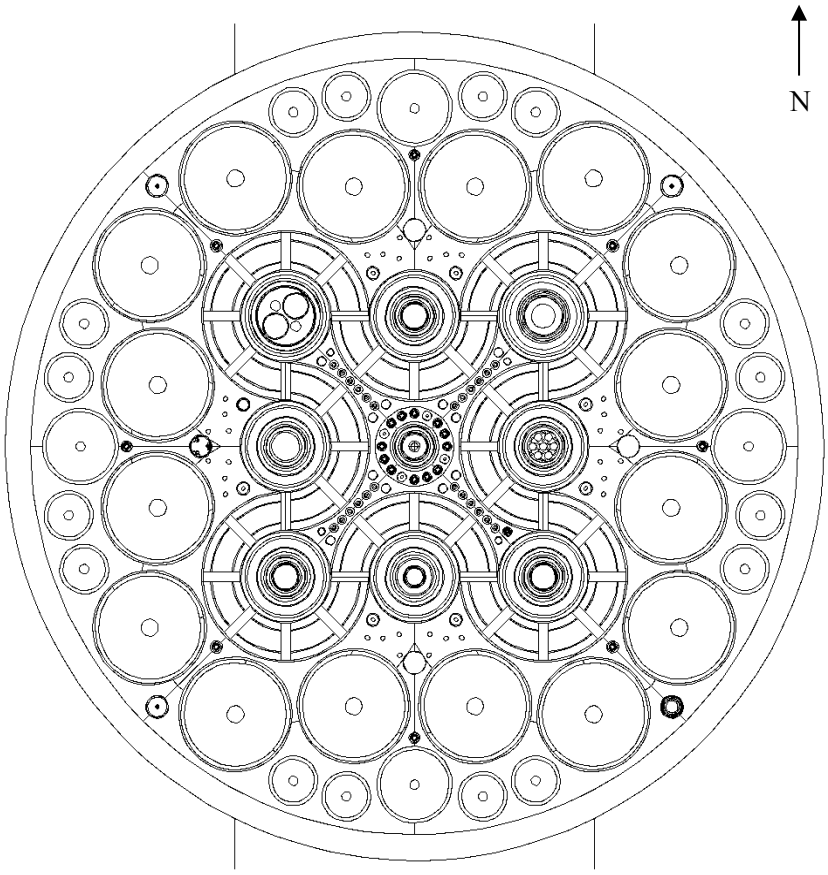

Figure 3.32 MCNP5 model of Cycle 152B configuration utilizing three-region driver fuel.

3.5.4.3 Computer Code Validation

MCNP5, a general purpose Monte Carlo N-Particle transport code, was used to model and evaluate the axial fission profile demonstrated during Cycle 152B. The depletion code ORIGEN2 was used to model and evaluate the depletion of the fuel for the driver fuel elements, providing an axial fission profile versus exposure time. The MCNP5 built-in cross-section data libraries and the JENDL-3.2 cross-section libraries were used to perform all MCNP5 evaluations for Cycle 152B. The ORIGEN2 library ATRXS as well as a MCNP5-generated fission profile were used to calculate the burnup within the driver elements. Both MCNP5 and ORIGEN2 are listed in the INL Enterprise Architecture Repository and are accepted as qualified scientific and engineering analysis software. MCNP5 has been validated for use at the INL by running the 42 sample problems transmitted on the Radiation Safety Information Computational Center (RSICC) installation CD and comparing the results against the standard results provided on the installation CD. Additionally, the input model for the ATR criticality benchmark was executed and results identical to the published results were obtained.

3.5.4.4 MCNP5 Methodology

The MCNP5-calculated power density multipliers were evaluated using the results from the ATR three radial-region detailed MCNP5 full core physics model of the driver fuel elements. The demonstration model utilized seven depleting axial regions to provide the evaluated axial results and included experiments from Cycle 152B, as described by Table 3.10. The MCNP5 model was then coupled to ORIGEN2 to provide depletion of the driver elements.

Fuel specifications (SPC-415, 2005) were used to develop fresh fuel zone loading information for each of the 21 driver element regions in the MCNP5 model. It was assumed that even axial distribution of the fuel was appropriate when modeling unirradiated fuel elements. Water densities were provided for each region that corresponded to a primary coolant temperature of 27°C. Each depleting region also contained a fission energy deposition tally to determine the fission characteristics of the region.

Table 3.10 Experiment Loading for Cycle 152B

Position	Actual Loading	Modeled Loading
NW Flux Trap	2E-NW-160	2E-NW-160
N Flux Trap	lD-N-106	lD-N-106
NE Flux Trap	AGR-3/4	AGR-3/4
W Flux Trap	1C-W-75	1C-W-75
C Flux Trap	2A-C-BU	2A-C-BU
E Flux Trap	AGC-3	AGC-3
SW Flux Trap	2D-SW-218	2D-SW-218
S Flux Trap	SPICE 9	SPICE 9
SE Flux Trap	2B-SE-192	2B-SE-192
A-1	IASFR	IASFR
A-2	IASFR	IASFR
A-3	IASFR	IASFR
A-4	IASFR	IASFR
A-5	IASFR	IASFR
A-6	IASFR	IASFR
A-7	IASFR	IASFR
A-8	IASFR	IASFR
A-9	SFROP	SFROP
A-10	AFC-3A	AFC-3A
A-11	SFROP	SFROP
A-12	SFROP	SFROP
A-13	LSFR	LSFR

Position	Actual Loading	Modeled Loading
A-14	EPRI-ZG-B	LSFR
A-15	EPRI-ZG-C	LSFR
A-16	EPRI-ZG-A	LSFR
B-1	YSFR	YSFR
B-2	YSFR	YSFR
B-3	YSFR	YSFR
B-4	YSFR	YSFR
B-5	YSFR	YSFR
B-6	YSFR	YSFR
B-7	HSIS Hardware	HSIS Hardware
B-8	YSFR	YSFR
B-9	MANTRA-1	Aluminum Filler
B-10	Aluminum Filler	Aluminum Filler
B-11	MANTRA-3	Aluminum Filler
B-12	AGR-2	AGR-2
H-1	LSA Cobalt	LSA Cobalt
H-2	Aluminum Filler	Flux Wire Monitor Holder
H-3	N-16 Monitor	N-16 Monitor
H-4	LSA Cobalt	LSA Cobalt
H-5	LSA Cobalt	LSA Cobalt
H-6	LSA Cobalt	LSA Cobalt
H-7	LSA Cobalt	LSA Cobalt
H-8	LSA Cobalt	LSA Cobalt
H-9	LSA Cobalt	LSA Cobalt
H-10	Aluminum Filler	Flux Wire Monitor Holder
H-11	N-16 Monitor	N-16 Monitor
H-12	LSA Cobalt	LSA Cobalt
H-13	LSA Cobalt	LSA Cobalt
H-14	LSA Cobalt	LSA Cobalt
H-15	LSA Cobalt	LSA Cobalt
H-16	LSA Cobalt	LSA Cobalt
I-1 through I-20	Beryllium Filler	Beryllium Filler
I-21	Aluminum Filler	Aluminum Filler
I-22	UCSB-2	UCSB-2
I-23	Aluminum Filler	Aluminum Filler
I-24	Aluminum Filler	Aluminum Filler

ORIGEN2-calculated depletions require fission energy deposition profile results to provide appropriate axial depletions. Average fission profiles were obtained from the ATR MCNP5 full core physics model by modeling a typical cycle loading (namely Cycle 144A) using high-resolution 3D depletion of driver elements (Sterbentz, 2011). This model provided the data needed to calculate power fractions by region. As a proof-of-concept approximation, a single set of average results over multiple timesteps and over all elements for each region were then provided as input into each of three Element Fuel Loading files, one for each element type available. This information was then used as a basis for depleting fresh fuel elements to the exposures necessary for a given cycle.

Element exposure for Cycle 152B was estimated based on the amount of U-235 present in each element, as calculated by PDQ (Poling, 2012). First, ORIGEN2-calculated depletions were generated for Mark VII elements over a range of exposures to correlate U-235 loadings, as listed in Table 3.11 and illustrated in Figure 3.33. A set of Python scripts, namely 'makeburn.py' and several underlying scripts, were used to generate the correlation. Note that the ORIGEN2-calculated depletions were evaluated using what was assumed to be an average fission profile.

Table 3.11 Mark VII element exposure vs. grams of fuel as obtained by ORIGEN2

Element MWD	**U-235 (g)**	**B-10 (g)**	**U-238 (g)**
1.00E-05	1075.325	0.662053	80.94429
15.00001	1056.184	0.565175	80.75731
20.00001	1049.803	0.536049	80.6947
25.00001	1043.424	0.508382	80.6315
30.00001	1037.046	0.482114	80.56791
35.00001	1030.665	0.457175	80.50331
40.00001	1024.288	0.433508	80.43929
45.00001	1017.91	0.411053	80.37464
50.00001	1011.543	0.38975	80.30972
55.00001	1005.168	0.369548	80.24393
60.00001	998.7941	0.35039	80.17808
65.00001	992.4183	0.332234	80.11162
70.00001	986.0475	0.315022	80.04551
75.00001	979.6745	0.298714	79.97862
80.00001	973.3013	0.283262	79.91113
85.00001	966.9379	0.268629	79.84357
90.00001	960.5673	0.254769	79.77575
95.00001	954.2063	0.241648	79.70705
100.00001	947.8383	0.229226	79.6384
105.00001	941.4752	0.217467	79.56917
110.00001	935.1106	0.206338	79.49975
115.00001	928.7513	0.19581	79.42962
120.00001	922.3825	0.185848	79.35933
125.00001	916.0255	0.176424	79.28848
130.00001	909.6641	0.16751	79.21771
135.00001	903.3076	0.159077	79.14615
140.00001	896.9499	0.151103	79.07422
145.00001	890.5976	0.143562	79.0017
150.00001	884.2384	0.136431	78.92934
155.00001	877.8871	0.129687	78.85637
160.00001	871.5353	0.123311	78.78301
165.00001	865.1806	0.117281	78.70931
170.00001	858.8309	0.111579	78.63458
175.00001	852.4817	0.106188	78.56062
180.00001	846.1327	0.101088	78.48582

Element MWD	U-235 (g)	B-10 (g)	U-238 (g)
185.00001	839.7818	0.096266	78.41008
190.00001	833.4408	0.091702	78.33457
195.00001	827.091	0.087387	78.25882
200.00001	820.7505	0.083305	78.18202
205.00001	814.4137	0.079443	78.10511
210.00001	808.072	0.075786	78.02803
215.00001	801.7286	0.072324	77.95038
220.00001	795.3879	0.069048	77.87277
225.00001	789.0574	0.065944	77.79414
230.00001	782.7204	0.063003	77.71561
235.00001	776.3869	0.060218	77.63641
240.00001	770.0508	0.057577	77.55716
245.00001	763.7237	0.055074	77.47728
250.00001	757.3951	0.052699	77.39731
255.00001	751.0677	0.050444	77.31666
260.00001	744.7453	0.048306	77.23594
265.00001	738.4219	0.046275	77.15514
270.00001	732.0936	0.044346	77.07345
275.00001	725.7761	0.042512	76.99177
280.00001	719.4607	0.040768	76.90986
285.00001	713.1441	0.039109	76.82742
290.00001	706.8282	0.037531	76.74463
295.00001	700.5157	0.036028	76.66202
300.00001	694.204	0.034596	76.57878
305.00001	687.8966	0.033232	76.49555
310.00001	681.5932	0.03193	76.41143
315.00001	675.2917	0.030689	76.32806
320.00001	668.9829	0.029505	76.24358
325.00001	662.6877	0.028373	76.15914
330.00001	656.3911	0.027292	76.07532
335.00001	650.0983	0.026259	75.99027
340.00001	643.8076	0.02527	75.90545
345.00001	637.5185	0.024325	75.82063
350.00001	631.2313	0.023419	75.73574
355.00001	624.9516	0.022552	75.65123
360.00001	618.6685	0.021722	75.56647
365.00001	612.3951	0.020925	75.48146
370.00001	606.1244	0.020162	75.39657
375.00001	599.856	0.019429	75.3122
380.00001	593.5881	0.018725	75.22822
385.00001	587.3298	0.01805	75.14438
390.00001	581.0729	0.017402	75.06065
395.00001	574.8215	0.016778	74.97722

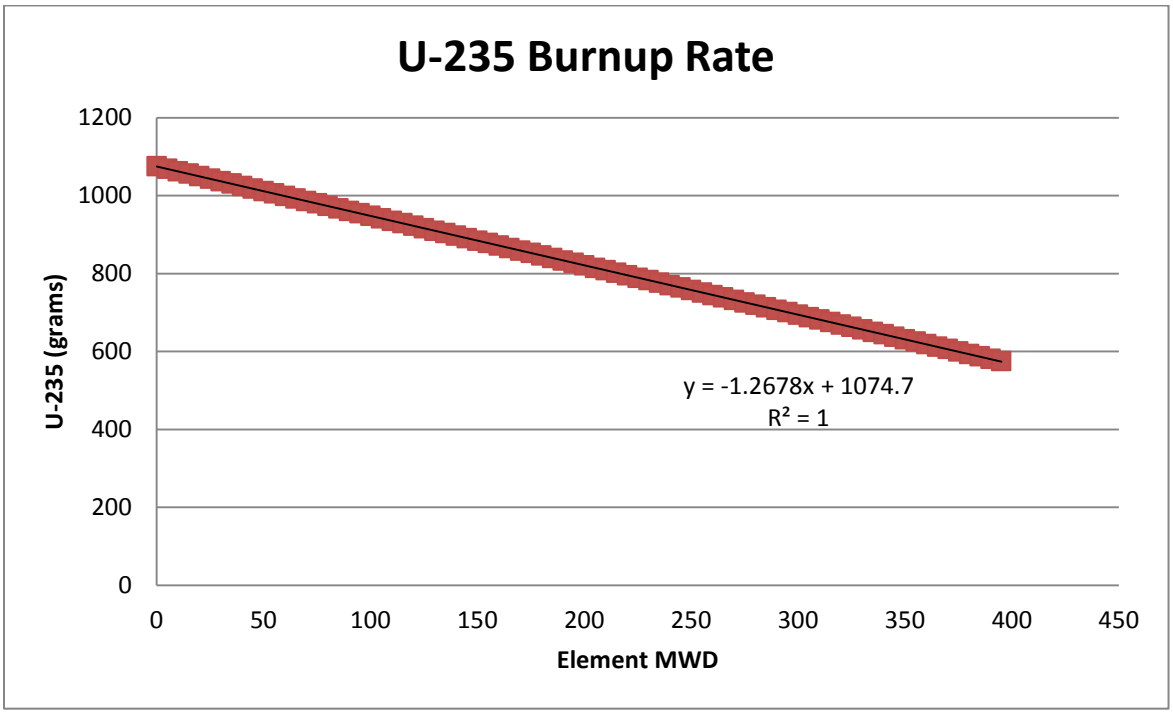

Figure 3.33 U-235 Burnup Rate.

Element powers requested during the parametric study were weighted to correspond to the fission energy deposition profile present in the typical MCNP5 model. Appropriate region power fractions were then used to obtain region exposures, as shown in Equation 3.32 below. To obtain accurate isotopic distributions over time, the requested element exposure was broken into 49 single-day time steps with corresponding region powers to obtain the intended total element exposure. Updated isotopic data were fed back into subsequent ORIGEN2 depletion time steps. The burnup rate of 1.268 grams per MWD of element exposure was calculated from this data and was used for all fuel types present in Cycle 152B.

$$\text{Region Exposure} = \left[\sum_{i=1}^{21} PF_i\right][P_e(t)][t] = \left[\sum_{i=1}^{21} PF_i\right][P_e(t)]\left[\frac{t}{49\ \text{Days}}\right][49\ \text{Days}]$$

$$\text{Region Exposure} = \left[\sum_{i=1}^{21} \text{PF}_i\right][\text{PC}(49\ \text{Days})][49\ \text{Days}] \qquad (3.32)$$

Where: PF_i is the region power fraction obtained from the assumed fission profile. P_e is the element power at time t. PC is the power conversion factor used when assuming a 49-day period of exposure.

Isotopic data provided by PDQ was then utilized to determine the exposure of each element in Cycle 152B. Via additional Python scripts ("makematcds.py" and supporting scripts) the element exposure for each Cycle 152B element was weighted with the average MCNP5 fission profile to determine the power level utilized for each region during ORIGEN2 depletions, similar to the approach used in Equation 3.32 above. To obtain accurate isotopic distributions over time, the requested element exposures were broken into 49 single-day time steps and updated isotopic data were fed back into subsequent ORIGEN2 depletion time steps. At the conclusion of each exposure calculation, ORIGEN2-calculated data was used to provide an update to the material and cell cards of each MCNP5 region.

The beginning-of-cycle state of each element was obtained for Cycle 152B as an input into a MCNP5 model for the cycle. The states represent three-dimensional effects due to burnup of driver fuel elements at various element exposures. A final set of fission energy deposition tallies were obtained from the MCNP5 model to provide comparable data to the point-to-average power density multipliers generated by ROSUB polynomials.

As shown in Equation 3.33, the fission profile was volume-weighted to obtain a peak-to-average power density for an element. The peak value was assumed to occur at the core centerline. Note that MCNP5 reports tally

results normalized per source particle and gram of material, requiring normalization factors to convert tally results to the quantity of interest.

$$A(t) = \frac{P_m(t)/V_m}{\sum P_i(t)/\sum V_i} = \frac{P_r(t)}{P_a(t)} \quad (3.33)$$

where: P_i = [type 7 tally (MeV/g/fission neutron)] [region mass (g)]

P_m = [core centerline type 7 tally (MeV/g/fission neutron)] [region mass (g)]

3.5.4.5 Axial Profile Comparisons

Comparisons between the newly developed method and the current set of multipliers, which utilize polynomial approximations calculated by ROSUB for axial power factors, were made. To provide a basis for comparison, a comparable exposure history was determined. ROSUB polynomial approximations are based upon exposures that are calculated from lobe power, not element power. Therefore, lobe exposure values for the newly developed method were derived for the purpose of utilizing the ROSUB polynomials. One simply needs to multiply the fuel element exposure in MWD by the number eight to obtain appropriate lobe exposure values. Additional ROSUB multipliers were determined based upon the exposure calculated via the U-235 burnup rate method. A direct comparison could then be made between the ROSUB polynomials and the axial profile provided by MCNP5 calculations.

Table 3.12 provides the lobe exposures determined via the two methods discussed in this report, the corresponding ROSUB multipliers as determined by the polynomials currently used in the PDQ-based methodology, and the peak-to- average power density multiplier determined from the axial profile produced during MCNP5 calculations. Note that the MCNP5 multiplier is only available for the exposure determined by the U-235 burnup rate method.

Table 3.12 Peak-to-average power density multiplier comparisons.

Element Position	Serial Number	Exposure Calculation Method	BOC Lobe Exposure (MWD)	ROSUB Multiplier	MCNP5 Multiplier
1	XA819T	PDQ	1191	1.359	--
		U-235 Rate	1448	1.315	1.275
2	XA764TNB	PDQ	1418	1.320	--
		U-235 Rate	1539	1.297	1.250
3	XA879T	PDQ	1289	1.343	--
		U-235 Rate	1577	1.290	1.250
4	YA534TM	PDQ	2070	1.189	--
		U-235 Rate	1767	1.252	1.168
5	YA538TM	PDQ	2342	1.133	--
		U-235 Rate	1943	1.215	1.134
6	XA874T	PDQ	2274	1.147	--
		U-235 Rate	2284	1.145	1.169
7	XA920T	PDQ	1849	1.235	--
		U-235 Rate	1748	1.256	1.240
8	XA842T	PDQ	1313	1.339	--
		U-235 Rate	1533	1.299	1.264
9	YA520TM	PDQ	1434	1.317	--
		U-235 Rate	1224	1.354	1.266

Element Position	Serial Number	Exposure Calculation Method	BOC Lobe Exposure (MWD)	ROSUB Multiplier	MCNP5 Multiplier
10	XA891T	PDQ	1157	1.364	--
		U-235 Rate	1432	1.318	1.296
11	XA024U	PDQ	1324	1.337	--
		U-235 Rate	1211	1.356	1.340
12	XA054U	New	0	1.434	1.375
13	XA055U	New	0	1.434	1.381
14	XA056U	New	0	1.434	1.387
15	XA938T	PDQ	755	1.409	--
		U-235 Rate	839	1.402	1.384
16	YA481TM	PDQ	433	1.423	--
		U-235 Rate	435	1.423	1.386
17	XA057U	New	0	1.434	1.388
18	XA058U	New	0	1.434	1.385
19	XA059U	New	0	1.434	1.379
20	XA946T	PDQ	966	1.389	--
		U-235 Rate	1110	1.371	1.336
21	XA959T	PDQ	965	1.389	--
		U-235 Rate	1098	1.373	1.352
22	XA060U	New	0	1.434	1.376
23	XA063U	New	0	1.434	1.379
24	XA954T	New	0	1.434	1.376
25	XA010U	PDQ	1059	1.378	--
		U-235 Rate	959	1.390	1.350
26	XA942T	PDQ	966	1.389	--
		U-235 Rate	1022	1.383	1.350
27	XA904T	PDQ	847	1.401	--
		U-235 Rate	940	1.392	1.359
28	XA967T	New	0	1.434	1.392
29	XA983T	New	0	1.434	1.367
30	XA244T	PDQ	1185	1.360	--
		U-235 Rate	1199	1.358	1.336
31	XA011U	PDQ	1289	1.343	--
		U-235 Rate	1293	1.342	1.304
32	XA985T	New	0	1.434	1.347
33	XA939T	PDQ	755	1.409	--
		U-235 Rate	669	1.414	1.327

Element Position	Serial Number	Exposure Calculation Method	BOC Lobe Exposure (MWD)	ROSUB Multiplier	MCNP5 Multiplier
34	YA490TM	PDQ	463	1.423	--
		U-235 Rate	461	1.423	1.301
35	XA863T	PDQ	663	1.415	--
		U-235 Rate	877	1.399	1.300
36	XA932T	PDQ	755	1.409	--
		U-235 Rate	839	1.402	1.311
37	YA529TM	PDQ	463	1.423	--
		U-235 Rate	442	1.423	1.316
38	YA527TM	PDQ	463	1.423	--
		U-235 Rate	423	1.424	1.309
39	XA986T	New	0	1.434	1.337
40	XA950T	PDQ	1324	1.337	--
		U-235 Rate	1394	1.325	1.280

Table 3.13 provides a comparison between the various means of calculating lobe exposure and the corresponding ROSUB multiplier. The two methods for calculation of lobe exposure resulted in fairly significant differences, with the maximum difference of 32.3% from the PDQ-based lobe exposure method. The PDQ methodology calculates lobe power and applies the corresponding lobe exposure to all eight elements in a lobe. The U-235 burnup rate methodology determines element powers via isotopic data that is retained for each element, which ultimately reflects element exposure. It is assumed that lobe exposure calculated as eight times the element exposure is a more accurate representation of the definition of lobe exposure assumed during the development of the ROSUB polynomials. Thus, the calculated exposure differences represent an increase in accuracy.

Ultimately, the effect of exposure differences on the corresponding ROSUB multiplier is significantly less than the direct effect on lobe exposure. The largest difference in calculated ROSUB multiplier was seen in Position 5 with an increase of 7.3% from the ROSUB multiplier calculated from the PDQ-based exposure determination. Note that the exposure calculation method seems to be a secondary effect since a disproportionally larger effect on the ROSUB multiplier is seen by elements with extensive exposure.

Table 3.13 Percent Difference Relative to the PDQ-based Methodology.

Element Position	Calculated Exposure Difference (PDQ vs MCNP5)	ROSUB Multiplier Difference
1	21.3%	-3.2%
2	8.6%	-1.7%
3	22.4%	-4.0%
4	-14.7%	5.3%
5	-17.0%	7.3%
6	0.4%	-0.2%
7	-5.5%	1.7%
8	16.8%	-3.0%
9	-14.6%	2.8%
10	23.8%	-3.4%
11	-8.5%	1.4%

Element Position	Calculated Exposure Difference (PDQ vs MCNP5)	ROSUB Multiplier Difference
12	--	0.0%
13	--	0.0%
14	--	0.0%
15	11.1%	-0.5%
16	0.5%	0.0%
17	--	0.0%
18	--	0.0%
19	--	0.0%
20	14.9%	-1.3%
21	13.8%	-1.2%
22	--	0.0%
23	--	0.0%
24	--	0.0%
25	-9.4%	0.9%
26	5.8%	-0.5%
27	11.0%	-0.7%
28	--	0.0%
29	--	0.0%
30	1.2%	-0.2%
31	0.3%	-0.1%
32	--	0.0%
33	-11.4%	0.4%
34	-0.5%	0.0%
35	32.3%	-1.1%
36	11.1%	-0.5%
37	-4.6%	0.0%
38	-8.7%	0.1%
39	--	0.0%
40	5.3%	-0.9%

Table 3.14 provides a comparison between the MCNP5 results used to develop a multiplier and the multipliers determined by the ROSUB polynomials utilizing the various calculated exposures. The second column of this table (titled 'Using PDQ Exposure') effectively provides a comparison between the current power density multiplier and the multiplier that would be generated using the MCNP5 method. The vast majority of the elements analyzed during this demonstration have a positive percent difference when compared to the MCNP5 multiplier. This would indicate that use of the MCNP5 multiplier should generally result in a decrease in multiplier value. Negative percent differences tend to be present in elements with extensive exposure, which can be expected to not limit operation of the core when used as a power adjustment factor but may provide overly conservative results when applied to the burnup adjustment factor.

Comparing the ROSUB polynomial and MCNP5 results that both utilized the lobe exposure determined by the U-235 burnup rate method provides an assessment of the ROSUB polynomial itself without the influence of the two exposure calculation methods. Some interesting trends emerge during this assessment, as shown in the last column of Table 3.14. For instance, most elements differ by only 1-5%. Another interesting trend is that elements with no exposure and outside the NW lobe are consistently near a 4% increase from the multiplier

calculated by MCNP5. However, this effect may be an artifact of the polynomials being used in ROSUB. It also may be due to the slight depression prevalent in the upper section of element profiles, as shown by Figures 3.34 – 3.37. This depression is expected to be a result of the safety rod bite present in the top 3 inches of the core, although this has not been confirmed.

Table 3.14 Percent Difference Relative to the MCNP5 Multiplier.

Element Position	Using PDQ Exposure	Using U-235 Exposure
1	6.6%	3.2%
2	5.7%	3.8%
3	7.5%	3.2%
4	1.8%	7.2%
5	-0.1%	7.2%
6	-1.9%	-2.1%
7	-0.4%	1.2%
8	6.0%	2.8%
9	4.1%	6.9%
10	5.2%	1.7%
11	-0.2%	1.2%
12	4.3%	4.3%
13	3.8%	3.8%
14	3.4%	3.4%
15	1.8%	1.3%
16	2.7%	2.7%
17	3.3%	3.3%
18	3.5%	3.5%
19	4.0%	4.0%
20	4.0%	2.6%
21	2.8%	1.5%

22	4.2%	4.2%
23	4.0%	4.0%
24	4.2%	4.2%
25	2.1%	3.0%
26	2.9%	2.4%
27	3.1%	2.4%
28	3.0%	3.0%
29	4.9%	4.9%
30	1.8%	1.6%
31	3.0%	3.0%
32	6.4%	6.4%
33	6.2%	6.6%
34	9.3%	9.3%
35	8.9%	7.6%
36	7.4%	6.9%
37	8.1%	8.2%
38	8.7%	8.7%
39	7.3%	7.3%
40	4.5%	3.5%

Another trend is that elements in Positions 32-39 consistently differ by 6-10% from the MCNP5 multiplier. Figure 3.37 shows the axial fission tallies for each element in Quadrant 4. Several elements in the NW lobe tend to deviate from the chopped cosine shape via a slight suppression in the center of the core. This trend may indicate that the experiment residing in the NW lobe (i.e. NW-160), the experiment holder (namely, the Dual Standard Holder), or the Large In-Pile Tube (LIPT) itself does not present a chopped-cosine axial shape to the driver fuel elements. Holtz, 2013 indicates that the NW-160 experiment appeared to disturb the axial fission shape.

Significant outliers from these trends also exists at Positions 4, 5, and 9. These positions correspond to the use of YA…M elements, which may indicate that the current method does not appropriately model the effects of these elements. The ROSUB multiplier in these locations is about 7% above the multiplier predicted by the MCNP5 calculations. Also of note is that several YA…M elements reside in the NW lobe and use of these elements corresponds to high percentage values in that lobe as well. Further investigation is needed to evaluate the proper modeling of the YA…M elements.

Position 6 has a multiplier at 2.1% below the multiplier predicted by the MCNP5 calculations. Position 6 contains a Mark VII (XA type) element, but may be compensating for errors introduced by the improper application of YA…M element modeling. However, this trend may also indicate that the experiment residing in the NE lobe (i.e. AGR-3/4) or the Large In-Pile Tube (LIPT) itself does not present a chopped-cosine axial shape to the driver fuel elements. Figure 3.34 shows what appears to be a localized depression in the axial profile that significantly affects Positions 4-6. Further investigation is needed to evaluate the cause of these differences and the potential effects on the results obtained for nearby elements in the NE lobe.

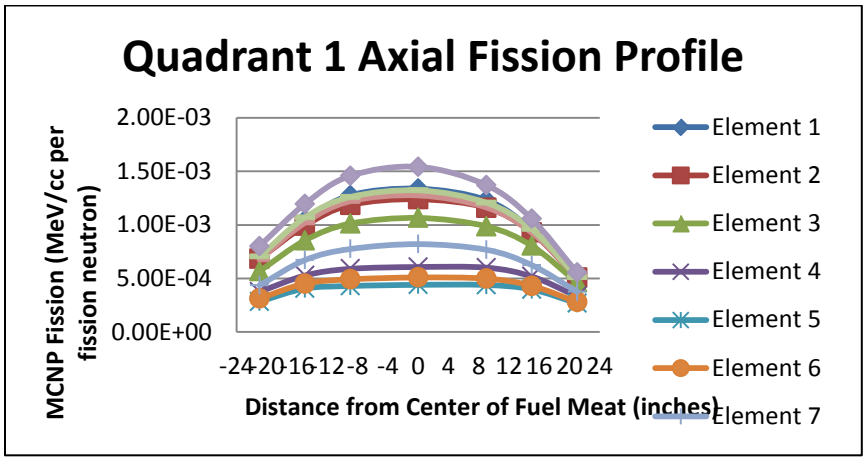

Figure 3.34 Quadrant 1 axial fission profile obtained from MCNP5 tallies (MeV/cc per fission neutron source particle). Plot represents the location of each tally as the volume centroid of the associated region.

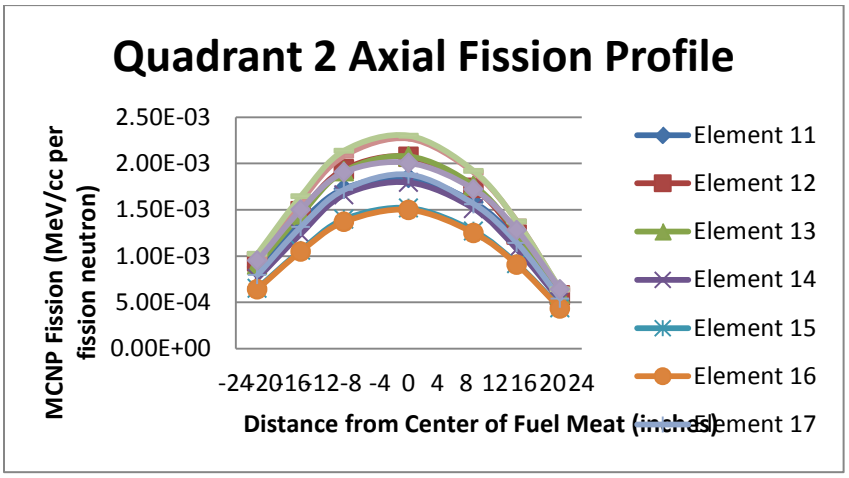

Figure 3.35 Quadrant 2 axial fission profile obtained from MCNP5 tallies (MeV/cc per fission neutron source particle). Plot represents the location of each tally as the volume centroid of the associated region.

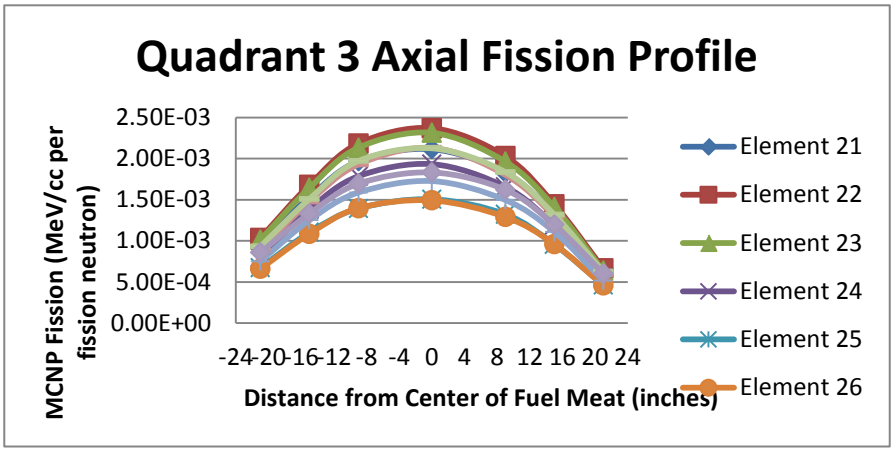

Figure 3.36. Quadrant 3 axial fission profile obtained from MCNP5 tallies (MeV/cc per fission neutron source particle). Plot represents the location of each tally as the volume centroid of the associated region.

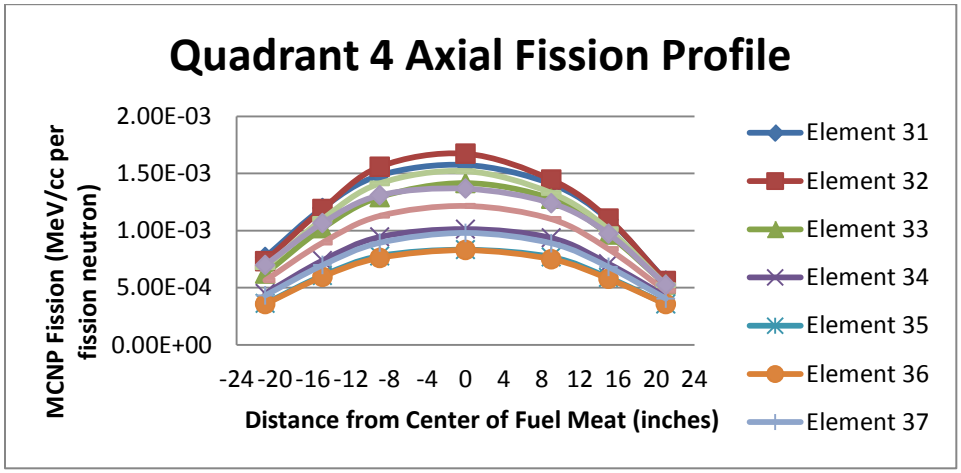

Figure 3.37. Quadrant 4 axial fission profile obtained from MCNP5 tallies (MeV/cc per fission neutron source particle). Plot represents the location of each tally as the volume centroid of the associated region.

3.5.5 Future Directions

Although the initial demonstrations provided here are promising, additional evaluations are needed to validate the eventual replacement of the ROSUB 3D-2D reactivity corrections and peak-to-average power density multipliers with MCNP5-based direct adjustments. Additional improvements to the calculation of lobe exposure should be explored. These improvements could include a change in the assumed rate of U-235 burnup (particularly at higher exposures where the rate of change in U-235 burnup increases as various poisons are built into the fuel matrix) or could include the use of HELIOS cycle modeling to determine appropriate lobe exposures to be used in comparison with ROSUB polynomials.

Validation of element isotopic and power fraction data in the MCNP5 model should also be performed. Currently, no confirmation of the U-235 loading provided to MCNP5 is utilized. Proper loading of the elements, particularly of the YA…M elements, as well as appropriate application of power fractions over the various fuel types will +be necessary to ensure that modeling errors that affect axial power density multipliers have been quantified. In future iterations of this analysis, corrections to the three zoneload.txt input files can easily be made that include removal of significant assumption errors and consistency of power fractions with the MO.PY depletion calculations.

Comparisons of the effects induced by core variations will need to be evaluated over a subset of core configurations such that a baseline axial profile can be determined. These variations could include homogenized representations of experiments. Preliminary homogenization of the experiment in the NW lobe at varying degrees of detail suggests that the presence of the DSH experiment holder may introduce axial perturbations that are as significant as the axial variations in the experiment itself and that the combination of these effects may explain the NW lobe deviations described above. Baseline axial profiles generated from this information can then be used to quantify when significant variations in the profile occur and what elements are potentially affected by the variation.

Axially-varied experiment effects may present long-term concerns on driver fuel as fuel shuffling over multiple cycles is performed. The internally-developed INL MO.PY code, still in the verification and validation process, could be used in the future to couple MCNP5 and ORIGEN2 so that time-dependent effects of flux on the compositions utilized within the MCNP5 model could be represented explicitly. Quantifying the effect of axially-varied experiments on the power density profile and in turn quantifying the amount of experimental axial variations that can be shown to be acceptable will need to be evaluated. Quantification of acceptable experimental axial variation will allow calculations involving multiple cycles and explicit fuel shuffling to be minimized.

Proper evaluation of the power density multiplier in a variety of situations may also need to be explored. Axially-varied experiments may require the multiplier to account for variations in how experiments are modeled in the 2D HELIOS code, such as in a manner inconsistent with the current peak-to-average axial experiment profile assumption. Multipliers may need to correlate other profile assumptions (namely, peak-to-extruded experiment axial profiles) to accommodate approximations made in the 2D model.

Additional axial regions may be needed to ensure that the axial fission profile in the driver elements is appropriately captured and thus the average power density is correctly determined. Additional axial regions would also ensure that axial shapes that significantly deviate from the assumed chopped-cosine shape are accurately evaluated. Current assumptions include the use of the centerline value of the axial profile as the axial profile peak, which does not fully capture the effects in the observed profile. Quantification of the error introduced through the use of this assumption may be necessary. Also, evaluations with additional radial regions in the fuel may be necessary to ensure that the three-radial-region model adequately captures the neutronic effects experienced by the fuel.

General modeling assumptions made in the MCNP5 model should also be explored. For instance, the atom density values utilized by the fuel assume a water density associated with water at 27°C. Quantification of variations in water temperature could be accomplished relatively easily by altering the atom density values used in the Python scripts. Proper modeling of the core as it heats up during cycle startup could provide valuable neutronic affects information.

Additional polynomial approximations provided by ROSUB include fission density axial distribution and axial reactivity effects. These effects will also need to be explored to fully replace the ROSUB assumptions and potentially remove the axial profile assumption from the analysis of driver fuel. While initial results of this methodology are promising for average power density multipliers, significant additional evaluations are necessary before implementation can be fully realized.

3.6 Calculation of UFSAR Power Peaking Limits

3.6.1 Derivation of Effective Plate Power and Related Quantities

The documentation sources for defining what is now commonly referred to as the EPtP and EPP has shown to have some minor inconsistencies. Foremost of which is the different naming conventions used by different report authors and code developers over the past four decades. However, a formal derivation can be made if one inspects a compilation of reference documents generated at different times in the ATR's history.

Point Power Generation Factor (f): Brown et al. (1990) describes the fundamental component to the derivation of EPtP and EPP. It contains the peak-to-average axial multiplier while at the same time compensating for discrepancies between calculated and nominally desired lobe-powers. It also adjusts power densities up in such a way that if the lobe powers were to exceed their maximum setpoints for the cycle, the local heating rates still fall within the heating rates generated by ATR-SINDA.

$$f = \left(\frac{\frac{P_{Lobe,max}}{T_{Core,max}}}{\frac{P_{Lobe,nom}}{T_{Core,nom}}} \right) \times P.D. \times T_{core,max} \tag{3.34a}$$

$$f = \left(\frac{P_{Lobe,max}}{P_{Lobe,nom}} \right) \times P.D. \times T_{core,nom} \tag{3.34b}$$

Where: $P_{Lobe,max}$ is the maximum permissible lobe power set point. $P_{Lobe,nom}$ is the nominal desired lobe power. $T_{Core,max}$ is the maximum permissible total core power level setpoint. $T_{Core,nom}$ is the nominal desired total core power. P.D. is the Point-to-Core Average Power Density Ratio.

Point-to-Average Power Density Ratio (P.D.): This is described in the text on Page 5-2 of Brown et. al. (1990).

$$P.D. = \frac{P_r}{P_T} \times A \times D \tag{3.35}$$

Where: P_r and P_T are the x-y regional power density and the average total core power density as produced by the driver fuel elements, respectively. A is the axial peak-to-average multiplier, which is the summation of the "continuous operation" and one of the xenon and samarium time-dependent axial factors ($A = A_1 + A_{5,10,25}$),. D is the Nominal Power Division Factor which is a normalization factor adjusting for the fact that the calculated lobe and total core power in all likelihood are not exactly the same as the desired nominal lobe and total core power.

P.D. is also described as the "Power Density Normalization Factor" in a 1980 ROSUB manual by S. Easson and A. Smith (1981).

*Partition Power (P.P.)***:** This is described by Easson and Smith (1981).

$$P.P. = \frac{P_r/V_r}{\sum P_r/\sum V_r} = \frac{P_r}{P_T} \tag{3.36}$$

Where: P_r and V_r are the x-y local power and volume of mesh region, "r".

$$N_i = \frac{A \times D}{R} \times M_i \tag{3.37}$$

Where: A is the axial peak-to-average multiplier. D is the Nominal Power Division Factor. R is a correction factor to account for total PDQ7 power not being equal to the power generated in the fuel elements, i.e., some power in PDQ7 may be produced in experiments, while the ATR measures only the power produced in the core. In the HELIOS /MCNP methodology, the power assumed in the reactor can be tallied over just the fuel, thus rendering the R corrector obsolete. M_i is the homogenized cell-to-matrix correction factor for plate "i". HELIOS models the fuel plates exactly, thus rendering M_i obsolete.

Multiplying Equation 3.36 with Equation 3.37 as suggested in the text of the Easson report gives the Power Density Normalization Factor which carries the same meaning as the description of the Point-to-Average Power Density Ratio, discussed only in text (on Page 5-2) in the Brown report given in Equation 3.35.

Nominal Power Division Factor (D): This has also been described by Easson and Smith (1981).

$$D = \frac{P_{Lobe,nom}/T_{Core,nom}}{P_{Lobe,calc}/T_{Core,calc}} \tag{3.38}$$

The word 'effective' occurring before 'point power' does not appear in the Brown report or any other reports of that time. Appendix A of TRA-ATR-840 (Polkinghorne, 1994) defines EPtP and EPP for possibly the first time during efforts to support updates to UFSAR.

Effective Point Power (EPtP): This has been defined by E. Swain in a comprehensive examination of the PDQ7 software suite in preparation for the low-enriched-uranium prototype fuel element test (Swain and Shatford, 2011).

$$EPtP = \frac{P_{lobe,max}}{P_{lobe,nom}} \times P.D. \times T_{core} \times \frac{\epsilon}{r_i} \tag{3.39}$$

Where: ε is a safety factor to account for core power monitoring instrument error. r_i is a safety factor to account for possible structural defects in any given fuel element "i". Equation 3.39 is consistent with Equation 3.34b with the exception of the ε and r_i safety factors.

Effective Plate Power: This is defined in the bounding thermal-hydraulic analysis for the UFSAR by S. Polkinghorne as the multiplication of the EPtP with the "average axial peaking factor" (Polkinghorne, 1994). The average axial peaking factor is derived in detail in a memorandum between A. Smith and R. McCracken dated July 12, 1994 (Smith, 1994).

$$EPP = EPtP \times A_2 \tag{3.40}$$

Where A_2 is the average axial peaking factor used to reverse the A_1 "continuous operation" axial factor described in section 3.4.1.

If one assumes that nominal power levels and calculated core power levels are equivalent within calculation uncertainty, several simplifications to EPP can be made. Combining Eqns. 3.35, 3.38, 3.39, and 3.40 and assuming that $T_{core,nom}$ is equivalent to $T_{core,calc}$ gives the following simplification.

$$SPP = \frac{P_r}{P_T} \times A \times A_2 \times \frac{\epsilon}{r_i} \times \left(\frac{P_{Lobe,nom}}{T_{Core,nom}}\right)\left(\frac{T_{Core,calc}}{P_{Lobe,calc}}\right)\left(\frac{P_{Lobe,max}}{P_{Lobe,nom}}\right) \times T_{core,nom} \tag{3.41a}$$

$$SPP = \frac{P_r}{P_T} \times A \times A_2 \times \frac{\epsilon}{r_i} \times \left(\frac{P_{Lobe,max}}{P_{Lobe,calc}}\right) \times T_{core,nom} \tag{3.42b}$$

If one recognizes that A and A2 are nearly reciprocals of each other then they essentially cancel each other.

$$SPP = \frac{P_r}{P_T} \times \frac{\epsilon}{r_i} \times \left(\frac{P_{Lobe,max}}{P_{Lobe,calc}}\right) \times T_{core,nom} \tag{3.43c}$$

Both EPP and SPP methodologies are encoded into the HELIOS/ZENITH post-processing scripts currently.

3.6.2 Development of the HELIOS Heat Structure for use with SINDA

The ATR-SINDA and SINDA-SAMPLE fuel plate models are input decks to the SINDA 1987/ANSI computer code, a general thermal analyzer. The ATR-SINDA model calculates the thermal response of ATR fuel plates during various hypothetical accidents, given time-dependent inputs of core power, top-of-core pressure, core pressure drop, and core inlet and outlet enthalpy. The SINDA computer code solves the heat conduction part of the problem. Hydraulic conditions in the coolant channels are evaluated using the hydraulic model developed for the RELAP5 pilot code. This hydraulic model is included as lines of FORTRAN coding in the SINDA input deck (called ATR-SINDA). The core power history and hydraulic boundary conditions needed for the flow evaluation are generally obtained from calculations performed with the RELAP5 computer code.

The SINDA-SAMPLE model uses output from ATR-SINDA to calculate statistical safety margins; i.e., the number of standard deviations (σ) to the critical heat flux (CHF), flow instability (FI), the fuel plate buckling temperature, and the aluminum-water ignition threshold (AWIT) temperature. The most important parameters calculated with SINDA-SAMPLE are the minimum margins to CHF and FI. Coolant flow rates, heat transfer rates to the coolant, and statistical safety margins are calculated in FORTRAN subroutines that are integral parts of ATR-SINDA and SINDA-SAMPLE.

The ATR-SINDA and SINDA-SAMPLE models represent one-half of a fuel plate (azimuthally) and a portion of the adjoining side plate (see Figure 3.24). Since azimuthal neutron flux profiles are generally flat over the center portion of a fuel plate, a half-plate model is adequate to predict thermal behavior. The model is divided into 9 axial levels. The user simulates different fuel plates by specifying appropriate radial and azimuthal dimensions.

As shown in Figure 3.38, the coolant channels adjacent to the fuel plate (channels 1 and 2) are divided into 6 subchannels or tracks, and the coolant channel adjacent to the side plate (channel 3) is divided into 3 subchannels. The hot track (i.e., hot-stripe) is the subchannel over which the maximum enthalpy (temperature) rise occurs. Since the hydraulic model in ATR-SINDA is one-dimensional, there is no mixing simulated between subchannels.

Figure 3.33 also illustrates the nodalization of the fuel meat. The ATR-SINDA model has 5 azimuthal regions within the fuel zone. Heating is applied to the fuel meat by application of azimuthal and axial power factors. Thus, the ATR-SINDA model requires 9 axial and 5 azimuthal heating factors.

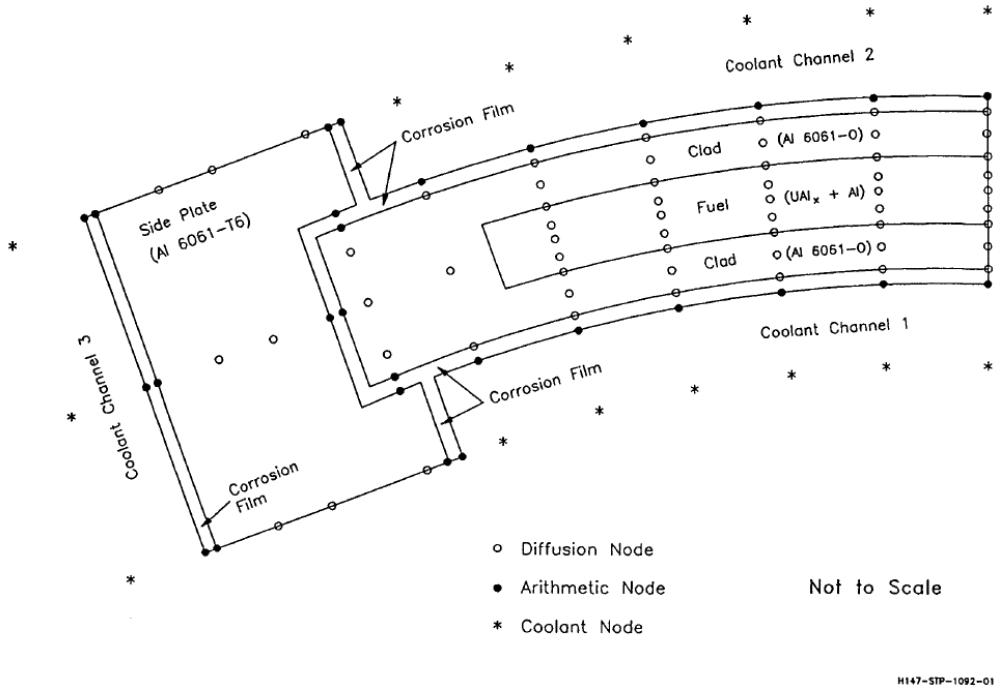

Figure 3.38. Transverse nodalization of the ATR-SINDA fuel plate model.

The analysis process begins with providing the time-dependent power, pressures and enthalpies obtained from the RELAP analysis to the ATR-SINDA model. This model is then fed into the SINDA program, and checks are made to make sure that the model and analysis has converged. The ATR-SINDA results are then fed to the SINDA-SAMPLE model, which performs a statistical analysis on the single coolant subchannel identified as the hot-stripe, randomly varying over 40 parameters that include fuel meat thickness, flow rate, power level, etc. The final result is a prediction of the approach margins (number of standard deviations) to the ATR safety criteria.

Chapter 15 of the ATR UFSAR outlines the thermal safety requirements for the ATR fuel. This chapter covers specific accident scenarios, and categorizes them by severity into “Conditions”. Condition 1 and 2 events (normal operations and anticipated accidents) must show 3 standard deviations to failure (primarily CHF and FI, but also AWIT, and plate buckling). More extreme scenarios have slightly reduced requirements.

From the transient and sensitivity analyses conducted by Polkinghorne et. al. in 1994 using ATR-SINDA and SINDA-SAMPLE, the EPP limits were established for two-pump and three-pump operation of the reactor primary coolant circuit, given in Table 3.15 (Polkinghorne, 1994). For plate 19, these limits apply between 10% and 90% of the fueled width of the plate. For all other interior plates, these limits apply between 5% and 95% of the fueled width of the plate.

Table 3.15. Effective Plate Power limits determined by bounding thermal-hydraulic analysis

	Two-pump Operation		Three-pump Operation	
	Interior Plates	Plate 19	Interior Plates	Plate 19
Maximum EPP (MW)	417	417	443	445

The nodal solution method employed by SINDA forced a minimum degree of azimuthal solution fidelity from PDQ7 and its supporting code, GOPP, for extracting azimuthal plate powers. This would be the 9 x 5 heating factors discussed above. ATR-SINDA contains a feature called the "hot-stripe optimizer" which changes the azimuthal range of applicability for each of the heating factors to ensure that the hot-stripe occurs in the track nearest to the side plate. The optimization of the hot-stripe azimuthal domain to ensure the maximum enthalpy deposition occurs near the side-plate is an explanation for why the hot-stripe is assumed to occur 10% from the side plate for plate 19 and within 5% for all other plates as shown in Table 3.16 (Polkinghorne, 1994).

Table 3.16. Optimum azimuthal hot-stripe domain to ensure computation of the peak enthalpy deposition near the side plate[†].

Lobe Power Split	Fuel Plate	Distance from Side Plate (%)
60/40	15	7%
60/40	19	14%
Enveloping 70	15	6%
Enveloping 70	19	13%

[†] Computed by the ATR-SINDA "hot-stripe optimizer"

Enthalpy deposition into a subchannel is an integral quantity of the fission heat leaving the fuel into the subchannel. Therefore, selection of the size of the hot-stripe is somewhat arbitrary so long as it reasonably approximates the azimuthal power shape that actually occurs in the reactor. Given that SINDA does not track cross-flow between subchannels, each subchannel can for all practical purposes be treated as a 1-D heated pipe insensitive to the width of the azimuthal discretization of the heating factor. Therefore, the decision to optimize the mapping of heating factors in such a way as to ensure the hot-stripe occurs on the side of the fuel plate seems reasonable. Hypothetically this assumption would not be valid if, for example, the hottest track occurred in the center of the fuel plate instead of near the side plate. However, this is not the case as the azimuthal peak almost always occurs near the side plate.

For the HELIOS methodology to be able to justify the safety case of an ATR cycle design, it must meet the thermal-hydraulic expectations of the SAR. Therefore, the HELIOS code will need to produce the heating factors needed by SINDA with the same azimuthal domain used to characterize the hot-stripe in the bounding analyses conducted in 1994. Figures 3.39a and 3.39b show the two levels of mesh fidelity recommended for Physics Analysis: (1) SINDA-mesh having 10 azimuthal meshes per plate, and (2) a fine-mesh with each plate being comprised of azimuthal segments, 1 mm in length on average. The SINDA-mesh model assumes that the fuel meat region nearest to the side-plate is 5% of the total arc-length of the active fuel zone for plates one through 18. The model assumes that this region is 10% of the total arc-length for plate 19. This reflects the Polkinghorne criterion for applying EPP and EPtP. There is in fact a course mesh option with only four azimuthal meshes per plate. This mesh was originally developed by Studsvik as part of the demonstration model, but is seldom used as the fuel element database library has been recast with 10 azimuthal meshes per plate.

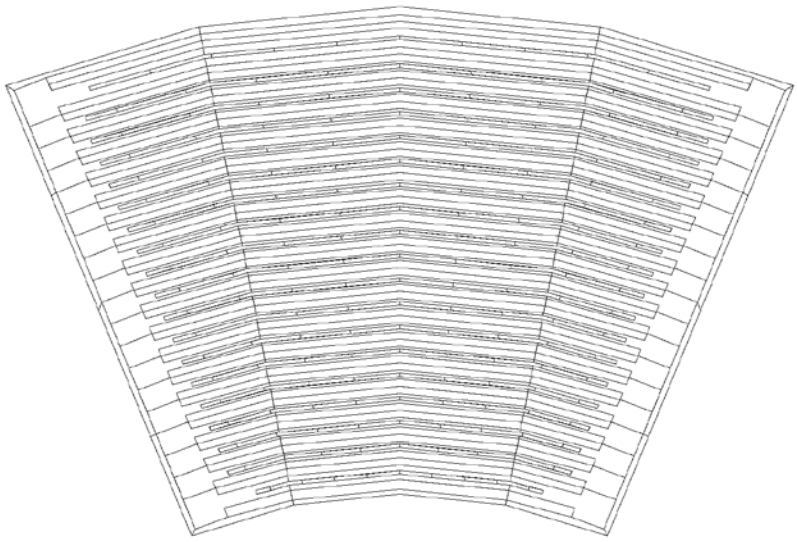

Figure 3.39a. Fuel element geometry for SINDA-mesh heat structures

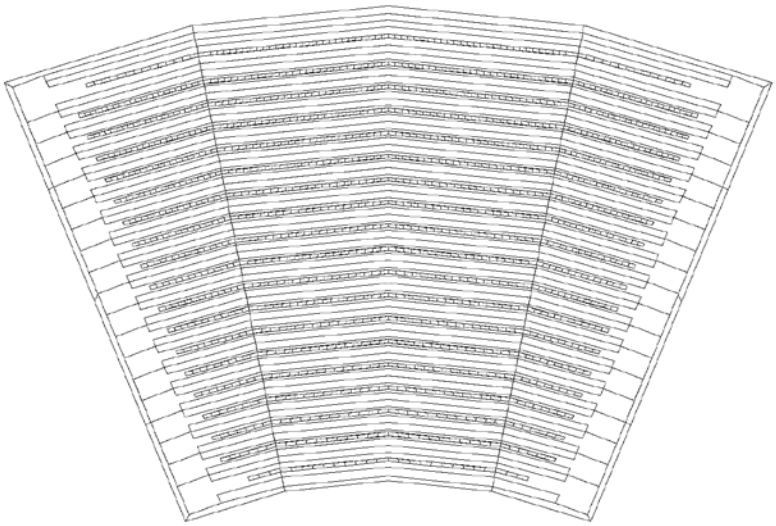

Figure 3.39b. Fuel element geometry for fine-mesh analysis.

Fuel element 19, of the ATRC 12-5 flux run was modeled with the fine-mesh model and compared with fission wire measurements from that flux run, see section 5.4. From a qualitative examination of the power profile, it became clear that there is an azimuthal bias near the side plates, which was later explained by the presence of side-plate "vents" cannot be modeled in the x-y plane by HELIOS. Next, all 40 fuel elements were modeled with the SINDA-mesh. The ATRC 12-5 model also contained the actual fission wires for comparison against the measured fission wire data. The resulting least squares adjustment showed that interior wires had a bias after adjustment of 1.28% and a reduced uncertainty of 8.16%. The exterior wires, those adjacent to the side-plates, had a bias after adjustment of 13.06% and a reduced uncertainty of 10.04%.

Table 3.17 shows the relationship between the applicable regions, azimuthal bias and reduced uncertainty. The bias and uncertainty adjustments for exterior wires are applied to the two azimuthal regions nearest the side plate. These regions of the SINDA-mesh model are nearest to the outer fission wires. Thus, when the power density

from these regions is adjusted according to Equation 3.10 and Equation 3.11, they receive the azimuthal bias and reduced uncertainty for the outer wires. The interior fuel regions receive the azimuthal bias and reduced uncertainty for the interior wires. The same rule applies for adjusting burnup according to Equation 3.18. Note that Equation 3.18 does not consider the reduced uncertainty of the azimuthal adjustment.

Table 3.17. Azimuthal adjustment factors used in ZENITH for EPP, EPtP and CFAD

Azimuthal Region	Adjustment Bias	Adjustment Uncertainty†	Arc-Length (Plates 1-18)	Arc-Length (Plates 19)	Used in EPP/EPtP	Used in CFAD
1	13.06%	10.04%	5%	10%	no	yes
2	13.06%	10.04%	11.25%	10%	yes	yes
3	1.28%	8.16%	11.25%	10%	yes	yes
4	1.28%	8.16%	11.25%	10%	yes	yes
5	1.28%	8.16%	11.25%	10%	yes	yes
6	1.28%	8.16%	11.25%	10%	yes	yes
7	1.28%	8.16%	11.25%	10%	yes	yes
8	1.28%	8.16%	11.25%	10%	yes	yes
9	13.06%	10.04%	11.25%	10%	yes	yes
10	13.06%	10.04%	5%	10%	no	yes

† Note that the adjustment uncertainty is not applied to the burnup adjustment.

It should be noted that the regions nearest the side-plates are excluded from the EPP and EPtP, per Polkinghorne's conclusions. Even though these regions are assigned to the hot-stripe coolant trac, their fuel and cladding temperatures are not the highest. This is because of the heat removal by conduction through the side-plate to the water gap between fuel elements.

3.6.3 Interfaces between HELIOS and SINDA analysis

If during the course of experiment design, it is found that the experiment will axially perturb the power shape in the fuel, follow-on analyses with RELAP, SINDA and SINDA-SAMPLE may be warranted to adjust the Polkinghorne limits for EPP and EPtP, as demonstrated by Davis and Roth, See ECAR-2179. The significant finding of Davis and Roth is that the most important axial region relative to thermal safety margins occurs two to 16 inches below the core mid-plane. This is because the ratio between critical heat flux (i.e., heat generation rate required for boiling) and actual heat flux is at its highest point in this region. This finding takes into account the fact that the enthalpy deposition in the downward flowing coolant is also a significant factor in determining the thermal safety margins, not just the localized heating rate.

When using the Davis and Roth analyses with the PDQ7 methodology, the verbatim ATRC measurement is assumed to be the axial power shape in the ATR. The HELIOS methodology deviates from the current Davis and Roth method in the following ways.

- With the HELIOS methodology, an ATRC MCNP model of the ATRC flux run will be created as well. Data from both ATRC and MCNP will be folded together to produce a covariance weighted least squares adjusted power shape. This adjusted shape, not the ATRC measured shape, is then used in the SINDA analysis.

- Another byproduct of the least squares adjustment is a reduced uncertainty. The current SINDA-SAMPLE analysis assumes that the hot spot peaking factor 90% confidence interval, used during statistical sampling, is ±8.2% (Table 2 of Polkinghorne, 1994). In the new methodology, the 90% confidence interval would be set to $1.64\times \sigma_z$. Where σ_z (or $\sigma_{z,r}$) is the reduced uncertainty of the least squares adjusted power shape. For example, the confidence interval used in SINDA-SAMPLE for the SE-192 experiment would be $\pm 1.64\times 3\% = \pm 4.9\%$, see section 5.5.

- Currently, the Davis and Roth SINDA-SAMPLE results are used to modify the Polkinghorne EPP and EPtP limits, or prompt the analyst to reduce the regional power. However, the axial shape assumed by the PDQ7 Physics Analysis is derived from the ROSUB polynomial. Thus, even though the bounding thermal-hydraulic analysis is assuming the real axial shape, the implementation in PDQ7 is not. In the HELIOS methodology, the same axial shape used by the Davis and Roth method will be used to analyze the peak power performance of the cycle-design, not just the peak power limits.

- Tthe Kim and McClure 60/40 case and bounding 70MW case can be analyzed with the same adjusted axial shape plus reduced uncertainty. Remember from section 3.2.5, the HELIOS computed regional peaking factors are corrected for both axial and azimuthal biases and also have the σ_z (or $\sigma_{z,r}$) values added to them. If the σ_z (or $\sigma_{z,r}$) term from Equation 3.9 and Equation 3.11 is replaced by $1.64\times \sigma_{z,r}$ the Davis and Roth evaluation of EPP and EPtP limits would be self-consistent with the HELIOS computation of the EPP and EPtP limits using the Kim and McClure test cases. This re-evaluation of the Kim and McClure bounding cases can be performed routinely as a configuration check to ensure that the ZENITH calculation using the adjusted axial shape produces analogous bounding EPP and EPtP results as reported by the associated SINDA-SAMPLE analysis.

3.7 Effective Plate Power

Because EPP and EPtP are derived metrics associated with the regional (i.e., intra-element) powers computed by the HELIOS transport solution, they cannot be directly validated with measurement. However, the intra-element powers can be validated against measurement as was done using the ATRC12-5 flux run, see section 5.4. Assuming that the computation of the fission rate is valid, then by extension the UFSAR metrics (e.g., P.D., EPP, EPtP) derived from the fission rate are also valid. So long as these down-stream derivations can be reproduced exactly from one hardware/software configuration to the next, this validation by extension to the validated intra-element powers holds true. It only remains to demonstrate that the UFSAR power metric derivations shown in section 3.6.1 do indeed produce reasonable values, comparable to PDQ7.

3.7.1 Physics Analysis EPP Results

Adjusted and Unadjusted EPPs have been computed for the sixteen prospective Physics Analyses performed by HELIOS since Cycle 145A. All cycles since Cycle 145A have been followed by HELIOS. Both prospective Physics Analyses and retrospective As-Run calculations have been conducted by HELIOS. Section 4.1.3 provides a detailed description of how the HELIOS Physics Analyses were conducted.

Figure 3.40 shows the unadjusted “peak” EPP for Cycles 145A through 154A. Note that the location of the peak EPP is not always the same between PDQ7 and HELIOS. Typically there are several peak locations that are within the azimuthal error of each other at any given time. The figure simply shows the absolute peak as a function of exposure. Note that the PDQ7 EPPs generally bound the unadjusted HELIOS EPPs. Generally, this is due to the fact that the azimuthal point-to-average power density ratio (PD) reported by the HELIOS GOPP code is generally more peaked than HELIOS near the side plates. Given that it is unknown whether or not the GOPP code has been validated against fission wire measurements, the accuracy of the GOPP code to predict azimuthal peak power is unknown. However, the HELIOS azimuthal power has been validated. This validation has led to the azimuthal bias and uncertainty calculations discussed earlier.

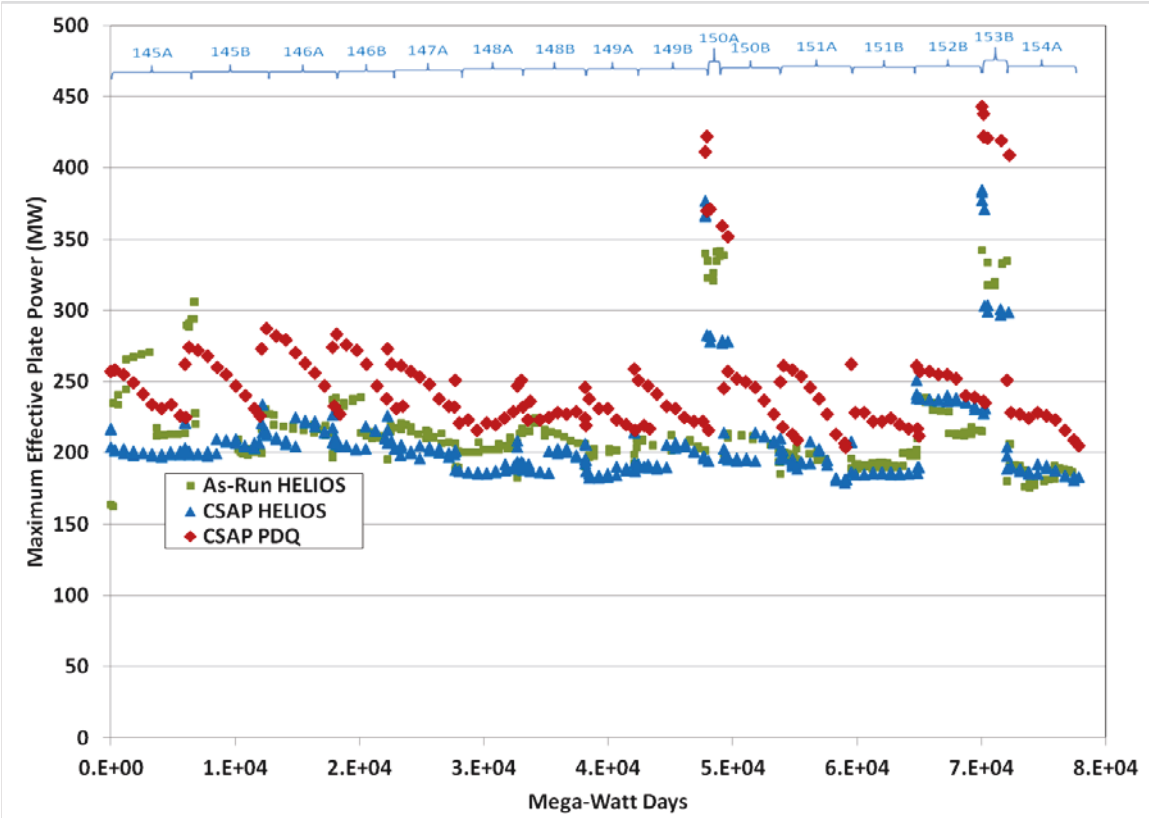

Figure 3.40. Unadjusted "Peak" EPP comparison between PDQ7 and HELIOS

Figure 3.41 shows the adjusted "peak" EPP for Cycle 145A through 154A. Notice the large degree of scatter in EPPs computed for the Cycle 145A and Cycle 145B As-Run calculations. This scatter is largely attributed to poor agreement between calculated and nominal lobe-powers propagating into the Nominal Power Division Factor (D), i.e., Equation 3.38. As the fidelity of the HELIOS fuel element database improves, the agreement between nominal and calculated lobe powers also improves, see section 5.6.

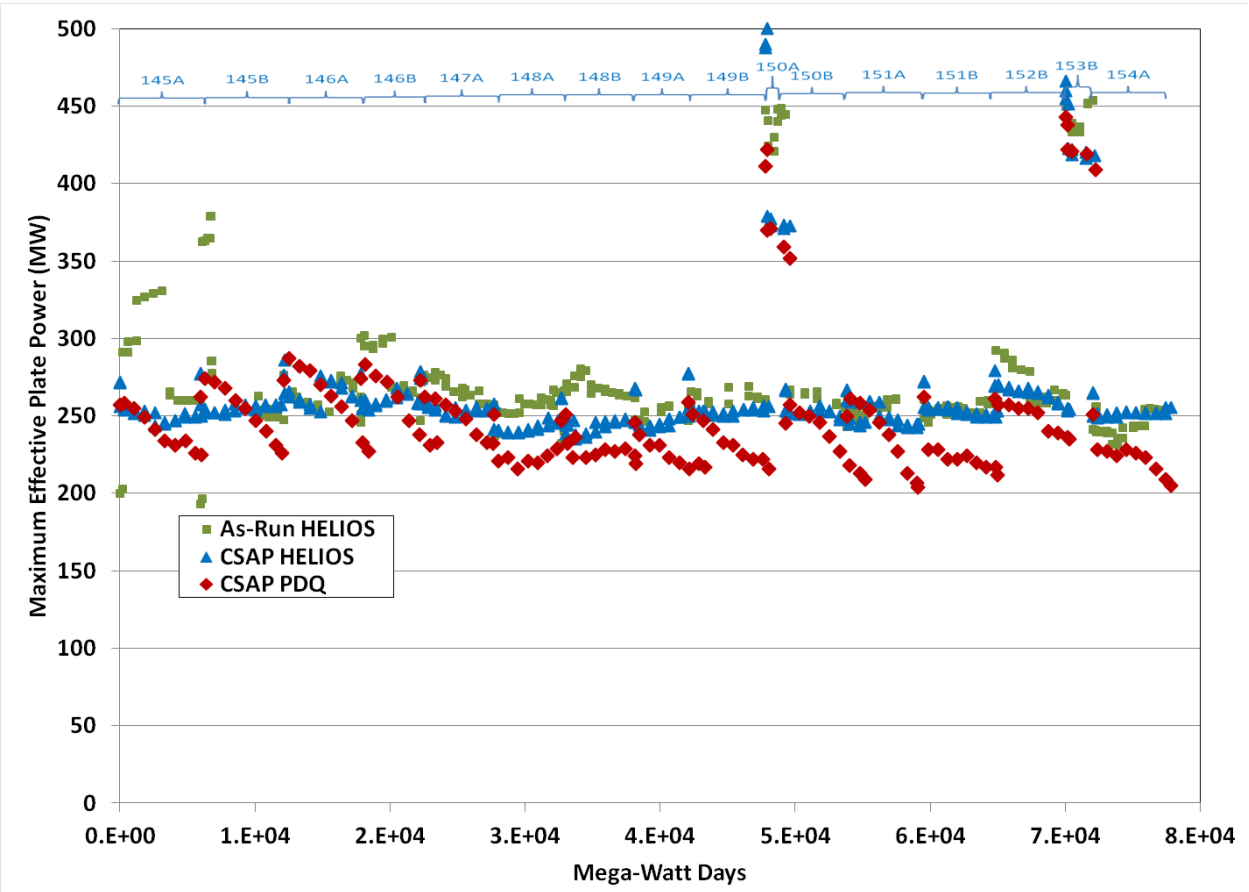

Figure 3.41. Adjusted "Peak" EPP comparison between PDQ7 and HELIOS

Note the "saw-tooth" behavior of the PDQ7 EPP values. Generally, the peak EPP moves from fuel element to fuel element through the cycle irradiation. This is true in both PDQ7 and HELIOS. Thus, not every point on the saw tooth belongs to the same location in the core. The differences in the PDQ7 and HELIOS peak power trends are likely attributable to differences in how azimuthal depletion is treated. The GOPP code simply constructs the power contour along a plate by interpolating between the x-y Cartesian coordinates from the PDQ7 model. However, PDQ7 depletes an intra-element Cartesian mesh that roughly approximates plates and groups of plates. Thus, the PDQ7 model does not have the same azimuthal detail in its depletion strategy. In contrast, the HELIOS model is depleting each azimuthal plate region independently. Said differently, HELIOS depletes the actual regions where the EPPs are being reported, whereas PDQ7 is not.

3.7.2 Bounding UFSAR Test Cases

Effective Plate Power (EPP), as an UFSAR metric, did not exist at the time Kim and McClure performed their bounding physics analysis. The metric transmitted to Polkinghorne was the point-to-average power density ratio (PD). The PD can be further reduced to the Partition Power (PP), i.e.., the ratio of the local x-y power density divided by the volumetric averaged core power density. The maximum PD, taken at 10% from the side of the fuel meat per Polkinghorne's definition (see Section 3.6.2), for the bounding 70MW case was 3.33 (Kim, 1993a).

$$P.D. = \frac{P_r}{P_T} \times A \times D = PP \times A \times \left(\frac{{}^{P_{Lobe,nom}}/_{T_{Core,nom}}}{{}^{P_{Lobe,calc}}/_{T_{Core,calc}}} \right) \quad (3.44a)$$

$$P.D. = PP \times 1.43 \times \left({}^{70}/_{70}\right) = 3.33 \quad (3.44b)$$

$$\text{Max } PP = {}^{3.33}/_{1.43} = 2.33 \quad (3.44c)$$

Note that the ratio of PLobe,nom/PLobe,calc is set equal to 70/70 due to the fact that the nominal value used to compute the PD=3.33 was 70MW. However, the calculation value that would have been needed to match Polkinhorne's result is 60MW. Thus, the PD reported by Kim and McClure in 1993 is higher than that needed to meet the Polkinghorne EPP criterion set in 1994 by an amount of 60/70.

PP can also be deduced from the Polkinghorne EPP limits, see section 3.6.1. Using the EPP limit for plate 19 during 3-pump operation, e.g., a PALM cycle, we can use the derivation of EPP to back out the "bounding" PP.

$$SPP = \frac{P_r}{P_T} \times \frac{\epsilon}{r_i} \times \left(\frac{P_{Lobe,max}}{P_{Lobe,calc}}\right) \times T_{core,nom} = PP \times 1 \times \left(\frac{60}{70}\right) \times 230 = 445 \quad (3.45a)$$

$$\text{Bounding } PP = {}^{445}\Big/_{\left(\frac{60}{70}\right) \times 230} = 2.26 \quad (3.45b)$$

Comparing the "max" PP result from Kim and McClure calculation with the "bounding" PP result from the Polkinghonre calculation, one finds that the bounding-PP is roughly 3% lower than max-PP. The significance of this is that if HELIOS can compute a max-PP of 2.33±3% when modeling the bounding 70MW test case (with SE lobe renormalized to 60MW), then it follows that the EPP derivation in section 3.6.1 encoded in ZENITH will reproduce the bounding EPP limit set by Polkinghorne. See section 4.1.2 for the HELIOS results of the UFSAR test cases.

3.8 Fission Density

3.8.1 Fission Density Limits

The ATR plate type fuel meat is a dispersion fuel produced by mixing and pressing UAl_x compounds and aluminum powders. The fuel performance for this type of fuel is generally quantified in terms of the fission density, or fissions per volume of the dispersion fuel form. To use the terminology of the PDQ methodology, fission density is referred to as the Cumulative Fissioned Atom Density (CFAD). The uranium aluminide dispersion fuel system had been well studied by 1979. Extensive Post Irradiation Examination (PIE) results from that time period provide the bounding CFAD limits for the ATR (Beeston, 1979). There are two fundamental failure modes for uranium aluminide dispersion fuel.

- Plate buckling due to axial compressive loads developed either from thermal stresses or irradiation growth stresses.
- Blister formation between fuel meat and cladding as a result of excessive fission gas buildup and release from the fuel matrix.

Some plate buckling had been experienced for Engineering Test Reactor (ETR) fuel elements in which flat fuel plates were pinned instead of roll swaged to side plates so that axial slippage was restricted. However, this has not been the case for ATR fuel plates due to the slippage allowed between fuel and side plates.

Blister formation during irradiation has been observed for 48 out of 1,700 fuel plates prior to 1979. These blisters occurred near the side plates. This blistering was later determined to be "pimples" associated with thin cladding over the ends, a manufacturing defect.

Blistering was studied closely by conducting blistering tests were the irradiated plates were slowly heated in an oven until blister formation was observed. The result of these "blister tests" revealed that after a CFAD of 1.5×10^{21} fissions/cm^3, the blistering temperature reached a minimum threshold of about 720K. At CFAD lower than 1.5×10^{21} fissions/cm^3 the temperature at which blisters would form was higher.

Generally, fuel swelling was observed from the onset of irradiation up to 2.3×10^{21} fissions/cm^3. The amount of swelling was found to be linear over this range. Little data exists above this range. Therefore, 2.3×10^{21} fissions/cm^3 is considered to be the upper CFAD limit

3.8.2 Physics Analysis CFAD Results

Adjusted CFAD values for each of the 40 elements have been computed for the sixteen prospective Physics Analyses performed by HELIOS since Cycle 145A. All cycles since Cycle 145A have been followed by HELIOS. Both prospective Physics Analyses and retrospective As-Run calculations have been conducted by HELIOS. Section 4.1.3 provides a detailed description of how the HELIOS Physics Analyses were conducted.

In the PDQ methodology, the only CFAD values explicitly tracked and recorded are points at the left and right sides (i.e., adjacent to the side plates) of plate 5 and plate 15. In HELIOS, the 2D regional burnup data is stored in a binary file called a single-fuel-element-HERMES (sfe-HRF) file. The cumulative 2D regional burnup value is tracked from cycle to cycle in the sfe-HRF files. However, HELIOS does not have a memory of the regional burnup values prior to cycle 145A. The fuel management code, THECPT, is used to integrate PDQ CFADs into the HELIOS system. The procedure works as follows. The PDQ "3D" CFAD value is divided by the axial peak-to-average value, effectively converting the value into the 2D frame. These 2D'd PDQ CFADs are input into the ZENITH code for all "pre-145A" elements. ZENITH sums the 2D'd PDQ CFADs with the HELIOS CFADs it computed and has tracked in the sfe-HRFs. The HELIOS CFADs are already azimuthally adjusted, but not axially adjusted at this point. The 2D'd PDQ CFADs do not receive the azimuthal correction, since the azimuthal bias factor has only been evaluated for the HELIOS code, see Section 5.4. After the summation, ZENITH applies the axial peak-to-average and azimuthal adjustments per Section 3.2.6.

Figure 3.42 is a frequency plot that shows the statistical variation of relative differences between PDQ and HELIOS for the "adjusted" CFAD for the four tracked points. As can be seen from the plot, the prediction of CFAD has a consistent bias and uncertainty for both plate 5 and 15, respectively. The mean and standard deviation of the relative differences for plate 5's are 3.5% and 10%, respectively. The mean and standard deviation of the relative differences for plate 15's are -0.5% and 10%, respectively. It is noteworthy to mention that the statistical uncertainty of the intra-element fission powers when compared with fission wire measurements was on the order of 10%, see Section 5.4.

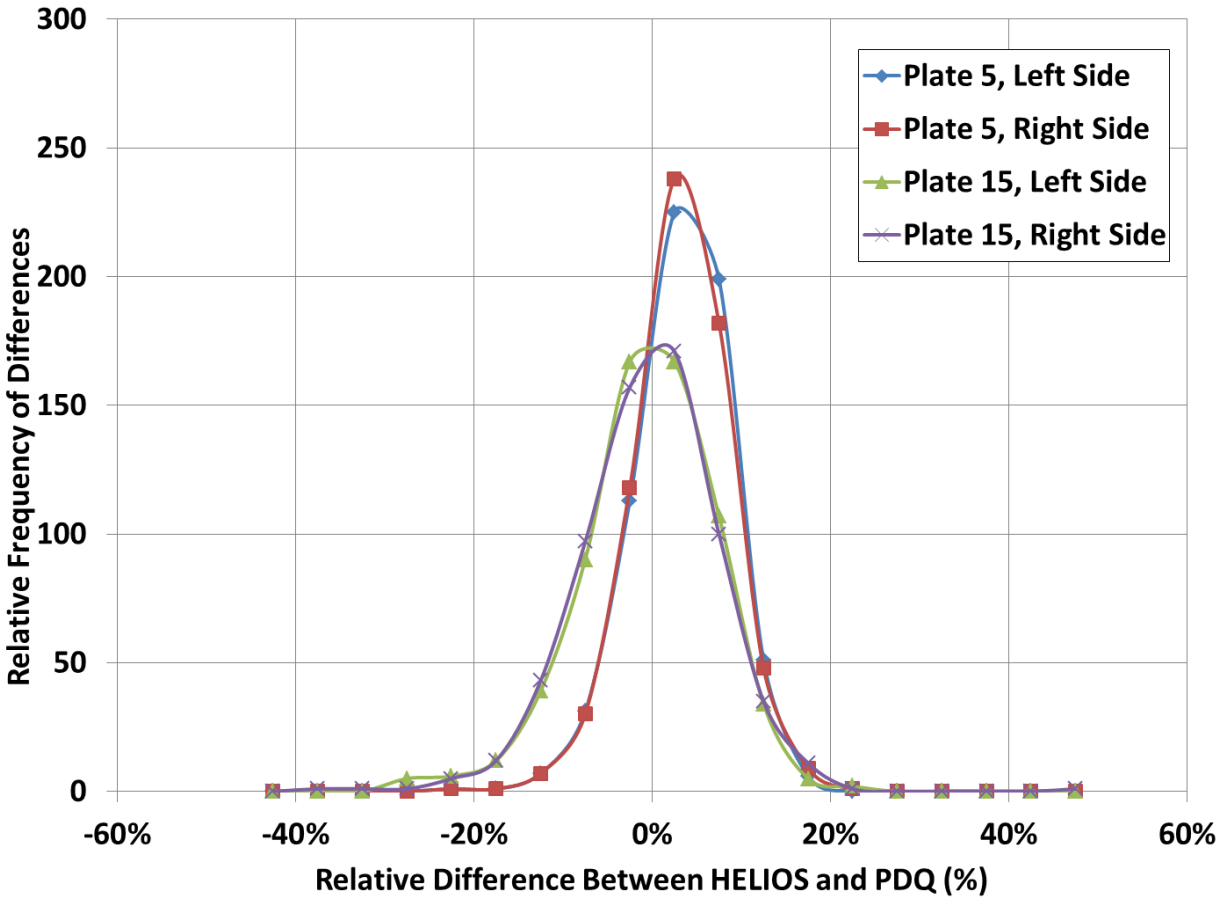

Figure 3.42. Frequency of relative differences in unadjusted CFAD between PDQ and HELIOS

Due to the statistical differences between the two codes, it should be expected that the ultimate end-of-life CFAD evaluation should be different between the PDQ and HELIOS databases. Figures 3.43 through 3.46 show the peak CFAD values for every fuel element eligible for recycle following cycle 155B as a function of remaining U235 mass. This data is tracked by THECPT in the ATRFUE.out file. Figure 3.47 shows the same information for the right side of plate 15 from the PDQ "rvout" file, following Cycle 155B.

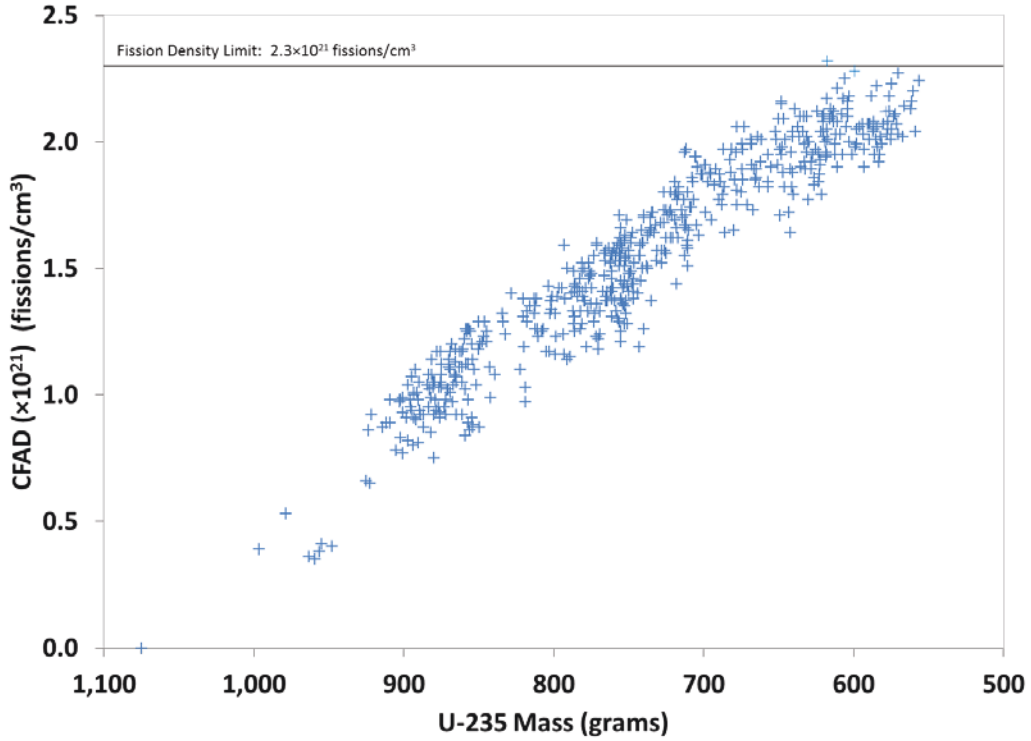

Figure 3.43. Snapshot of peak CFAD data on the left side of plate 5 as a function of remaining U235 mass in all fuel elements available for recycle following cycle 155B as computed by HELIOS.

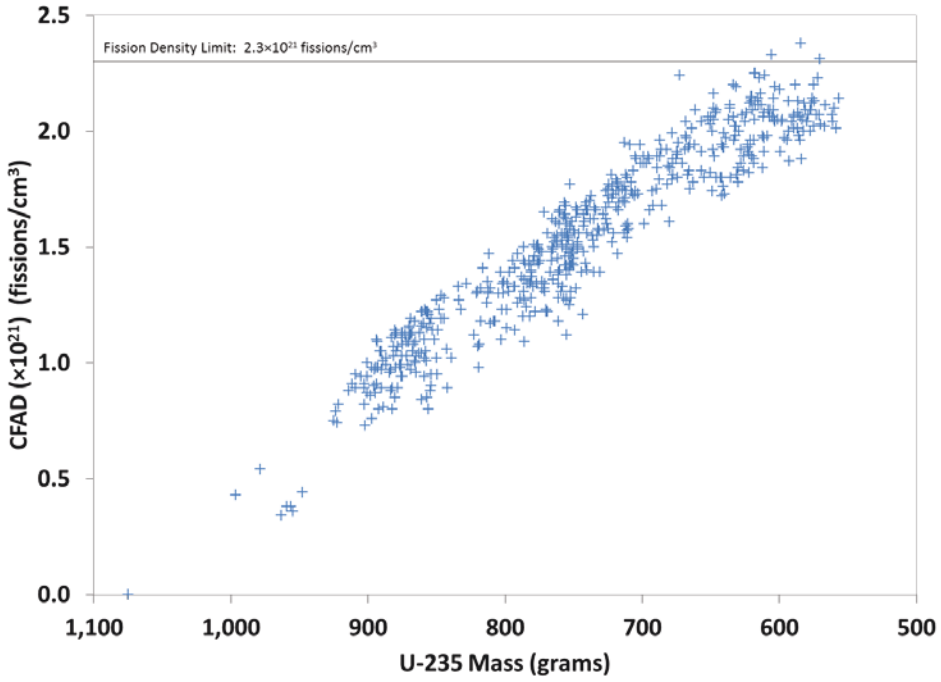

Figure 3.44. Snapshot of peak CFAD data on the right side of plate 5 as a function of remaining U235 mass in all fuel elements available for recycle following cycle 155B as computed by HELIOS.

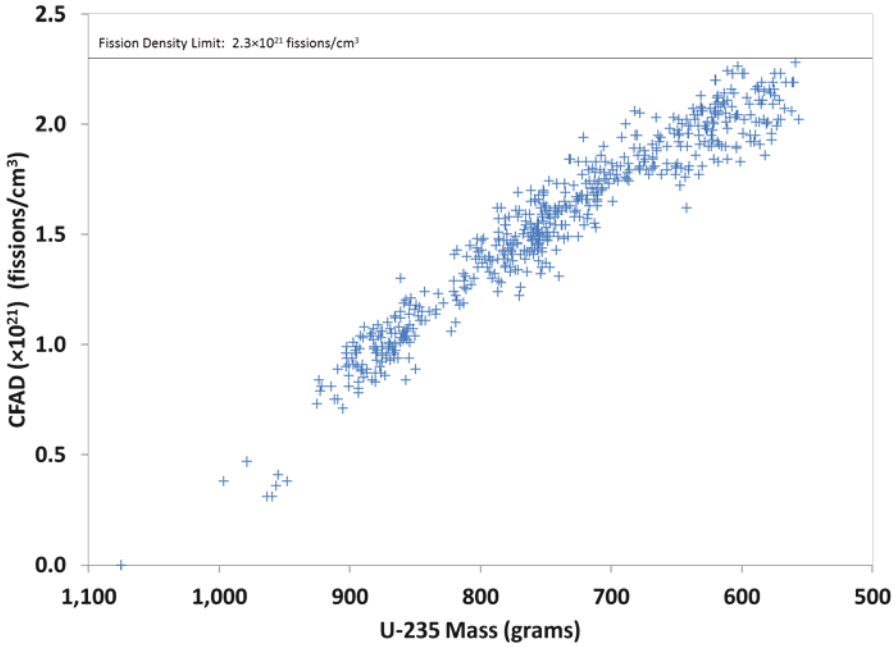

Figure 3.45. Snapshot of peak CFAD data on the left side of plate 15 as a function of remaining U235 mass in all fuel elements available for recycle following cycle 155B as computed by HELIOS.

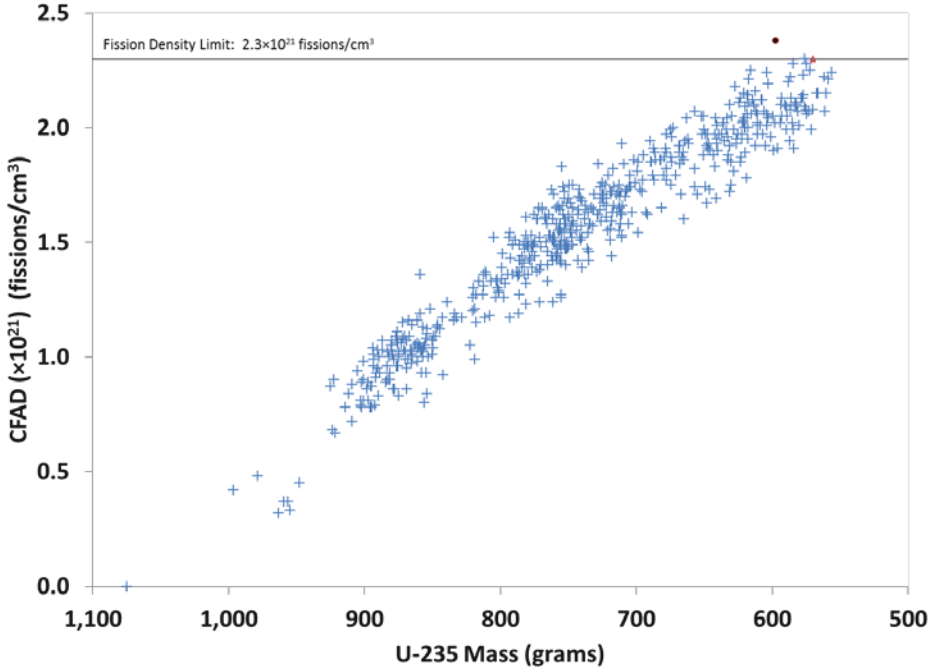

Figure 3.46. Snapshot of peak CFAD data on the right side of plate 15 as a function of remaining U235 mass in all fuel elements available for recycle following cycle 155B as computed by HELIOS.

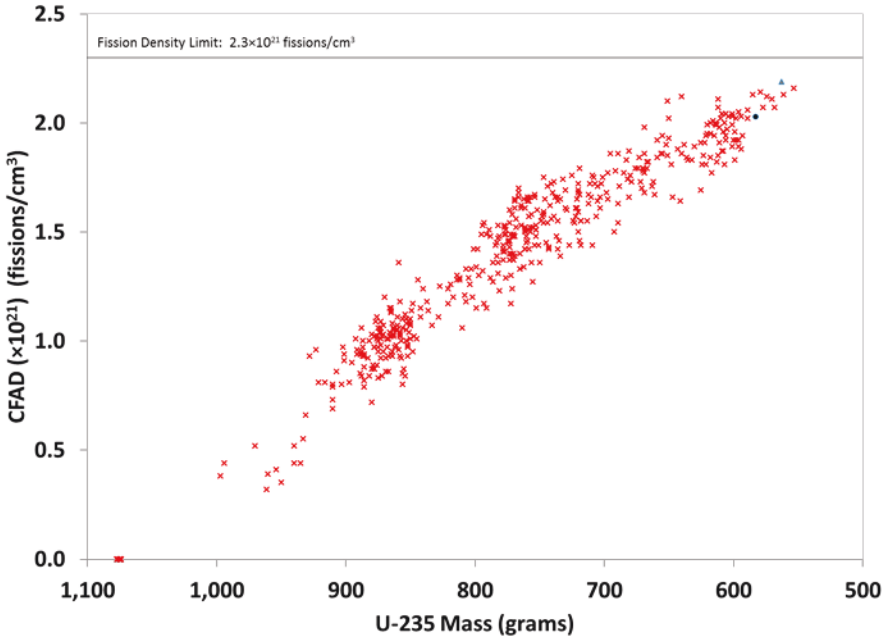

Figure 3.47. Snapshot of peak CFAD data on the right side of plate 15 as a function of remaining U235 mass in all fuel elements available for recycle following cycle 155B as computed by PDQ.

Notice that some of the HELIOS peak CFAD values are greater than the 2.3×10^{21} fission/cm^3 limit. Comparison of Figure 3.46 with Figure 3.47 shows that the peak CFAD in HELIOS is not the peak CFAD in PDQ and vice versa. This should be expected considering the random variability in the outcome between PDQ and HELIOS as depicted in Figure 3.42.

3.9 Fast Fluence Tracking

The fast neutron flux (E>1 MeV) is needed to predict the lifetime of the pressurized loop facilities within the ATR due to neutron damage. There were five pressurized In-Pile Tubes (IPTs) prior to cycle 152A. Addition of the reactivated Loop 2A facility prior to cycle 152A brought the total to six. Note that the IPT in the northwest flux trap is the Large In-Pile Tube (LIPT). All other IPTs are Standard In-Pile Tubes (IPT). Fast flux values are computed at the annular mid-point within each pressure tube wall at eight equal-angle azimuthal locations. Regardless of core location, the 0 degree position is aligned to north. In addition to computing fast flux in the IPTs, fast flux is also computed for the four irradiation thimbles within the safety rod followers (SRF), see Figure 3.48. There are six safety rods currently in the ATR. The SRF irradiation thimbles are actual hardware features of the ATR. Nickel (Ni-58) is routinely irradiated in these facilities to gather fast flux measurement histories. There are no "real" irradiation locations within the IPTs. However, small circular regions are modeled in HELIOS within each IPT for the explicit purpose of tallying the fast flux during the HELIOS transport solution. These regions are modeled as stainless steel, the same as the rest of the pressure tube. Thus, the presence of these detector regions in the model does not perturb the local flux solution.

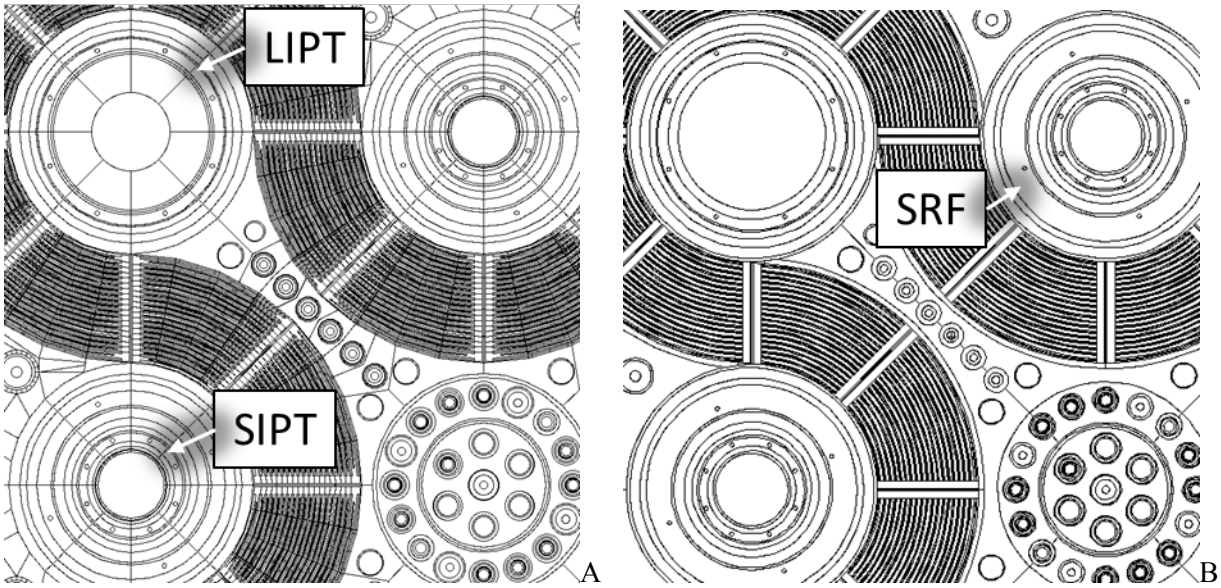

Figure 3.48. Models of azimuthal detection points for tallying the fast flux in the In-Pile Tubes and SRFs for: 94CIC with HELIOS (A), 94CIC with MCNP (B).

3.9.2 Computation of new fast flux multipliers

The PDQ method of computing fast flux requires several multipliers to accommodate spatial and spectral corrections. Much of this methodology was incorporated into the ZENITH post processing system. Though the fast flux formulation remains the same, the value of the multipliers were recomputed using 3D and 2D models of the 94CIC using the MCNP code. The same tally locations in the LIPT, SIPT, and SRFs were used in both models, see Figure 3.48. Eqn 3.46 gives the fast flux formulation that was first introduced by Smith and Cook in 1981 (Smith, 1981a), (Smith, 1981b), (Cook, 1981).

$$\phi = \phi_{calc} \times A_{flux} \times H \times C \times F \qquad (3.46)$$

Where: ϕ is the fast flux (E>1MeV) used to determine fast neutron damage to the IPT. ϕ_{calc} is the flux computed by HELIOS (0.5MeV<E<20MeV). Note that the fast flux tallied in HELIOS is for 0.5MeV to 20MeV, whereas the flux required is for E>1MeV. A_{flux} is the axial peak-to-average multiplier for fast neutrons. H is the explicit multi-group transport to few group diffusion correction. H is inherently one for HELIOS because the HELIOS geometry description is explicit and solved for with transport theory. C is the conversion factor to the measured activation basis. F is the lobe power normalization factor.

The axial peak-to-average multiplier, A_{flux}, was computed using a 3D 94CIC MCNP model. This model contained 24 and 40 detection points in the SRFs and IPTs, respectively. The SRF detection regions begin at the bottom of the fueled zone and extend to the bottom of the withdrawn safety rod, i.e., three inches below the top of the fueled zone. The IPT detection regions run the height of the fueled zone. A second model was created where the top and bottom of the detection regions are ±5cm about the core mid-plane. This later model was used to capture the axial peak at the mid-plane, whereas the former was used to capture the axial average. The formulation for the axial peak-to-average fast flux multiplier is identical to that for the axial peak-to-average power multiplier, Eqn 3.47.

$$A_{flux} = \frac{\int_{-5}^{+5} \phi(z)dz/10.0cm}{\int_{-60.96}^{+60.96} \phi(z)dz/121.92cm} = \frac{\phi_{mid}}{\phi_{avg}} \qquad (3.47)$$

Where: ϕ_{mid} is the fast flux tallied in the ±5cm detection region. ϕ_{avg} is the fast flux tallied in the full height detection region. Note the above correlation can also be further modified by the ratio of the average axial fast flux from the 3D MCNP model over the extruded flux from the same x-y locations in the 2D MCNP model, giving Eqn 3.48.

$$A_{flux} = \frac{\phi_{mid}}{\phi_{avg}} \times \frac{\phi_{avg}}{\phi_{ext}} \quad (3.48)$$

A 2D MCNP model was also created by bounding the 3D model within a flattened 2D universe with a reflective boundary ±0.5cm about the core mid-plane. Figure 3.49 and Figure 3.50 shows the agreement between the 2D MCNP and HELIOS models in SRFs and IPT, respectively. Also plotted is the 3D MCNP model where the detector regions run the full height of the fuel meat. All models assumed a reactor power of 1.58kW in the 3D frame. The PDQ and MCNP values for A_{flux} (as well as other useful comparisons) are given in Table 3.18.

Table 3.18. Comparison of SCAMP/PDQ with MCNP/HELIOS fast flux multipliers.

	PDQ A_{flux}	MCNP A_{flux}	SCAMP σ^{Ni58}	MCNP σ^{Ni58}	PDQ C_{fact}	MCNP C_{fact}
LIPT	1.347	1.42×1.05	102.3	50.8	0.746	0.37
SIPT	1.299	1.42×1.03	105.0	52.6	0.766	0.38
SRF	1.299	1.45×1.08	107.7	54.7	0.786	0.40

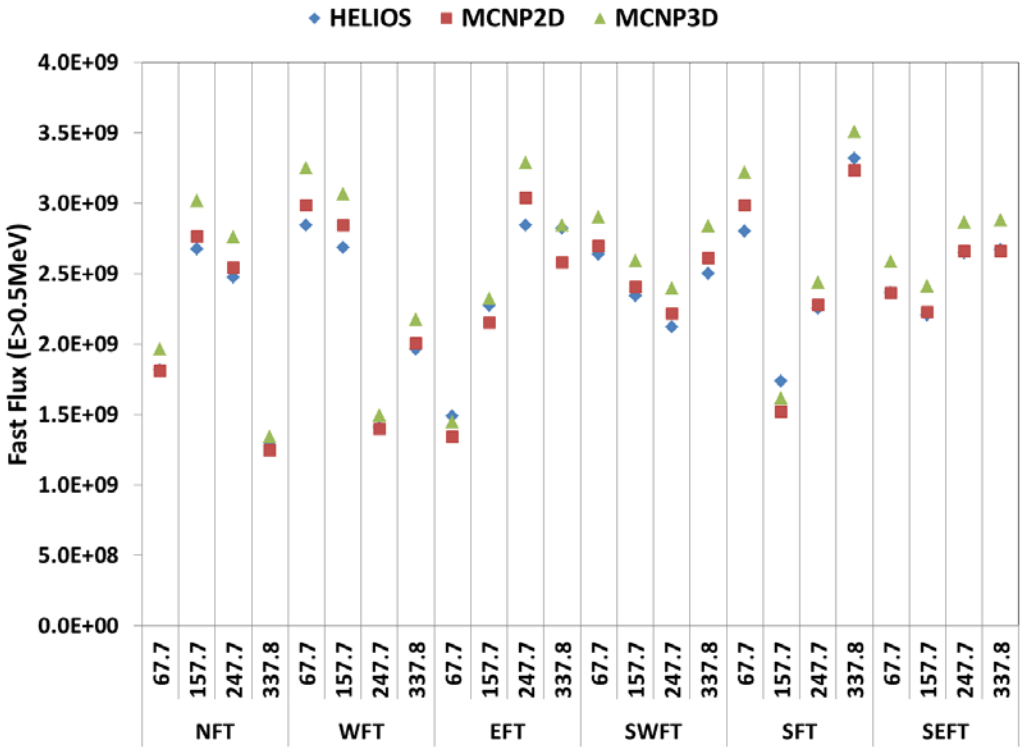

Figure 3.49. Inter-code comparison between HELIOS and MCNP in 2D and 3D of computed neutron fast flux (E>0.5MeV) in Safety Rod Followers for the 94CIC benchmark.

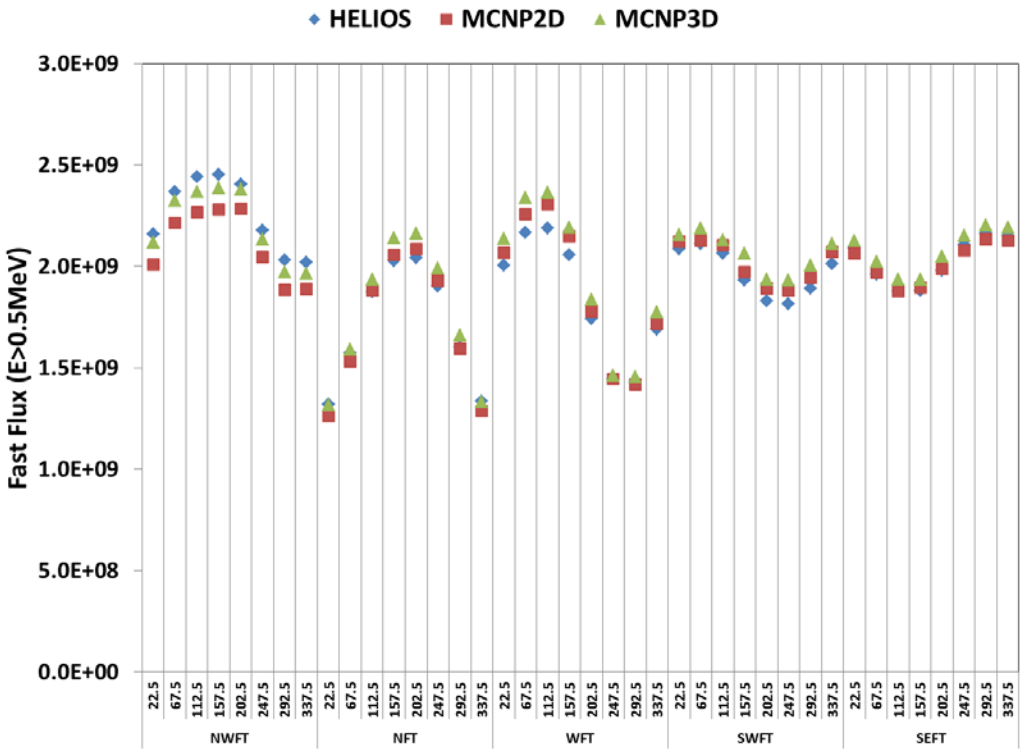

Figure 3.50. Inter-code comparison between HELIOS and MCNP in 2D and 3D of computed neutron fast flux (E>0.5MeV) in In-Pile Tubes for the 94CIC benchmark.

The SRF measured fast flux is considered to be the activation rate of the ^{58}Ni(n,p) threshold reaction divided by a generic dosimetry cross section (135mb) (Cook, 1981). This dosimetry cross-section was computed by averaging the point-wise cross-section over a fission spectrum at energies greater than 1 MeV (Smith, 1981a). The "conversion factor to the measured activation basis," C, accounts for the fact that the original PDQ methodology uses this ^{58}Ni(n,p) dosimetry cross-section to rescale the PDQ calculated fast group flux from 0.821<E<10MeV to 1.0<E<10MeV. Not only does the C factor rescale the fast flux to a different energy range but it also rescales it by the ratio of the ^{58}Ni(n,p) reaction rate in the calculated ATR spectrum over the reaction rate in the fission spectrum. The rescaling of the PDQ calculated fast flux, mimics what is done to the raw activation data. Recall that the ^{58}Ni(n,p) activation rate is divided by the cross section from the fission spectrum, even though the activation measurement itself is taken in the ATR spectrum.

The PDQ group 1 (i.e., fast group) cross-section was condensed using the SCAMP code from five fast group fluxes and cross-sections between 0.831MeV and 10MeV giving a value of 105mb. Thus, the PDQ C factor is the ratio of the coalesced fast group over the ATR spectrum using SCAMP from 0.821 MeV to 10MeV divided by coalesced fast group over the fission spectrum using point-wise data from 1.0 MeV to 10MeV. Hence, C=105mb/135mb=0.766 (value is for SIPT).

To re-compute C for HELIOS, the ^{58}Ni(n,p) activation cross-section is found in the energy range 0.5<E<20MeV by using the flux multiplier option of MCNP for all detection points in the 3D 94CIC model. Note that the lower energy limit of 0.5MeV is used instead of 0.821MeV even though HELIOS has a fast group with nearly the same lower bound. The reason for the 0.5MeV lower limit is that the ^{58}Ni(n,p) cross-section has a threshold for reaction just above 0.5MeV. Therefore, the coalesced flux over 0.5<E<20MeV computed by HELIOS (and MCNP) corresponds to the entire energy range that an actual ^{58}Ni(n,p) dosimeter would see.

The flux multiplier feature of MCNP multiplies the point-wise ^{58}Ni(n,p) cross section $\sigma(E)$ value by the flux contribution $\phi(E)$ of the tallied neutron. After all pre-multiplied tallies are summed, the final tally produces the integral reaction rate $R=\int\sigma(E)\phi(E)dE=\sigma\times\phi$ over the integrand 0.5MeV to 20MeV. Dividing the tallied multiplied

flux by the tallied non-multiplied flux, $\phi=\int\phi(E)dE$, gives the coalesced ^{58}Ni(n,p) in the range 0.5<E<20MeV, $\sigma=R/\phi$. The coalesced ^{58}Ni(n,p) activation cross-section for LIPT, SIPT, SRF are given in Table 3.18, above.

The "lobe power normalization factor", F, scales the computed fast flux by the ratio of the desired lobe power divided by what is actually computed by HELIOS, Eqn 3.49. This has the effect of scaling the fast flux from the calculation to be consistent with the expectations of the cycle design. For flux traps not contained within a lobe (i.e., N, S, E, W), the simple average of the lobe-power of the three adjacent lobes is taken to be the equivalent lobe power.

$$F=\frac{P_{lobe,nom}}{P_{lobe,calc}} \quad (3.49)$$

3.9.2 Fast Fluence Results from As-Runs

The neutron fast flux (E>1MeV) as derived in Eqn 3.46 was computed for each of the azimuthal detection points during the HELIOS As-Run analyses of cycles 145A through 155B. Figure 3.51 shows the cycle averaged fast flux in the northwest flux trap LIPT for each As-Run as computed by both PDQ and HELIOS. The PDQ and HELIOS codes trend well with each other. However, the agreement between the two codes can be off by as much as 35%.

Figure 3.52 shows the frequency of relative differences between PDQ and HELIOS. Unlike most other comparisons of power, burnup, nuclide density between PDQ and HELIOS, the relative differences in fast flux are not normally distributed. In fact for most of the plots, there are two distinct distributions; each distribution on separate sides of the zero axis. Part of the differences between codes is due to the fact that different multipliers were used to scale the raw computed fast group flux (E>0.821 for PDQ, E>0.5 for HELIOS) in 2D to the "measured activation basis" at E>1MeV in 3D. Though the same multipliers were used for all HELIOS calculations, i.e., the same values for A_{flux} and C did not change from cycle to cycle. A minor source of differences is the angular fidelity of the HELIOS data because it is a neutron transport solution, whereas PDQ is a neutron diffusion solution. However, the primary reason for the two separate distributions is that a few cycles were found to error in the direction contrary to the rest of the cycles. In other words, most of the relative differences can be attributed to a given cycle as opposed to any given set of azimuthal angles around the IPT.

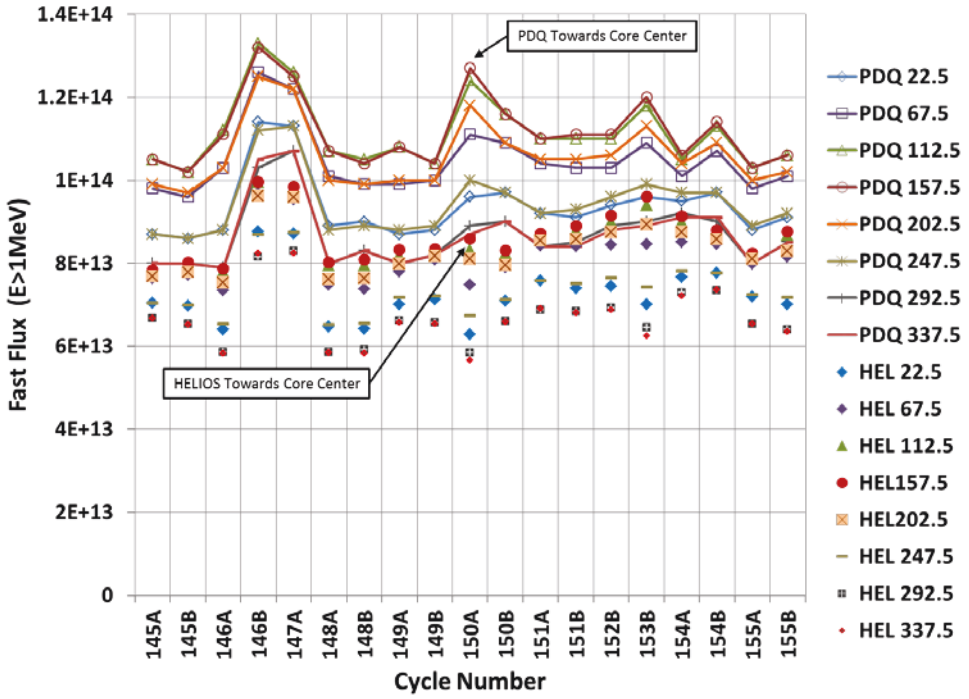

Figure 3.51. Cycle average fast flux (E>1MeV) in the northwest LIPT for As-Run calculations 145A through 155B.

Figure 3.53 shows the relative difference between PDQ and HELIOS as a function of azimuthal angle around the IPTs. Notice that some flux traps in some cycles have an angular dependence on the azimuthal angle around the IPT. However, predominately the discrepancies between PDQ and HELIOS are a function of the cycle number itself. For example, it was found that the two PALM cycles, 150A and 153B, had a code-to-code bias contrary to the bulk of the other cycles. It is not surprising that the two codes would diverge the greatest for PALM cycles given other code-to-code difference, such as lobe power. However, differences in lobe power computation are factored out as both PDQ and HELIOS methodologies. The lobe power normalization is handled by the lobe power normalization factor (F), see Section 3.9.1. If the conversion factor to the measured activation basis (C) was a significant cause of differences, all the plots in Figure 3.53 would be biased one way or the other by the same magnitude, which they are not. Thus, the differences between the PDQ and HELIOS fast flux calculation are associated primarily with the flux solution itself.

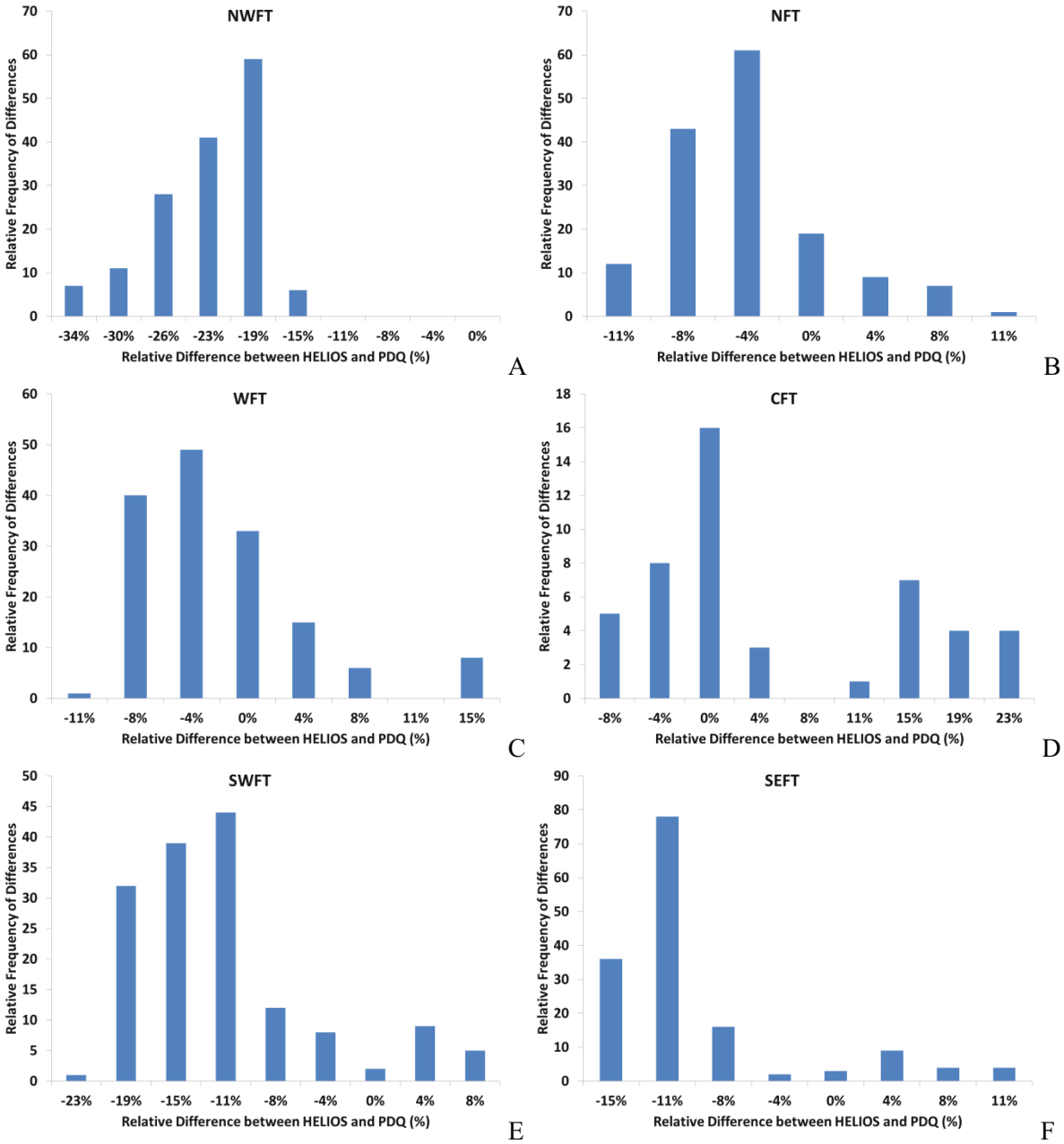

Figure 3.52. Frequency of relative differences in computed fast flux (E>1MeV) for As-Runs 145A through 155B at the azimuthal detection points between PDQ and HELIOS in IPTs: northwest (A), north (B), west (C), center (D), southwest (E), and southeast (F).

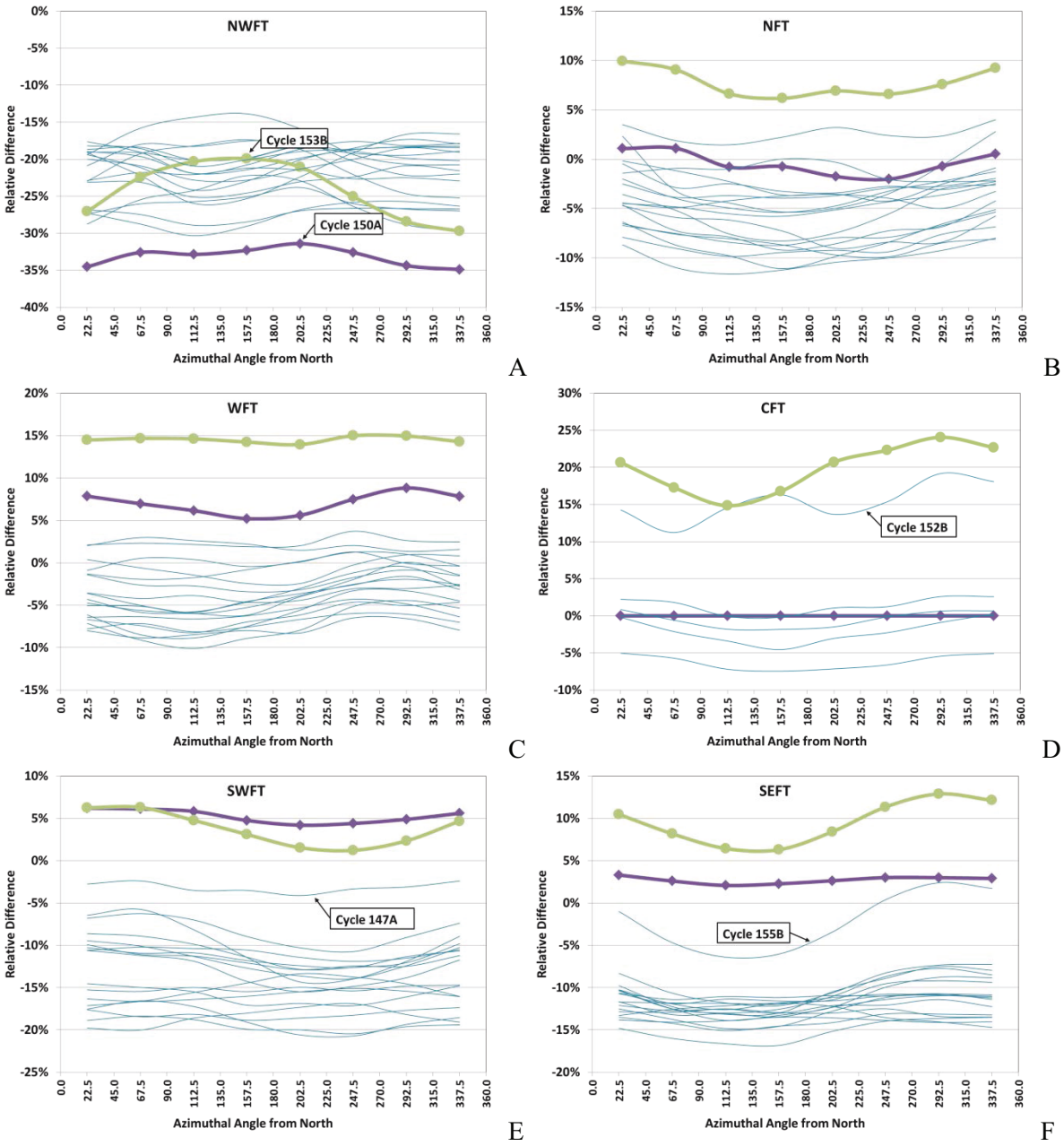

Figure 3.53. Relative differences between PDQ and HELIOS for As-Runs 145A through 155B in IPTs as a function of azimuthal angle around the IPT: northwest (A), north (B), west (C), center (D), southwest (E), and southeast (F).

4.0 VERIFICATION OF THE NEW METHODOLOGY

Samuel E. Bays and David W. Nigg

The various codes incorporated into the new ATR reactor physics suite are either industry standard tools (e.g. HELIOS) or mature National Laboratory codes (e.g. MCNP5) as noted earlier. All have been subjected to extensive verification testing per ANS 19.3 (ANS, 2005) by their developers to demonstrate application-independent mathematical accuracy and portability among computer hardware and operating systems, compilers etc. Accordingly, further verification *per se* of the various software modules described in Section 1 has been largely beyond the scope of the ATR Core Modeling Update project as noted earlier. Nonetheless, in the interest of completeness and continuing improvement, the project has included a few ATR-specific verification benchmark exercises that can be used for additional quality assurance. In that context, a number of cross-comparisons of HELIOS results and legacy PDQ results were completed during 2014 and are summarized in this section. Although this does not constitute a direct verification of the HELIOS model in the sense of ANS 19.3 (because PDQ7 is not a code that is "of comparable or higher accuracy" compared to HELIOS), it is nonetheless instructive to note that in general HELIOS and PDQ7 calculations for the ATR generally produce results that are quite consistent with each other.

4.1 Fuel Element Powers – Cycle 103A

Figure 4.1 provides a comparison of *a priori* HELIOS-computed fuel element powers against corresponding PDQ7 calculations and corresponding measurements for ATR Cycle 103A Test NT3, which was used for nuclear requalification following the 1994 CIC (McCracken et. al., 1994). Also shown on the plot are the measured fuel element power data from the corresponding ATRC 94-3 flux run in support of that nuclear requalification test series. Note that the measured data in Figure 4.1 reflect the assumption that Fuel Elements 16-19 in ATR have the same powers as the corresponding elements in the 12-15 positions in reverse order, as documented in the Benchmark Specification (Kim et al, 2008). The largest difference between HELIOS results and ATR NT-3 measured data occurred in Fuel Element 5. Coincidentally, this element had one of the largest differences between the ATR NT-3 measured data and the ATRC 94-3 measured data. The follow-up report for NT3 attributes this difference to a "difference in critical shim positions between the two reactors."

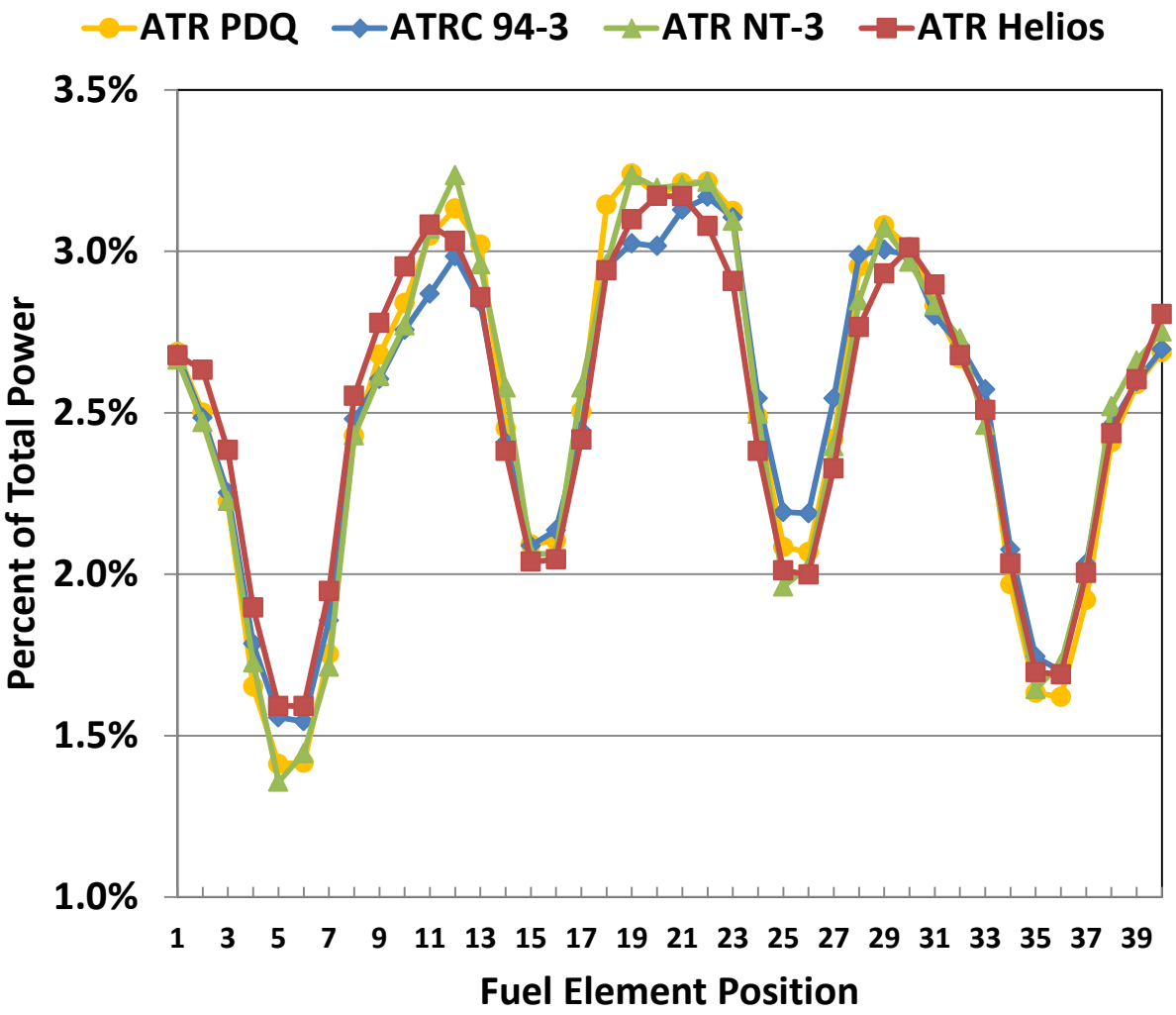

Figure 4.1. Comparison of calculated and measured fuel element-to-element fission power distributions associated with Nuclear Requalification Testing of ATR Core Number 103A-2 subsequent to the 1994 CIC. Measured data for the ATRC analogue of the corresponding ATR configuration are included for completeness along with the ATR measurements and the corresponding computed results from PDQ7 and HELIOS

4.2 Fuel Element and Point Powers for UFSAR Safety Basis Calculations

The Kim and McClure 50/50, 60/40 and "bounding 70MW" analyses were used to provide the azimuthal power distribution, i.e., point-to-average power density ratio, to Polkinghorne's bounding thermal-hydraulic analysis (Kim, 1992). Polkinghorne found that in order for RIAs "to demonstrate compliance with core safety criteria," the southwest lobe power from the 60/40 case had to be scaled back to 56MW, down from 60MW (when total core power is normalized to 250MW) (Polkinghonre, 1994). The actual reactor power used in PDQ7 for the 60/40 case was 204.5MW. Also, the southeast lobe had to be scaled back to 60MW, down from 70MW for the bounding 70MW case. The reactor power of the bounding 70MW case was 230MW. Table 4.1 provides a brief synopsis of the core configurations used by Kim and McClure to create the bounding physics cases. Table 4.2 provides a brief synopsis of the Polkinghorne adjustments necessary to make these bounding physics analyses comply with the EPP (and EPtP) limits established by the bounding thermal-hydraulic analyses. All IPT were assumed to be filled with a homogeneous mixture of 50v/o zirconium and 50v/o H2O. The limiting PD for the 60/40 case occurred on day 0 of the cycle (Kim, 1993b). The limiting PD for the bounding 70MW case occurred on day 1 of the cycle (Kim, 1993a).

Table 4.1. Core configuration for bounding UFSAR physics analyses

	50/50	60/40*	Bounding 70
Total Core Power (MW)	250	204.5	230
NW Lobe Power (MW)	50	34	26
NE Lobe Power (MW)	50	34	26.3
Ctr Lobe Power (MW)	50	43.2	45.7
SW Lobe Power (MW)	50	49.1	62
SE Lobe Power (MW)	50	44.2	70
Reactor Loading			
NWFT, NEFT†	SIPT	LIPT	LIPT
NFT,WFT,CFT,SEFT	SIPT	SIPT	SIPT
SWFT°	SIPT	SIPT (Voided)	SIPT
SFT°	SIPT	SIPT	SIPT (Voided)
EFT‡	SIHA	SIHA	SIHA

*Core power *would be later scaled, artificially, to 250MW for SINDA analysis.*
†The Kim and McClure report is not absolutely explicit that LIPTs were used in the NWFT and NEFT
‡The SWFT and SFT was not modeled as voided in the original Kim and McClure report, PG-T-90-003,r1. However, the SWFT and SFT were assumed to be voided for the 60/40 and bounding 70MW cases, respectively, as documented in two letters from Kim to Wagner, SSK-03-93, SSK-09-93. In Polkinghorne's assumption 4 it is stated that the SWFT was assumed flooded for the 60/40 case.
°A PDQ7 CSAP manual of the day did not report SIPT being in the EFT. It is assumed here that a 50/50 Zr filled SIHA is neutronically equivalent to the same mixture in a SIPT.

Table 4.2. Core configuration for bounding UFSAR thermal hydraulic analyses

	50/50	60/40	Bounding 70
RELAP Power (MW)	250	250	250
Number of Coolant Pumps	--	2	3
After Scaling and Adjustments†			
NW Lobe Power (MW)	50	41.6	28.3
NE Lobe Power (MW)	50	41.6	28.6
Ctr Lobe Power (MW)	50	52.8	49.7
SW Lobe Power (MW)‡	50	60 (56.0)	67.4
SE Lobe Power (MW) ‡	50	54.0	70.0 (60.0)

†In Polkinghorne's assumption 5, he states that "it was necessary to scale reactor power as follows in order to demonstrate compliance with core safety criteria.
‡The number outside of parenthesis is the lobe power assuming the Kim and McClure total core power is scaled to 250 MW. The number in parenthesis is the lobe power adjustments stipulated by Polkinghorne.

The 50/50, 60/40, and bounding 70MW cases were run with HELIOS. Figure 4.2 provides a plot of the geometry for the bounding 70MW case. The exact OSCC and neck shim configurations for the first day of depletion, as given in the Kim and McClure report, were used to model the HELIOS test cases. All fuel was defined as fresh 7F fuel elements. Figure 4.3, Figure 4.4 and Figure 4.4 shows the fuel element powers for the 50/50, 60/40, bounding 70MW splits, respectively. Generally, the relative differences between HELIOS and PDQ7 were less than 10%. The largest relative difference was 20% for fuel element 8 in the bounding 70 MW case. However, this region of the core between the northeast and east flux trap experienced a steep power gradient as the configuration deliberately pushes power into the southeast lobe. Table 4.3 gives the lobe power breakdown for each test case.

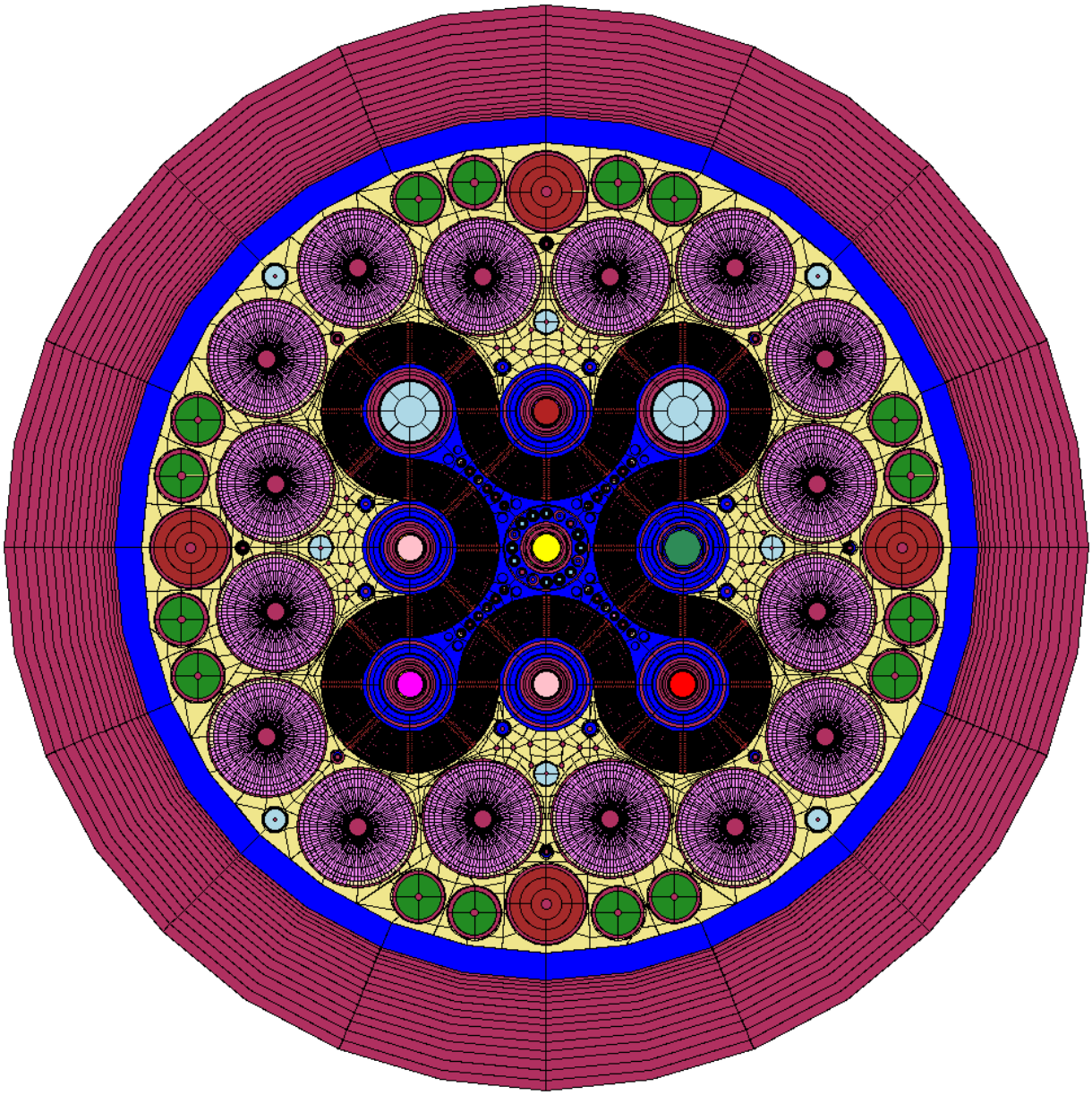

Figure 4.2. Bounding 70MW UFSAR test case

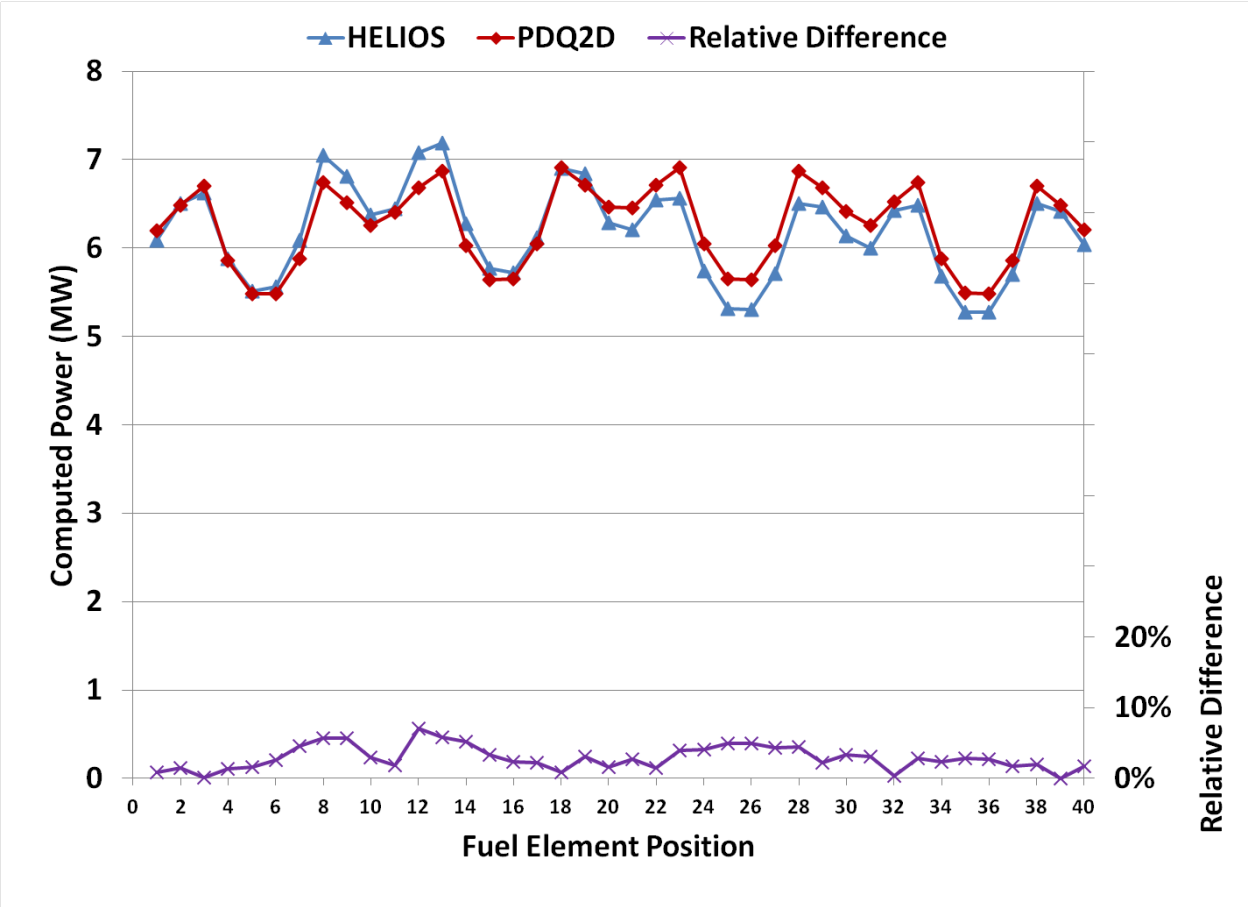

Figure 4.3. Element-to-element fission power distribution comparison between PDQ7 and HELIOS for the 50/50 UFSAR test case

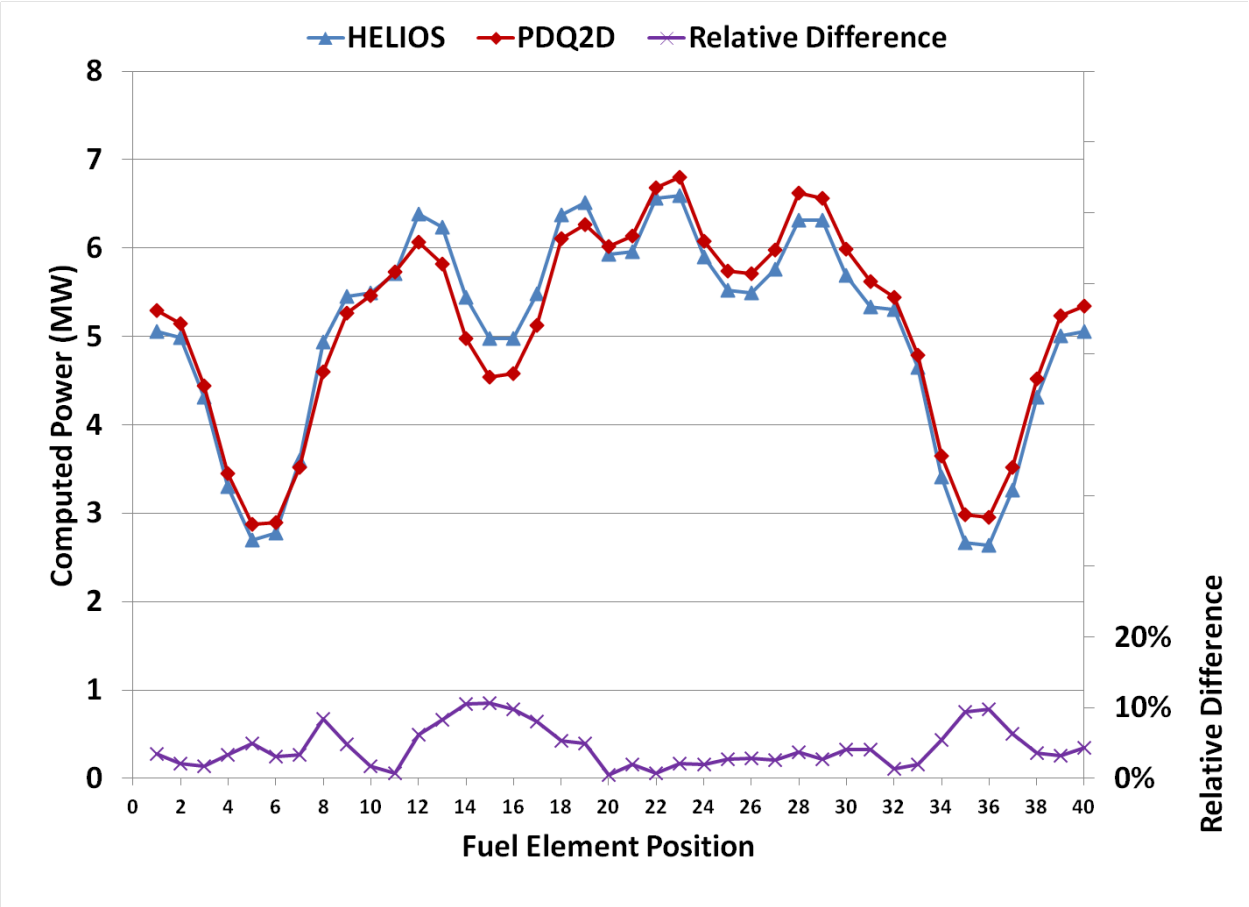

Figure 4.4. Element-to-element fission power distribution comparison between PDQ7 and HELIOS for the 60/40 UFSAR test case

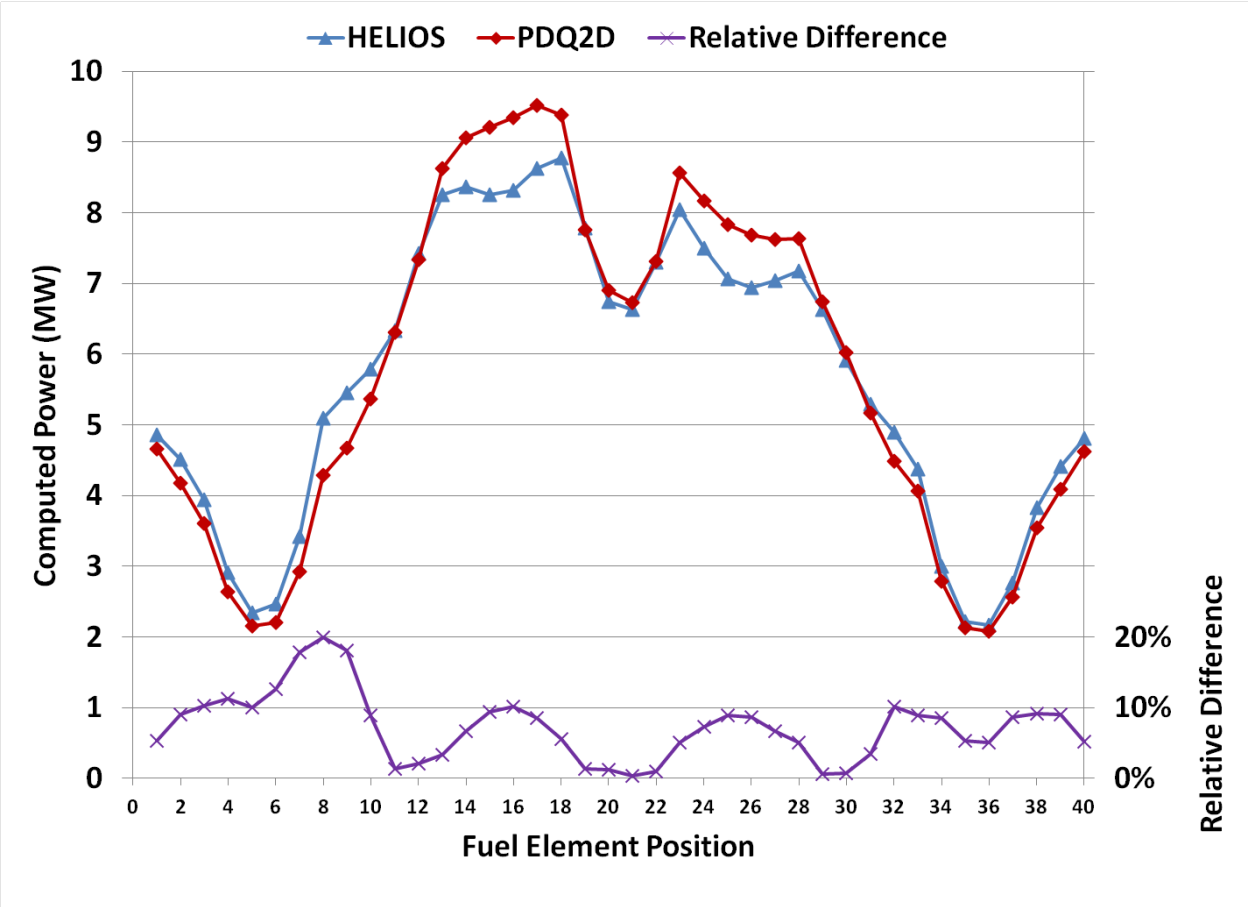

Figure 4.5. Element-to-element fission power distribution comparison between PDQ7 and HELIOS for the bounding 70MW UFSAR test case

Table 4.3. Lobe power comparison between PDQ7 and HELIOS for the UFSAR test cases†

	50/50		60/40		Bounding 70MW	
	PDQ7	HELIOS	PDQ7	HELIOS	PDQ7	HELIOS
NW Lobe Power (MW)	49.2	47.8	33.1	31.3	25.8	27.7
NE Lobe Power (MW)	49.1	50.0	32.2	32.1	26.7	30.1
Ctr Lobe Power (MW)	50.7	49.6	45.6	44.2	45.8	46.4
SW Lobe Power (MW)	50.5	48.1	50.2	48.4	61.6	57.7
SE Lobe Power (MW)	50.5	51.9	43.5	46.4	70.2	65.8

†After one day of depletion

More important than the lobe- or fuel element powers is the computation of point-to-average power density ratio (PD). Figures 4.6a through 4.6f illustrate the max-PD for plates 15, 17, and 19 for the 60/40 case and for the bounding 70MW case. These correspond to the plates considered to be the "hot plates" for each of the two elements for which data are shown (Kim, 1993a, 1993b). After azimuthal adjustment, the maximum PD for HELIOS is 3.61. It is fortuitous that the PDQ7/GOPP result agrees so well with the adjusted HELIOS result, 3.63. The Partition Power (PP) for this point after azimuthal adjustment (see Equation 3.10) and after scaling the calculated 65.8 MW to the 60 MW ceiling suggested by Polkinghorne is 2.20. The physics analysis max-PP and thermal-hydraulic bounding-PP from the discussion in section 3.7.2 are 2.18 and 2.26, respectively.

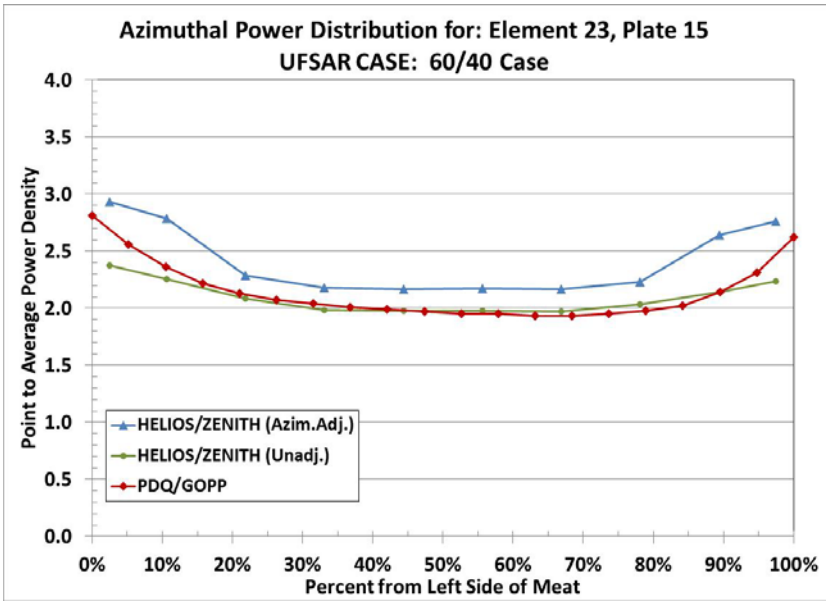

Figure 4.6a. Comparison of plate azimuthal power distribution between PDQ7 and HELIOS for the bounding 70MW test case.

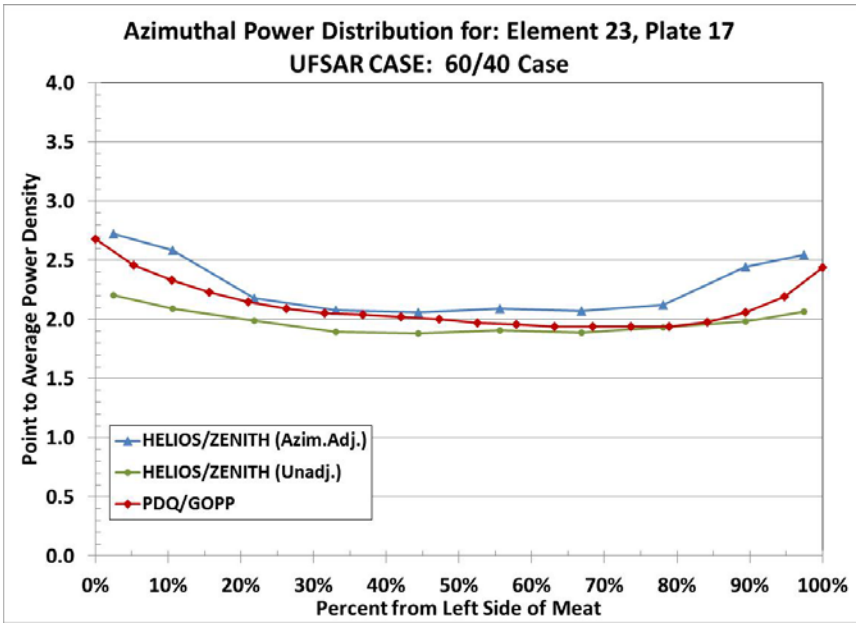

Figure 4.6b. Comparison of plate azimuthal power distribution between PDQ7 and HELIOS for the bounding 70MW test case.

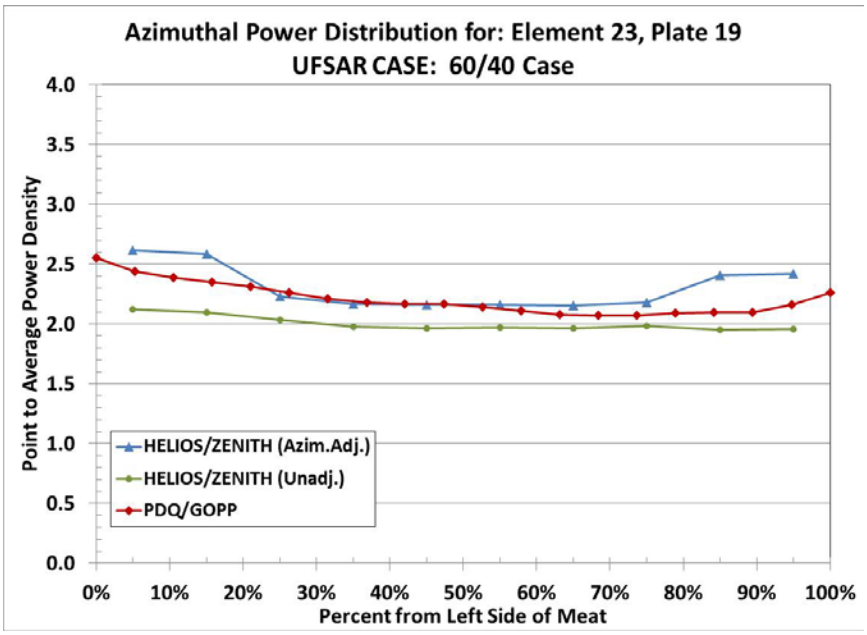

Figure 4.6c. Comparison of plate azimuthal power distribution between PDQ7 and HELIOS for the bounding 70MW test case.

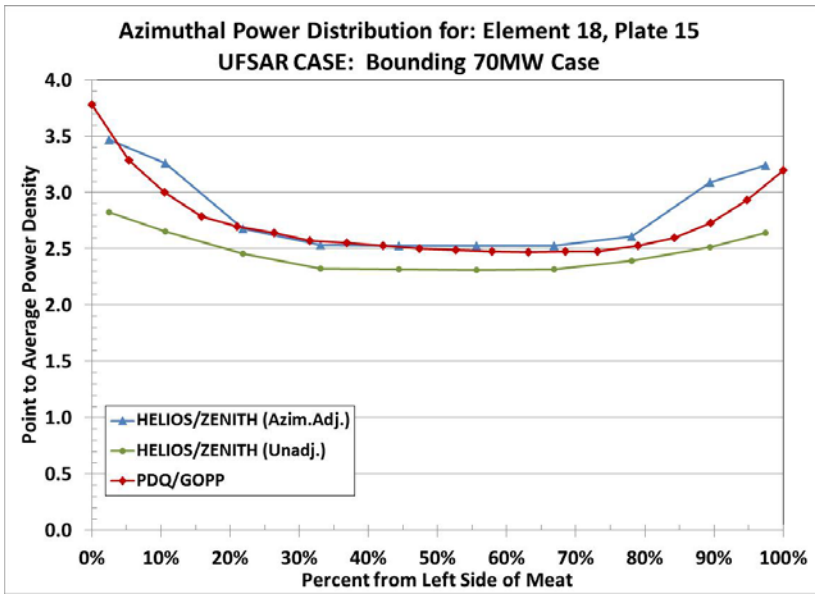

Figure 4.6d. Comparison of plate azimuthal power distribution between PDQ7 and HELIOS for the bounding 70MW test case.

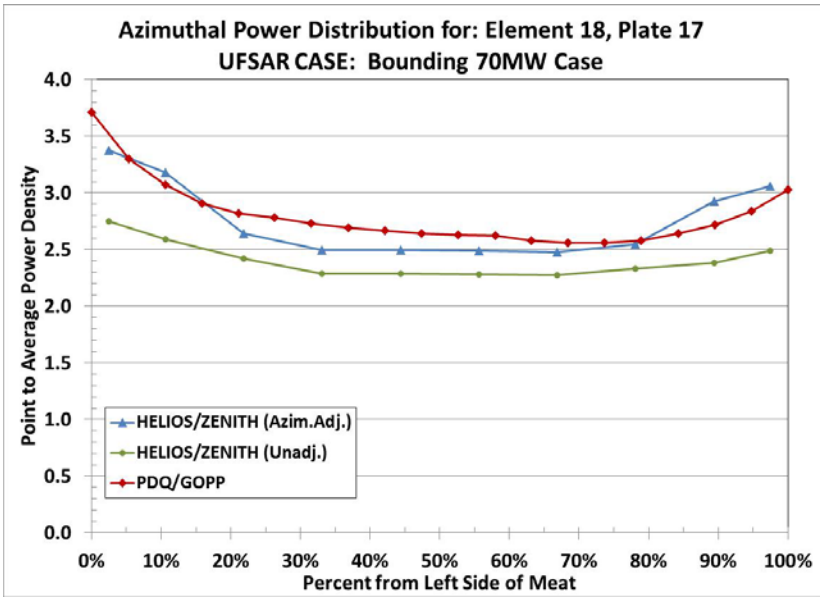

Figure 4.6e. Comparison of plate azimuthal power distribution between PDQ7 and HELIOS for the bounding 70MW test case.

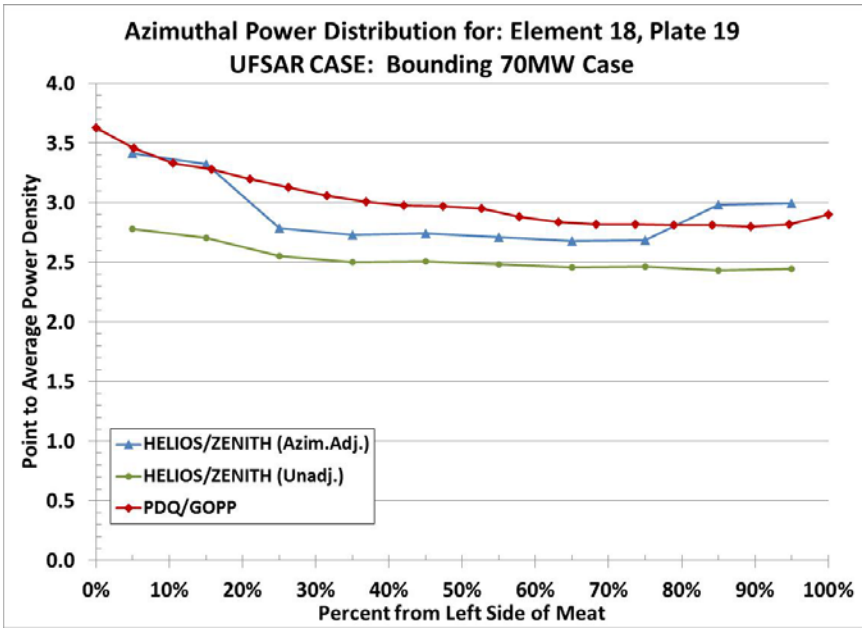

Figure 4.6f. Comparison of plate azimuthal power distribution between PDQ7 and HELIOS for the bounding 70MW test case.

4.3 Lobe Powers for Physics Analyses

Many of the software features of the ATR HELIOS model are designed to support the derived metrics defined by the ATR UFSAR. These metrics are computed using the post processing models defined using the HELIOS/ZENITH code. These metrics cannot be compared with measurement, because they are not measurable quantities. However, assuming that the fundamental k-eff, flux, and cross-section data are valid, then it follows that the derivations performed by ZENITH are also valid, assuming the software/hardware configuration is still valid and error free. In an ideal benchmark, the fundamental k-eff, flux and cross-section data from PDQ7 (and all of the myriad of its support codes) would be input into ZENITH and the ZENITH models tested for

satisfactory configuration testing. However, such a test is not practical given the incongruence between the PDQ7 and HELIOS physics methodologies. Nevertheless, it is instructive to answer the question of "How would HELIOS perform if it were used to prospectively predict ATR cycles and produce the derived data types that are normally expected of PDQ7."

All cycles since Cycle 145A have been followed by HELIOS. Both prospective Physics Analyses and retrospective As-Run calculations have been conducted by HELIOS. The ATR fuel, hafnium (neck shim) and beryllium (reflector) nuclide concentrations have been tracked and inventoried in databases through careful following of these cycles with As-Run analyses using HELIOS. Thus, the nuclide information in Section 3.3 is a result of the As-Run analyses, discussed in greater detail in Section 5.6. However, the primary function of EPP and CFAD is to predict core performance prior to operation of an ATR cycle. Thus, the EPP and CFAD data given in Section 3.7 and Section 3.8 are the result of the HELIOS prospective Physics Analyses.

The HELIOS Physics Analyses for Cycles 145A to 154A have been reconstructed from the exact fuel loading, power levels, neck shim and OSCC configuration used by PDQ7 for prospective Physics Analysis. The fuel, hafnium and beryllium nuclide compositions are from the databases created via the HELIOS As-Runs. The experiment configuration used to create the Physics Analyses is identical to the As-Run Analyses in Section 5.6. Table 4.4 gives a listing of the published PDQ7 Physics Analysis reports used to reconstruct these PDQ7 Physics Analyses with HELIOS.

Table 4.4. PDQ7 Physics ECARs used to create each HELIOS Physics Analysis

ATR Cycle	Engineering Calculation and Analysis Report (ECAR)
145A	ECAR-731
145B	ECAR-807
146A	ECAR-872
146B	ECAR-956
147A	ECAR-1032
148A	ECAR-1158
148B	ECAR-1253
149A	ECAR-1400
149B	ECAR-1524
150A	ECAR-1608
150B	ECAR-1660
151A	ECAR-1742
151B	ECAR-1804
152B	ECAR-2080
153B	ECAR-2200
154A	ECAR-2220

The lobe-power result of this modeling effort is given in Figures 4.7 through 4.12. As can be seen from the curves, the HELIOS lobe power predictions were consistent with the PDQ7 predictions. Just as with the As-Run analyses, the agreement between PDQ7 and HELIOS seems to improve with increasing cycle number. This is the result of the HELIOS fuel inventory improving in fidelity with increasing cycle number. Remember from section 3.3.3, recycle fuel elements originally entering the HELIS framework do not have fission product information because HELIOS uses a lump fission product model, whereas HELOS does not. Also, the recycle fuel elements entering HELIOS from PDQ7 do not have azimuthal detail as this information is not transferred from PDQ7 into HELIOS. Thus, fuel nuclide isotopic detail and azimuthal resolution improves with increasing cycle number.

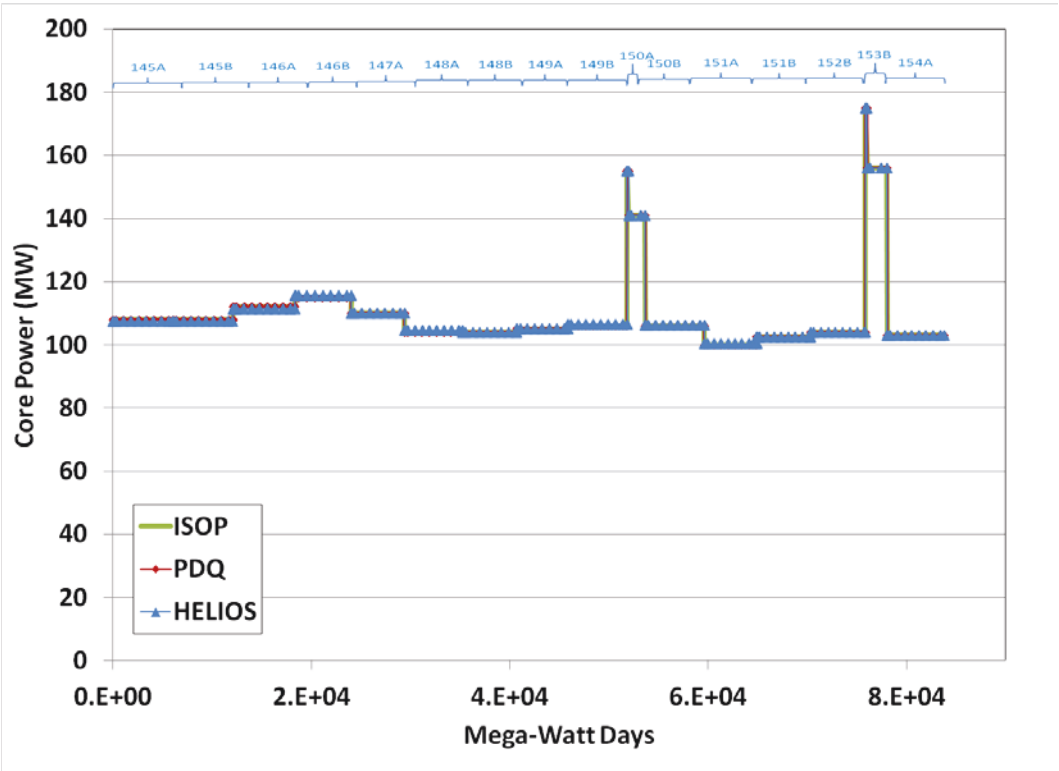

Figure 4.7. Total core power comparison between the ISOP design target, PDQ7 and HELIOS. This plot is provided simply to that the code computed reactor power should explicitly agree with the input specified power.

It is noteworthy that the northeast and southeast lobe powers for the two PALM cycles, 150A and 153B do not agree well between PDQ7 and HELIOS. However, the agreement between HELIOS and ASUDAS, See Section 5.6, is much greater. The differences between PDQ7 and HELIOS can be ascribed to the differences between the diffusion and transport theory. In a PALM cycle, the fuel loading of fresh fuel elements is much heavier in the southern lobes. In the case of Cycle 153B a hafnium fixed shim was used in the H-facility. Also, the OSCC rotation is much more aggressive in a PALM cycle to try to achieve a significant lobe-power split between northern and southern lobes. With these extreme variations of moderator-to-absorber ratios across the core, it should be expected that the angular dependency of the flux is non-isotropic and varies, particularly in the areas of the core where there is a steep power gradient along the fuel serpentine.

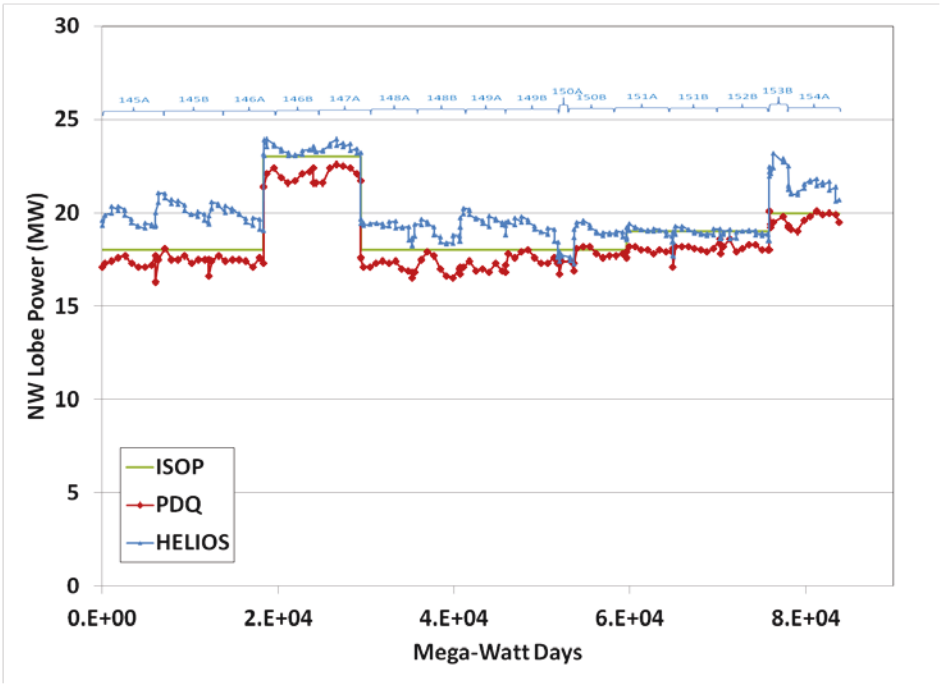

Figure 4.8. Northwest lobe power comparison between the ISOP design target, PDQ7 and HELIOS

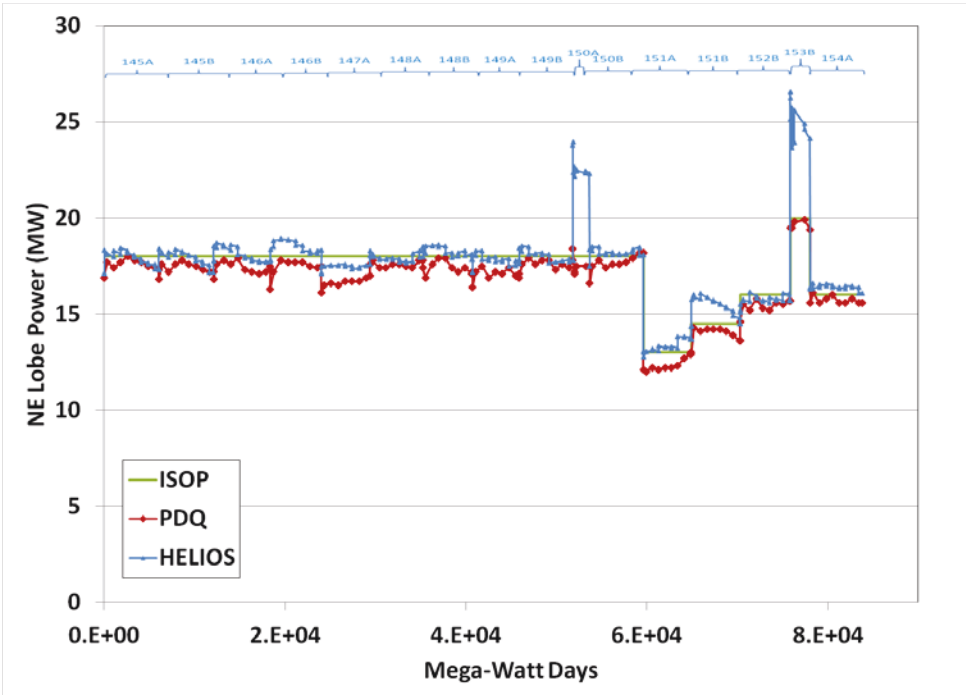

Figure 4.9. Northeast lobe power comparison between the ISOP design target, PDQ7 and HELIOS

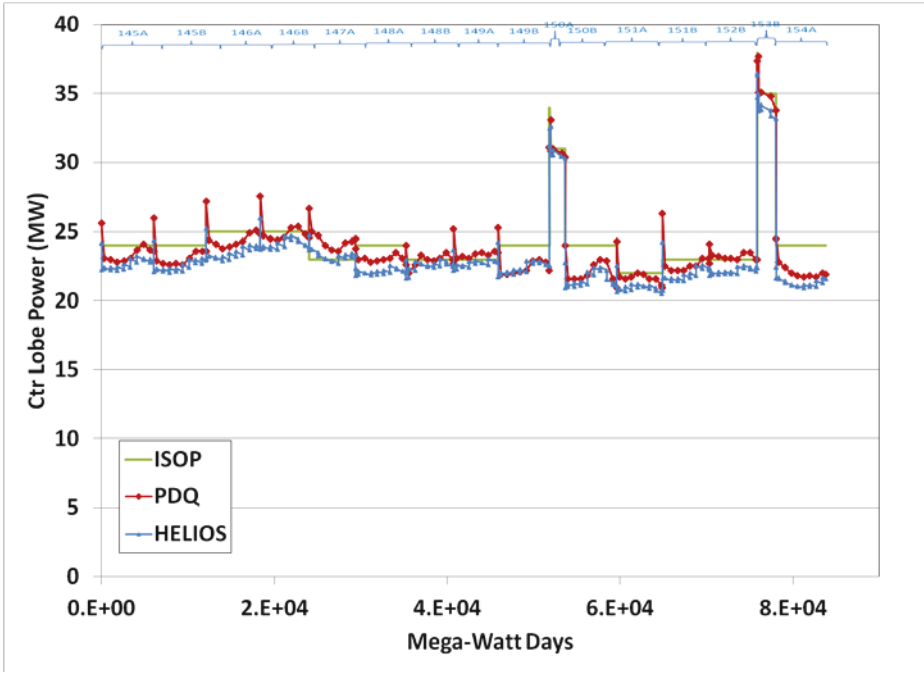

Figure 4.10. Center lobe power comparison between the ISOP design target, PDQ7 and HELIOS

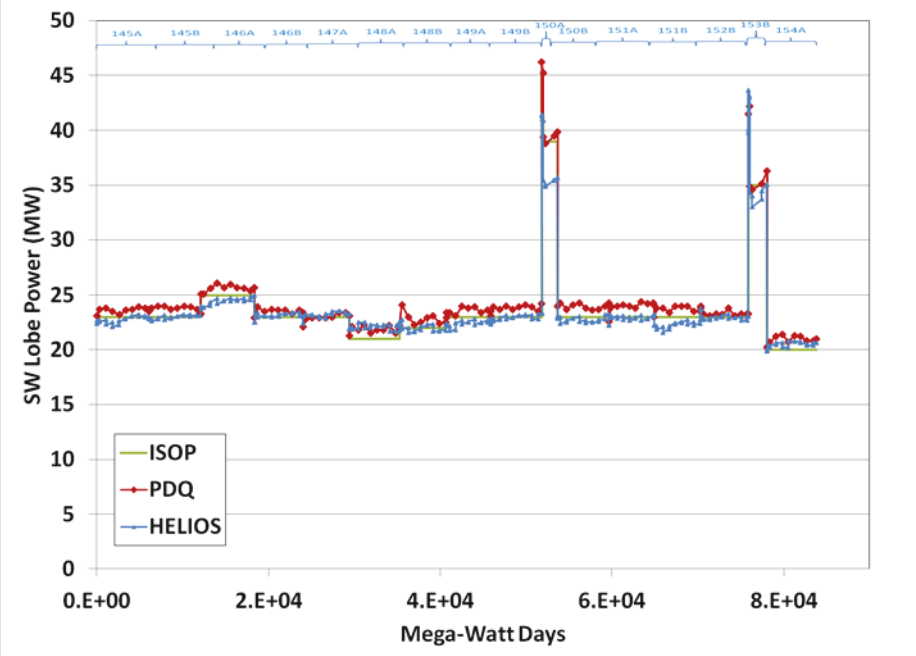

Figure 4.11. Southwest power comparison between the ISOP design target, PDQ7 and HELIOS

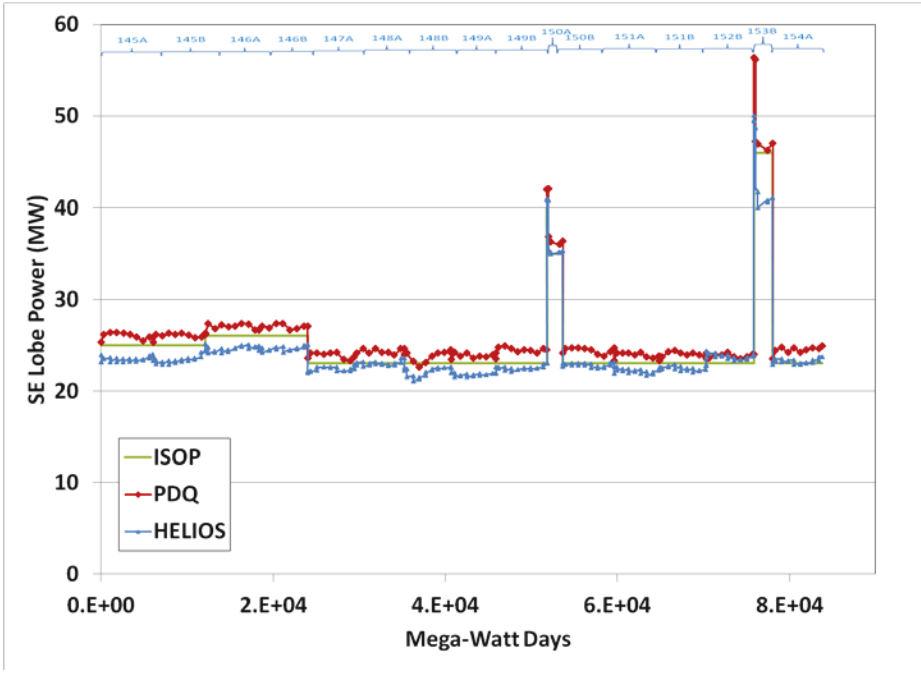

Figure 4.12. Southeast power comparison between the ISOP design target, PDQ7 and HELIOS

5.0 VALIDATION PROTOCOLS FOR THE NEW METHODOLOGY

David W. Nigg and Joseph W. Nielsen

Validation protocols are required for qualifying the nuclear modeling software used to routinely establish the physics basis of each for operating the ATR as well as for many other purposes. An extensive series of neutron spectrum, fission power distribution, and critical shim prediction validation protocols that have been developed for the new ATR and ATRC models (Nigg and Steuhm, 2012, 2013). Ultimately, a complete set of standard validation measurement protocols using neutron activation spectrometry in both the ATRC and, when feasible, in the ATR itself will be available for future code and model validation purposes as needed. The work described here builds on previous related INL experience at the ATR (e.g. Rogers and Anderl, 1995) as well as at other research reactor and accelerator facilities worldwide (e.g. Nigg et al., 2000). It is also intended that detailed Evaluated Benchmarks based on these measurements will ultimately be published for use by the international community under the auspices of the Organization for Economic Cooperation and Development (OECD, 2012). Taken together these protocols will form the basis for a relatively simple, robust, and repeatable validation procedure that is applicable as needed to all of the transport codes and associated models that are included in the new suite of ATR core physics modeling tools. Additional validation capabilities focused on the depletion models, using post-irradiation burnup measurements for selected fuel elements, are anticipated in the longer term as well. This section summarizes several new components of the overall validation protocol development process that were completed during 2014.

5.1 Revisiting the Fission Power Distributions for the 1994 CIC Configuration

The original HELIOS model of the ATR 1994 CIC configuration (Figure 5.1) was developed by Studsvik Scandpower and INL in collaboration under the auspices of the INL/Studsvik Center for Nuclear Systems Design and Analysis. This model, with many refinements since its initial creation, reflects a well-defined critical configuration of the ATR at the time of the earliest historical measurements for which refereed benchmark measurement data and a corresponding baseline MCNP5 model have been widely published in the internationally-defined format for this type of integral reactor physics validation data (Kim et al., 2008). Selected results from the HELIOS model have been compared against the reported measurements as well as against results from the equal-fidelity NEWT code and the higher-fidelity MCNP5 code to demonstrate the basic feasibility of the HELIOS system for the intended ATR modelling application.

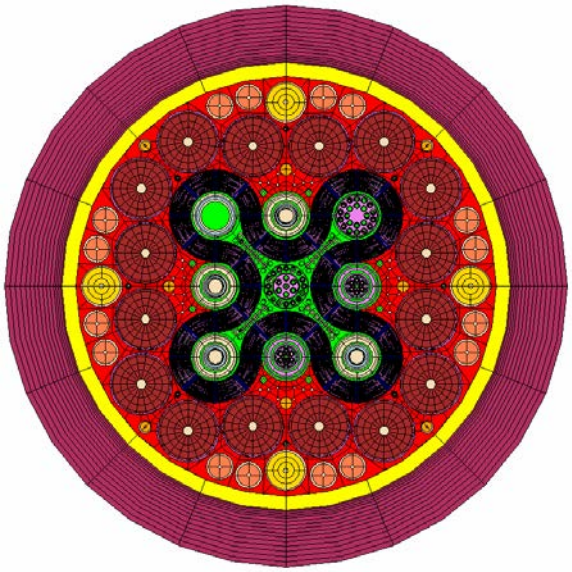

Figure 5.1. HELIOS ATR model geometry - 1994 CIC.

A corresponding NEWT model of the ATR (Figure 5.2) is likewise based on the information provided in the ATR 1994 CIC criticality benchmark documentation (Kim et al., 2008). The NEWT model uses Mark VII fuel element properties represented explicitly as 19-plate fuel elements (Figure 5.3) just as was done in the HELIOS model. The experiment locations in the reactor contain the materials as designated in the ATR 1994 CIC benchmark specification. A corresponding KENO6 model of the 1994 CIC configuration was also created as part of this cross-validation exercise.

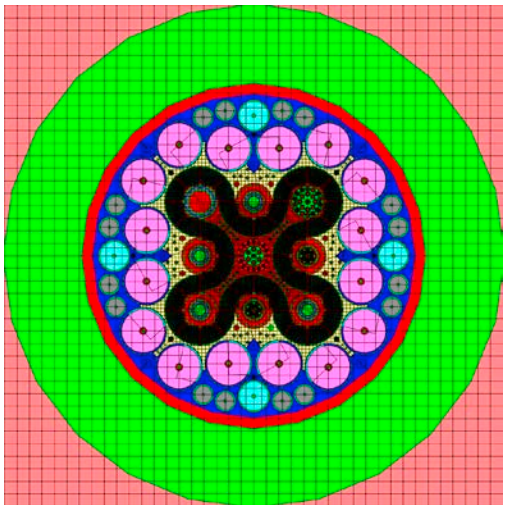

Figure 5.2. NEWT model of the 1994 ATR CIC core configuration (Core Number: 103A-2, MCNP5 Reference K_{eff}=0.9968).

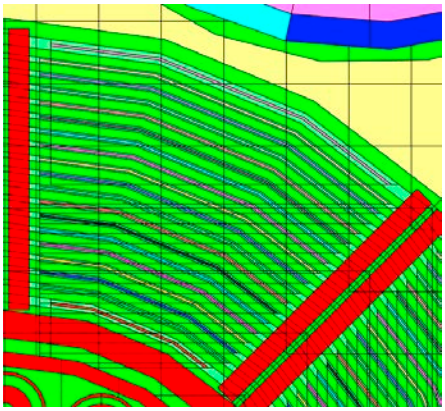

Figure 5.3. NEWT 19-plate fuel element detail.

The HELIOS results successfully demonstrated reasonable eigenvalues (K_{eff} =1.0306 with no axial leakage and K_{eff} = 0.9967 with critical axial leakage) relative to the MCNP5 baseline. Reasonable relative fuel element-to-element power distributions were also demonstrated. Figure 5.4 shows the HELIOS and NEWT results for the element powers, along with the measurements and the results of the baseline reference MCNP5 calculation from the benchmark documentation (Kim et al, 2008). It can be seen that the computed element-to-element profiles are generally within approximately 5% of each other and within 10% of the measurements, which have experimental uncertainties reported as 5% (1σ).

Figure 5.5 shows the results of a more-rigorous, least-squares based statistical adjustment analysis of the HELIOS element power results relative to the measurements using an extension of the ASTM-944 spectral unfolding methodology that was specifically developed for this type of ATR fission power distribution analysis (Nigg and Steuhm, 2012). The reduced uncertainties for the adjusted element powers ranged from 3.1% to 3.7%. The adjustments ranged from -11% in Element 5 to +7.5% in Element 13, and 68% of the adjustments (i.e. those within a 1 standard deviation band around the mean adjustment) were within ±5%, indicating a possible degree of conservatism in the *a priori* uncertainties ($1\sigma = 10\%$) assumed for the computed element powers. Note also that the mean adjustment was essentially zero (within round-off error for the number of significant figures provided), reflecting the fact that that the calculation was normalized to the total measured power, taken as the sum of the 40 measured element powers.

Figures 5.6 -5.8 show the results of corresponding least-squares statistical analyses for the cases where the *a priori* element power calculations were done with NEWT, MCNP5 and KENO6, respectively. As anticipated, the MCNP5 results had the smallest standard deviation of adjustments about the mean adjustment. The reduced uncertainties for the adjusted powers for all cases were all in the range of 3%-4%, similar to the case with HELIOS. In all cases the standard deviations of the adjustments were also once again well within the assumed *a priori* uncertainty of the calculations. It is also interesting to note that the PDQ results for the element powers in this particular case had a remarkably small standard deviation of the adjustments (1.9% about the mean adjustment), slightly less than even the MCNP5 results. However, it must be recognized that, in contrast to all of the other modeling codes, PDQ is not computing the powers from first principles. Therefore the degree to which the excellent statistical consistency of the PDQ results and the measurements that was demonstrated in this case is dependent on the various empirical and equivalence theory based corrections that are inherent in the PDQ model is an important consideration that is not well documented in the available early ATR physics reports. Thus it is not clear just how far the range of applicability of the PDQ methodology can be extrapolated beyond this specific case.

We also note that the radial plate-to-plate power profiles for the fuel elements, computed by HELIOS and shown in Figure 5.9, are in very close agreement with results from the other codes (although for clarity only the comparison with NEWT is shown in the cited illustration).

Finally, although the SERPENT code is not yet formally a part of the updated ATR physics methods suite, an analysis of the element power distribution computed by this particular code (DeHart, 2012b) is included for informational purposes. Figure 5.10 shows the SERPENT geometry for this configuration and Figure 5.11 shows the results of the corresponding least-squares power distribution analysis.

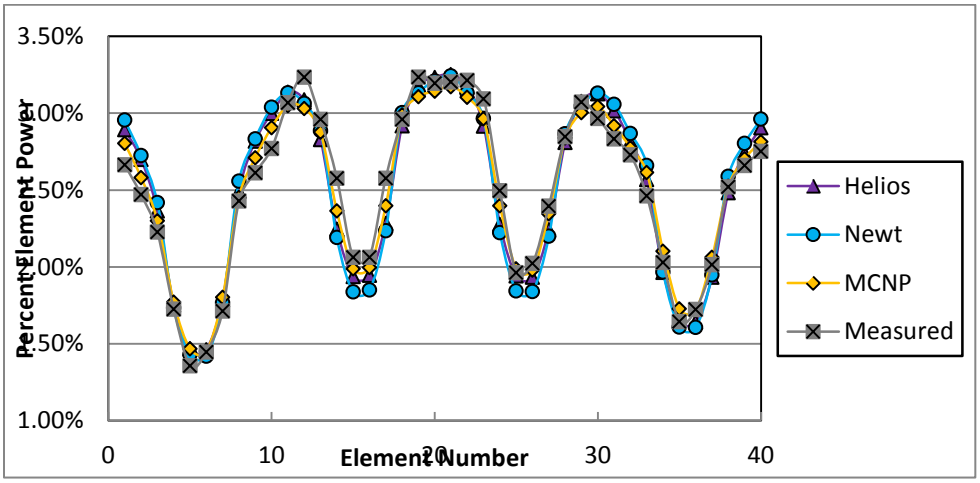

Figure 5.4. Fuel element powers (element % of total core power). Measurements (Kim et al., 2008) vs. results from the HELIOS, NEWT and MCNP ATR models for the 1994 CIC.

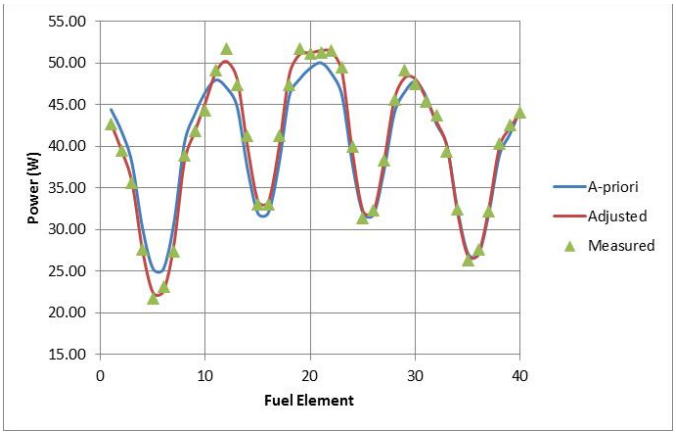

Figure 5.5. Fuel element fission rate distribution adjustment results for ATR 94CIC (HELIOS *a priori).* The standard deviation of the adjustments about the mean adjustment was 5.0%.

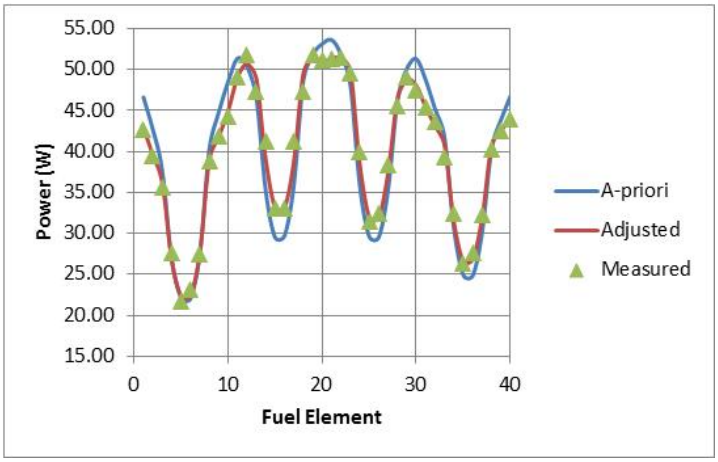

Figure 5.6. Fuel element fission rate distribution adjustment results for ATR 94CIC (NEWT *a priori).* The standard deviation of the adjustments about the mean adjustment was 5.9%.

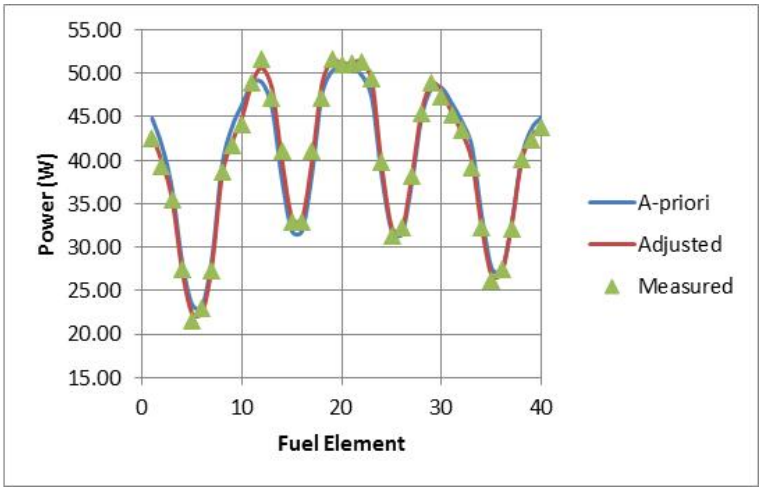

Figure 5.7. Fuel element fission rate distribution adjustment results for ATR 94CIC (MCNP *a priori).* The standard deviation of the adjustments about the mean adjustment was 3.1%.

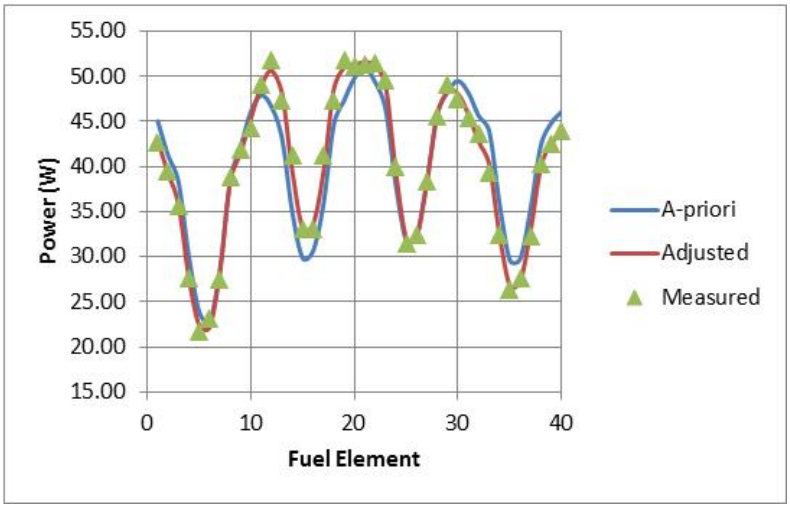

Figure 5.8. Fuel element fission rate distribution adjustment results for ATR 94CIC (KENO6 *a priori).* The standard deviation of the adjustments about the mean adjustment was 6.5%.

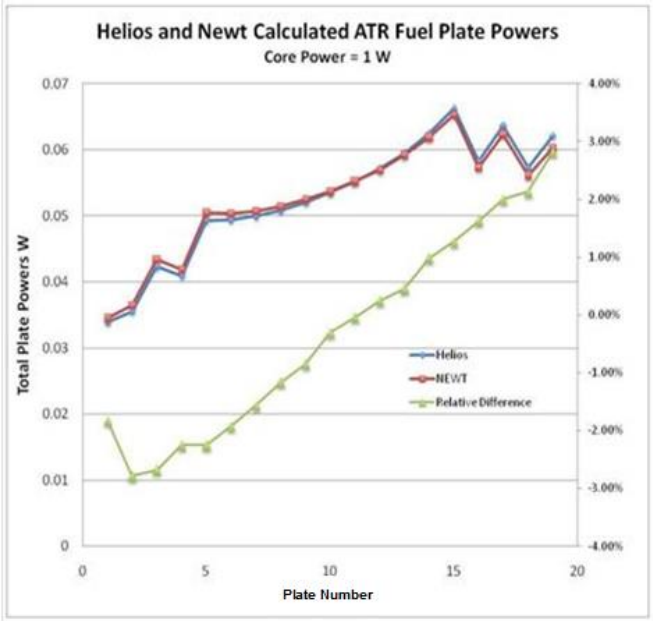

Figure 5.9. Relative plate powers (left axis) for the HELIOS and NEWT ATR 94 CIC Models. Data for each plate are averaged over all 40 fuel elements. Percentage difference between HELIOS and NEWT results is shown in the right axis.

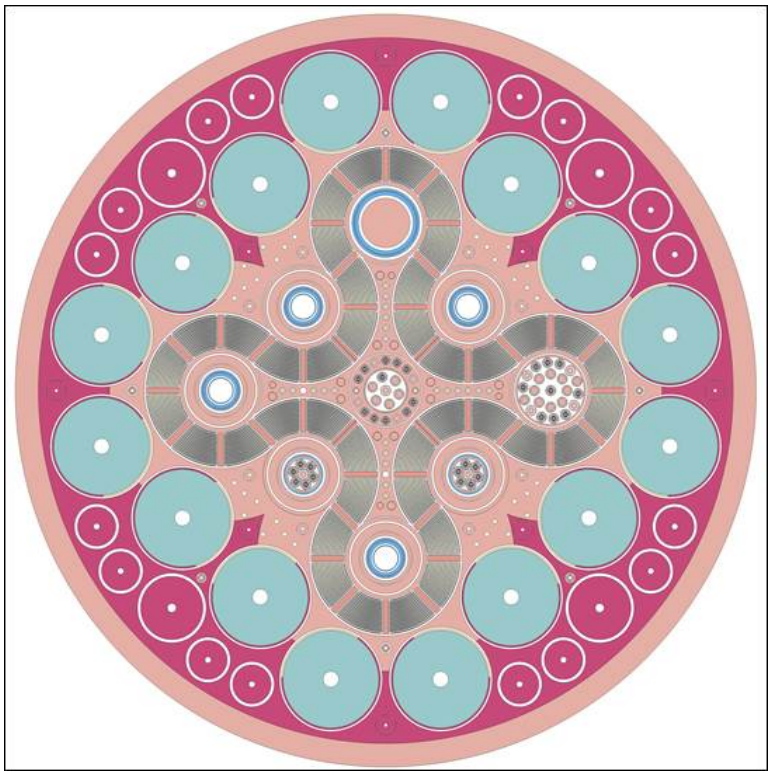

Fig. 5.10. SERPENT geometry for the ATR 94-CIC configuration (x-y slice at the axial midplane).

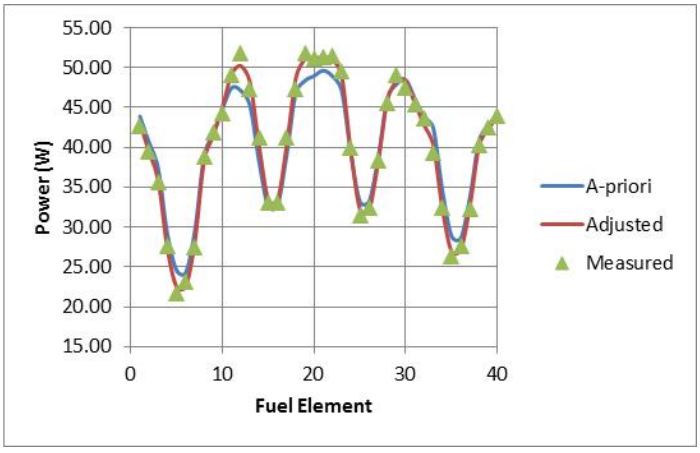

Figure 5.11. Fuel element fission rate distribution adjustment results for ATR 94CIC (SERPENT *a priori)*. The standard deviation of the adjustments about the mean adjustment was 4.1%.

5.2 ATRC Validation Experiments Specific to the ATR Core Modeling Update Project

Some basic equipment for activation experiments in the ATRC Northwest Large In-Pile Tube (NW LIPT) and in the surrounding NW Lobe core fuel elements as well as in the diametrically opposite SE Lobe fuel elements was fabricated during 2010. Initial scoping measurements to determine neutron flux spectra in these regions were completed during 2011. Corresponding fuel element fission power distribution measurements throughout the ATRC core were also completed during this experiment series using standard ATRC "flux run" protocols. There

have been five (of six planned) ATR Core Modeling Update project-specific ATRC validation experiments completely analyzed so far. Results of the first four have been documented extensively in the 2012 and 2013 Annual reports for the Modeling Update Project (Nigg and Steuhm, 2012, 2013). Measured results and corresponding statistical analyses for the fifth experiment are presented here. The sixth experiment will be completed during 2015.

This section is followed by an extensive update of a previous analysis (Nigg and Steuhm, 2013) of some additional closely-related fission power distribution measurements made during 2012 in the ATRC to support a "depressurized" ATR cycle (152A) that was conducted late in that year. The depressurized run was a series of nuclear requalification tests for calibrating the PDQ7 based methodology (as well as the ATR instrumentation systems) to support an unusually complex experiment configuration associated with Cycle 152B. These measurements were unanticipated at the beginning of the ATR Core Modeling Update Project, but they have provided some additional extremely useful validation data for the overall protocol.

5.2.1. Spectral Measurements in the ATRC Southeast In-Pile Tube: AFM5 - AFM6 .

As noted earlier, the ATR Core Modeling Update Project includes a total of six project-specific code and model validation experiments. Four of the six LEP-specific experiments were completed prior to 2014. The fifth planned LEP-specific validation experiment was conducted in the ATRC very late in 2013. This experiment (referred to here as "Irradiation 5") used the same NW LIPT hardware as was used for Irradiations 1-3 (Nigg and Steuhm, 2012), with minor changes in specific loading of the NW LIPT hardware. In addition, detailed neutron spectrum measurements were made in the Southeast IPT during Irradiation 5 using new hardware inserts fabricated for this purpose during 2011.

Figure 5.12 shows the loading of the NW LIPT foil positioning strips for Irradiation 5. In this case the foil packages consisted only of duplicate bare and cadmium –covered gold foils to provide a simple 2-group confirmation of the neutron spectrum in the NW LIPT that was measured during Irradiations 1-3. Au/Cu flux wires were also loaded positioning strips as before, but only on one side of each foil positioning strip. Each corresponding wire position on the other side of each positioning strip (see Figure 3.3 for detail) contained a uranium-aluminum flux wire, with 10% by weight ^{235}U. These latter wires were identical to the wires used for the core fuel element fission power distribution measurements described for the depressurized run support experiment (see Section 5.3). The foil positioning strips were then loaded into the NW LIPT insert in the same manner as for Irradiations 1 and 2, with solid dummy strips in the other 8 positions.

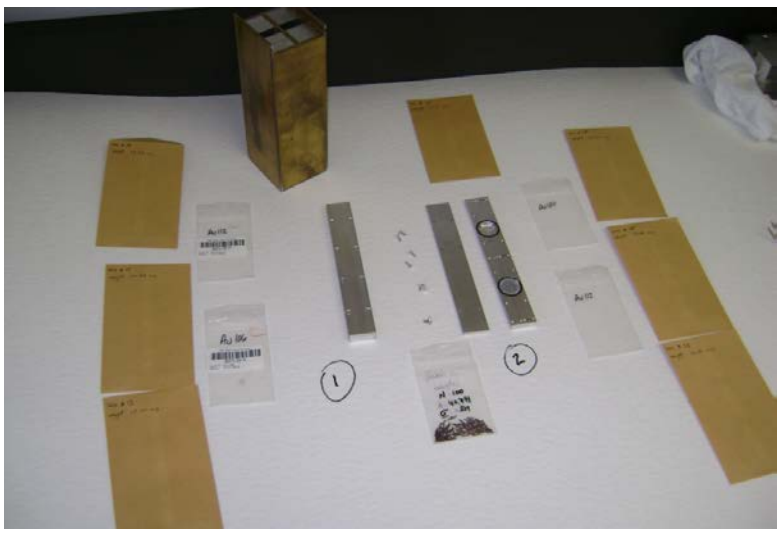

Figure 5.12. Northwest Large In-Pile Tube Fittings and Foil Positioning Strips for Irradiation 5.

Figure 5.13 shows the new SE IPT insert with a new solid aluminum fitting designed to hold a single foil positioning strip. This strip was loaded with a set of cadmium-covered indium, gold, tungsten, manganese, copper, titanium, nickel, zinc, iron and niobium foils in one foil position and a set of bare gold and manganese foils in the other foil position. In addition to obtaining detailed spectral data for the SE IPT this arrangement was also intended to test the ability of the threshold foils (In, Ti, Ni, Zn, Fe, Nb) to detect the high-energy part of the spectrum without the use of the boron sphere that was used in Irradiation 3 to suppress resonance interactions.

Figure 5.14 shows some additional detail of the foil positioning strip and the solid insert fitting for the SE IPT. Figure 5.15 shows a close up of the foil positioning strip, with the Au/Cu and the ^{235}U/Al wires in place at each of the three axial locations. Figure 5.16 shows the assembled insert fitting as it slides into the cylindrical SE IPT insert.

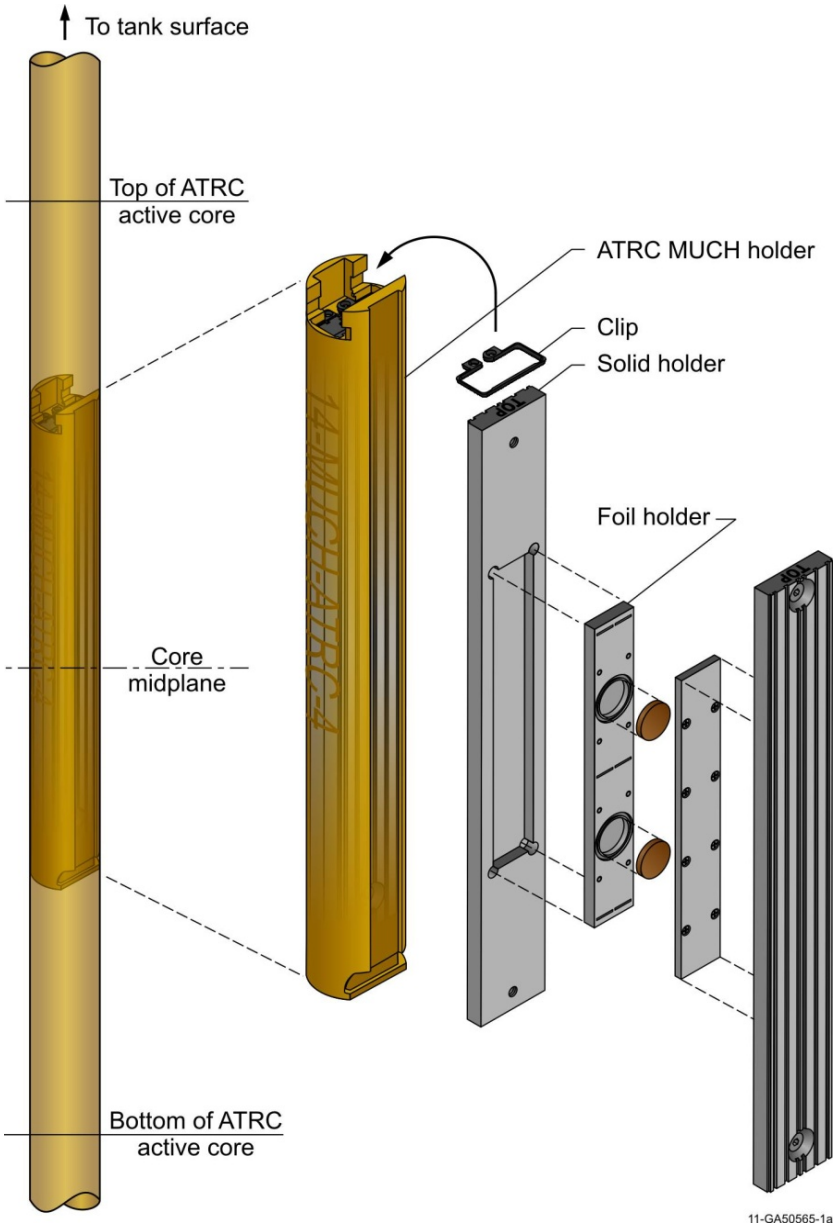

Figure 5.13. Southeast In-Pile Tube Insert Assembly (Low Water Fraction).

Figure 5.14. Foils, Foil Positioning Strip, and Insert Fitting for Southeast in-Pile Tube – Irradiation 5.

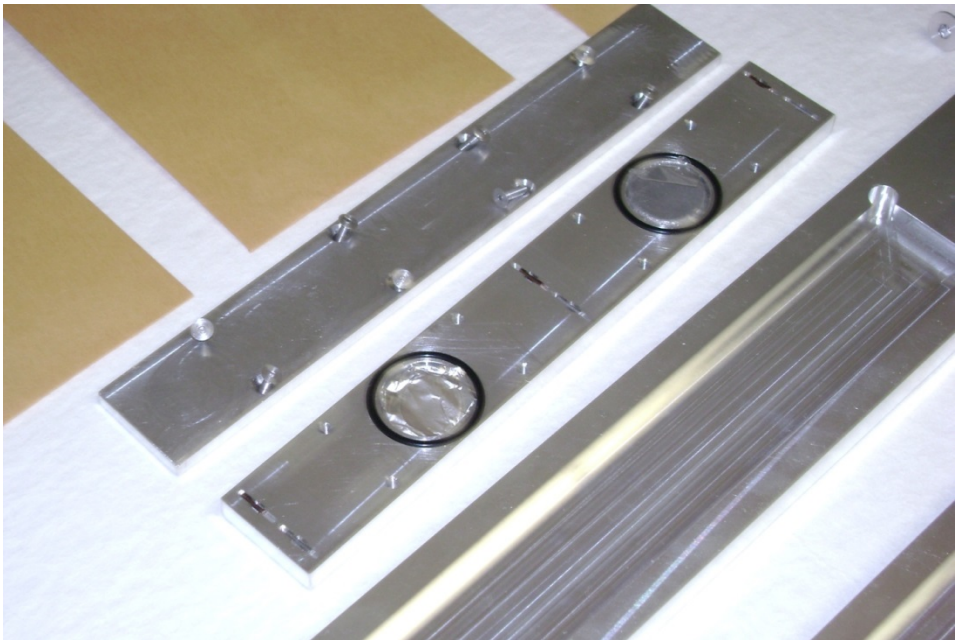

Figure 5.15. Detail of Foil and Flux Wire Positioning Strip for Southeast In-Pile Tube – Irradiation 5.

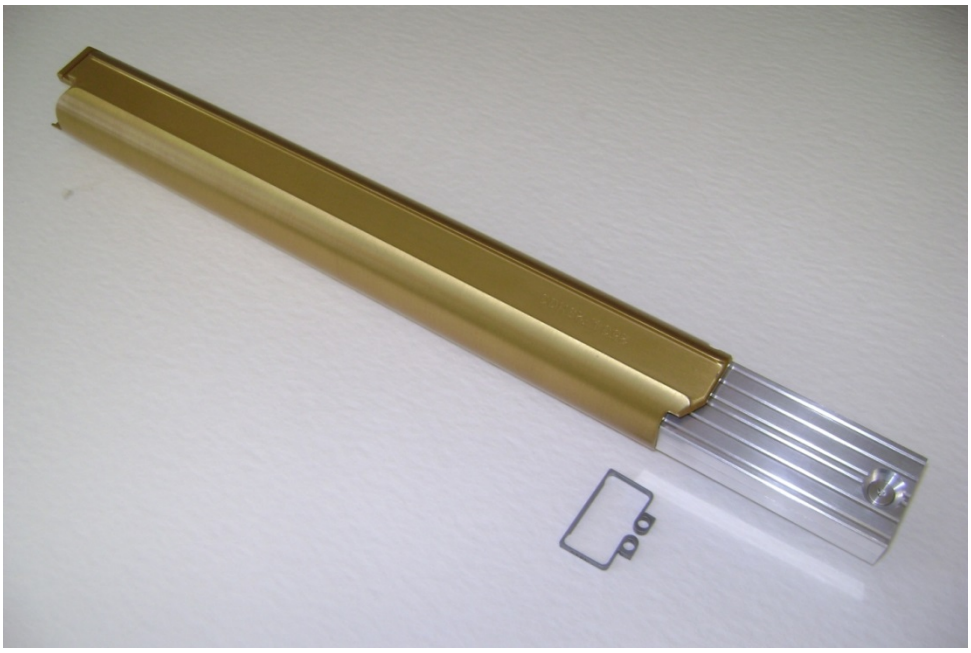

Figure 5.16. Assembled Hardware for Southeast In-Pile Tube – Irradiation 5

The Irradiation 5 experimental hardware for both the NW LIPT and the SE IPT was assembled in early 2012 and Irradiation 5 was successfully conducted on August 13, 2013. All 20 even-numbered core fuel elements were instrumented with three Au/Cu wires each along the central rib in the same manner as was the case for the instrumented fuel elements in Irradiation 4. Irradiation 5 was intended to provide confirmatory spectral data for the NW LIPT as well as detailed new spectral data for the SE IPT. In addition, this experiment provided some experience with pairing of the Cu/Au wires with the ^{235}U/Al wires for the purpose of exploring techniques for statistically combining the ^{235}U fission rate with the Au and Cu capture rates to produce an estimate for the adjusted neutron flux spectrum at these positions that is also tied to the local fission rate. Some results for the basic measured activation responses of primary interest are summarized below.

Table 5.1 shows the measured results for the foil interaction rates in the southeast IPT. The measured rates for the Northwest LIPT are also shown for comparison. It should be noted that the southeast lobe of the ATRC typically operates at a power level that is about 35% higher than that of the northwest lobe in the case of these validation experiments. Taking this into account it can be seen that the spectrum in the southeast lobe still appears to be somewhat harder than that in the northwest lobe. This is not unexpected, and will be discussed in further detail below

Table 5.1. Measured saturation activities for the foils irradiated in the southeast in-pile tube, Irradiation 5 and in the northwest large in-pile tube, Irradiations 1 and 3.

Interaction	Measured σΦ (Southeast)	±1σ (%)	Spectral Index (SE)*	Measured σΦ (Northwest)***	Spectral Index (NW)	Rate Ratio SE/NW
^{93}Nb (n, 2n)	3.66E-19	17.79	2.06E-06	2.64E-19	2.44E-06	1.39
^{54}Fe (n,p)	1.04E-16	14.65	5.86E-04	4.10E-17	3.80E-04	2.54
^{56}Fe (n,p)	8.58E-19	7.31	4.82E-06	5.12E-19	4.74E-06	1.68
^{64}Zn (n,p)	3.59E-17	2.52	2.02E-04	2.05E-17	1.90E-04	1.75
^{58}Ni (n,p)	9.66E-17	2.51	5.43E-04	5.72E-17	5.30E-04	1.69
^{47}Ti (n,p)	1.86E-17	2.52	1.04E-04	1.17E-17	1.08E-04	1.59
^{46}Ti (n,p)	1.06E-17	42.61	5.95E-05	5.00E-18	4.63E-05	2.12
^{48}Ti (n,p)	2.52E-19	7.15	1.42E-06	1.35E-19	1.25E-06	1.87
^{115}In (n,n')	2.38E-16	2.05	1.34E-03	1.24E-16	1.15E-03	1.92
^{55}Mn(n, γ)	1.81E-15	2,.29	1.02E-02	9.81E-16	9.08E-03	1.84
^{186}W(n, γ)	5.33E-14	2.11	2.99E-01	2.83E-14	2.62E-01	1.89
^{197}Au (n, γ)	9.18E-14	2.29	5.16E-01	5.00E-14	4.63E-01	1.84
^{115}In (n, γ)	1.44E-13	2.02	8.11E-01	8.30E-14	7.69E-01	1.74
^{55}Mn(n, γ)	1.30E-14**	2.03	7.28E-02	8.50E-15*	7.87E-02	1.52
^{197}Au (n, γ)	1.78E-13**	2.36	1.00E+00	1.08E-13*	1.00E+00	1.65

* Spectral index is defined here as the ratio of the activity of a particular foil to that of a bare Au foil.
** Bare foils, unshielded by cadmium.
*** Nigg and Steuhm (2012)

Table 5.2 and Figures 5.17-5.18 show an 8-group adjusted neutron spectrum for the SE IPT corresponding to the foil measurement results of Irradiation 5. The adjusted spectrum was determined using the least-squares methodology outlined in a previous Annual Report (Nigg and Steuhm, 2012) for the overdetermined case with the *a priori* flux covariance matrix included, assuming 10% fully-correlated (normalization) uncertainty, 20% partially-correlated random uncertainty with correlation matrix parameters θ=0.8 and Γ=4. The adjustment calculations were performed using an Excel™ spreadsheet implementation of the governing matrix equations. All 15 measured activation responses listed in Table 5.1 were used for the adjustment. The elements of the 15 x 8 coefficient matrix as well as the *a priori* flux vector for the adjustment procedure were computed using an MCNP5 model of the experimental apparatus. The bias of the *a priori* model for the conditions being calculated is the difference between the *a priori* flux and the adjusted flux with its corresponding uncertainty. It can be seen in this case that the adjustment tended to slightly increase the fast flux and slightly reduce the thermal flux. The adjusted fast/thermal flux ratio is slightly larger than the corresponding parameter for the NW LIPT (Irradiations 1-3 (Nigg and Steuhm, 2012), confirming that the spectrum is slightly harder in the SE IPT.

Table 5.2. Eight-group neutron flux spectrum from foils – Southeast In-Pile Tube, Irradiation 5, 605.5 W. MCNP5 *a priori.* Combined correlated and uncorrelated uncertainty of the *a priori* fluxes is 22.4%.

Energy Group	Upper E (eV)	Lower E (eV)	*A priori* Flux (n/cm**2-s)	Adjusted Flux (n/cm**2-s)	Propagated Uncertainty (1σ)
1	2.00E+07	1.92E+05	4.57E+08	4.51E+08	1.67
2	1.92E+05	2.97E+05	1.20E+09	1.32E+09	6.43
3	2.97E+05	4.54E+02	1.49E+09	1.64E+09	42.46
4	4.54E+02	3.73E+01	4.60E+08	5.41E+08	9.88
5	3.73E+01	1.07E+01	2.30E+08	2.30E+08	2.45
6	1.07E+01	1.86E+00	3.13E+08	2.81E+08	2.92
7	1.86E+00	4.14E-01	2.88E+08	2.09E+08	2.44
8	4.14E-01	1.0000E-05	1.35E+09	1.21E+09	2.22
Total Fast Flux (Groups 1-7)	2.00E+07	4.14E-01	4.44E+09	4.67E+09	
Fast/Thermal Ratio			3.29	3.85	

Note: X^2 per degree of freedom = 2.3

Table 5.3 shows some preliminary measured activation rates for the Au/Cu flux wires rates and the corresponding spectral indices that were measured for both southeast IPT and the NW LIPT. It can be seen that the spectral indices for the southeast IPT are somewhat larger than for the northwest LIPT, indicating a somewhat harder spectrum, consistent with the results obtained with the foil packages.

Figure 5.19 shows the MCNP5 *a priori* , adjusted, and measured element fission powers for Irradiation 5, plotted as a function of element number around the serpentine azimuthal axis of the core. All adjustments are seen to be consistent with the stated uncertainty of the *a priori* element powers, as expected, and the adjusted uncertainties for all elements are reduced from the *a priori* uncertainties, again as expected. Figure 5.20 shows the same fuel element power distribution information for the case where the HELIOS code is used for the *a priori* power distribution calculation. In both cases, adjustments are within the stated uncertainties and excellent consistency is observed.

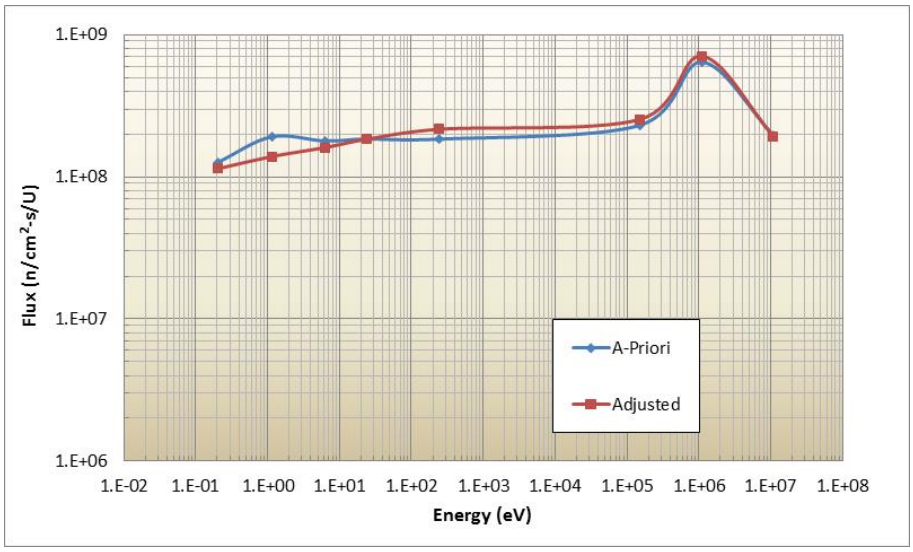

Figure 5.17. Eight-group spectrum adjustment for Experiment 5 (MCNP *a-priori*), corresponding to the group flux data in Table 5.2 (θ=0.8, Γ=4). The *a priori* normalization uncertainty is assumed to be 10% and the *a priori* random uncertainty is assumed to be 20%. Combined correlated and uncorrelated uncertainty of the *a priori* fluxes is 22.4%.

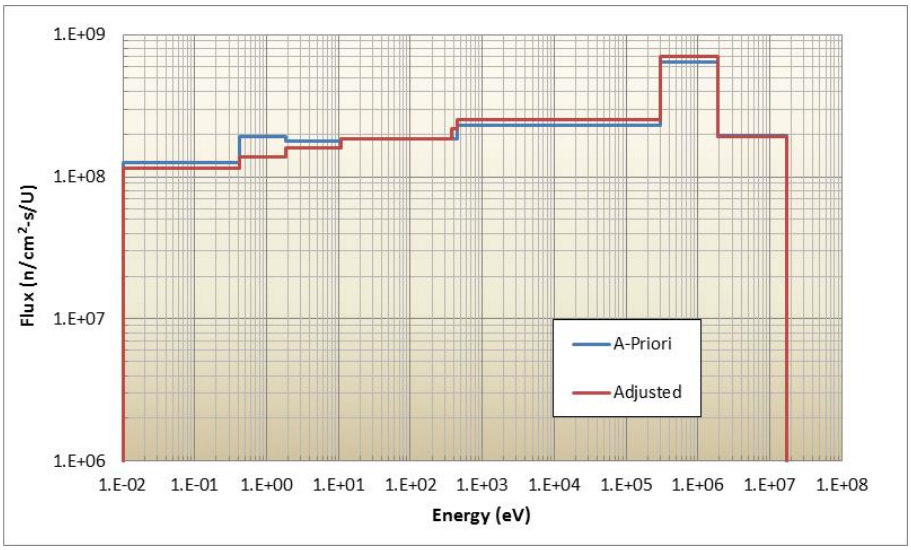

Figure 5.18. Eight-group spectrum adjustment for Experiment 5, histogram format.

Table 5.3. Measured saturation activities for the Au/Cu wires irradiated in the southeast and northwest in-pile tubes, Irradiation 5.

Wire ID	**SE Top**	**SE Top**	**SE Middle**	**SE Middle**	**SE Bottom**	**SE Bottom**
Nuclide	Au	Cu	Au	Cu	Au	Cu
Measured σΦ	2.78E-13	4.00E-15	2.96E-13	4.30E-15	2.79E-13	4.25E-15
±1σ (%)	2.73	2.67	2.51	2.62	3.04	2.60
Spectral Index (Au/Cu)	69.54		68.99		65.61	
Wire ID	**NW Top Wire 1**	**NW Top Wire 1**	**NW Middle Wire 1**	**NW Middle Wire 1**	**NW Bottom Wire 1**	**NW Bottom Wire 1**
Nuclide	Au	Cu	Au	Cu	Au	Cu
Measured σΦ	1.90E-13	3.76E-15	1.75E-13	3.07E-15	2.01E-13	4.02E-15
±1σ (%)	2.62	2.72	2.84	2.70	2.54	2.59
Spectral Index (Au/Cu)	50.61		56.86		49.91	
Wire ID	**NW Top Wire 2**	**NW Top Wire 2**	**NW Middle Wire 2**	**NW Middle Wire 2**	**NW Bottom Wire 2**	**NW Bottom Wire 2**
Nuclide	Au	Cu	Au	Cu	Au	Cu
Measured σΦ	1.92E-13	3.86E-15	1.81E-13	3.18E-15	1.89E-13	3.89E-15
±1σ (%)	2.66	2.73	2.68	2.79	2.79	2.61
Spectral Index (Au/Cu)	49.69		57.03		48.59	

Figure 5.21 shows a variation of the SE IPT hardware that has been fabricated for Irradiation 6, which is scheduled for late 2014. In this case the insert fitting that holds the foil positioning strip will be a light aluminum framework with approximately 80% water in the same volume as the solid holder used for Irradiation 5. A large water fraction makes these flux trap positions more uniform in the axial dimension, with less axial streaming and attenuation of thermal neutrons than is the case for the solid insert fitting used in Irradiation 5. In the case of the NW LIPT insert, the same higher water fraction can be achieved by simply removing the 8 dummy strips visible in Figure 5.12. These modifications should make Irradiation 6 somewhat more suitable as a validation benchmark for the two-dimensional transport codes in the suite. Furthermore, Irradiations 5 and 6, taken together, will provide a validation benchmark for quantification of spectral shifts in both the small and large in-pile tubes. This will be of particular interest to the Office of Naval Reactors, especially if the ATR is converted to LEU fuel.

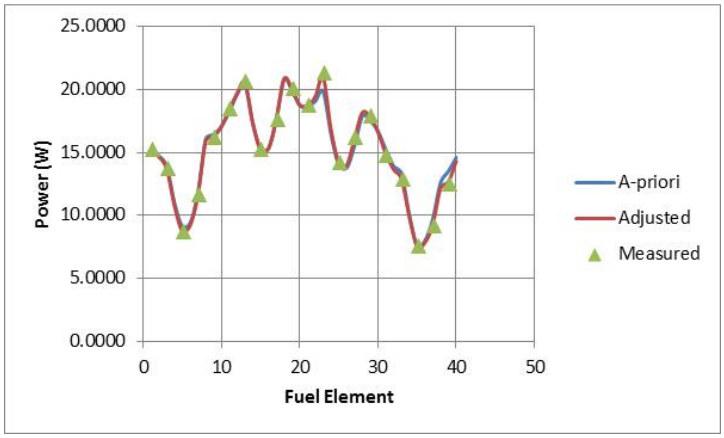

Figure 5.19. Fuel element fission rate distribution adjustment results for Irradiation 5 (MCNP5 *a priori).* The *a priori* normalization uncertainty is assumed to be 5% and the *a priori* random uncertainty is assumed to be 10%. Total correlated plus uncorrelated *a priori* uncertainty =11.2%. Adjustment performed with covariance matrix constructed from ASTM-944 using θ=1.0 and Γ=1. The adjusted powers are computed using the measured data for only the odd-numbered fuel elements. 68% of the adjustments fall within ±2.2% (1σ). Reduced uncertainties for the adjusted powers are in the range of 4.5% - 9.3%

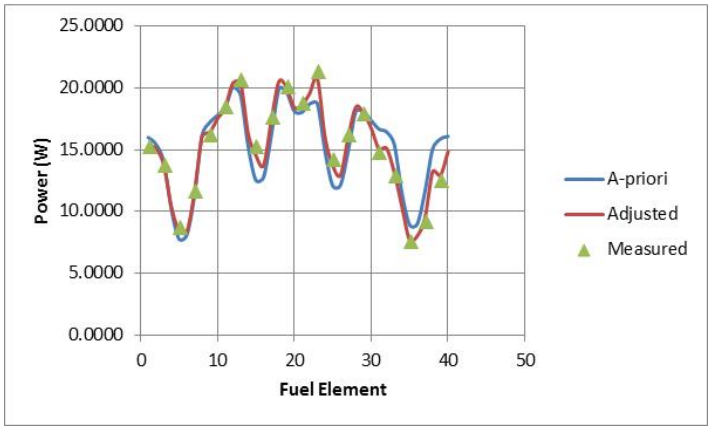

Figure 5.20. Fuel element fission rate distribution adjustment results for Irradiation 5 (HELIOS *a priori).* The *a priori* normalization uncertainty is assumed to be 5% and the *a priori* random uncertainty is assumed to be 10%. Total correlated plus uncorrelated *a priori* uncertainty =11.2%. Adjustment performed with covariance matrix constructed from ASTM-944 using θ=1.0 and Γ=1. The adjusted powers are computed using the measured data for only the odd-numbered fuel elements. 68% of the adjustments fall within ±8.4% (1σ). Reduced uncertainties for the adjusted powers are in the range of 4.5% - 10.2%

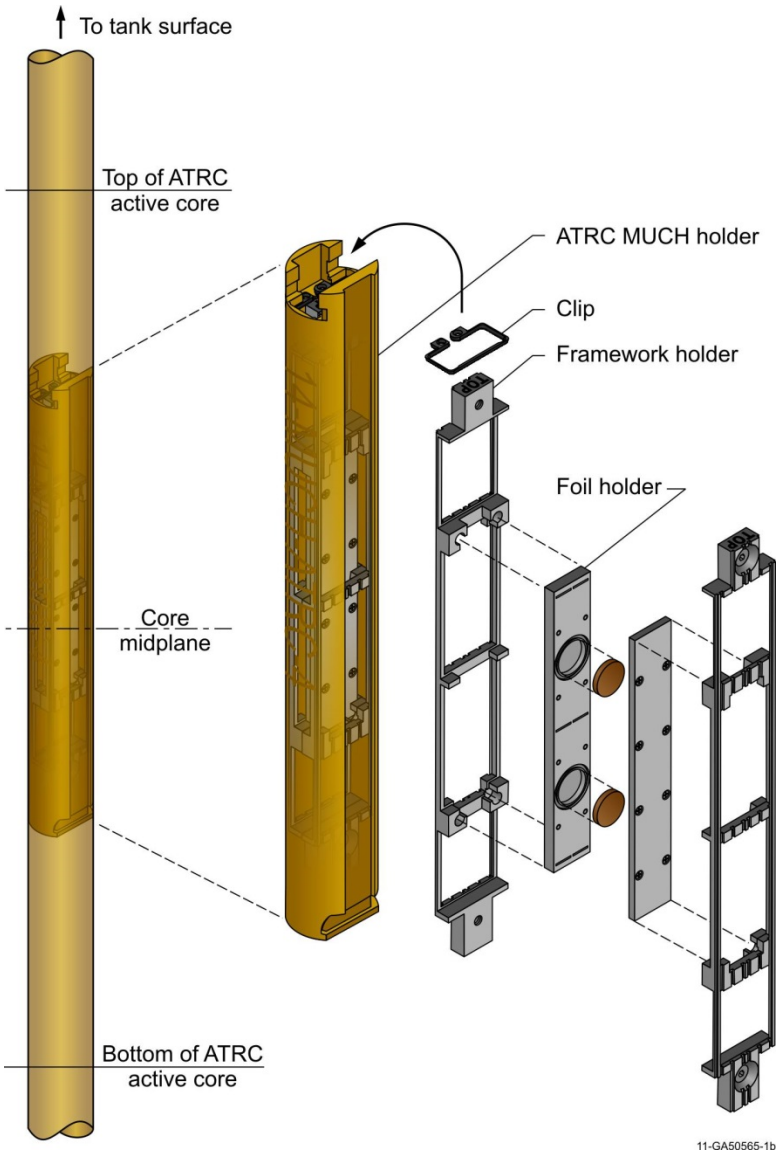

Figure 5.21. Southeast In-Pile Tube Insert Assembly (High Water Fraction).

5.3 Power Distribution Measurements in the ATRC to Support ATR Cycle 152B

In an unanticipated development during 2012, it was determined that additional core physics measurements would be required to support an ATR operational cycle (152B) that was planned for startup late in the year. These measurements were incorporated into a "depressurized" ATR cycle (152A), to be run in early 2013 prior to startup of Cycle 152B. In depressurized operations, the ATR is brought to a critical state at a very low power, well below the level that requires significant fission heat removal, permitting access to the core for more detailed neutronics measurements than are normally done to support startup of each cycle. In particular, fission power measurements can be made in selected fuel elements using the fission wire technique described earlier. Detailed control shim reactivity worth measurements can also be performed.

In the case of Cycle 152A, the ATR was loaded with 40 fresh fuel elements and the various experiment locations were loaded in a manner that was as close to what will be the case for the follow-on high-power Cycle (152B). In addition, the ATR Critical Facility was also loaded with 40

fresh fuel elements of the same type (Mark 7F) that are used in the ATR. (Ordinarily the ATRC has its own fuel elements that are geometrically identical to ATR elements, but the fuel and boron content in the plates are slightly different). In addition, the experiment locations in the ATRC were loaded with surrogate experiments that were as neutronically identical to the actual experiments loaded in the ATR itself.

Here we present an extended analysis of one of the supporting ATRC experiments used to plan the corresponding ATR depressurized operation described above. This experiment, referred to as ATRC Cycle 152A Support Test 12-5, involved a detailed measurement of the fission power in all 40 fuel elements, rather than only the odd-numbered elements as is the usual practice. This offered an excellent opportunity for some additional validation of the various ATRC models using several different codes of interest, with a relatively complicated set of experiments loaded into the flux traps and exactly the same core fuel loading as the ATR. It also permitted a valuable test of a new, much more rigorous, method for obtaining the fuel element fission power covariance matrix needed with the least-squares adjustment algorithm used for bias and uncertainty quantification with this type of validation measurement (Nigg and Steuhm, 2013, Nielsen et al., 2013).

5.3.1. Experiment Description and Measured Results.

In the new validation experiment of interest, conducted to support startup of ATR Cycle 152B, 40 ATR-type fuel elements (7F) were loaded into the ATRC in place of the standard ATRC fuel elements as noted earlier. Activation measurements that can be related to the total fission power of each fuel elements were then made with the same type of fission wires discussed earlier, composed of 10% by weight ^{235}U in aluminum. The wires were 1 mm in diameter and approximately 0.635 cm (0.25") in length and were placed in 17 locations within the cooling channels of each fuel element as shown in Figure 5.22, at the core axial midplane. The total measured fission powers for the fuel elements are estimated using appropriately-weighted sums of the measured fission rates in the U/Al wires located in each element (Durney and Kauffman, 1967), again as discussed earlier.

Figure 5.33 shows the computed *a priori* (MCNP5) fission powers for the 40 ATRC 7F fuel elements, along with the measured element powers based on the fission wire measurements. The top number (black) in the center of each element is the *a priori* element power (W) calculated by MCNP5. The bottom number (red) is the measurement. Total measured power was 875.5 W. Uncertainties associated with the measured element powers were reported as 5% (1σ). The powers for the five 8-element ATR core "lobes" are also key operating parameters and are formed by summing the powers of Elements 2-9 for the Northeast Lobe, Elements 12-19 for the Southeast Lobe, Elements 22-29 for the Southwest Lobe, Elements 32-39 for the Northwest Lobe and Elements 1, 10, 11, 20, 21, 30, 31, and 40 for the Center Lobe. The significance of the lobe powers will be discussed in more detail later

5.3.2. Statistical Analysis of Fuel Element Power Bias and Uncertainty

The MCNP5 *a priori* and measured power distributions from Figure 5.23 are plotted in Figure 5.24, along with an adjusted power distribution obtained by the least-squares method described by Nielsen et al. (2013) using the measured powers of all 40 elements. The covariance matrix for the *a priori* power vector was computed as described by Nielsen et al. (2013) and is based on the so-called "fission matrix". The covariance matrix was normalized to an estimated *a priori* absolute uncertainty of 10% (1σ) for the diagonal entries, based on historical experience. The covariance matrix for the measured powers was assumed to have only diagonal entries of 5% (1σ) for this example. It is a simple matter to include appropriate off-diagonal elements in the latter matrix to account for correlations, for example from a common calibration of the detector used to measure the activity of the fission wires, if desired. The reduced uncertainties for the adjusted element powers ranged from 3.1% to 3.7%. The adjustments ranged from -9.8% in Element 37 to +6.8% in Element 25 and in fact 68% of the adjustments were within ±4%. Thus all of the adjustments fell well within the assumed *a priori* uncertainty (1σ=10%), indicating a possible degree of conservatism in the *a priori* uncertainties assumed for the computed element powers.

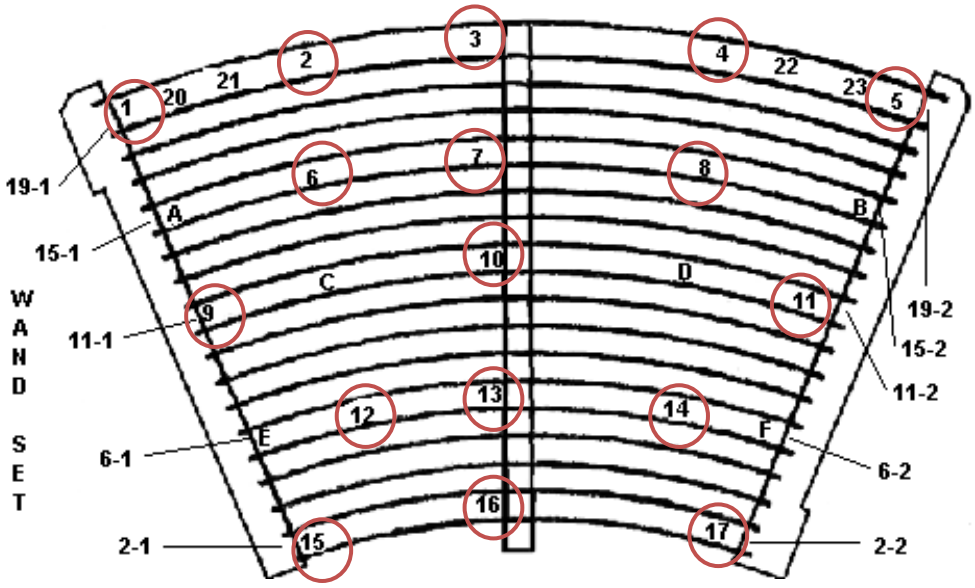

Figure 5.22. ATR Fuel element geometry, showing standard fission wire positions used for total element power measurements and for intra-element power distribution measurements.

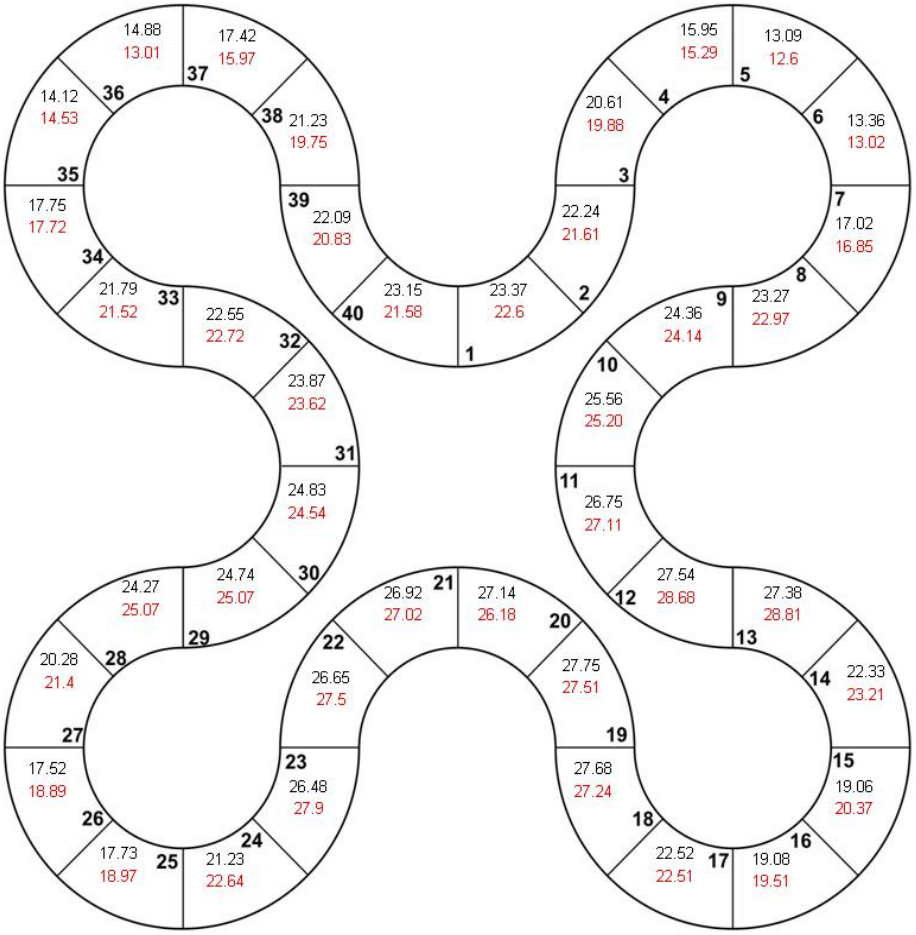

Figure 5.23. MCNP5 *a priori* Calculated (black, upper) and measured (red, lower) fuel element powers (W) for ATRC Depressurized Run Support Test 12-5. The fuel element numbers are in bold type.

The correlation matrix associated with the fission power covariance matrix used to compute the adjusted power vector in Figure 5.24 is shown as a contour plot in Figure 5.25. Key off-diagonal structural features, such as the correlations between nearby, but non-adjacent, Elements 1 and 10, or Elements 11 and 20, etc. are readily apparent. The underlying fission matrix for this example is shown in Figure 5.26. The fission matrix is used in the covariance matrix computation process. The same general structure is apparent. Note however that the fission matrix is not necessarily symmetric, while the fission correlation matrix is symmetric by definition.

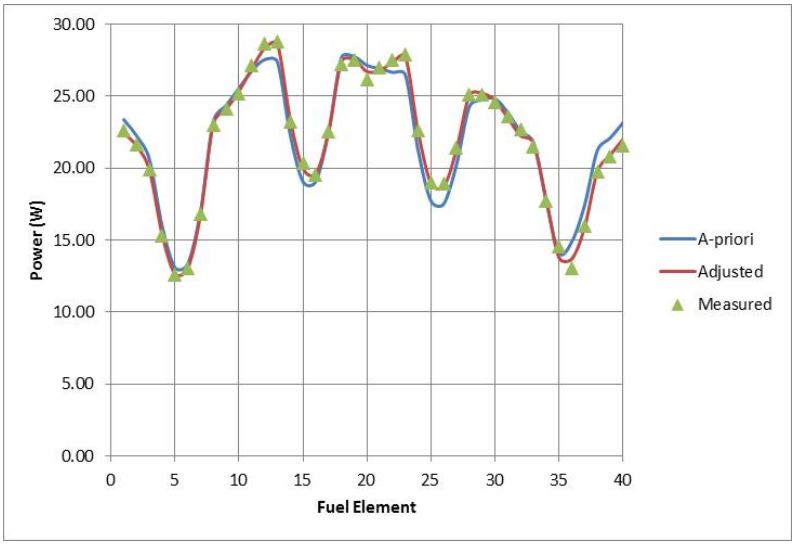

Figure 5.24. Fuel element power distribution adjustment results for ATRC Cycle 152B Support Test 12-5 (MCNP5 *a priori)*. The adjusted power is computed using the measured powers of all 40 fuel elements.

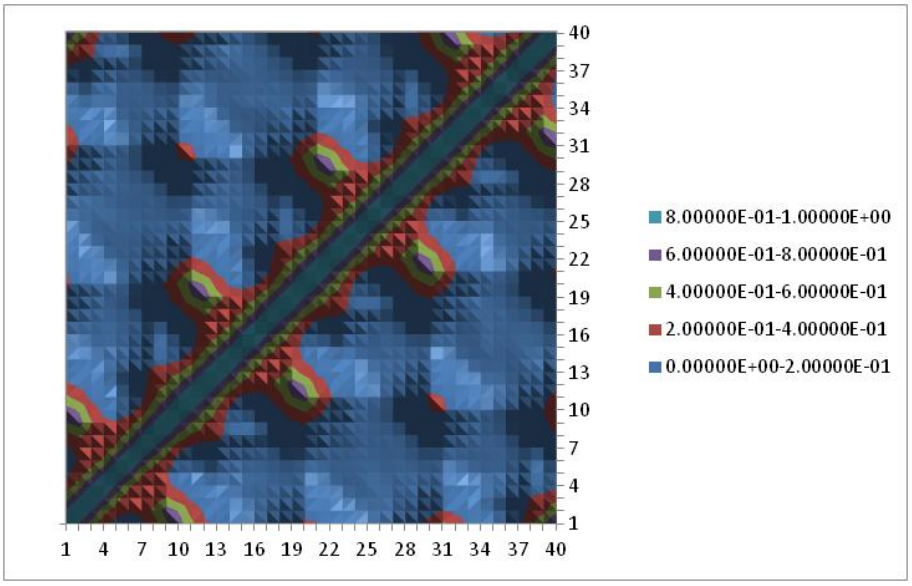

Figure 5.25. Fission power correlation matrix based on the fission matrix computed for the ATRC using MCNP5. The axis numbering corresponds to the fuel element numbers shown in Figure 5.25.

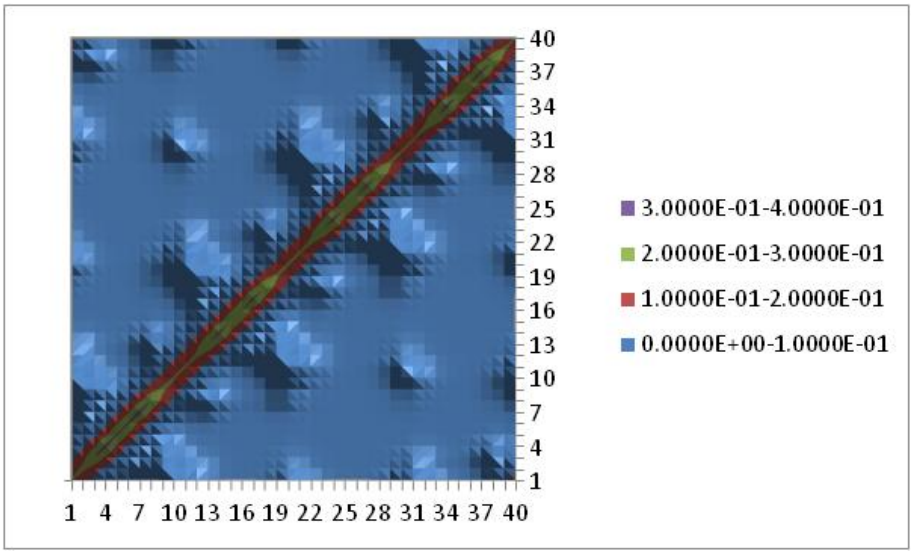

Figure 5.26. Fission matrix computed using MCNP5 for the ATRC. The axis numbering corresponds to the fuel element numbers shown in Figure 5.23.

Figure 5.27 shows the result of an adjustment of the MCNP *a priori flux* where only the powers of the odd-numbered fuel elements in Test 12-5 were included in the analysis. This simulates the relatively common ATR practice mentioned earlier where only the odd-numbered fuel element powers are actually measured, and the power for each even-numbered element is assumed to be equal to the measured power in the odd-numbered element on the opposite side of the same lobe. For example, the power in Element 2 is assumed equal to the power in Element 9, the power in Element 4 is assumed equal to the power in Element 7, and so forth around the core. The often-questionable validity of this assumption depends on the overall symmetry of the reactor configuration. In the future the assumption of symmetry can be easily replaced by rigorous covariance-weighted the least-square adjustment procedure described here to estimate the powers in the even-numbered elements. The reduced uncertainties for the adjusted element powers in Figure 5.27 ranged from 3.9% to 4.3% for the odd-numbered elements and from 4.0% to 5.2% for the even-numbered elements, demonstrating how significant uncertainty reduction can occur in the adjusted powers even for elements for which no measurement is included. This is a result of the weighted interpolation effect provided by the element power covariance matrix.

Economizing on the number of measurements even further, Figure 5.28 shows an adjustment where only the measured powers for Elements 8, 18, 28, and 38 were included in the analysis. This arrangement simulates another ATR protocol that is sometimes used because these elements are representative of the usual highest-powered elements in each outer lobe. In this case the reduced uncertainties for the adjusted element powers ranged from 4.4% to 4.5% for Elements 8, 18, 28 and 38, from 6.6% to 7% for the immediately adjacent elements and up to 9.9% for the elements that were the most distant from the elements for which measurements were made. It is notable here that some uncertainty reduction and element power adjustment occurs even for the most remote fuel elements.

Proceeding further with this 4-element example, summing the 40 element powers corresponding to the adjusted power curve in Figure 5.24 yields a total adjusted reactor power of 867.95 watts with an uncertainty of 3.1% (1σ). The absolute uncertainty quoted for the total adjusted power is computed by the usual formula:

$$\sigma_p = (\mathbf{TCov(P)T}^T)^{½} \qquad (5.1)$$

where **T** is a 40-element row vector whose entries are all 1.0 and **Cov(P)** is the same as was used for the adjustment. This adjusted power is in excellent statistical agreement with the measured total reactor power of 875.56 ± 1% that is obtained by simply summing the original 40 measured element powers, illustrating how the

total reactor power and its uncertainty can be estimated in a statistically valid manner to good accuracy using the least-squares approach even when only four fuel element powers are actually measured.

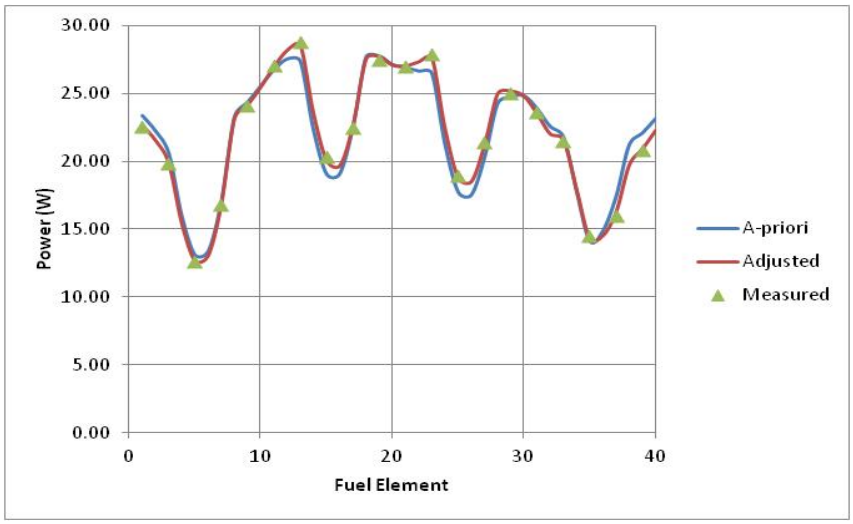

Figure 5.27. Fuel element power distribution adjustment results for ATRC Depressurized Run Support Test 12-5 (MCNP5 *a priori)*. The adjusted power is computed using the measured powers of only the 20 odd-numbered fuel elements.

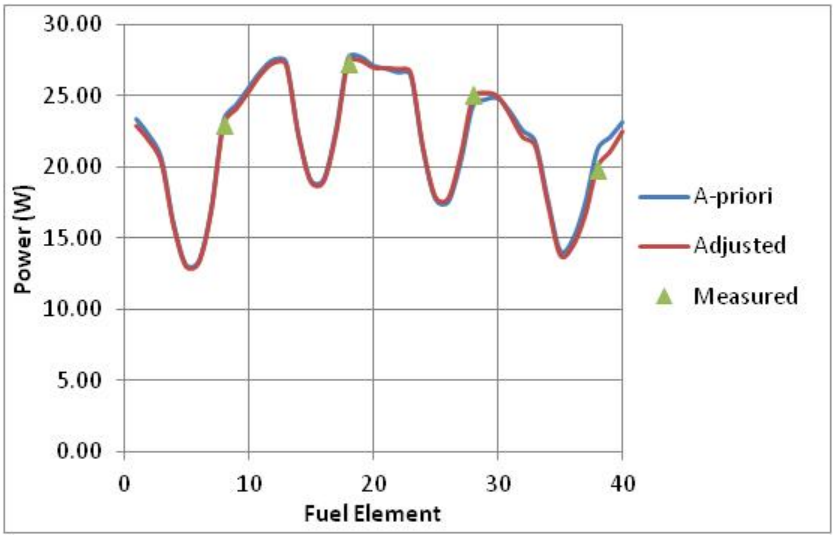

Figure 5.28. Fuel element power distribution adjustment results for ATRC Depressurized Run Support Test 12-5 (MCNP5 *a priori)*. The adjusted power is computed using the measured powers of elements 8, 18, 28 and 38 only.

5.3.3. Potential Applications to Online Lobe Power Monitoring in the ATR

Figure 5.29 illustrates another possible use of the techniques developed in connection with this validation experiment. The ATR has an online lobe power measurement system but it does not have an online system for

measurement of individual fuel element powers. Measurements of individual element powers currently can only be done by the rather tedious fission wire technique described earlier. The least-squares methodology outlined here also offers a simple, but mathematically rigorous, approach for estimating the fission powers of all 40 fuel ATR fuel elements and their uncertainties using the online lobe power measurements as follows:

In the case of Figure 5.29 the online lobe power measurements are simulated by the fission wire measurements used for the previous examples. The first five rows of the matrix on the left-hand side of Equation 1of Appendix C describe the five simulated online lobe power measurements. These rows each contain entries of 0.125 on the left-hand side for the elements included in the lobe corresponding to that row and entries of zero elsewhere. The right hand side of each of these first five rows contains the average of the measured powers from the fission wires for the lobe represented by that row. For example the first row (Lobe 1) contains entries of 0.125 for elements 2 through 9, and the average of the measured powers for elements 2 through 9 appears on the right hand side, and so forth for the other lobes. The reduced uncertainties for the adjusted powers shown in Figure 5.31 for the 40 elements range from 6.4% to 8.3%. We also note that summing the 40 element powers corresponding to the adjusted power curve in Figure 5.29 yields a total adjusted reactor power of 874.65 watts with an uncertainty of 2.0% (1σ). Once again this is in excellent statistical agreement with the measured total reactor power of 875.56 ± 1% that is obtained by summing the original 40 measured element powers.

The results shown in Figure 5.29 thus illustrate a practical application where the online-measured powers for each ATR lobe could be entered into the adjustment equations each time they are updated (every few seconds), and a corresponding estimate for all of the individual element powers could be immediately produced. Of course the *a priori* power vector would need to be recalculated regularly as the core depletes, control drums rotate, and neck shims are pulled during a cycle. This could however be automated to a large extent, and it should ultimately be quite practical, for example, to update the *a priori* power vector from the model at least daily.

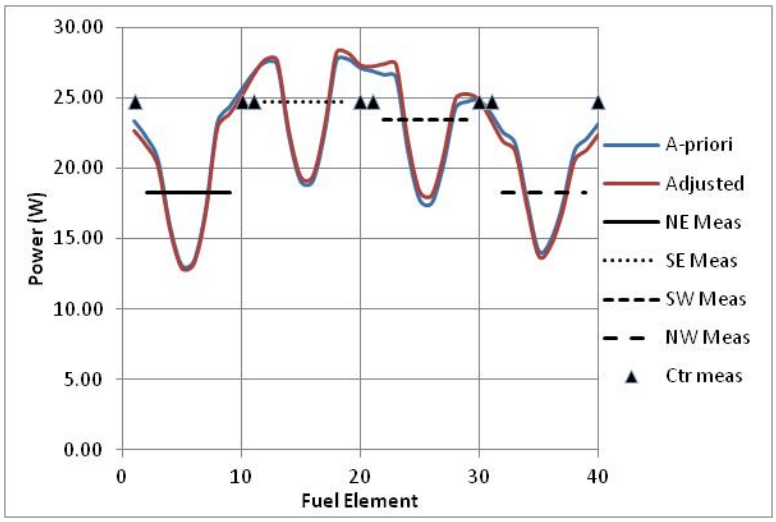

Figure 5.29. Fuel element power distribution adjustment results for ATRC Depressurized Run Support Test 12-5 (MCNP5 *a priori)*. The adjusted power is computed using the measured powers of the five core lobes.

Finally Figure 5.30 shows a comparison of the *a priori* element powers and the adjusted element powers based on the lobe power measurements (Figure 5.29) with the original detailed 40-element measured power data. Recall that the adjusted powers in this figure are based only on the measured *lobe* powers that were pre-computed by averaging the detailed element power measurements for each lobe. It is interesting to note that the adjusted power distribution curve still recaptures a significant amount of the detailed shape change relative to the *a priori* power distribution that is seen in Figure 5.24, even though the details in the measured power distribution were

largely averaged out when computing the simulated measured lobe powers used for the adjustment. The covariance matrix plays a key role in this process.

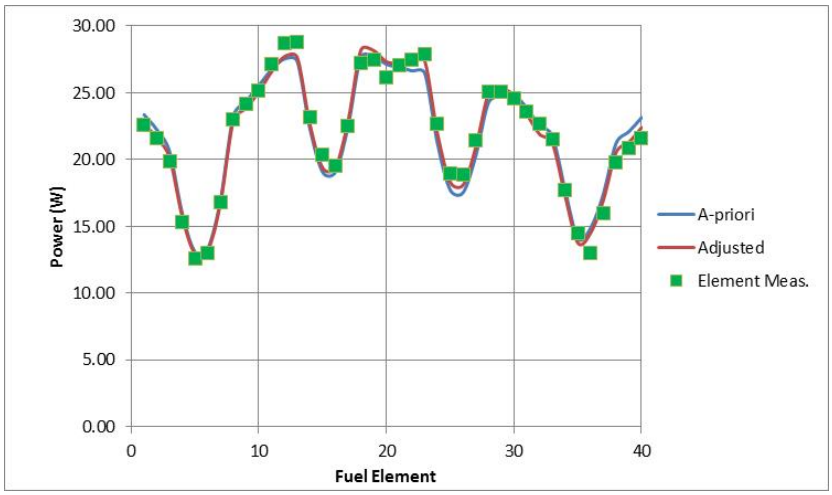

Figure 5.30. Comparison of *a priori* element powers (MCNP5), the adjusted element powers based on the measured lobe powers formed from the original detailed fuel element power measurements, and the actual detailed element power measurements.

5.3.4. Discussion and Extension of Uncertainty Analysis to SERPENT, HELIOS and NEWT

SERPENT, HELIOS and NEWT were also used to model the Cycle 152A 12-5 configuration of the ATRC in addition to MCNP5. As before, the *a-priori* fuel element powers were adjusted against the measurements using the same new covariance-weighted least-squares technique. Figures 5.31, 5.32, and 5.33 show the results of the adjustments for the three additional codes, respectively. Once again in all cases that 68% of the adjustments fell well within the estimated *a priori* uncertainty (1σ=10%) and the maximum adjustments in both directions fell well within two *a priori* standard deviations. This is illustrated for one case in Figure 5.34, which shows a histogram of the adjustment factors associated with the HELIOS results. The reduced uncertainties for the adjusted element powers were again in the range of 3.5% (1σ), consistent with the estimated 5% (1σ) uncertainties of the measured powers used for the adjustment. As expected, the adjustments associated with the 3D codes (MCNP5, SERPENT) were generally smaller than was the case for the 2D (NEWT, HELIOS) codes, reflecting somewhat greater *a priori* consistency of the 3D results with the measurements.

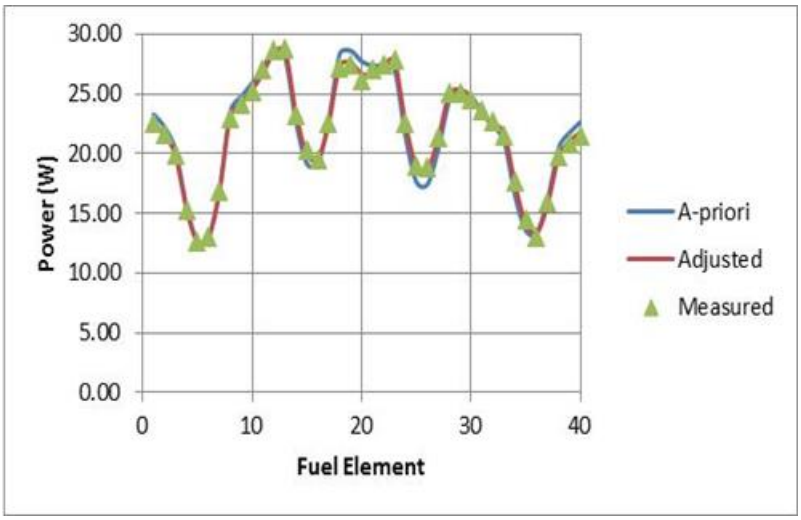

Figure 5.31. Fuel element fission rate distribution adjustment results for ATRC Depressurized Run Support Test 12-5 (SERPENT *a priori).* The *a priori* uncertainty was assumed to be 10% (1σ). The adjustments ranged from -3.7% in Element 20 to +7.1% in Element 26 and 68% of the adjustments were within ±3.2%. Reduced uncertainties for the adjusted powers are in the range of 3.2% to 3.6% for all elements.

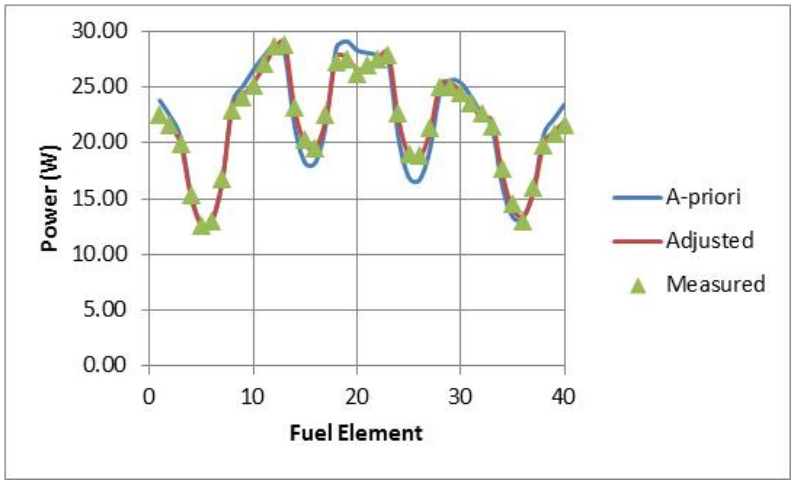

Figure 5.32. Fuel element fission rate distribution adjustment results for ATRC Depressurized Run Support Test 12-5 (NEWT *a priori).* The *a priori* uncertainty was assumed to be 10% (1σ). The adjustments ranged from -6.4% in Element 40 to +11.8% in Element 26 and 68% of the adjustments were within ±5.1%. Reduced uncertainties for the adjusted powers are in the range of 3.2% to 3.6% for all elements.

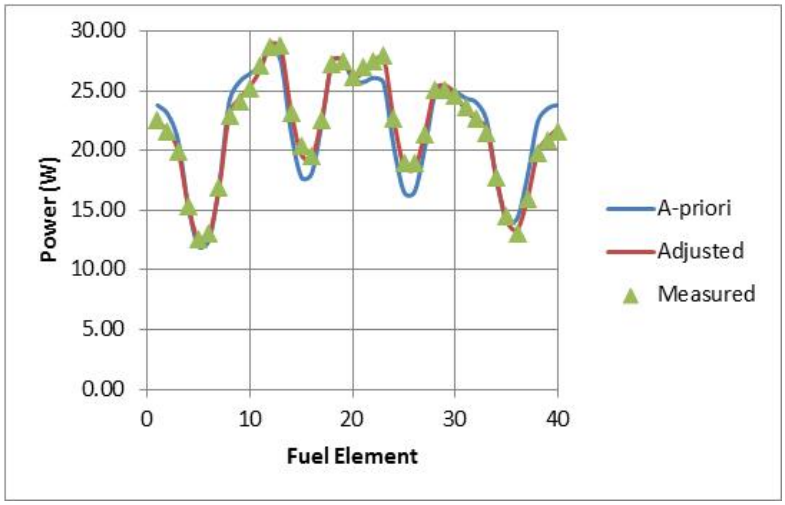

Figure 5.33. Fuel element fission rate distribution adjustment results for ATRC Depressurized Run Support Test 12-5 (HELIOS *a priori)*. The *a priori* uncertainty was assumed to be 10% (1σ). The adjustments ranged from -11.5% in Element 38 to +13.2% in Element 25 and 68% of the adjustments were within ±6.3%. Reduced uncertainties for the adjusted powers are in the range of 3.1% to 3.7% for all elements

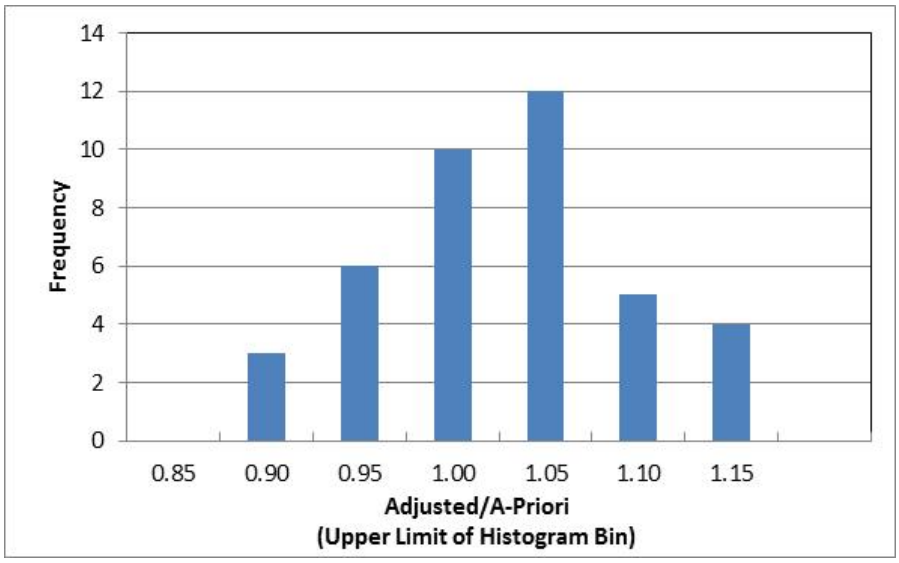

Figure 5.34 Histogram of HELIOS adjustment factors for ATRC Depressurized Run Support Test 12-5.

5.3.5. Alternate Statistical Methods for Bias and Uncertainty Quantification

It may be noted that the statistical spread of the adjustments reported here for the element powers in each case is stated in the form of a two-sided 68% confidence interval (1σ). It is also common, especially in the nuclear-electric power plant community regulated by the US Nuclear Regulatory Commission (NRC), to report this type of information in the form of one-sided 95% confidence intervals (e.g. Horneck, 1999), where in the case of element powers it is ordinarily the 95% likelihood of not being in the highest 5% of the uncertainty band that is of interest. The results reported in the previous sections may be restated using this convention as follows, using the HELIOS results as an example:

As noted in Figure 5.43 the adjustments of the *a priori* HELIOS element powers ranged from -11.5% in Element 38 to +13.2% in Element 25, and 68% of the adjustments were within ±6.3%. Furthermore, a detailed examination of the data shows that the mean adjustment was less than 0.1%, reflecting the fact that the HELIOS *a priori* results were pre-normalized to the measured total ATRC power. Strictly speaking, the mean adjustment should therefore be exactly zero, but the complex matrix manipulations required for the adjustment process are subject to minor round-off error since the computed and measured input data are stated to only two decimal places.

Following the notation of Hornek (1999) we now wish to compute a so-called "Reliability Factor" RF that can be used to increase the *a priori* element powers, $P_{0,i}$ from the calculation to the point where there is a 95% probability at the 95% confidence level that they are conservative relative to the actual best-estimate element powers obtained from the least-square adjustment process. This reliability factor is given by:

$$RF = K_c \sigma \tag{5.2}$$

Where σ is the standard deviation of the adjustments (in this case 6.3%) and K_c is a standard statistical factor that is sample size dependent. For an infinite sample size K_c is 1.65. This factor must be increased to 2.13 for our case where the sample size is only 40 (Hornek, 1999). Thus, a conservative estimate, $P_{95,i}$ for the power of fuel element i in a vector containing the 40 ATR fuel element powers may be computed for this example using the following formula:

$$P_{95,i} = P_{0,i} + \mu + K_c \sigma \tag{5.3}$$

Where μ is the mean adjustment and the standard deviation σ is expressed in absolute power units consistent with the element power vector $\mathbf{P_0}$. Thus in the case featured in this examples the *a priori* HELIOS element powers would be increased by 13.4% (=2.13 x 6.3%) to produce the desired 95/95 single-sided conservative estimates (neglecting the fact that the mean adjustment μ was not exactly zero).

Finally, as one last illustration of the fuel element power distribution results described in this section, Figure 5.35 directly compares the *unadjusted* MCNP5 and SERPENT *a priori* element powers with the measurements. The 5% (1σ) nominal uncertainty bands for the measurements are also shown. It can be seen that for the most part the MCNP5 and SERPENT results are quite consistent with each other as well as with the measurements, even prior to the statistical adjustment process. This provides an additional measure of confidence in the cross-verification of SERPENT against MCNP5 as described earlier.

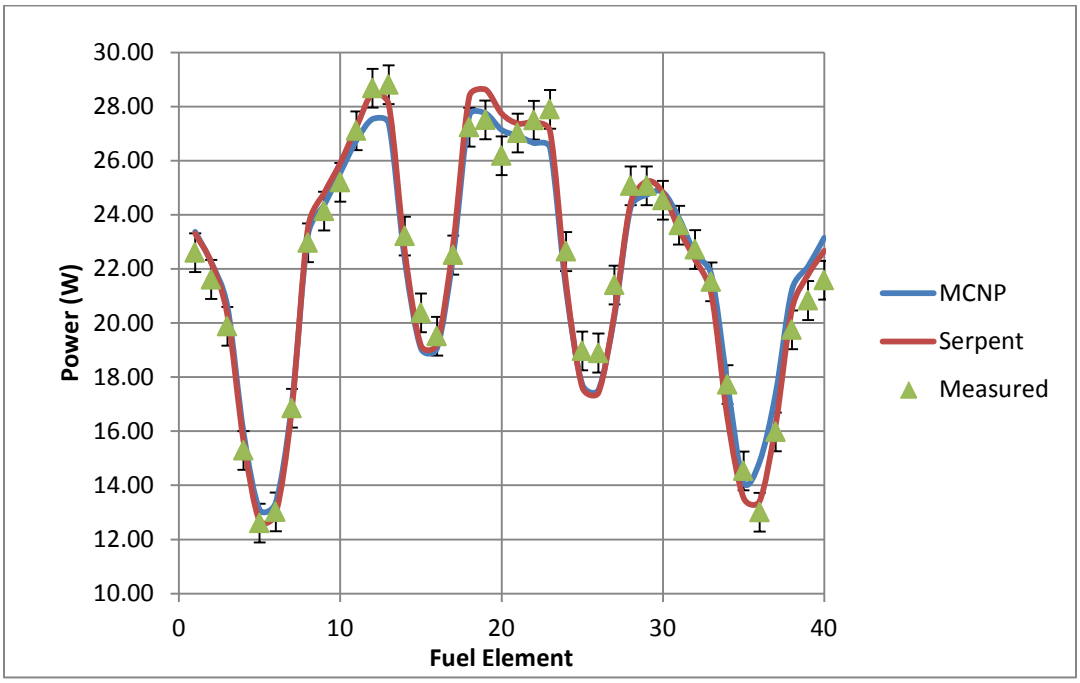

Figure 5.35. MCNP5 and SERPENT *a priori* ATRC fuel element powers, and measured element powers, for ATRC Depressurized Run Support Test 12-5. Uncertainties (5% 1σ) are shown for the measurements. Tally statistics for the computations are comparable to the line widths (<< 1% 1σ).

5.4 Intra-element Power Distribution Analysis for ATRC Validation Experiment 12-5

The fission wires placed in each ATRC fuel element as described previously also provided a method for quantifying the fission rate distributions within each element at the axial midplane because the fission rate in a given wire is representative of the fission rates in the immediately-adjacent fuel plates at the same axial and azimuthal locations (Durney and Kauffman, 1967). The measured flux wire results from for Fuel Element 19 are provided as a typical example in Table 5.4. The results of the HELIOS calculations for the adjacent fuel plates are compared to the measured values for the wires in ATRC Flux Run 12-5 for Channels 2, 6, 11, 15, and 19 as functions of azimuthal position are shown in Figures 5.36 through 5.40. An axial power peaking factor of 1.4 was used for the HELIOS model. A 5% uncertainty is associated with the measured values for the fission rates in the wires (Durney and Kauffman, 1967).

In general, there was good agreement between the HELIOS results and the measured results for the flux wires that were located azimuthally within the fuel meat in the two corresponding adjacent fuel plates (Channels 6, and 10). Channel 2 and 11 measured versus calculated results show disagreement at the ends where the flux wires are located azimuthally outside of the fuel meat. Flux wire 10 in channel 11 however showed good agreement with the measured results. Channel 19 showed relatively good agreement in the interior of the fuel meat but diverged on the two outside wire positions.

Table 5.4. Fuel Element 19 Fission Wires - Measured Powers (W/gU).

Channel	Wire Number	% Distance From Left Side of Plate	Measured Power (W/g)
2	15	25%	6.528E-02
	16	46%	5.310E-02
	17	75%	6.870E-02
6	12	25%	3.553E-02
	13	46%	3.369E-02
	14	75%	3.461E-02
11	9	3%	4.452E-02
	10	47%	2.961E-02
	11	97%	4.900E-02
15	6	25%	2.927E-02
	7	47%	2.940E-02
	8	75%	3.126E-02
19	1	4%	3.331E-02
	2	25%	3.313E-02
	3	46%	3.806E-02
	4	75%	4.423E-02
	5	96%	5.724E-02

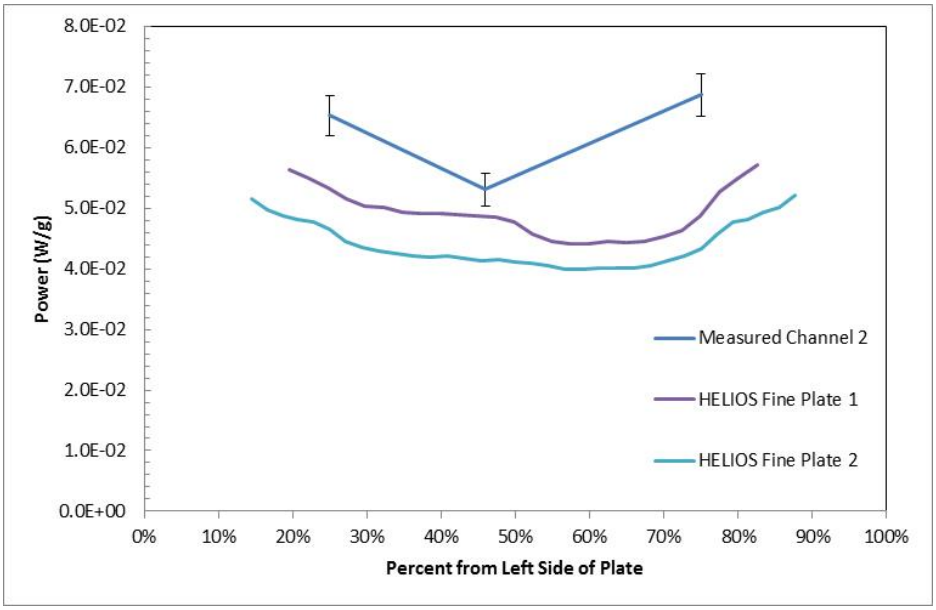

Figure 5.36. Channel 2 measured flux wire powers versus predicted specific power in the adjacent fuel plates.

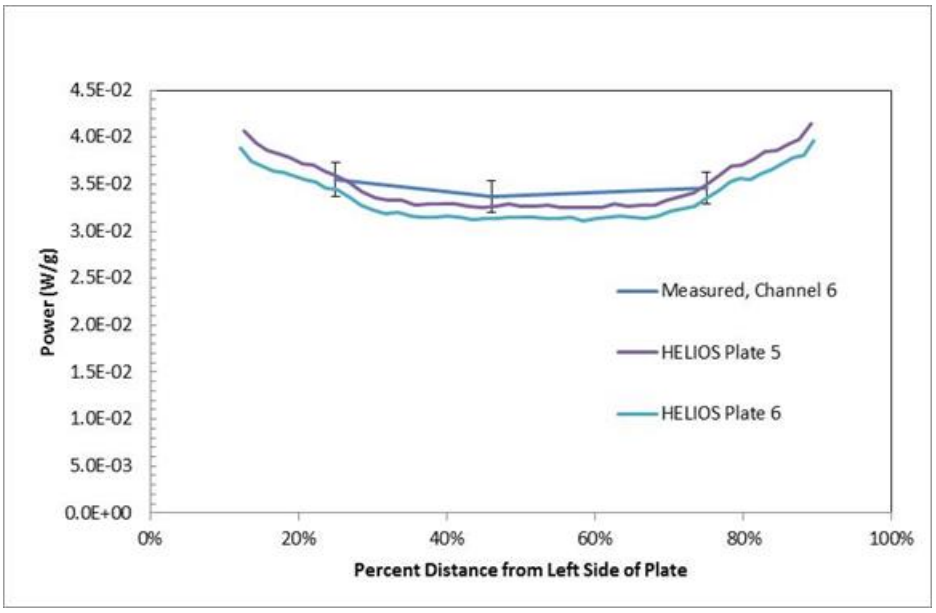

Figure 5.37 Channel 6 measured flux wire powers versus predicted specific power in the adjacent fuel plates.

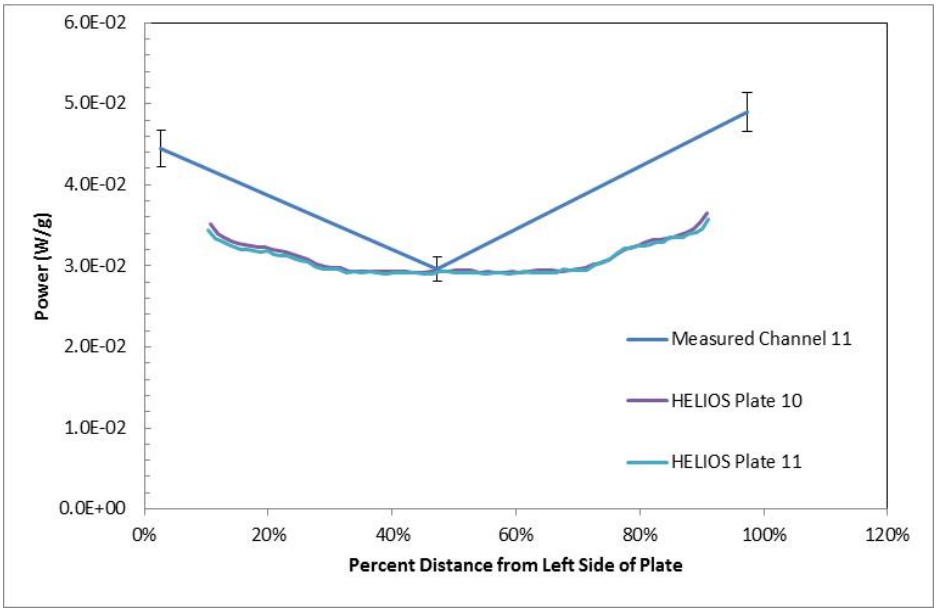

Figure 5.38. Channel 11 measured flux wire powers versus predicted specific power in the adjacent fuel plates.

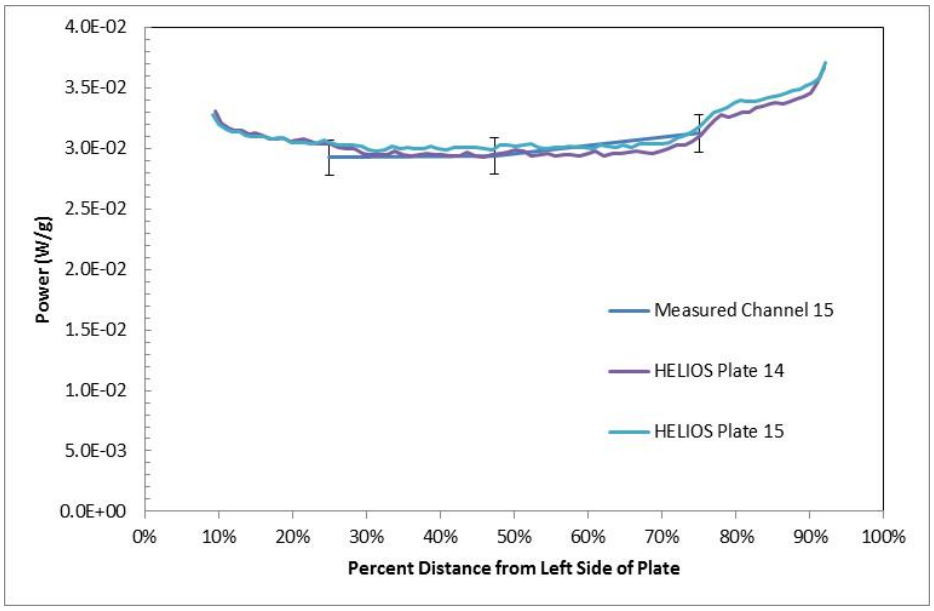

Figure 5.39. Channel 15 measured flux wire powers versus predicted specific power in the adjacent fuel plates.

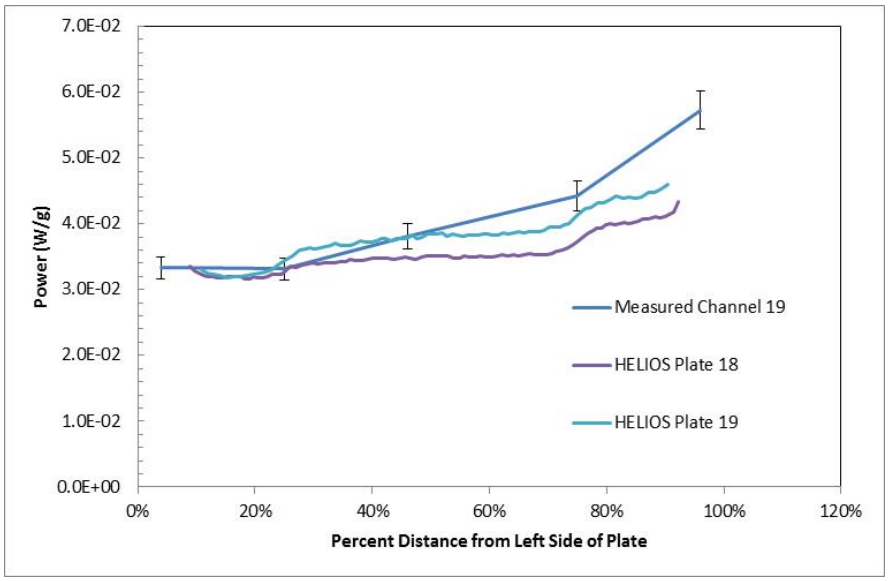

Figure 5.40. Channel 19 measured flux wire powers versus predicted specific power in the adjacent fuel plates.

Although the data shown in Figures 5.36 - 5.40 are qualitatively illustrative, a quantitative statistical comparison of the measured fission powers in the wires against the HELIOS-calculated values for the wires themselves provides a somewhat more rigorous validation metric. Accordingly the wires were represented explicitly in the HELIOS model and the fission powers for element 19 were computed directly, again assuming an axial peaking factor of 1.4. The results were scaled to the average of the measured wire powers for fuel element 19 in order to allow a direct comparison of the *relative* radial and azimuthal distribution of wire powers in this element. The computed powers were then adjusted against the measured wire powers using the method described in the previous section. The required covariance matrix for the adjustment was constructed using a 5% uncertainty for the measured wire powers as noted above and a 10% *a priori* uncertainty for the calculated wire powers, consistent with the element analysis outlined earlier. However, in this case no off-diagonal entries were included in the covariance matrix for the calculated powers, reflecting the fact that a fission neutron emitted in a particular

wire is not very likely to cause a fission in any other wire. It is much more likely that it will cause a fission in the surrounding fuel instead. The scaled *a priori* calculated wire powers for Element 19 are shown in Table 5.55.

Figures 5.41 – 5.45 compare the measured and scaled *a priori* wire powers graphically for each channel where wires were located. The adjusted wire powers are listed in Table 5.6 and the percentage adjustments relative to the *a priori* powers are shown in Table 5.7. The percentage adjustments ranged from 11% downward to about 17% upward. 68% of the adjustments were within approximately 7.5% of the average *a priori* calculated wire power for the element, well within the 10% estimated uncertainty for the *a priori* calculated powers.

Repeating the analysis described here for the other 39 fuel elements and combining results showed that 68% of the adjustments to the scaled *a priori* calculated powers of all 680 fission wires in the core fell within about 8.7% of the core-average scaled *a priori* calculated wire power, again well within the estimated *a priori* uncertainty. The distribution of percentage adjustments to the scaled *a priori* powers for all of the wires is illustrated in Figure 5.46. The distribution tends to be skewed to the right, reflecting the larger number of upward adjustments occurring for the wires located azimuthally outside the active fuel regions of the fuel plates as discussed earlier. The likely source of this non-normal distribution will be discussed below.

Table 5.5. Fuel Element 19 Fission Wires – HELIOS Calculated Powers (W/gU) scaled to the average of the measured wire powers for the element.

Channel	Wire Number	Position Relative to Azimuthal Center (in)	Calculated Power (W/g)
2	15	-0.85	6.350E-02
	16	-0.08	5.077E-02
	17	0.85	6.493E-02
6	12	-0.59	3.708E-02
	13	-0.08	3.559E-02
	14	0.59	3.690E-02
11	9	-1.29	3.778E-02
	10	-0.08	3.186E-02
	11	1.29	3.981E-02
15	6	-0.83	3.238E-02
	7	-0.08	3.238E-02
	8	0.83	3.364E-02
19	1	-1.79	3.812E-02
	2	-0.94	3.807E-02
	3	-0.08	4.040E-02
	4	0.94	4.275E-02
	5	1.79	5.387E-02

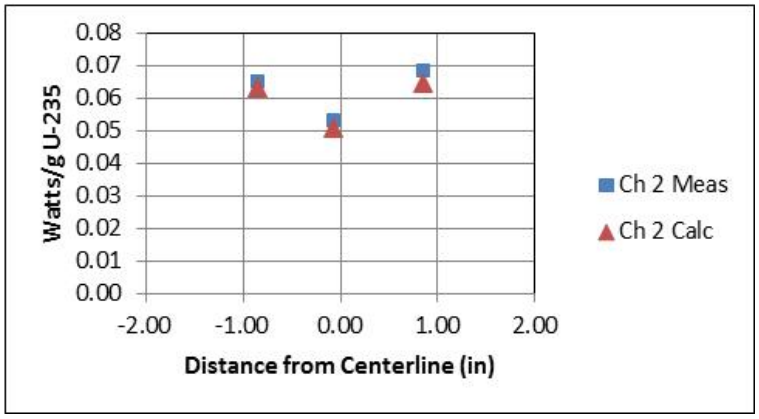

Figure 5.41. Measured fission wire powers and *a-priori* calculated wire powers (scaled to the average measured wire power) for Fuel Element 19, Channel 2.

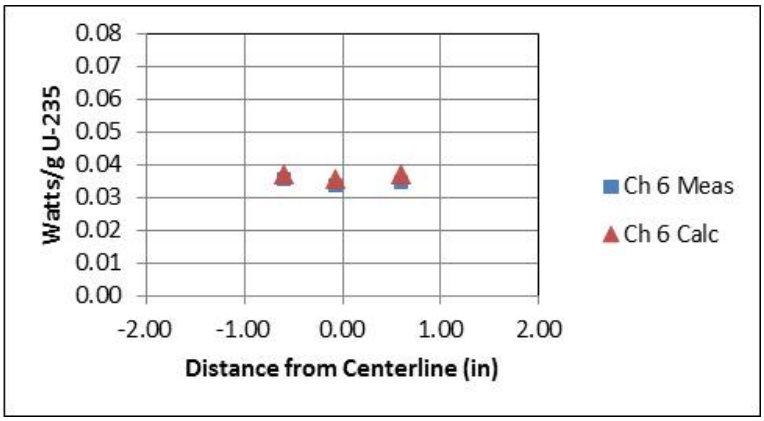

Figure 5.42. Measured fission wire powers and *a-priori* calculated wire powers (scaled to the average measured wire power) for Fuel Element 19, Channel 6.

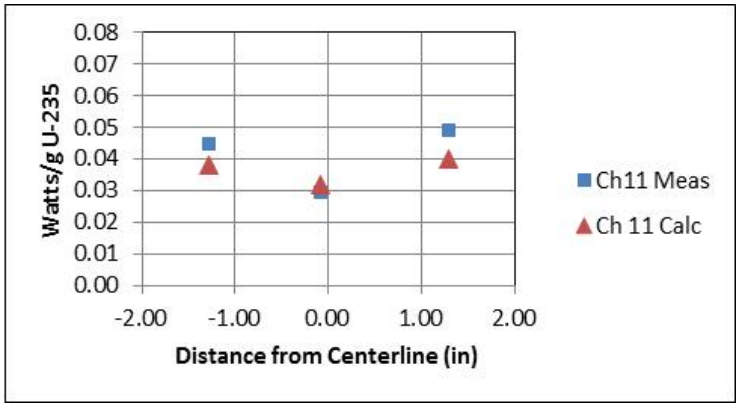

Figure 5.43. Measured fission wire powers and *a-priori* calculated wire powers (scaled to the average measured wire power) for Fuel Element 19, Channel 11.

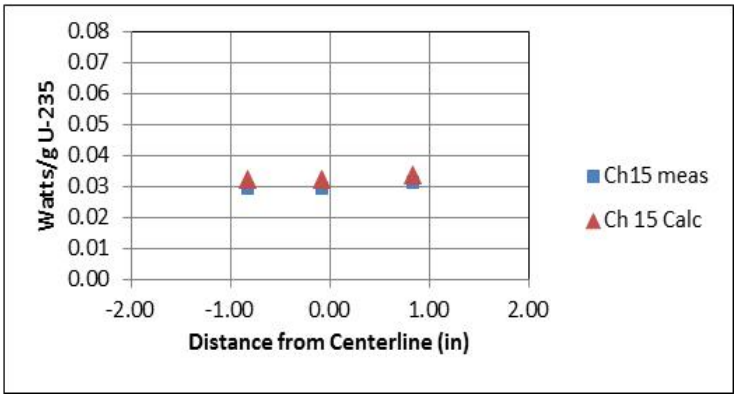

Figure 5.44. Measured fission wire powers and *a-priori* calculated wire powers (scaled to the average measured wire power) for Fuel Element 19, Channel 15.

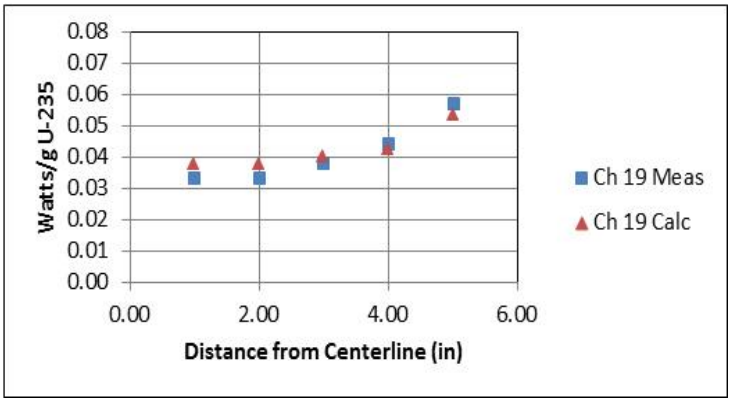

Figure 5.45. Measured fission wire powers and *a-priori* calculated wire powers (scaled to the average measured wire power) for Fuel Element 19, Channel 19.

Table 5.6. Fuel Element 19 Fission Wires – Adjusted Powers (W/gU).

Channel	Wire Number	Position Relative to Azimuthal Center (in)	Adjusted Power (W/g)
2	15	-0.85	6.491E-02
	16	-0.08	5.260E-02
	17	0.85	6.788E-02
6	12	-0.59	3.582E-02
	13	-0.08	3.404E-02
	14	0.59	3.502E-02
11	9	-1.29	4.278E-02
	10	-0.08	3.001E-02
	11	1.29	4.648E-02
15	6	-0.83	2.980E-02
	7	-0.08	2.991E-02
	8	0.83	3.168E-02
19	1	-1.79	3.408E-02
	2	-0.94	3.392E-02
	3	-0.08	3.849E-02
	4	0.94	4.392E-02
	5	1.79	5.650E-02

Table 5.7. Fuel Element 19 Fission Wires – Percent Adjustments.

Channel	Wire Number	Position Relative to Azimuthal Center (in)	Percent Adjustment
2	15	-0.85	2.22
	16	-0.08	3.60
	17	0.85	4.53
6	12	-0.59	-3.39
	13	-0.08	-4.37
	14	0.59	-5.10
11	9	-1.29	13.25
	10	-0.08	-5.81
	11	1.29	16.74
15	6	-0.83	-7.96
	7	-0.08	-7.63
	8	0.83	-5.81
19	1	-1.79	-10.60
	2	-0.94	-10.92
	3	-0.08	-4.75
	4	0.94	2.73
	5	1.79	4.88

Table 5.8. Fuel Element 19 Fission Wires – Calculated and Adjusted Powers Relative to Measured Powers

Channel	Wire Number	*A Priori*/Measured	Adjusted/Measured
2	15	0.993	0.994
	16	0.956	0.991
	17	0.945	0.988
6	12	1.044	1.008
	13	1.056	1.010
	14	1.066	1.012
11	9	0.849	0.961
	10	1.076	1.013
	11	0.813	0.949
15	6	1.106	1.018
	7	1.101	1.017
	8	1.076	1.013
19	1	1.144	1.023
	2	1.149	1.024
	3	1.062	1.011
	4	0.967	0.993
	5	0.941	0.987

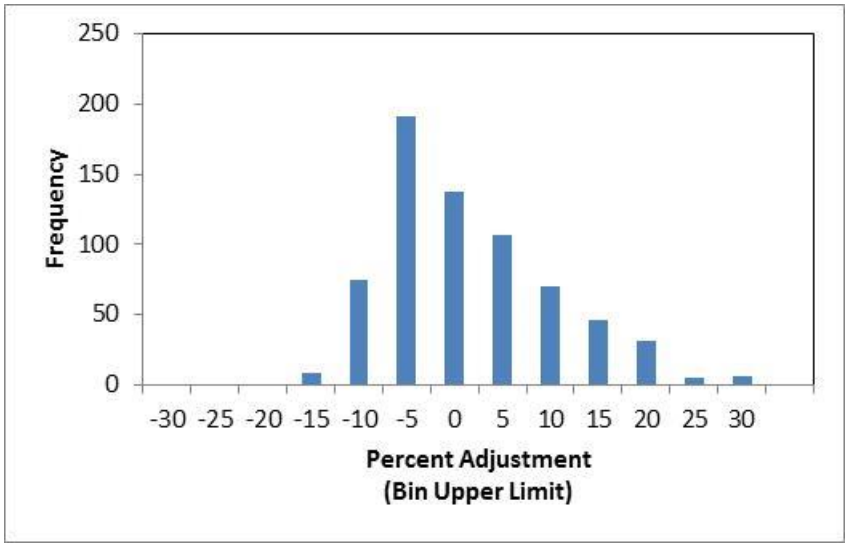

Figure 5.46. Histogram showing the distribution of percentage adjustments of the scaled *a priori* calculated fission wire powers for all 40 fuel elements combined (total of 680 fission wires).

We now examine the *absolute* fission wire powers, unscaled to the element averages, since in the final analysis these are more indicative of the overall bias and uncertainty of the computational model. When the unscaled *a priori* wire powers from the HELIOS model (multiplied only by the axial peaking factor 1.4) are adjusted against the unscaled wire measurements, 68% of the adjustments still fall within about 10.5% of the *a priori* calculated wire power, therefore continuing to lend credence to the 10% (1σ) *a priori* uncertainty estimate in an absolute sense. A histogram of the adjustments of the absolute wire powers is shown in Figure 5.47. The width of the

distribution is greater, reflecting the fact that differences between the measured and calculated element average fission wire powers (which is proportional to the differences between the measured and calculated element powers themselves) have not been normalized out in this case. As can be seen from Figure 5.47 the distribution of the absolute adjustments is still skewed to the right and it appears plausible that this distribution of adjustments is a superposition of two normal distributions. Separating the adjustment data into two sets accordingly, one for the 6 "outer" wires in each fuel element that are nearest to the element side plates and another for the remaining 11 "inner" wires in each fuel element as shown in Figures 5.48 and 5.49 respectively tends to confirm this idea. The mean adjustment of the outer wire data is approximately +13% but much smaller (+1.3%) for the inner wire data, providing a measure of the downward bias of the computed wire powers for both data sets. Finally, weighting the standard deviations of the outer and inner wire adjustments (10.0% and 8.2%, respectively) by the relative number of outer and inner wires (240 and 440 respectively) produces a combined wire adjustment standard deviation of 8.8%. This is within the historical acceptance criterion of ±9% (1σ) for comparison of measured and computed pointwise fission power data (McCracken et al, 1994).

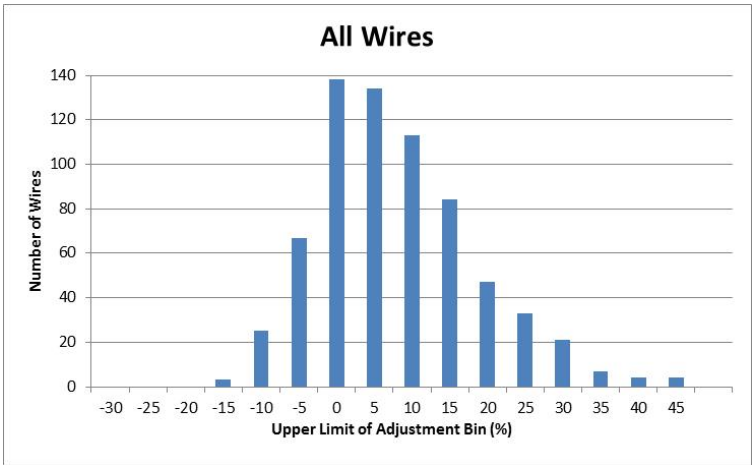

Figure 5.47. Histogram showing the distribution of percentage adjustments of the absolute *a priori* calculated fission wire powers for all 40 fuel elements combined (total of 680 fission wires). The mean adjustment is 5.4% upward. 68% of the adjustments fall within 10.5% of the mean.

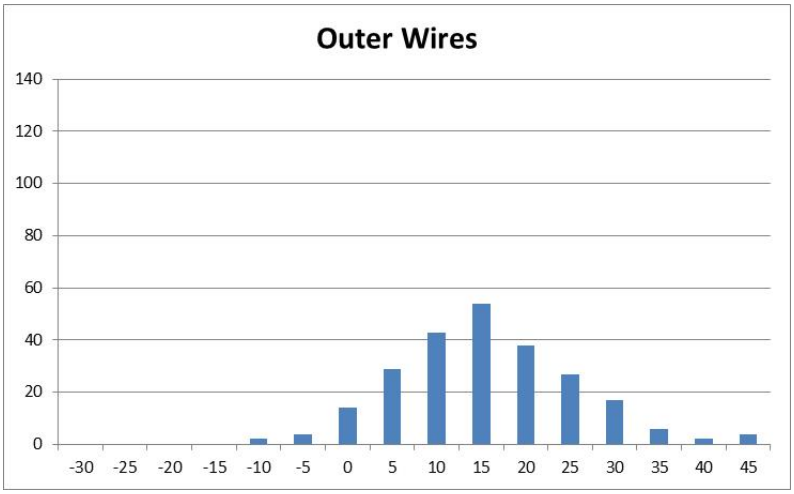

Figure 5.48. Histogram showing the distribution of percentage adjustments of the absolute *a priori* calculated fission wire powers of the inner wires (Wires 1, 5, 9, 11, 15 and 17) of all 40 fuel elements combined (total of

240 wires). The mean adjustment is 13.1% upward. The standard deviation of the outer wire adjustments is 10.0%

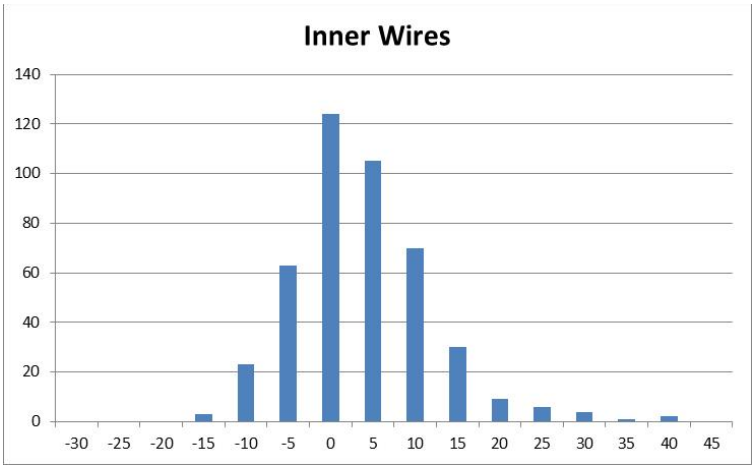

Figure 5.49. Histogram showing the distribution of percentage adjustments of the absolute *a priori* calculated fission wire powers of the inner wires (Wires 2, 3, 4, 6, 7, 8, 10, 12, 13, 14 and 16 in Figure 5.32) of all 40 fuel elements combined (total of 440 wires). The mean adjustment is 1.3% upward. The standard deviation of the adjustments is 8.2%

Two plausible causes of the behavior of the distributions in Figures 5.47- 5.49 have been identified. First, it may be noted that the nature of the numerical method used by HELIOS to solve the transport equation (current-coupled collision probability) is such that some angular flux detail may be lost at interfaces between geometric structures such as fuel elements. This could conceivably cause at least some of the observed behavior. However, at this juncture it appears that most of the observed behavior is likely due to the presence of so-called "side plate vents" in the ATR and ATRC Mark 7F fuel elements. These vents are shown in Figure 5.50. Each fuel element has a set of four vents that straddle the axial core midplane as shown. Since the fission wires used to measure the element powers are placed at the axial midplane in all of the fuel elements, the additional water in the vent regions would be expected to cause a slight thermal flux peak that would not be present in the axial regions of the fuel element away from the vents. Furthermore, the flux peak would be most noticeable in the fission rates of the wires nearest the side plates (the "outer" wires) and least noticeable in the inner wires, as is consistently observed in all of the data presented here. Finally it is interesting to note that the same azimuthal peaking effect relative to measurement was also observed with the legacy PDQ7 based methodology (McCracken et al, 1994), lending additional credence to the idea that it is a real physical phenomenon and not a numerical artifact.

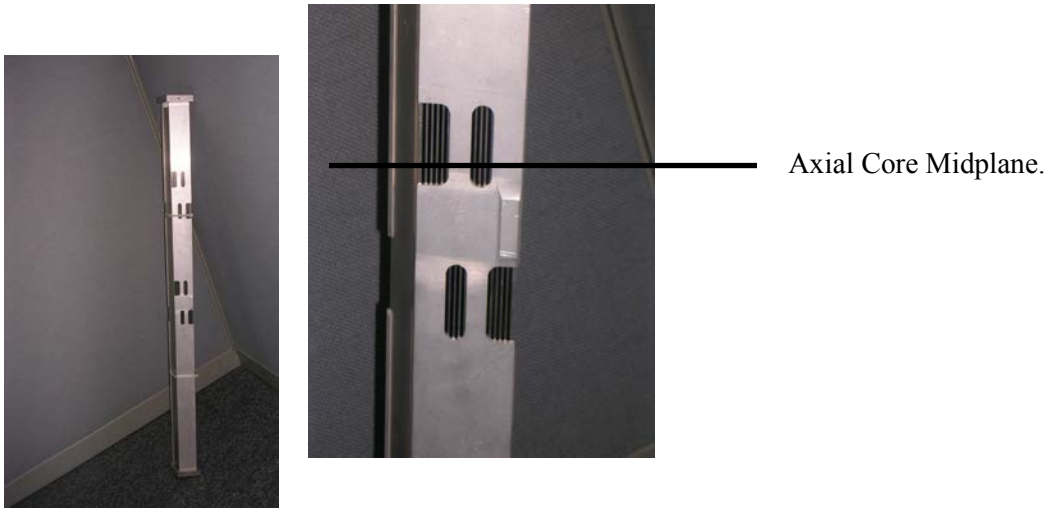

Figure 5.50. ATR Mark 7F fuel element (L) showing side plate vents and location (R) of core midplane.

The local thermal flux peaking from the presence of additional water is a three-dimensional effect that cannot not be explicitly captured in the HELIOS 2D model, nor is it captured in the 3D Monte Carlo models used for the Depressurized Run physics analyses presented here, since the side plates are modeled as solid aluminum in the 3D models as well, for consistency with the HELIOS model. The assumption of solid side plates is currently made in the models since this is representative of most of the axial length of the active fuel. However, as one final confirmation, a few exploratory HELIOS calculations were run with varying Al/H2O volume fractions in the side plates to approximately quantify the effect of the fuel element vents located at the mid-plane. The Al/H2O volume fractions were varied from 100/0 to 0/100 to cover the entire range. As expected, when the volume fraction of water increased, the calculated power of the fission wires located near the side plates also increased, with little effect on the inner wires. Furthermore, the range of magnitudes of the calculated increases in the outer wires was consistent with the measured data. In the long term, it is likely that all computational support for ATR operations and fuel management will be conducted using full 3D Monte Carlo simulations as noted in the introduction. In the meantime, the effects of the side plate vents on the outer fission wires (and therefore on the outermost parts of the fuel plates) can simply be incorporated as a quantified bias with associated uncertainty where appropriate, based on the statistical analyses outlined here.

5.6 Validation of HELIOS against ATR As-Run Online Data

This section summarizes validation of the Studsvik-Scandpower deterministic transport code against available operating data Since August, 2009 (Nigg and Steuhm, 2012, 2013). Results are presented in this section for core reactivity and initial critical shim positions as well as for lobe powers Much of the work presented here deals with transitioning reactivity accountancy and fuel database strategies from PDQ7 to HELIOS. It is shown that the HELIOS code can reliably simulate the actual ATR power history and core reactivity comparable to current expectations with PDQ7. However, during the course of the transitional process, opportunities for improvement of the current bookkeeping of axial effects were discovered and are under development.

5.6.1. Description of As-Run Analysis

Core-follow of the ATR is performed after each cycle for the purpose of tracking fuel nuclide inventories and updating models against online data. The ATR Reactor Data Acquisition System (RDAS) records surveillance data of lobe powers and OSCC and neck shim position throughout the cycle. The suite of RDAS programs that collects this information is called ATR Surveillance Data Acquisition System (ASUDAS). This data is used to create a PDQ7 model that is more true to the actual operating history than the one used to prepare the CSAP. Note that validation of the PDQ7 code suite is not a primary deliverable of these core-follow, or As-Run

calculations. As-Run calculations are performed primarily for updating the PDQ7 nuclide inventory. In a typical As-Run, the control configuration of the model is set to ensure correct lobe-average exposures. The core follow in this work with HELIOS follows a similar strategy as a PDQ7 As-Run, but with some significant improvements. The most noteworthy difference is that the reactor surveillance data for each lobe, including lobe powers and positioning of the various reactivity control systems, is matched throughout the cycle of interest in HELIOS as closely as reasonably achievable. The other primary difference between the HELIOS and PDQ7 As-Runs is that with HELIOS, the critical eigenvalue from the previous cycle (or cycles) are leveraged to predict the criticality of the target cycle. With PDQ7, a series of zero power physics "requalification tests" following the 1994 CIC is used to give the starting estimate for the computational critical eigenvalue.

The HELIOS fuel nuclide inventory files use the historical PDQ7 fuel nuclide database to seed the beginning-of-cycle (BOC) fuel element loading in the absence of nuclide data with a HELIOS pedigree. As end-of-cycle (EOC) HELIOS data become available, it is used instead of the PDQ7 data. Also, the hafnium concentrations of the neck shims are tracked explicitly. Note that HELIOS does not track depletion of beryllium and its activation products. Instead, THECPT is used to deplete the beryllium reflector for each cycle using reflector flux data from the As-Run, See Section 3.3.2.

A significant challenge for following the ATR core is related to the time discretization of hourly ASUDAS data. Following the ATR hourly or even daily data in all of its detail would require an excessive amount of computer resource. However, a time step greater than ten days is not sufficient to update the flux/criticality calculation. The ATR HELIOS model has an OSCC mesh discretization of 3.75^{o}. Therefore, an OSCC rotation less than that amount is insignificant to trigger creation of a new burn-step. It was found that time increments on the order of two to ten days was sufficient to represent significant OSCC maneuvers. The same is true of neck shim movement. This discretization scheme was usually course enough to have at least one neck shim removal every burn step. Also during the course of this time interval, reactor power and lobe-power splits may have evolved slightly as the ATR operators strive to maintain constant lobe power. Thus, the ASUDAS hourly information was time averaged into burn steps, each representative of a unique control configuration and power state.

5.6.2 Results – Core Reactivity

To begin each cycle the ATR is brought to critical with all neck shims inserted, one of the regulating rods (SW4 and SE4) fully withdrawn, and the other regulating rod partially withdrawn. Approach to criticality is performed using the OSCCs only. The OSCCs are rotated in equal increments, i.e., balanced configuration. Once cold criticality is achieved with balanced OSCC rotation, the core is brought to full power; again using OSCCs to attain the desired lobe-power split.

The startup criterion for ATR stipulates that the initial cold critical condition must fall within +\$0.75 and -\$1.00 of the predicted OSCC position, aside: β_{eff}=0.0075. In the legacy methodology, the OSCC position is computed with both PDQ7 as well as using an empirical tabulation method based off of each experiment's reactivity worth as measured in the ATRC. These two estimates are averaged together to arrive at the startup prediction. If after two reactor power doublings it becomes apparent that the +\$0.75/-\$1.00 criterion will not be met, the approach to critical is terminated to resolve the disparity.

Table 5.9 shows the OSCC position predicted by HELIOS for each cycle of interest (Cycle 145A + 155B) using the detailed techniques outlined in Chapter 3 and compares that result with the actual measured critical position and the historical results from PDQ7 and the empirical method. As noted in Section 3.5, the axial correction methodology based on the ROSUB polynomials was retained for this demonstration. With the exception of Cycle 148A, 150A, and 153B (the latter two are PALM cycles), all the HELIOS cases were within the acceptance criteria when converted to equivalent reactivity difference using the applicable shim worth curve. Note that the OSCC drive mechanism may contribute an uncertainty in the measured critical position of up to about two degrees, which is the amount of play between the teeth of the drive gear and the connecting gear. Also, note that the HELIOS model OSCC mesh discretization is 3.75 degrees. The standard deviation of the differences between HELIOS predicted and the actual reported OSCC position is ten degrees. Ten degrees is worth roughly \$1.2 in the linear region of the OSCC worth curve. The standard deviations of the PDQ7 and empirical method differences are 3.8 degrees and 5.4 degrees, respectively.

Figure 5.51 shows the reactivity value of the difference between predicted and reported OSCC position. From the figure, it is evident that the HELIOS-based methodology largely predicts the critical OSCC position within the bounds of the startup criteria. The average prediction is \$0.23 higher than the reported value. The reactivity worth of the standard deviation is similar to that of the empirical method. The large discrepancy for 148A, 150A and 153B lend to this large variability. Possible reasons for the discrepancy with Cycles 146A and 148A may be uncertainties associated with insufficient fission product nuclides transcribed from PDQ7 into HELIOS. Recall that PDQ7 uses a lump fission product. Another possible source of discrepancy for these two cycles is inadequacy of the lobe-exposure polynomial to represent the burnup reactivity decrement of either the target or known critical, or both. Discrepancies may also arise from the axial homogenization scheme used to describe experiments and fuel.

Cycle 150A was a high power "PALM" cycle. This cycle has a higher loading of fresh fuel in the southwest and southeast lobes. Thus, it is possible that Cycle 149B is not a useful starting point for predicting criticality of 150A per the HELIOS standard algorithm for reference to critical.. The next PALM cycle was Cycle 153B. If using Cycle 152B as the known critical for this cycle, the predicted critical position was 86.7^{o} or \$1.28 too high. If using Cycle 150A, the predicted critical position was 50.7^{o} with a value of \$0.99 low.

Table 5.9. Predicted and actual reported critical OSCC positions for initial cold startup.

Cycle	PDQ7	Empirical	Actual	HELIOS
145A	48.4	37.7	45.4	48.2
145B	53.2	42.8	42.8	42.1
146A	42.9	42.2	37.9	43.6
146B	44.9	38.0	33.6	39.7
147A	51.4	47.9	45.5	43.5
148A	59.2	52.3	50.3	64.0
148B	57.8	48.5	50.2	51.9
149A	53.4	54.6	52.5	52.9
149B	43.0	44.7	38.7	35.9
150A	82.1	73.7	82.1	114.0
150B	51.9	47.3	48.8	55.0
151A	37.5	46.3	37.9	44.7
151B	36.7	34.9	38.8	30.6
152B	57.2	45.8	54.3	57.4
153B	70.9	59.7	67.8	57.6
154A	49.8	45.3	45.8	38.6
154B	54.8	45.7	44.0	54.6
155A	35.8	29.0	34.9	26.3
155B	48.7	43.6	49.4	42.6

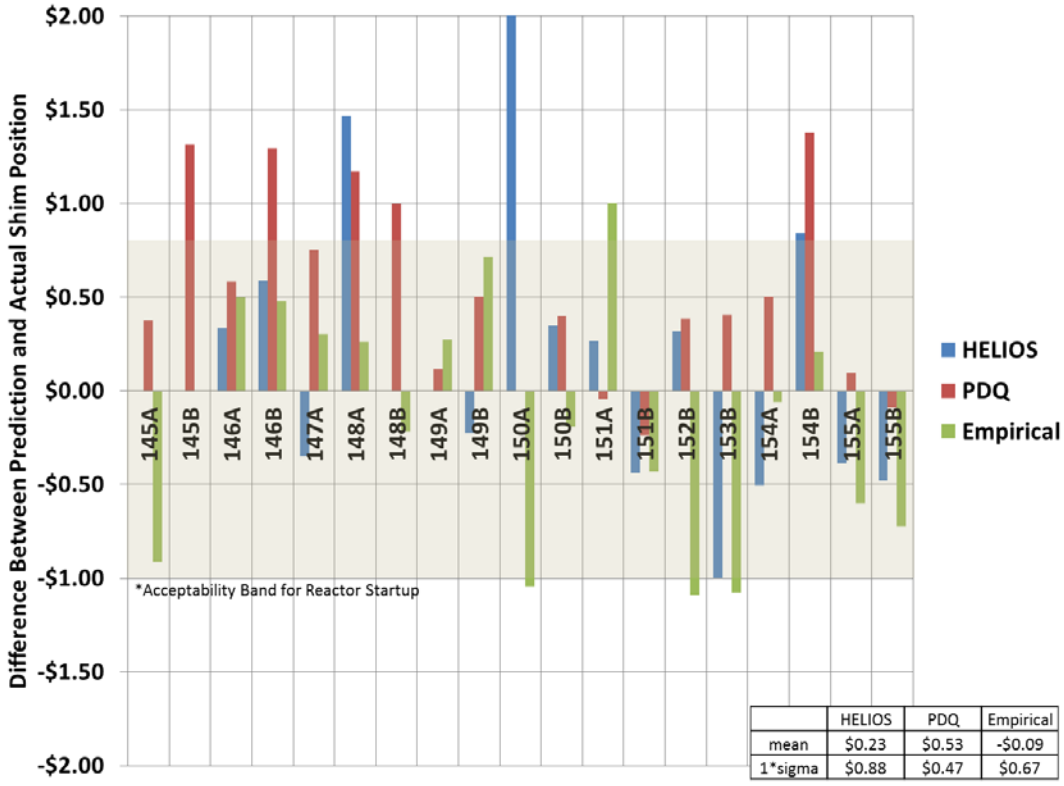

Figure 5.51 Reactivity worth of differences between predicted and reported OSCC critical position. If no result is shown for a particular methodology in a cycle then the difference between predicted and actual critical shim position was negligible.

5.6.3 Results – Lobe Powers

The lobe-power distribution in the ATR is sensitive to fuel loading, flux trap and capsule loading, OSCC and neck-shim position. To create an accurate representation of the ATR lobe powers, the exact configuration of the reactor had to be represented as faithfully as possible for all of the 16 cycles. Over the course of this work it was found that even the smallest capsules had to be modeled with sufficient resolution to capture localized spatial shielding, local reactivity importance or both. Lack of sufficient capsule detail could lead to lobe-power errors, $\varepsilon=({}^{lobe}P_{HELIOS} - {}^{lobe}P_{ASUDAS})/{}^{lobe}P_{ASUDAS}$, in excess of 15% (Nigg and Steuhm., 2012), a finding that is not surprising with an *a priori* high-fidelity code such as HELIOS. Thus, in the course of this work the following non-fuel features required careful modeling attention: 22 capsule experiments, four isotope production capsule types, seven civilian flux trap experiments, 20 flux-trap experiments for the United States Navy, and five flux-trap backups (i.e., place-holder hardware). In addition, ten different types of fillers, plugs, flow-reducers and fixed burnable shims were modeled.

The lobe-power results are compared with the ASUDAS data as a function of integrated core burnup for all 16 cycles for each lobe separately in Figures 5.52 – 5.56. Figure 5.57 then shows a statistical analysis of the differences between HELIOS lobe powers and corresponding measurements as a function of integrated core burnup for all five lobes together. As can be seen from the curves, the standard deviation of the all of the differences between HELIOS and measurement over the entire set of cycles was on the order of 5%. This is comparable to the reported uncertainty of the measurements themselves (Atkinson and McCracken, 1997). The mean difference was near zero, once again because the total core power of the HELIOS model was forced to be essentially equal to the total measured reactor power. Finally, a one-sided 95% confidence interval may be estimated using the methodology in section 5.3.5, now using a value of 1.65 for the factor K_c because of the large sample size for the data shown in Figure 5.57. This yields value of approximately 8.3% for the one-sided 95%

confidence interval, indicating that only 5% of the lobe powers may be expected to exceed the measurement by more than 8.3% based on the data of Figure 5.57.

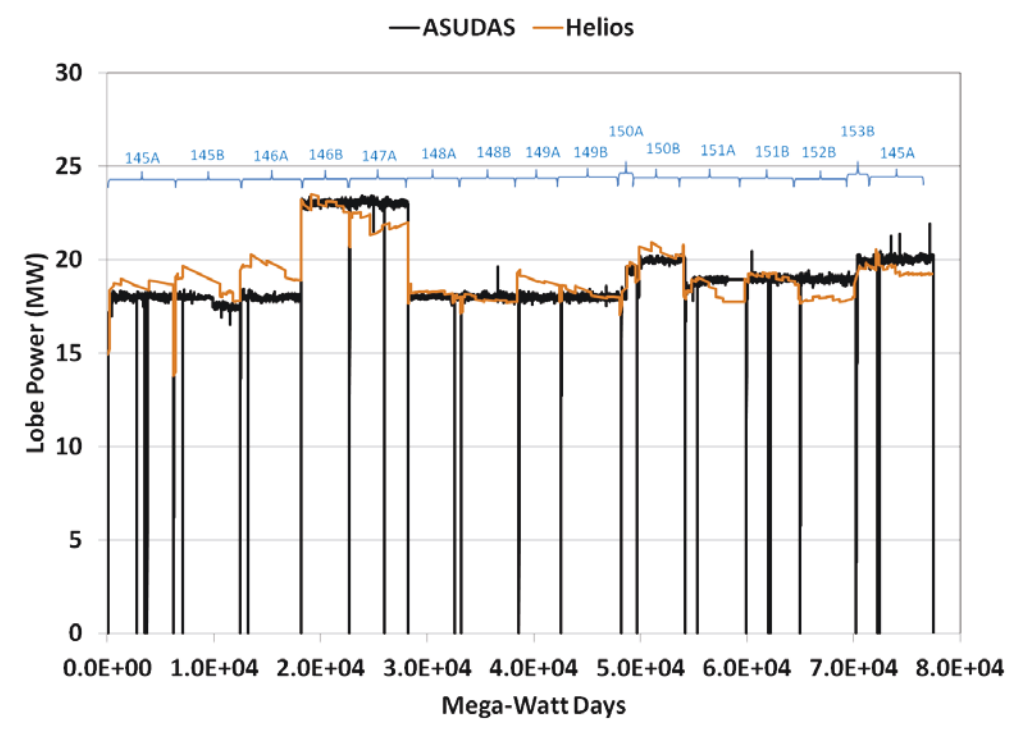

Figure 5.52 Northwest lobe power comparison between ASUDAS surveillance data and HELIOS

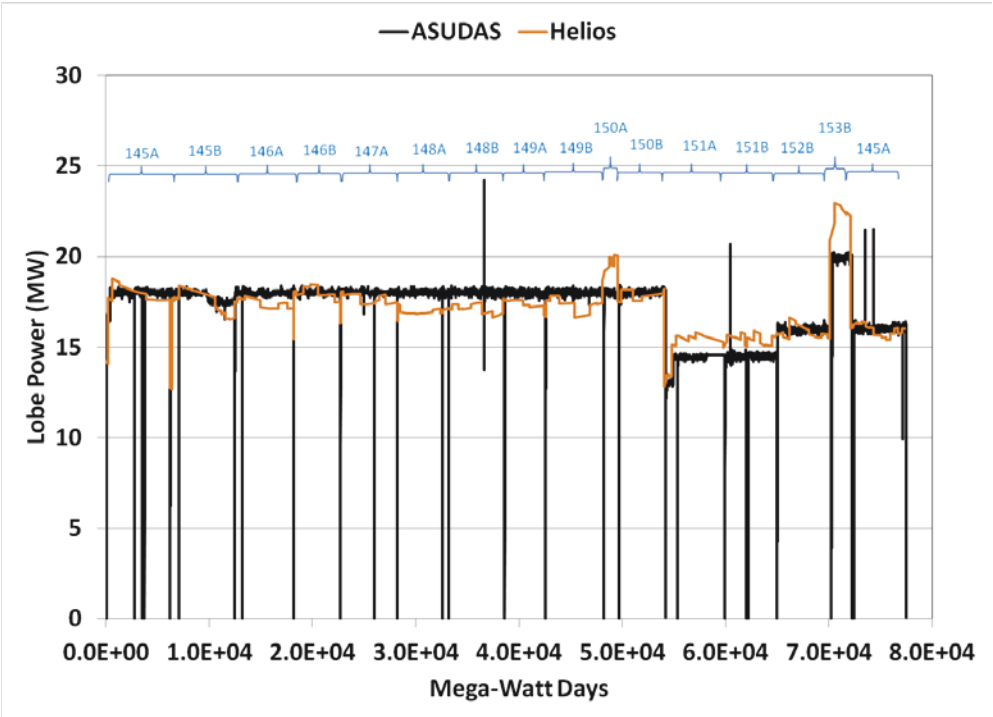

Figure 5.53 Northeast lobe power comparison between ASUDAS surveillance data and HELIOS

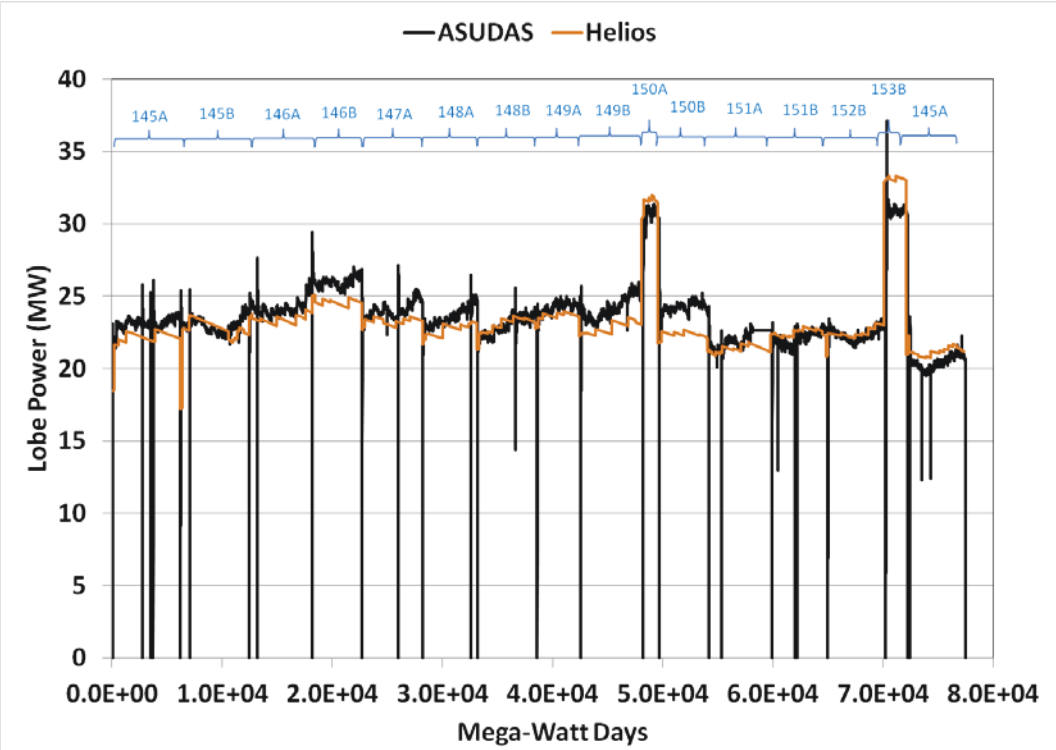

Figure 5.54 Center lobe power comparison between ASUDAS surveillance and HELIOS

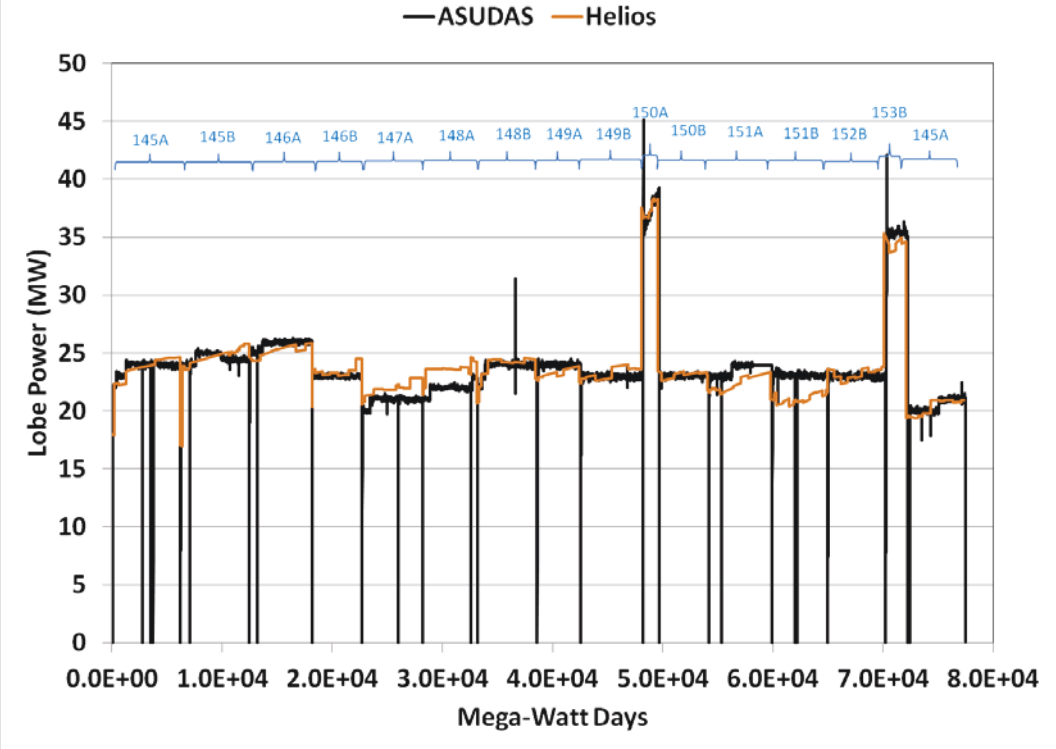

Figure 5.55 Southwest lobe power comparison between ASUDAS surveillance and HELIOS

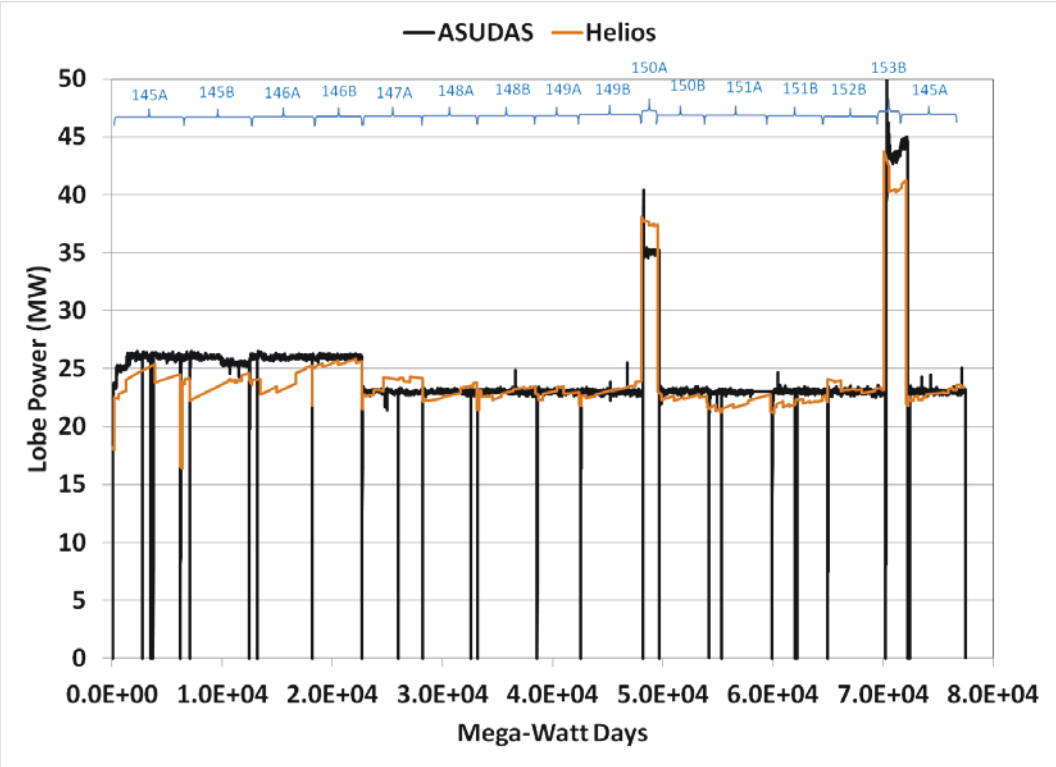

Figure 5.56 Southeast lobe power comparison between ASUDAS surveillance and HELIOS

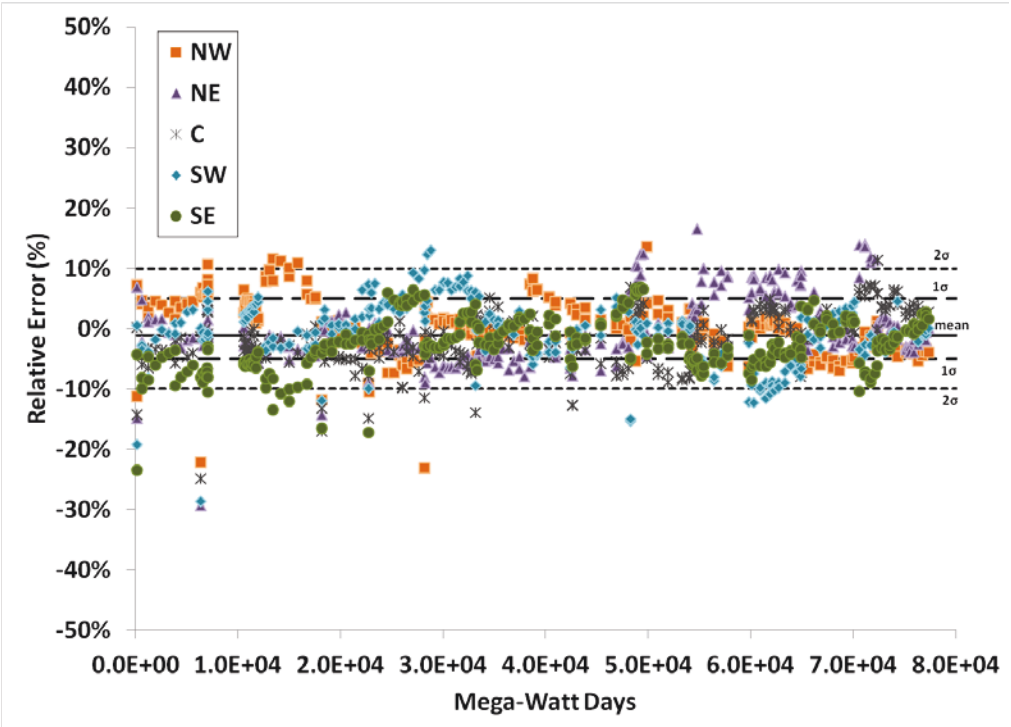

Figure 5.57 Relative error between lobe-powers reported by ASUDAS versus calculated by HELIOS

Another check for accuracy of the core-follow, including the effect of fuel burnup during the cycle, is the adherence to criticality throughout the entire cycle. Figure 5.58 shows the 2D transport eigenvalue for each state and burnup point from the core-follow analyses plotted against the reference 2D transport eigenvalue associated with the cold startup criticality. As can be seen from the plot, the discretization methodology chosen for establishing each core state (i.e., burn step) was sufficiently fine to closely match the critical eigenvalue from

startup. Note that the negative temperature feedback effect on core reactivity is not considered in this comparison. Also plotted in Figure 5.58 is the reactivity worth for each burn-step, $\rho=(k-k_c)/(k\times k_c)$. This curve shows that the discretization methodology very rarely, if ever, deviated from the actual critical condition by more than one dollar once xenon equilibrium is attained.

The occasional spikes in the BOC eigenvalues for each cycle is due in part to the fact that the core-follow cycles do not consider the first few hours between cold startup and hot-full-power. The HELIOS "C" option was used for all burn steps which is a standard predictor-corrector treatment. The predictor step uses the flux from the beginning-of-step transport solution to create end-of-step nuclide densities. The corrector step uses these end-of-step nuclide densities to re-deplete the beginning-of-step nuclides. The final end-of-step nuclide densities reported by HELIOS are the average of the predictor and the corrector steps. Therefore, the BOC transport calculation for each cycle considers the xenon concentration to be zero when in reality it has had some time to buildup. The lack of the negative reactivity contribution from this neutron poison results in the seemingly large BOC reactivity spikes.

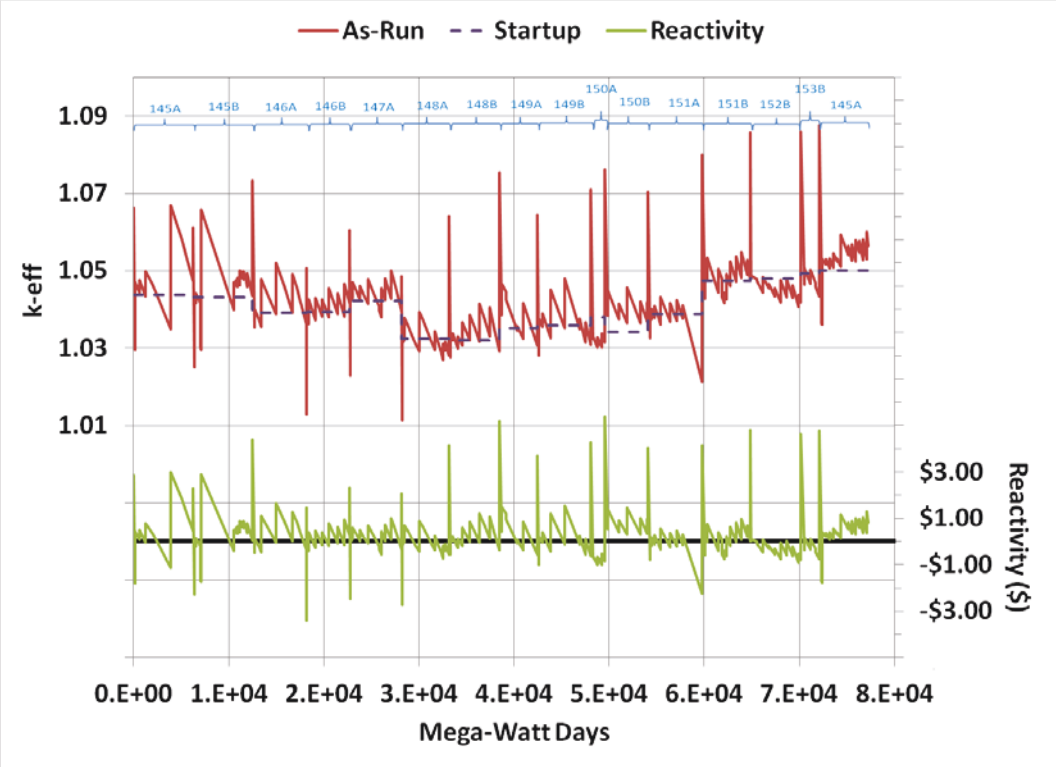

Figure 5.58. Reactivity worth at beginning and end of each burn step

6.0 DISCUSSION AND CONCLUSIONS

David W. Nigg, Samuel E. Bays

Although the comprehensive demonstration of a few detailed procedure-specific technical capabilities for CSAP support remains to be completed during the 2015 implementation campaign for the new physics methodologies, the new computational reactor physics methodologies are now generally operational, they have been applied retrospectively to all cycles since 145A, and they are now being used for informal preparation of prospective CSAP physics data in parallel with the established PDQ7-based CSAP physics support process. Furthermore, extensive neutron flux and fission power distribution verification and validation protocols based on current national standards have been established and demonstrated for all of the key new reactor physics codes of primary interest.

Based on experience to date, it may be concluded that the computational reactor physics methodology based on the HELIOS code and the supporting auxiliary software described in this Annual Report and its predecessors can replace the capabilities of the legacy PDQ7-based methodology via a focused formal deployment campaign within the next 6-12 months, with the relatively minor caution that significant additional validation will be needed prior to deployment of the planned MCNP-based method for correction of two-dimensional HELIOS results for axial effects as a routine replacement for the legacy ROSUB formulations. In the meantime, the established ROSUB methodology will continue to be used, augmented as needed on a case by case basis by the MCNP-based approach as it matures.

The new methodology will provide significantly higher fidelity with fewer mathematical approximations via a transport theory-based approach, in contrast to the diffusion theory-based legacy methodology. Furthermore, the new verification and validation protocols offer significantly improved rigor for quantification of uncertainties associated with computed fission power distributions throughout the core fuel elements as well as for neutron spectra within the ATR core fuel elements and within the various experiment positions (although it must be noted that rigorous validation of fission power distributions in cores containing fuel elements that are being re-used in a particular cycle after use in one or more previous cycles is currently constrained to the lobe level of geometric fidelity by the lack of element-level experimental data). In addition, the new methodology permits direct, detailed, explicit modeling of experiment hardware loaded in the flux traps and other experiment positions, with or without fissile content as described in more detail below. It is not necessary to pre-compute effective diffusion theory parameters for experiments based on equivalence theory approximations. This will greatly facilitate the management of multiple, potentially interacting experiments in each cycle.

One key feature of the new methodology includes a much-improved capability to analyze lobe power splits and to assimilate measured ATR lobe power data into the analysis on a continuous basis if desired. Both PDQ7 and HELIOS are able to model power splits by adjusting the OSCCs to discrete positions, modeling each neck shim as fully in or fully out, and estimating fuel element powers from the eight elements that make up each lobe. In addition, the HELIOS model is capable of representing each OSCC position explicitly and independently. Thus, extremely precise lobe powers can be modeled by HELIOS for bounding analyses, which is expected to reduce engineering uncertainty in limitations presented in the SAR. Furthermore, a methodology for rigorously quantifying the uncertainties of the lobe powers based on the ATR ASUDAS lobe power measurement system is presented. Finally, a new covariance matrix based method for continuously estimating individual element powers and their uncertainties based on the lobe power measurements that are periodically recorded during ATR operations is provided.

Estimates of the spatial power distributions within in the individual fuel plates of each core fuel element are also needed for SAR analyses. In the legacy methodology the GOPP interpolation program provides azimuthal power distributions in 11 of the 19 plates in an element. This information is used to determine power density values that ultimately feed into effective plate power calculations. Approximations are used in the PDQ7 code such that the areas used for flux calculations do not coincide with the areas used to define compositions. Thus, the power in each point on a plate is not calculated using consistent area definitions. Additional approximations in power are introduced within the PDQ7-based methodology through the use of homogenization within fuel elements and the

extensive use of linear interpolation between relatively few independent data points to define the azimuthal power profile over a plate. In contrast, HELIOS performs explicit fuel plate power calculations utilizing consistent areas, precise fuel meat representations, and explicitly determines the azimuthal power profile at a similar resolution as the profile provided by the PDQ7 methodology. HELIOS performs no linear interpolation between data points to provide this level of profile resolution. In addition, power profiles are provided for all 19 plates of an element. Furthermore, a methodology for quantifying the uncertainties of the plate power distributions is presented. All of these features should result in a significant decrease in engineering uncertainty with regard to SAR calculations.

Another capability is related to the need for modeling the ATR core when it is loaded with fresh fuel as well as a mix of fresh and burned fuel. Both PDQ7 and HELIOS are able to analyze any of the standard element types in any position of the core. HELIOS is capable of modeling non-standard element types as well with minimal alterations to the model. The PDQ7 methodology has been used to model non-standard element types, but this required an extensive amount of research and customization and resulted in large amounts of restrictions on the use of the non-standard element type, Swain et. al. (2011).

Additionally, the 2D PDQ7 methodology requires a fairly significant amount of approximation with regards to composition placement as well as composition precision and isotopic simplifications. HELIOS models individual fuel elements and maintains the composition of those elements explicitly. The HELIOS cross sections used to represent the neutronic effects within elements have also been significantly refined from those used by PDQ7. Thus, the use of HELIOS will greatly reduce the effort needed to represent new element designs while significantly increasing the fidelity of the calculations performed for these designs.

Returning briefly to management of experiments, modeling of experiments within the baseline ATR core fuel management model is also a required capability, since the characteristics of a given set of experiment loadings can have a notable effect on the core excess reactivity and power distribution. Currently, standard cell spectrum codes are used to provide macroscopic cross sections to PDQ7. These codes require significant simplifications and adjustments to experiment geometry and composition. The geometry input into PDQ7 itself requires additional geometry simplifications. HELIOS is able to model experiment geometry and composition explicitly or as homogenized components without the need for separate cross section generation codes. Changes to experiment locations, such as replacing LIPTs with SIPTs during a perturbation study, can be performed extremely easily utilizing HELIOS. This same evolution would require extensive model changes utilizing the PDQ7 code. Thus, HELIOS is able to represent the 2D effects on the fuel elements due to ATR experiments, whether they are inside or outside the in-pile tubes, with greater precision and ease than then the PDQ7 model.

The SAR is also supported by bounding PDQ7 calculations that model reactor SCRAM recoveries and restarts with various SCRAM durations. Both PDQ7 and HELIOS are able to model the major fission products as they are produced and decayed. HELIOS is also able to model all of the relevant fission products, not just the major isotopes. This allows a precise calculation of the cumulative effect of fission products in the core. The cumulative fission product effect is modeled in PDQ7 using a surrogate isotope that approximates the expected effects. This approximation is likely to have the largest uncertainty when modeling SCRAM recoveries. Thus, the results obtained via HELIOS are expected to be accurate such that any potentially non-conservative assumptions made by PDQ7 are eliminated.

7.0 REFERENCES

Aboanber, "Numerical Solution of the Chain Model of Fission Product Nuclides. Effect on the Reactivity of the Reactor," Annals of Nuclear Energy, vol. 28, pp 923-933 (2001)

ANS (American Nuclear Society), "Determination of Steady-State Neutron Reaction Rate Distributions and Reactivity of Nuclear Power Reactors", ANSI/ANS-19.3-2005.

R. Aryaeinejad, D. Crawford, M. DeHart, G. Griffith, B. Gross, D. Lucas, J. Nielsen, D. Nigg, J. Navarro, J. Parry, J. Peterson, K. Steuhm, "Advanced Test Reactor Core Modeling Update Project – Annual Report for Fiscal Year 2010," Idaho National Laboratory, INL/EXT-10-19940, (September 2010).

ASTM (American Society for Testing and Materials), "Standard Practice for Determining Neutron Fluence, Fluence Rate, and Spectra by Radioactivation Techniques", ASTM-E261-10 (2010)

ASTM (American Society for Testing and Materials), "Standard Test Method for Determining Thermal Neutron ReactionRates and Thermal Neutron Fluence Rates by Radioactivation Techniques", ASTM-E262-08 (2008)

ASTM (American Society for Testing and Materials), "Standard Guide for Application of Neutron Spectrum Adjustment Methods in Reactor Survieillience", ASTM-E944-08 (2008)

Atkinson, S.A. and McCracken, R.T. "Advanced test reactor Lobe Power Uncertainty", TRA-ATR-1211, Revision 1 (March 1997).

J. Beeston, R. Hobbins, G. Gibson, W. Francis, "Development and Irradiation Performance of Uranium Aluminide Fuels in Test Reactors," Nuclear Technology, Vol. 49, Pg. 136-149, (1980).

Bowman, S. M. (Ed.), *SCALE: A Modular Code System for Performing Standardized Computer Analyses for Licensing Evaluation*, ORNL/TM-2005/39, Version 6, Vols. I–III, Oak Ridge National Laboratory, Oak Ridge, Tennessee, January 2009. Available from Radiation Safety Information Computational Center at Oak Ridge National Laboratory as CCC-750.

R. Breen, O. Marlowe, C. Pfeifer, "HARMONY: System for Nuclear Reactor Depletion Computation," Idaho National Laboratory, WAPD-TM-478, (January 1965).

W. Cook, "Calculated Fast Flux Data for ATR LIPT Facilities," EG&G Idaho, Inc., RE-P-81-081, (1981).

C. Davis, G. Roth, "Evaluation of Variations in the ATR Axial Power Distribution on Core Safety Margins," Idaho National Laboratory, ECAR-2179, (2014).

DeHart, M. D., Advancements in Generalized-Geometry Discrete Ordinates Transport for Lattice Physics Calculations, A154.pdf in Proc. of PHYSOR–2006, American Nuclear Society Topical Meeting on Reactor Physics: Advances in Nuclear Analysis and Simulation, September 10–14, 2006, Vancouver, British Columbia, Canada.

Durney, J. L. and N.C. Kaufman, Calculating Reactor Power from Activation Techniques as Applied to Unusual Fuel Geometry (ATRC), IN-1047, January, 1967

S. Easson and A. Smith, "Assessment of ROSUB for ATR/CSAP Applications," EG&G Idaho, Inc., RE-P-81-076, (1981).

B. El Bakkari, T. El Merroun, Ch. El Younouussi, Y. Boulaich, E. Chakir, "Development of an MCNP-tally based burnup code and validation through PWR benchmark exercises," Annals of Nuclear Energy, vol. 36, pp. 626-633 (2009).

W. Gegory letter to J. Durney, "ATR Hafnium Burnup Program," Idaho National Laboratory, INL Internal Document GRE-33-78, (1978).

Goorley, T. Bull, J., Brown, F. et. al., "Release of MCNP5_RSICC_1.30," MCNP Monte Carlo Team X-5, LA-UR-04-4519, Los Alamos National Laboratory, November 2004 and, X-5 Monte Carlo Team, "MCNP—A General Monte Carlo N-Particle Transport Code, Version 5," Volume I, LA-UR-03-1987, Los Alamos National Laboratory, April 24, 2003 (Revised 6/30/2004) and Volume II, LA-CP-0245, Los Alamos National Laboratory, April 24, 2003 (Revised 6/30/2004).

Harker, Y.D., Anderl, R.A., Becker, G.K., Miller, L.G., Spectral Characterization of the Epithermal Neutron Beam at the Brookhaven Medical Research Reactor, Nuclear Science and Engineering **110:**355-368 (1992).

Hollenbach, D.F., Petrie, L.M., Landers, N.F., KENO-VI: A General Quadratic Version of the KENO Program, ORNL/TM-13011, Lockheed Martin Energy Research Corp., Oak Ridge National Laboratory, 1996.

M. R. Holtz, "Usage of ATR Fuel Elements Exposed to an Asymmetric Axial Flux Adjacent to Standard Inpile Tube Tests", TEV-1671, February 4, 2013.

Horneck, D.G. , "Prairie Island Nuclear Power Plant – Qualification of Reactor Physics Methods for Application to Prairie Island", Northerns States Power Company Topical Report NSPNAD-8101, Revision 2, December 1999.

Kim, S. S. and Schnitzler, B. G., Advanced Test Reactor: Serpentine Arrangement of Highly Enriched Water-Moderated Uranium-Aluminide Fuel Plates Reflected by Beryllium" HEU-SOLTHERM-022, *International Handbook of Evaluated Criticality Safety Benchmark Experiments*, NEA/NSC/DOC(95)03, OECD-NEA (2008).

Kitada, T. and Takeda, T., "Effective Convergence of Fission Source Distribution in Monte Carlo Simulation", *J. Nuclear Science and Technology,* **38:**324-329 (2001).

J. Hykes and R. Ferrer, "Solving the Bateman Equations in CASMO5 Using IMPLICIT ODE Numerical Methods for Stiff Systems," Proc. of M&C 2013, pp. 1551-1564, (2013).

S. Kim and J. McClure, "PDQ Reactor Physics Analysis for the ATR-FSAR UPGRADE," EG&G Idaho, Inc., PG-T-92-003, rev. 1, (1992).

Leppänen, J., 2012. "Serpent Progress Report 2011", VTT Technical Research Centre of Finland (2012), VTT-R-05444-12.

G. Marchuk, "A Survey of Nuclear-reactor Design Methods," Atommaya Energiya Vol. 11, No. 4, pp. 356-369, 1961.

R. McCracken, J. Abrashoff, W. Cook, L. Loret, A. Smith, W. Yarbrough, "Results of Nuclear Requalification Testing Following the ATR Reflector V Core Internals Changeout Outage," Idaho National Engineering Laboratory, INEL-94/089, (1994).

McGhee, J.M., Wareing, T.A., Barnett, D.J., ATTILA Version 5: User Manual, Transpire Inc., Gig Harbour WA, USA (2006).

J.W. Nielsen, D.W. Nigg, A.W. LaPorta, A Fission Matrix Based Validation Protocol for Computed Power Distributions in the Advanced Test Reactor, International Conference on Mathematics and Computational Methods Applied to Nuclear Science & Engineering (M&C 2013), Sun Valley, Idaho, USA, May 5-9, 2013.

D.W. Nigg, K. Steuhm (Editors), Advanced Test Reactor Core Modeling Update Project Annual Report for Fiscal Year 2011, INL/EXT-11-23348, September 2011.

D.W. Nigg, J.W. Nielsen, B.M. Chase, R.K. Murray, K.A. Steuhm, T. Unruh, Improved Computational Neutronics Methods and Validation Protocols for the Advanced Test Reactor, Proceedings of the American Nuclear Society International Topical Meeting on Advances in Reactor Physics (PHYSOR-12), Knoxville, Tennessee, April 15-19, 2012 (2012a)

D.W. Nigg, J.W. Nielsen, G.K. Taylor, Validation Protocols to Support the Neutronics Modeling, Simulation, and V&V Upgrade for the Advanced Test Reactor, *Trans ANS,* **106:**890-893 (2012b)

D.W. Nigg and K.A. Steuhm (Editors), Advanced Test Reactor Core Modeling Update Project Annual Report for Fiscal Year 2012, INL/EXT-12-27059. September 2012 (2012)

D.W. Nigg and K.A. Steuhm (Editors), Advanced Test Reactor Core Modeling Update Project Annual Report for Fiscal Year 2013, INL/EXT-13-30085. September 2013 (2013)

Organization for Economic Cooperation and Development (OECD), Nuclear Energy Agency, "International Handbook for Evaluated Reactor Physics Benchmark Experiments", NEA/NSC/DOC (2012).

Pfeifer, C.J., PDQ Reference Manual II, WAPD-TM-947(L), 1971.

S. Polkinghorne, "ATR-SINDA and SINDA-SAMPLE Calculations for Chapter 15 of the ATR's Updated FSAR," Idaho National Laboratory, TRA-ATR-840, (1994).

J. E. Poling, "Results of Reactor Physics Safety Analysis for Advanced Test Reactor Cycle 152B-1", ECAR-2080, November 5, 2012.

Radiation Safety Information Computational Center, NJOY99- Code System for Producing Pointwise and Multigroup Neutron and Photon Cross Sections from ENDF/B Data and AMPX77- Modular Code System for Generating Coupled Multigroup Neutron-Gamma Libraries from ENDF/B, Oak Ridge National Laboratory (http://www-rsicc.ornl.gov), 2010.

Rhoades W.A., and Childs R.L., The DORT Two-Dimensional Discrete-Ordinates Transport Code, Nuclear Science and Engineering **99**:88-89 (1988).

JW Rogers, R.A. Anderl, "ATR Neutron Spectral Characterization", INEL-95/0494, Idaho National Laboratory, USA (1995).

R.W. Roussin, "BUGLE-80 Coupled 47-Neutron, 20 Gamma-Ray P3 Cross Section Library", DLC-75, Radiation Shielding Information Center, Oak Ridge National Laboratory, USA (1980).

J. Shultis, R. Faw, Fundamentals of Nuclear Science and Engineering, Marcel Dekker, Inc., (2002)

A. Smith, "Comparison of Measured and Calculated Fast Flux in ATR Loops with Standard Pressure Tubes," EG&G Idaho, Inc., RE-P-81-039, (1981a).

A. Smith, "Revised Comparison of Measured and Calculated Fast Flux in ATR Loops with Standard Pressure Tubes, EG&G Idaho, Inc., RE-P-81-054, (1981b).

A. Smith, W. Yoon, D. Auslander, W. Cook, "Reactivity Effect of Beryllium Reflector Poison in the ATR," Idaho National Laboratory, NRRT-N-90-021, (1990).

A. Smith to R. McCracken, "Average Axial Peaking Factors for Calculating Effective Plate Powers," Tracked Internal Communication, EG&G, Idaho, Inc., ACS-11-94, July 12, (1994).

"Specification For Advanced Test Reactor Mark VII Zone Loaded Fuel Elements, IN-F-9-ATR, Revision 17", SPC-415 Rev. 2, November 2, 2005.

C. J. Stanley, "Advanced Test Reactor Cycle 152B Preliminary Experiment Requirements Letter, Revision 5", Internal INL Document CJS-05-12, Rev. 5, November 27, 2012.

J. W. Sterbentz, "JMOCUP As-Run Daily Depletion Calculation for the AGR-1 Experiment in ATR B-10 Position", ECAR-958 Rev. 1, August 18, 2011.

Studsvik Scandpower, HELIOS Methods (Version 1.10), 2008.

Studsvik Scandpower, "HELIOS Methods (Version-2.0)," Studsvik Scandpower, (March 2009).

Sutton, T.M., et al., The MC21 Monte Carlo Transport Code, Knolls Atomic Power Laboratory and Bettis Laboratory, LM-06K144, 2007.

E. Swain, J. Shatford, "Development of a Computer Model of the RERTR Full-size Element," Idaho National Laboratory, ECAR-1148, (2011).

Tomberlin, T. A. "ATR Critical Facility Axial Fission Profile Acceptance Criteria (with assessments of ICE and MICE Experiments)", TRA-ATRC-1546, Rev. 0, March 2000.

T. H. Trumbull and E. Caro, NDEX – A Nuclear Data Processing System for the MC21 Monte Carlo Transport Solver, ARP-NE-08-031/B-R(D)-652, Knolls Atomic Power Laboratory, Niskayuna, NY (2009).
V. Vladimirov, "Ph.D. Dissertation," Stecklova Mathematics Institute, USSR. Quoted by Marchuk 1961, (1959)